THE ELECTRIC FORM FACTOR OF THE NEUTRON AT LOW MOMENTUM TRANSFERS AS MEASURED AT BATES LARGE ACCEPTANCE SPECTROMETER TOROID

by

Eugene J. Geis

A Dissertation Presented in Partial Fulfillment
of the Requirements for the Degree
Doctor of Philosophy

ARIZONA STATE UNIVERSITY

May 2007

Holla to my Immediate Family

and Pseudo-Extended Quasi-Families (PEQF, pronounced 'PeeQueeFam')

THE ELECTRIC FORM FACTOR OF THE NEUTRON AT LOW MOMENTUM

TRANSFERS AS MEASURED AT

BATES LARGE ACCEPTANCE SPECTROMETER TOROID

by

Eugene J. Geis

has been approved

May 2007

APPROVED:

_____, Chair

_____

_____

_____

_____

Supervisory Committee

ACCEPTED:

_____

Department Chair

_____

Dean, Graduate College

ABSTRACT

Elastic form factors are characteristic signatures of the electromagnetic properties of hadronic matter. The more precisely we can measure these values, the more powerful becomes the predictability of our theory.

The proton's form factors (G_E^p, G_M^p) have been measured remarkably well compared to the neutron. While the Magnetic form factor of the neutron is reasonably well known, the Electric Form Factor still retains difficulties due to its small magnitude and the relative inefficiency of detecting neutral particles. The lack of a pure neutron source is another obstacle.

Although we are in pursuit of the elastic form factors, the two-nucleon system of deuterium has been shown to be a worthy target for extracting data on the structure of nucleons as well as properties of few-body hadronic systems. Data from unpolarized cross-section measurements have proven insufficient for extracting G_E^n, but polarized scattering from a polarized Deuterium target has been shown to be well suited for determination of G_E^n. The double polarization observables of a vector polarized Deuterium target and polarized electron beam is proportional to the product of the electric and magnetic form factors of the neutron.

The Bates Large Acceptance Spectrometer Toroid (BLAST) has been developed specifically to measure the scattering of a polarized electron beam off a vector and tensor polarized deuterium target and thus fulfills our needs for extracting G_E^n. The Bates accelerator provides a high-duty polarized electron beam stored in the South Hall Ring (SHR) that is that is passing through an internal target of both vector and tensor polarized monatomic deuterium as well as polarized monatomic hydrogen provided by an Atomic

Beam Source (ABS). A large acceptance detector, BLAST, has been installed to measure several scattering reactions including the directly applicable ${}^2\vec{H}(\vec{e}, e'n)p$ reaction.

This work summarizes the experimental investigations of the extraction of G_E^n from the BLAST data. Points were extracted at four values of four-momentum transfers (Q^2 = 0.14, 0.20, 0.29, 0.41 GeV^2). The world's data and the new BLAST data were fit to determine G_E^n to $\pm 5.8\%$ from $0 < Q^2 < 1.8$ GeV^2. The best fit includes model dependent contributions from a low Q^2 bump and a smooth dipole term. A second fit is shown using a model independent sum of gaussians in order to provide a more reliable determination of the uncertainty of the world's measurement of G_E^n from double polarized scattering.

ACKNOWLEDGMENTS

Dear Ricardo, Tancredi, Michael, Doug, Karen, Jim, Ernie, Genya, Bill, Townsend, Taylan, Hauke, Dr. Alaine Young, Dr. Vitaly Ziskin, Dr. Chris Crawford, Dr. Aaron Maschinot, Dr. Peter Karpius, Dr. Adrian Sindile, Dr. Jason Seely, Dr. Chi Zhang, Dr. Octavian Filoti, Poet Adam DeGrush, Yuan Xiao, Ben Clasie, Richard, Bill, John, Dr. Daniel Martin, and Lucy Arvallo LMT,

Friends I have found. Strange work united us into subgroups analogous to *PEQF*'s. At least that is the extent of how "at-ease" I felt amongst each one of you. (Maybe... that could be why I'm so lazy ... ?) It's gonna be bright, bright, like a sunshiny day.

I hope there is a decent future ahead for physicists outside of the realm where bigger, uglier weapons made to destroy less economically feasible human beings still seems a necessity. Or potentially brighter and more optimistic than running code for rich cronies seeking to swallow as much virtual wealth as possible. Or possibly a fulfilling endeavor that restricts the boundaries of our current fossil fuel use and systematically forces an investment in highly efficient technology. I think I'm doomed for a life of wishful thinking followed by disappointment: such is the bane of idealism amongst a more powerful middle-aged ambivalence.

Sincerely, EuG_E^ne (BLAST Shift Taker #1 from 2/04-5/05)

TABLE OF CONTENTS

Page

Page

Page

LIST OF TABLES

LIST OF FIGURES

Figure Page

Figure Page

Figure Page

CHAPTER 1: **INTRODUCTION**

Physics is an interdependent foundation that gives and takes from all sciences in order to make itself as complete and adaptive as possible. Problems need to be solved and physicists solve them. Mathematicians live in the abstract, engineers are mundane, and physicists operate on that horizon in between.

Within the subject, there are interesting factions of scientists that also bridge a similar divide. Experimentalists and theorists represent the symbiotic shores with few historical heroes who have cleverly championed both with genius. Physics enables its constituencies to communicate using a common language of ideas and these ideas have enabled humanity to conquer natural laws and mold a new reality of lifestyle and perspective.

The foundations of physics took many years and mistakes to evolve. Electromagnetism has been a well-developed cornerstone of physics with roots in the development of optics and skeptical interpretations of electricity and magnetism. Eventually the conglomerate of well-defined mathematical theories used to describe electromagnetic phenomena were unified under James Clerk Maxwell's equations. These equations are utilized ubiquitously amongst all genres of science and are famous in their applicability and universality.

In the early 1900's, the nucleus of the intangible atom was discovered. Among the properties of the constituents of atoms to be experimentally verified, electric charge was proven to exist in clumps called *quanta*. Magnetism was also verified in playing a fundamental role, existing in close relation to these clumps of charge in a well-defined fashion. Maxwell's equations show that moving charge gives rise to a magnetic field and vice versa. A magnetic moment is created and defined by the angular momentum of a charge distribution which must exist for every subatomic clump of charge, e.g. the electron and the nucleus. These values of magnetic moments were solved and identified as the Bohr

magneton or the nuclear magneton. These are results of the *quantum* properties of the angular momentum of the electron and nucleus when solved in accordance with Maxwell's equations. This relationship even held when the nucleus was determined to consist of constituent particles known as the proton and neutron. The proton was considered as a massive clump of charge and the neutron was a clump of neutral mass.

In 1934, from the measurement of the magnetic moment of the deuteron and the proton, the neutron was assumed to have a calculable magnetic moment[1]. The magnetic moment has been measured using many experimental methods and has been well accounted for in relation to its nuclear interactions within the nucleus, nuclear scattering, and even neutron scattering from low to very high energies. Yet, as an individual particle, no presently existing strict theory gives the sign and value of the anomalous neutron magnetic moment. This indicates a complex internal structure that must be accounted for. Intuitively, we must make a conjecture that the actual existence of the magnetic moment is as a point-like magnetic dipole (the Bloch model) or is due to inner currents within a dynamic model of the neutron (the Schwinger model). This dynamic model must account for the neutron's properties as a result of the dynamics of the quark constituents or the existence of a virtual meson cloud or both. Model-dependent experiments have been done to distinguish whether the neutron's properties are consistent with the Schwinger model or the Bloch model, and all presently available experimental data agree with former and disagree with Bloch.

This brings us to the question of the description of the dynamics of the neutron. Theoretically and experimentally, physics must meet the challenge of establishing the vivification of the *neutral* neutron's charge distribution. The neutron's large magnetic moment creates a considerable difficulty in measuring the charge distribution since it so easily overwhelms most reproducible electromagnetic interactions providing measured observables at

the nucleon scale. Since there is no free neutron source, measurements on small nucleon systems also become subject to dynamic models and nucleonic potentials used to describe them. The solution to lowering these systematic errors of the scattering experiments on small nuclei is to use the polarizability of the small target nuclei and the electromagnetic probe. To this end, polarized electron beams were developed along with polarized monatomic hadronic targets.

Using polarization experiments, nuclear physicists have established a parameterization of the fourier transform of the neutron's charge distribution that is currently fit with an uncertainty of $\sim 6\%$[1] and even the charge radius has been measured at an accuracy of $\sim$5%[2]. Despite the experimental success, theory is still lagging and shows substantial discrepancies with measured results. Theory that well predicts the charge distribution at the outer region of the neutron systematically falls short of predicting the distribution within the inner region of the neutron and vice versa. The best current predictions are very recent and come from Dispersion Theory. Phenomenological fits to the world's data are diverse and well motivated yet lack fundamental reinforcement.

This work sums up the measurement of the neutron's charge distribution via the neutron's electric charge form factor, G_E^n, as measured in the outer region of the neutron as described by low momentum-transfer scattering from a deuterium target. Since we are probing the electric properties of the neutron, electron scattering is our method of examination. We must have a source of neutrons but since there is no stable free neutron target, deuterium is chosen as a best alternative by which to maintain minimal systematic errors while using a pre-existing well-developed dynamic nuclear model contributed by Hartmuth

[1]This number is a result of a global fit to the world's data, including the results of this work. This fit is a model dependent phenomenology, while a second fit will also be discussed in chapter 5 that is model independent and provides an uncertainty that does not include any assumptions about the structure of the neutron. That which is more valid may depend on who you talk to.

Arenhövel.

CHAPTER 2: **THEORY**

The electromagnetic structure of nucleons is complicated by and a result of the hadronic structure itself. Point particle interactions are well developed in quantum mechanics and relativistically treated in Quantum Electrodynamics (QED), yet the nucleon is an extended object consisting of more elementary particles quite different in composition and interaction than the leptonic probes we use to delve into their structure. Electron Scattering will be our weapon of choice in probing the structure of the neutron since the interaction of electrons with hadrons is given by QED and can hence be used to probe the structure of hadrons. The ensuing discussion will continue as a pedagogical overview.

When discussing scattering, the notable observable in all scattering experiments is the number of collisions that take place and the region, or solid angle, in which the outgoing products of the collision are detected in a solid angle $\Delta\Omega$. Written in terms familiar to nuclear physics experiments:

$$\dot{N}_{recoil} = \dot{N}_{incident} \times \rho_{target} \times L_{cell} \times \frac{d\sigma}{d\Omega} \times \Delta\Omega \tag{2.1}$$

where $\dot{N}_{recoil}$ is the number of particles scattered per unit time, $\dot{N}_{incident}$ is the number of incident particles per time used for scattering, ρ_{target} is the density of the target, L_{cell} is the length of the cell[1], $\frac{d\sigma}{d\Omega}$ is the *differential scattering cross-section*[2] or the probability of scattering incident particles impinging on a cross-sectional area $d\sigma$ into a solid angle $d\Omega$ relative to the scatterer (see Figure 2.1). This equation also assumes no multiple scattering.

In particle physics, scattering has been used since J. J. Thomson used an electric field to determine the mass of an electron in 1897[3]. The general construction of the theory

[1]This equation can also be written in terms more appropriate to the language of Experimental Particle Physics where Luminosity $\mathcal{L}$ is a commonly quoted quantity where $\mathcal{L} = \dot{N}_{incident}\rho_{target}L_{cell}$

[2]Nearly all the theory in this chapter is convoluted into this term

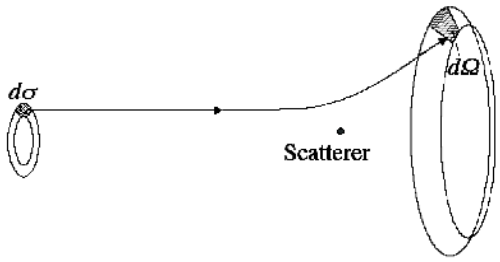

FIG. 2.1. Simple demonstration of the differential scattering cross-section.

of scattering can be developed using Classical Mechanics[4] or Wave Mechanics[5]. The most notable scattering experiment and equation may be from an experiment in 1909 in which Hans Geiger and Ernest Marsden, under the direction of Ernest Rutherford, fired α-particles at a gold leaf only a few atoms thick[6]. The general Rutherford differential scattering cross-section of an α-particle incident on a Coulomb potential of a point charge can easily be derived within Classical Mechanics or a Quantum Mechanics formalism and is written as:

$$\frac{d\sigma}{d\Omega} = \frac{\alpha^2 Z^2}{4m^2 v_\alpha^4 \sin^4(\theta_e/2)} \tag{2.2}$$

with α as the fine-structure constant, Z is the atomic number of the target, m is the mass of the scatterer, v_α is the velocity of the scattered α-particle and θ_α is the angle between the incoming and the outgoing momentum of the scattered α-particle. Equation 2.2 is derived using several assumptions,

Assumption I: it assumes an infinitely dense target;

Assumption II: it is purely Newtonian;

Assumption III: it assumes point particle interactions;

Obviously, all three assumptions in this list will have to be modified in order to accommodate our current objective.

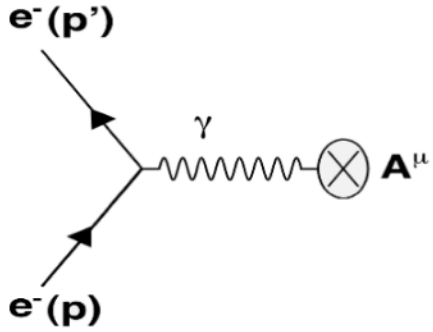

FIG. 2.2. Feynman diagram of a relativistic electron coulomb scattering from a massive target ($m_e \ll M_{target}$).

Nucleons, firstly, are not infinitely dense, i.e. they are not point-like. They are rather light in the ultimate scheme of things and show substantial recoil velocities at low momentum transfers. Secondly, to probe the structure of nucleons, the wavelength λ of the incident radiation must be on the order of or smaller than the nucleon ($\sim$1 fm). This means that the *de Broglie* wavelength of an electron used to probe the nucleon must satisfy the condition $\lambda_e = \frac{h}{p_e} < 1$ fm. This necessitates an electron velocity of at least $0.99999c$ where c is the speed of light. Therefore, we definitely necessitate a relativistic theory *and* we must certainly account for the recoil of the target since we are using ultrarelativistic incident electrons.

Before we ponder **Assumption III**, we will must modify our differential cross-section. In order to model the behavior with a relativistic quantum field theory, we must take on the accomplices of Dirac spinors and Weyl matrices and use the relativistic formalism for energy and momentum conservation[3]. The Feynman Diagram associated with relativistic Coulomb Scattering from a massive target ($m_e \ll M_{target}$) is depicted in Figure 2.2. In relativistic quantum field theory, taking on the typical convention $\hbar = c = 1$, all cross-

[3]I will follow the formalism of Peskin and Schroeder until otherwise noted.

sections can be computed from the general formula:

$$\begin{aligned} d\sigma &= \frac{1}{2E_{\mathcal{A}}2E_{\mathcal{B}}|v_{\mathcal{A}}-v_{\mathcal{B}}|}\left(\prod_f \frac{d^3p_f}{(2\pi)^3}\frac{1}{2E_f}\right)\times \\ &\qquad \overline{\sum_{if}}|\mathcal{M}_{fi}(p_{\mathcal{A}},p_{\mathcal{B}}\rightarrow\{p_f\})|^2(2\pi)^4\delta^{(4)}(p_{\mathcal{A}}+p_{\mathcal{B}}-\Sigma p_f) \end{aligned} \tag{2.3}$$

where p_i, v_i, and E_i refer to the kinematics of our interacting particles and *invariant scattering matrix element* is labeled $\mathcal{M}_{fi}(p_{\mathcal{A}}, p_{\mathcal{B}} \rightarrow \{p_f\})$, denoting the transition from initial state i to final state f. The delta function and phase space factors conserve momentum and energy for the reaction.

Going back to our initial (heuristic) problem of scattering from a Coulomb potential,

$$\mathcal{M}_{fi} = -ie\bar{u}^{s'}(p_f)\gamma^0 u^s(p_i)\tilde{A}_0(q) \tag{2.4}$$

where $\bar{u}^{s'}(p_f)$ and $u^s(p_i)$ are Dirac spinors associated with the outgoing and incoming electron and their respective spins s' and s which are summed and averaged, $ie\gamma^0$ corresponds to the QED electrostatic vertex, and $\tilde{A}_0(q) = \frac{Ze}{q^2}$ which is the Fourier transform of the Coulomb potential $A_0(r) = \frac{Ze}{4\pi r}e^{-\mu r}$ and q is the 4-momentum transfer $(p_f - p_i)$. $\mathcal{M}_{fi}$, in general, always enters our calculation as a contraction of the leptonic and hadronic currents corresponding to the Feynman rules invoked from the calculation of a particular diagram. $\mathcal{M}$ also consists of a sum over final states and an average over the initial states as depicted by the generality of the indices appropriated to Equation 2.3. When inserting Equation 2.4 into 2.3, the final cross-section can be computed (known as the Mott differential cross-section):

$$\frac{d\sigma}{d\Omega_e} = \frac{(Z\alpha)^2}{4v_e^2|\vec{p}^2|\sin^4(\theta_e/2)}[1 - v_e^2\sin^2(\theta_e/2)], \tag{2.5}$$

which reduces to the Rutherford cross-section at low momentum.

2.1. Unpolarized Elastic electron-nucleon Scattering and Form Factors

Experimental attempts to verify Equation 2.5 have been carried out and verified it to a good degree of accuracy with heavy elements ($Z \geq 12$) but only when convoluting the experimental cross-section with what became known as a *Form Factor*[7], e.g. $\frac{d\sigma}{d\Omega_e}_{exp} = \frac{d\sigma}{d\Omega_e}_{Mott} \times |F(q^2)|^2$. This Form Factor that we must invoke in order to reproduce the Mott cross-section is the Fourier transform of an extended spatial distribution of charge and further, allowed the phenomenological modeling of the size of the nucleus as $r = r_0 A^{1/3}$ where $r_0 = 1.2 \times 10^{-15}$m and A is the atomic number. This form factor immediately affects **Assumption III** and forces alteration of the concept of point-like interactions. Further, if we decrease the charge and size of our nucleus and attempt to probe nucleons themselves, we must increase our probe's energy and account for the recoil of the target. The recoil can be accounted for by simply inserting the divisor f_{rec} where E_e^0 is the initial energy of the scattered electron:

$$f_{rec} = 1 + 2\left(\frac{E_e^0}{m_N}\right) sin^2\left(\frac{\theta_e}{2}\right). \tag{2.6}$$

When moving to the case of a single nucleon or a small nucleus, spin effects add a magnetic interaction term to the coulombic term via the virtual photon coupling to the electromagnetic current in the target which is associated with the magnetic moment.

When using QED to obtain information regarding an applied field (all particles in quantum field theory can be thought of as *fields*), Lorentz invariance, discrete symmetries of QED, and the Ward Identity[4] will greatly constrain the form of the vertex function Γ^μ of the field. To lowest order, as in the $-ie\gamma^0$ term in Equation 2.4, $\Gamma^\mu = \gamma^\mu$. The mathematics constrains the final form of the QED vertex function to all orders to be a function of the

[4]Any quantum field theory book will contain a reference to the Ward Identity

4-vectors q^μ, p_i^μ, p_f^μ and the Weyl matrices γ^μ:

$$\Gamma^\mu(p_f, p_i) = \gamma^\mu F_1(q^2) + \frac{i\sigma^{\mu\nu}q_\nu}{2m}F_2(q^2), \qquad \text{where } \sigma^{\mu\nu} = \frac{i}{2}[\gamma^\mu, \gamma^\nu]. \tag{2.7}$$

The factors F_1 and F_2 are the *Dirac and Pauli form factors*, respectively, that are unknown functions of the Lorentz-invariant q^2. The *Dirac form factor* F_1 can be thought of as the fourier transform of the spatial distribution of the nucleon's charge and associate with the Dirac magnetic moment, and the *Pauli form factor* F_2 can be associated with the spatial distribution of the anomalous magnetic moment. This form (Equation 2.7) is used to phenomenologically model electron scattering from complex fields, notably neutrons, protons, deuterons, and an assortment of particles that can also be electromagnetically probed using leptonic scattering. To demonstrate the ideas implicit in this formulation of the vertex function, boundary conditions of these form factors for the proton and neutron can be inferred from the static electromagnetic properties of these nucleons, e.g.

$$F_1(q^2 = 0) = \begin{cases} 1 & \text{proton} \\ 0 & \text{neutron} \end{cases} \tag{2.8}$$

$$F_2(q^2 = 0) = \begin{cases} 0.79 & \text{proton} \\ -1.91 & \text{neutron} \end{cases} \tag{2.9}$$

A common form of the differential cross-section arising from a little algebra and the general form of the vertex function is known as the *Rosenbluth cross-section*[8] and is used to model the data from elastic electron-nucleon scattering where the nucleon has a mass m_N,

$$\left(\frac{d\sigma}{d\Omega_e}\right)_{ros} = \left(\frac{d\sigma_e}{d\Omega}\right)_{Mott} f_{rec}^{-1}\left[(F_1^2 + \tau F_2^2) + 2\tau(F_1 + F_2)^2 \tan^2\left(\frac{\theta_e}{2}\right)\right] \tag{2.10}$$

where $\tau \equiv Q^2/4m_N$ and $Q^2 \equiv -q^2$.

Sachs and collaborators suggested that certain linear combinations of the Dirac and Pauli form factors allowed for a physical interpretation of the structure of the nucleon[9]. The suggested form was,

$$\left.\begin{array}{rcl} G_E(Q^2) &=& F_1(Q^2) - \tau F_2(Q^2), \\ G_M(Q^2) &=& F_1(Q^2) + F_2(Q^2). \end{array}\right\} \left\{\begin{array}{rcl} F_1(Q^2) &=& \frac{1}{1+\tau}(G_E(Q^2) + \tau G_M(Q^2)), \\ F_2(Q^2) &=& \frac{1}{1+\tau}(G_M(Q^2) - G_E(Q^2)). \end{array}\right. \tag{2.11}$$

These *Sachs form factors* G_E and G_M are the well-known electric and magnetic form factors most often quoted in nuclear physics. In the "Breit Frame"[5], often referred to as the "brick-wall" frame where the kinematics of the reaction are boosted into a frame where the nucleon remains at rest, the Sachs form factors can be interpreted as the Fourier transforms of the spatial distributions of the charge density $\rho_{ch}(\vec{r})$ and the magnetic moment density $\rho_{magn}(\vec{r})$, i.e.

$$\begin{array}{rcl} G_E(Q^2) &=& \int \rho_{ch}(\vec{r}) e^{-i\vec{q}\vec{r}} d^3\vec{r}, \\ G_M(Q^2) &=& \mu \int \rho_{magn}(\vec{r}) e^{-i\vec{q}\vec{r}} d^3\vec{r} \end{array} \tag{2.12}$$

where μ is the total magnetic moment in units of μ_N, the nuclear magneton. If F_1 and F_2 and thus G_E and G_M are known, these physical interpretations immediately allow a calculation of the rms radius of the charge or magnetic moment distribution inside the neutron and proton, or conversely, an experiment where the rms radius of nucleons is measured would allow for the constraint of the slope at $Q^2 = 0$ since

$$< r_{ch}^2 >= -6 \left(\frac{dG_E(Q^2=0)}{dQ^2} \right), \qquad < r_{magn}^2 >= -\frac{6}{\mu} \left(\frac{dG_M(Q^2=0)}{dQ^2} \right). \tag{2.13}$$

The Rosenbluth differential cross section can also be rewritten in terms of G_E and G_M:

$$\left(\frac{d\sigma}{d\Omega_e} \right)_{ros} = \left(\frac{d\sigma}{d\Omega_e} \right)_{Mott} f_{rec}^{-1} \left(\frac{1}{1+\tau} \right) \left(\epsilon G_E^2 + \tau G_M^2 \right) \tag{2.14}$$

[5]The Breit Frame is described by a boost into the kinematic reference frame where the nucleon remains at rest, i.e. the incoming electron's momentum equals the outgoing momentum, $k_e = -k'_e$ and the energy transfer $\omega = 0$.

where ϵ is the transverse virtual photon polarization:

$$\epsilon \equiv 1 + 2(1+\tau)\tan^2(\theta_e/2). \tag{2.15}$$

It is obvious from the form in Equation 2.14 that we can divide out the Mott cross-section, recoil divisor, and the factor $(1+\tau)^{-1}$ and retain a quantity directly proportional to the Sachs form factors. This is known as the Rosenbluth Separation and has been historically employed in measuring the elastic electromagnetic form factors of the proton.

Equation 2.15 shows that τ and thus Q^2 plays a major role in our ability to accurately measure the form factors. Electron-proton scattering is highly sensitive to G_E^p at low momentum transfers but highly insensitive at high momentum transfers where the cross section is dominated by $\tau(G_M^p)^2$. Experiments[11, 12, 13, 14, 15, 17] have extracted data points on G_E^p up to $Q^2 \approx 10$ (GeV/c)^2 with error bars up to 40% at the highest Q^2 points[17]. G_M^p has been measured[10, 13, 14, 16, 18] up to $Q^2 \approx 30$ (GeV/c)^2 with error bars of $\sim 6\%$ at the highest Q^2 points[16].

Both form factors of the proton seem to conform well with the Dipole form factor ansatz:

$$G_E^p \approx \frac{G_M^p}{\mu_p} \approx G_D = \frac{1}{(1+Q^2/\Lambda)^2} \tag{2.16}$$

Λ comes from a global fit to the world's data and is usually quoted as 0.71 (GeV/c)^2. The dipole form factor is the Fourier transform of a radially symmetric distribution decaying exponentially and thus is a physically driven ansatz. The form factors conform well to G_D and G_E^p deviates no more than $\sim$6% up to 1 (GeV/c)^2 and G_M^p deviates no more than $\sim$6% up to about 8 (GeV/c)^2.

Measurements of the form factors of the neutron from elastic scattering are difficult since there is no free neutron source. The data on the form factors of the neutron

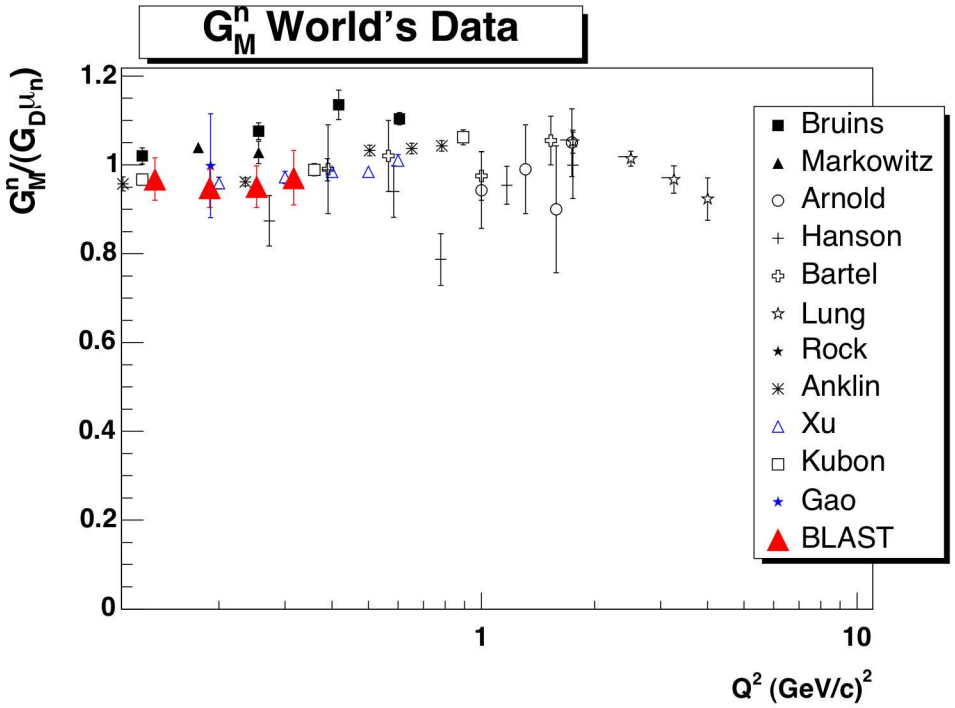

FIG. 2.3. The World's data on G_M^n. Unpolarized and polarized scattering experiments included. The form factor is shown divided by $\mu_n G_D$, again signifying the conformation of the data to the dipole form factor ansatz. They can be found in [19, 13, 20, 21, 22, 23, 24, 25, 26, 27, 28, 29, 30, 31, 32]. The BLAST data shown is preliminary.

from unpolarized scattering comes from deuterium targets and recently ^{3}He. Since G_M^n is nearly two orders of magnitude greater than G_E^n, the unpolarized exclusive quasielastic scattering cross section will do well to model the form factor G_M^n but G_E^n necessitates more precise experimental techniques. And though we may exclusively detect neutrons from the multi-nucleon target, the situation is further complicated by the initial state of the target, final-state interactions occurring after electrodisintegration, and the relatively low efficiency of neutral particle detection. This latter difficulty can be overcome by using polarized scattering where the detection efficiency cancels out to first order.

Shown in Figure 2.3 is the world's data on G_M^n. The conformation of the data to the dipole fit is immediately apparent by noticing the range over which the data points remain

close to one. The data on G_E^n from unpolarized electron scattering will be discussed in Section 2.4.2. Since the target from which we intend to extract our data from is deuterium, a solid introduction to the deuteron's properties is in order.

2.2. The Deuteron

The only bound two-nucleon system in nature is the deuteron consisting of a proton and neutron lightly bound together. The isospin, angular momentum, and parity are $I(J^P) = 0(1^+)$. Since the theoretical prediction and experimental measurement of the deuteron's magnetic moment have shown discrepancies, it has since been concluded and affirmed that there is an admixture of $^3S_1$ and $^3D_1$ states in the deuteron's wave function. The D-wave contribution asserts a tensor component to the attractive force that keeps the nucleons bound and thus allows us to use the deuteron also to probe the tensor component of the NN interaction. Though the proper model of the potential of the deuteron is still under debate, a discussion can be found in [36]. Once given a potential, solving the Schrödinger equation for the system at rest allows the following description of the ground state wave function.

The deuteron's wave function in space is

$$\Psi_M(\mathbf{r}) = \frac{u(r)}{r}\mathcal{Y}^M_{101}(\theta,\phi) + \frac{w(r)}{r}\mathcal{Y}^M_{121}(\theta,\phi), \tag{2.17}$$

where

$$\mathcal{Y}^M_{JLS} = \sum_{m_L,m_S} \langle J,M|L,m_L;S,m_S\rangle Y_{LM}(\theta,\phi)|S,m_S\rangle \tag{2.18}$$

are the spin-spherical harmonics where M refers to the m_J substates and the z-axis ($\theta = 0$) is the axis of polarization. $u(r)$ and $w(r)$ are the radial wave functions of the S and D

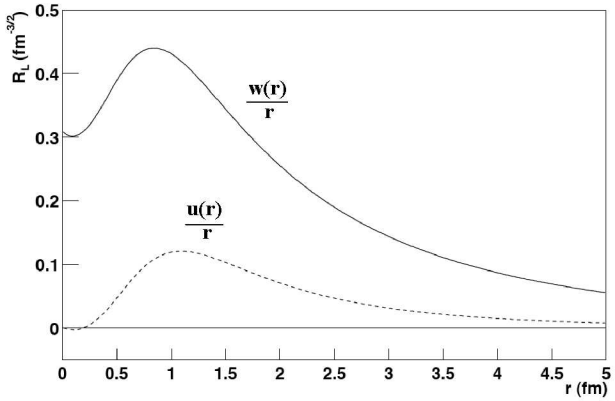

FIG. 2.4. The spatial wave functions of the S and D states in the deuteron when calculated using the *Bonn-Qb* potential.

wave states, respectively, where the probability densities are defined as their squares and the total normalization of the wave function must satisfy

$$\int_0^\infty (u^2(r) + w^2(r))dr = 1 \tag{2.19}$$

and the densities of the respective states of the deuteron are defined as

$$\begin{aligned}
\rho_0(\mathbf{r}) &= \Psi_0^\dagger(\mathbf{r})\Psi_0(\mathbf{r}) \\
&= \frac{1}{4\pi}\left[\frac{u(r)}{r} - \sqrt{2}\frac{w(r)}{r}\left(\frac{3}{2}\cos^2\theta - \frac{1}{2}\right)\right]^2 + \frac{9}{8\pi}\left(\frac{w(r)}{r}\sin\theta\cos\theta\right)^2 \\
\rho_2(\mathbf{r}) &= \Psi_2^\dagger(\mathbf{r})\Psi_2(\mathbf{r}) \\
&= \frac{1}{4\pi}\left[\frac{u(r)}{r} - \frac{w(r)}{\sqrt{2}r}\left(\frac{3}{2}\cos^2\theta - \frac{1}{2}\right)\right]^2 + \frac{9}{32\pi}\left(\frac{w(r)}{r}\sin\theta\right)^2(1+\cos^2\theta).
\end{aligned} \tag{2.20}$$

The radial wave functions of the *bonn* potential are demonstrated in Figure 2.4. The significant reduction of the radial S wave function is a result of the repulsive nature of the NN interaction at distances < 1 fm. The one-boson exchange or long-range description also creates the quick drop-off of both radial functions after the maximum at approximately 1 fm. The densities of the deuteron wave functions $\Psi_0(\mathbf{r})$ and $\Psi_1(\mathbf{r})$ are shown in Figure 2.6 and demonstrated for several potentials in Figure 2.5. When $m_J = 0$, the density along

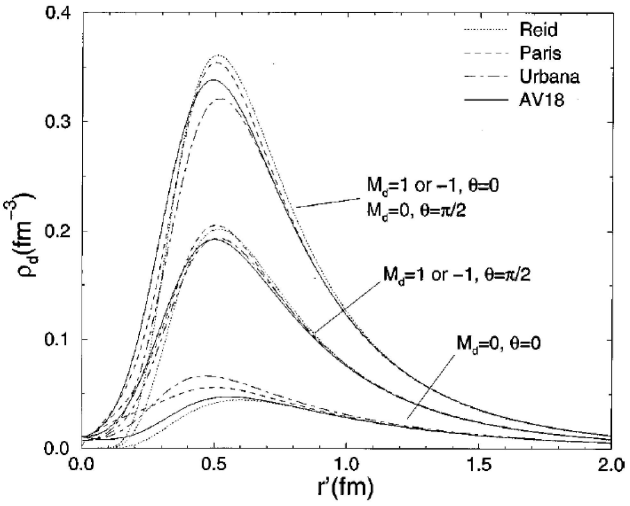

FIG. 2.5. The density of the deuteron along the axis of the projection of m_J and the transverse axis for the states $m_J = 0, \pm 1$. The densities are shown for several choices of the deuteron potential.

the axis of polarization is very small and results in a toroidal or "doughnut" shape. In the $m_J = \pm 1$ substates, the density is centered along the z-axis and gives a "barbell" shape.

The magnetic moment of the deuteron,

$$\mu_d = \mu_n + \mu_p - \frac{3}{2}\left(\mu_n + \mu_p - \frac{1}{2}\right) P_D \tag{2.21}$$

provides a general indication of the admixture of the D wave state thanks to the factor P_D, or the probability of the D-state $P_D = \int_0^\infty w^2(r)dr$. $\mu_n = -1.91304\mu_N$ and $\mu_p = 2.79285\mu_N$ are the nuclear magnetic moments expressed in units of the nuclear magneton μ_N. The experimental value of the magnetic moment predicts $P_D \sim 4\%$[38]. The quadrupole moment of the deuteron is also a function of the radial wave functions:

$$Q_d = \frac{1}{\sqrt{50}} \int_0^\infty w(r) \left[u(r) - \frac{1}{\sqrt{8}} w(r)\right] r^2 dr \tag{2.22}$$

Both equations 2.21 and 2.22 are static properties and are further modified by extensions to the simple potential model, i.e. the magnetic moment's dependence on the D-state

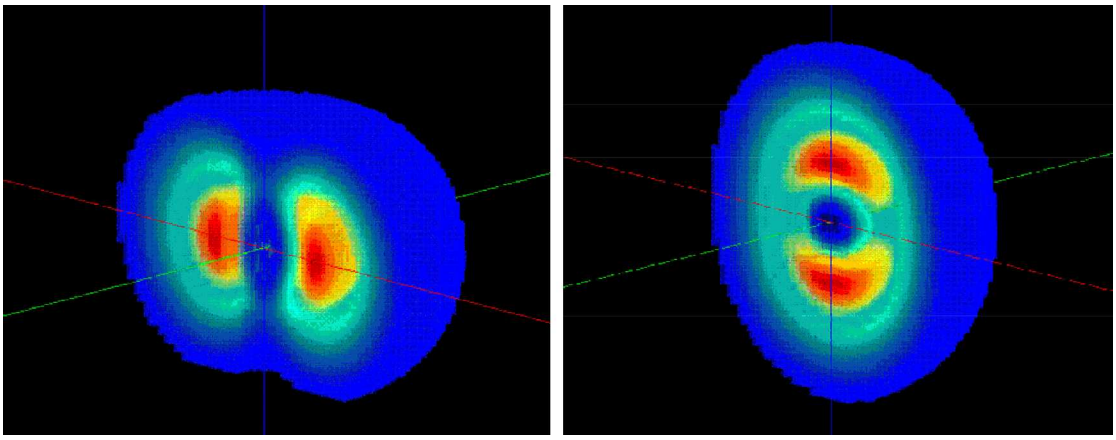

FIG. 2.6. Calculated density of the deuteron for the $\Psi_0(\mathbf{r})$ and $\Psi_1(\mathbf{r})$ substates corresponding to $m_J = 0$ and $m_J = \pm 1$, respectively. These are commonly referred to as the *doughnut* and *barbell* shapes of the deuteron.

probability is broken in more realistic potential models asserting relativistic corrections and meson exchange currents and thus does not define the probability P_D as an observable[37].

The asymptotic form of the wave functions are easily determined by modeling them on a finite range nuclear force but still in the $p \to 0$ limit.

$$u(r) \sim A_S e^{-\gamma r} \quad and \quad w(r) \sim A_D e^{-\gamma r}\left[1 + \frac{3}{\gamma r} + \frac{3}{(\gamma r)^2}\right] \quad \text{as} \quad r \to \infty \tag{2.23}$$

$\gamma \simeq \sqrt{\varepsilon m}$, with m being the reduced np mass and ε is the binding energy of the deuteron. A_S and A_D are normalization factors and are determined by matching equation 2.23 to the interior region where the potential is significant. The ratio

$$\eta_d = \frac{A_D}{A_S} \tag{2.24}$$

is directly related to tensor observables, e.g. the tensor asymmetry (to be discussed later in this section).

For the wave functions in momentum-space, applying a Fourier transform to Equation 2.17 where we expand $e^{-i\vec{p}\cdot\vec{r}}$ in spherical harmonics and integrate, one obtains for the

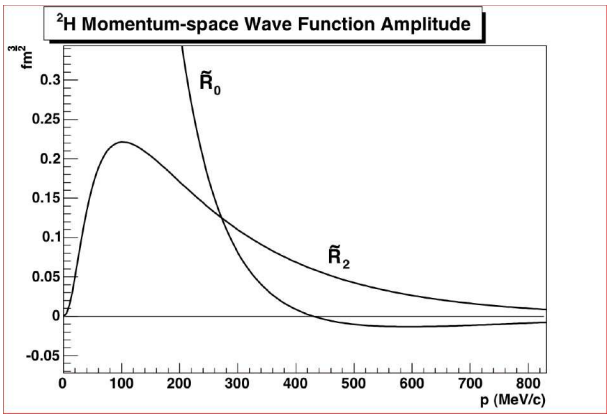

FIG. 2.7. The momentum space wave functions of the S and D states in the deuteron.

S and D state momentum-space wave function

$$\tilde{\Psi}_M(\mathbf{p}) = \int \Psi_M(\mathbf{r}) e^{-i\mathbf{p}\cdot\mathbf{r}} d^3\mathbf{r}. \tag{2.25}$$

where in order to simplify later calculations we define

$$\begin{aligned} \tilde{R}_0(p) &= \int j_0(pr) u(r) r \cdot dr, \\ \tilde{R}_2(p) &= \int j_2(pr) w(r) r \cdot dr. \end{aligned} \tag{2.26}$$

In eq. 2.26, $j_M(pr)$ are spherical Bessel functions. A plot of $\tilde{R}_0$ and $\tilde{R}_2$ can be seen in Figure 2.7. It can be noticed that there is a node in the S-state at $\sim$400 $\frac{\text{MeV}}{c}$ and around this momentum the D-state is highly dominant.

Using the same density calculation from the spatial wavefunctions, we get

$$\begin{aligned} \tilde{\rho}_0(\mathbf{p}) &= \Psi_0^\dagger(\mathbf{p})\Psi_0(\mathbf{p}) \\ &= 4\pi \left[\tilde{R}_0 + \sqrt{2}\tilde{R}_2 \left(\frac{3}{2}\cos^2\theta - \frac{1}{2} \right) \right]^2 + 18\pi \left(\tilde{R}_2 \sin\theta\cos\theta \right)^2 \\ \tilde{\rho}_2(\mathbf{p}) &= \Psi_2^\dagger(\mathbf{p})\Psi_2(\mathbf{p}) \\ &= 4\pi \left[\tilde{R}_0 - \frac{1}{\sqrt{2}}\tilde{R}_2 \left(\frac{3}{2}\cos^2\theta - \frac{1}{2} \right) \right]^2 + \frac{9\pi}{2}\tilde{R}_2^2 \sin^2\theta(1+\cos^2\theta). \end{aligned} \tag{2.27}$$

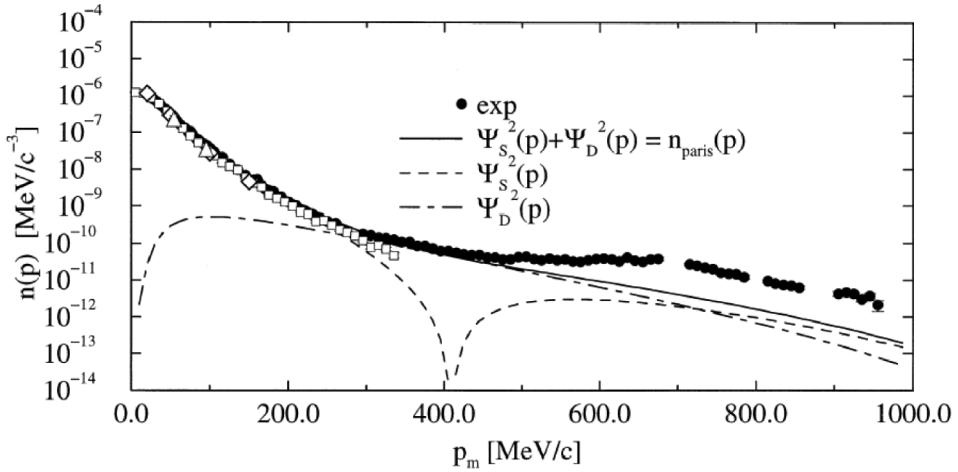

FIG. 2.8. The measured and calculated deuteron momentum distributions. Included measurements are open squares[46], open diamonds[50], open triangles[51] and the closed circles[49]. $n(p)$ is Blomqvist's notation for momentum density, and the calculations are done with the Paris potential by H. Arenhövel for the purpose of Blomqvist's paper[49].

These densities offer initial intimations of how polarization will affect the results of measurements made on the momentum density in the deuteron.

As a pedagogical example, in the Plane Wave Impulse Approximation (PWIA), formerly known as the one-photon exchange impulse approximation, the incident electron transfers momentum $\mathbf{k}$ and energy ω to a proton with initial momentum $\mathbf{p}$ within the deuteron. The proton is ejected with a final momentum $\mathbf{p}'$. The residual neutron recoils at $\mathbf{n}'$. In such a straightforward example, by momentum conservation, $\mathbf{p} = -\mathbf{n}' = \mathbf{p}' - \mathbf{k}$. This approximation gives the definition of the oft quoted *missing momentum* $p_m = -\mathbf{p} = \mathbf{n}'$ and p_m is approximately analogous to p in eq. 2.27.

The total momentum distribution in the unpolarized deuteron in PWIA can be given by

$$\rho(p_m) = \frac{1}{3}(\tilde{\rho}_{+1} + \tilde{\rho}_0 + \tilde{\rho}_{-1}) = 4\pi(\tilde{R}_0^2 + \tilde{R}_2^2). \tag{2.28}$$

This exact quantity has been measured[46, 47, 48, 49] and is shown in Figure 2.8. The

momentum distribution suggests the possibility of the measurement of an *asymmetry*. The short-dashed and long-dashed curves in Figure 2.8 are the contributions from the S and D wave functions. When quantizing the spin of the deuteron along the axis of momentum transfer, we can form an asymmetry corresponding to the respective terms in the total deuteron's momentum density $\rho(p_m)$. This is called a *tensor asymmetry* A_d^T since the measurement of the resulting difference in momentum distributions can be correlated with the ratio of S and D wave amplitudes within the deuteron. The asymmetry is written

$$\begin{aligned} A_d^T(p_m,\theta) &= \frac{\frac{1}{2}(\tilde{\rho}_{+1}+\tilde{\rho}_{-1})-\tilde{\rho}_0}{\tilde{\rho}_{+1}+\tilde{\rho}_0)+\tilde{\rho}_{-1}} \\ &= \frac{1}{2}\left(\frac{\tilde{R}_0\tilde{R}_2\sqrt{8}+\tilde{R}_2^2}{\tilde{R}_0^2+\tilde{R}_2^2}\right)\left(\frac{1}{2}-\frac{3}{2}\cos^2\theta\right). \end{aligned} \tag{2.29}$$

θ is the angle between $\vec{p}_m$ and the momentum transfer. The asymmetry would obviously be zero were $\tilde{R}_2 = 0$ and it also crosses zero when $\cos\theta = \pm\frac{1}{\sqrt{3}}$. When finding the maxima of this function, we find that at $p_m \sim 300$ MeV $\tilde{R}_0 = \frac{1}{\sqrt{2}}\tilde{R}_2$. In PWIA, this would be the essential measurement with which to observe the ratio A_D/A_S motivated in equation 2.24. Also, in the limit where $\tilde{R}_0 \gg \tilde{R}_2$, $A_d^T(p_m,\theta)$ is directly proportional to the ratio $\frac{\tilde{R}_2}{\tilde{R}_0}$ and this, further, makes A_d^T ideal for measuring the D-state contribution.

In order to further motivate the need for more precise experiments, e.g. polarization experiments, Table 2.1 demonstrates some inconsistencies between nuclear potential models and the measured values of the deuteron's static properties. There are still major discrepancies and heavy debate concerning the predictability of these values, especially that of Q_d.

TABLE 2.1. The experimental data is taken from a table in [38] and the respective citations can be found there. The Argonne $v18$ calculations of $\mu_d, Q_d, A_D/A_S, r_d, \varepsilon_d$ can be found in [42] while r_{ch} comes from [43]. The calculations of $\mu_d, Q_d, A_D/A_S$ and ε_d can be found in [44] while r_d and r_{ch} were taken from [45].

Quantity	Measured	Argonne $v18$	Bonn[6]
μ_d	$0.8574382284(98)\mu_N$	$0.871\mu_N$	$0.852\mu_N$
Q_d	0.2859(3) fm^2	0.275 fm^2	0.270 fm^2
A_D/A_S[7]	0.0256(4)	0.0250	0.0256
r_d[8]	1.975(3) fm	1.967 fm	1.966 fm
r_{ch}[9]	2.130(10) fm	2.123 fm	2.1345 fm
ε_d	2.22456612 MeV	2.224575 MeV	2.224575 MeV

2.3. Polarized Elastic electron-deuteron scattering

The diagram of observables within polarized electron scattering is shown in Figure 2.9. Variables in the diagram are assigned assuming scattering off of a deuterium target though $\mathbf{p}_{np}$ can be taken as a completely general momentum. The overview of polarized

[6] μ_d and Q_d not including relativistic or meson-exchange corrections.

[7] Taken from polarization experiments.

[8] As defined in [44], the deuteron's *structure radius* r_d is defined as the square root of the sum of the rms-half distance r_m^2 between the two nucleons, i.e.

$$r_m^2 = \frac{1}{4}\int_0^\infty [u^2(r) + w^2(r)]r^2 dr,$$

a relativistic correction r_{SO}^2 following from the spin-orbit part of the one-nucleon charge operator, i.e.

$$r_{SO}^2 = -6(2G_M^S(0) - G_E^S(0))\frac{P_D}{8m_N^2}$$

where $G_{E/M}^S(Q^2)$ are the isoscalar magnetic Sachs form factors of the nucleon, and a two-nucleon piece $r_{[2]}^2$ including two nucleon meson exchange, relativistic boost corrections, Δ-isobar contributions, and short-ranged quark exchange effects and potentially a host of other small contributions that may yet be accounted for, i.e.

$$r_{[2]}^2 = r_{MEC}^2 + r_{boost}^2 + r_{\Delta\Delta}^2 + r_{QEC}^2 + \ldots.$$

Thus, we can write r_d as

$$r_d^2 = r_m^2 + r_{SO}^2 + r_{[2]}^2.$$

[9] The deuteron's charge radius is defined in the same way as the nucleons, i.e. equation 2.13, except the form factor in the derivative is the charge monopole form factor G_C defined in the next section. There has been a $\sim$1% discrepancy between atomic physics experiments and electron-scattering [39, 40] and this discrepancy has been troubling though Coulomb distortion is postulated to be the solution to the Rosenbluth and polarization transfer measurements [41] and may account for this difference in the deuteron's charge radius.

electron-nucleon scattering has been well developed and will largely be based on the work and conventions described by two seminal papers by Donnelly and Raskin [33, 34], and a series of papers by Arenhövel, Leidemann, and Tomusiak [35].

The incoming and outgoing electron's four-vectors $\mathbf{k}^\mu = (E_0, \vec{k})$ and $\mathbf{k'}^\mu = (E', \vec{k'})$ along with the four-momentum transfer $\mathbf{q}^\mu = (\omega, \vec{q}) = (E' - E_0, \vec{k'}, -\vec{k})$, from the exchange of a virtual photon, define the *Scattering Plane*. The polarization $\mathbf{S}$ of the target is oriented within the *Orientation Plane* at $\Omega^* = (\theta^*, \phi^* + \phi)$ with respect to the Scattering Plane. The recoil 4-vector of the target is labeled $\mathbf{p}^\mu_{np}$ and is confined to the *Reaction Plane*. When boosting into the CM-frame of the final scattered neutron and proton, the momentum will be denoted with the superscript ^{cms}, i.e. $\mathbf{p}_{np} \rightarrow \mathbf{p}^{cms}_{np}$, and the outgoing trajectory as well, $\Omega_{np} = (\theta_{np}, \phi_{np}) \rightarrow \Omega^{cms}_{np} = (\theta^{cms}_{np}, \phi^{cms}_{np})$. The key Lorentz-invariant quantity in nearly all of the following kinematically weighted variables characteristic of the deuteron and the constituent nucleons is $Q^2 = -\mathbf{q}^2 = 4EE' \sin^2 \frac{\theta_e}{2}$.

Assuming parity conservation and time reversal invariance, the elastic electron-deuteron scattering cross section can be written as the unpolarized cross-section multiplied by a linear combination of terms dependent upon the longitudinal polarization of the electrons h and vector polarization P_z of the target, as well as the tensor polarization of the target P_{zz},

$$\frac{d\sigma}{d\Omega}(h, P_z, P_{zz}) = S_0(1 + \sqrt{\frac{3}{2}} h P_z \Delta + \sqrt{\frac{1}{2}} P_{zz} \Gamma). \tag{2.30}$$

The factors of $\sqrt{\frac{3}{2}}$ and $\sqrt{\frac{1}{2}}$ are taken from Arenhövel's formalism. In this form,

$$S_0 \equiv \frac{d\sigma}{d\Omega}(0,0,0) \equiv \left(\frac{d\sigma}{d\Omega}\right)_{Mott} f^{-1}_{rec} \left[A(Q^2) + B(Q^2) \tan^2\left(\frac{\theta_e}{2}\right)\right], \tag{2.31}$$

which is of the same form as the Rosenbluth cross-section (equation 2.10) where all relevant form factors and other variables explicit to the structure of the deuteron are now implicit in

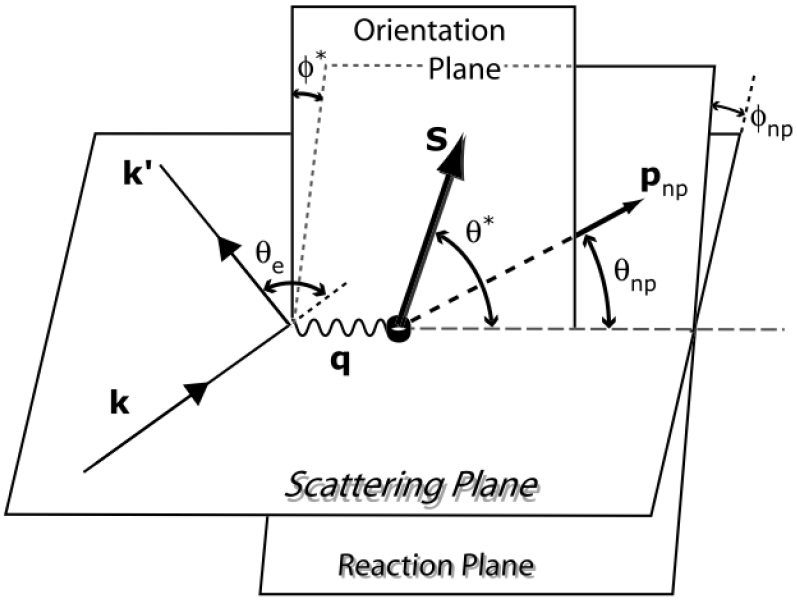

FIG. 2.9. Diagram of Polarized electron Scattering on Deuterium.

the structure functions $A(Q^2)$ and $B(Q^2)$. These kinematically weighted structure functions are linear combinations of three physically motivated form factors corresponding to the charge monopole $G_C(Q^2)$, the magnetic dipole $G_M(Q^2)$, and the charge quadrupole $G_Q(Q^2)$ of the deuteron.

$$A(Q^2) \equiv G_C^2(Q^2) + \frac{8}{9}\eta^2 G_Q^2(Q^2) + \frac{2}{3}\eta G_M^2(Q^2) \tag{2.32}$$

$$B(Q^2) \equiv \frac{4}{3}\eta(1+\eta)G_M^2(Q^2) \tag{2.33}$$

where $\eta = \frac{Q^2}{4m_d}$. The respective form factors must obviously be normalized to the charge, quadrupole moment and magnetic moment of the deuteron in order to have physical meaning. Further linear combinations of these form factors have been constructed to allow connections to observables separately proportional to hP_z (the vector correlation parameters T_{1m}^e) and P_{zz} (the Tensor analyzing powers T_{2m}), e.g.

$$T_{20} \equiv -\frac{\sqrt{2}\eta}{3\tilde{S}}\left[4G_C(Q^2)G_Q(Q^2) + \frac{4\eta}{3}G_Q^2(Q^2) + \left(\frac{1}{2}+\epsilon\right)G_M^2(Q^2)\right] \tag{2.34}$$

$$T_{21} \equiv \frac{2}{\tilde{S}}\sqrt{\frac{\eta^3(1+\epsilon)}{3}}G_Q(Q^2)G_M(Q^2) \tag{2.35}$$

$$T_{22} \equiv \frac{\eta}{2\sqrt{3}\tilde{S}}G_M^2(Q^2) \tag{2.36}$$

$$T_{10}^e \equiv \frac{\eta}{\tilde{S}}\sqrt{\frac{2}{3}(1+\eta)\left(1+\eta\sin^2\frac{\theta_e}{2}\right)}\frac{\sin\frac{\theta_e}{2}}{\cos^2\frac{\theta_e}{2}}G_M^2(Q^2) \tag{2.37}$$

$$T_{11}^e \equiv \frac{2}{\sqrt{3}\tilde{S}}\sqrt{\eta(1+\eta)}G_M(Q^2)\left[G_C(Q^2)+\frac{1}{3}\eta G_Q(Q^2)\right]\tan\frac{\theta_e}{2} \tag{2.38}$$

where $\tilde{S} \equiv A(Q^2)+B(Q^2)\tan^2\left(\frac{\theta_e}{2}\right)$ and $\epsilon \equiv (1+\eta)\tan^2\frac{\theta_e}{2}$. Measurement of at least one of these *tensor analyzing powers* or *vector correlation parameters*, T_{20} being the most common, on a tensor or vector polarized target is necessary in order to separate all three form factors since G_C and G_Q are not separated using the unpolarized Rosenbluth separation. The superscripts ^{e} in the latter two equations are indicating the necessity of a polarized electron in order to measure *spin correlation* parameters. Using these terms allows definition of the Γ and Δ terms in Equation 2.30 which are proportional to the vector and tensor polarization, respectively, of the internal target.

$$\Gamma \equiv \frac{1}{\sqrt{2}}\left[\left(\frac{3}{2}\cos^2\theta^* - \frac{1}{2}\right)T_{20} - \sqrt{\frac{3}{2}}\sin 2\theta^*\cos\phi^* T_{21} + \sqrt{\frac{3}{2}}\sin^2\theta^*\cos 2\phi^* T_{22}\right] \tag{2.39}$$

$$\Delta \equiv \sqrt{3}\left[\frac{1}{\sqrt{2}}\cos\theta^* T_{10}^e - \sin\theta^*\cos\phi^* T_{11}^e\right] \tag{2.40}$$

2.3.1. G_E^n From Elastic Electron Scattering on the Deuteron. Within the formalism of the deuteron's electromagnetic structure elicited within the previous subsection, it is possible to extract information on the constituent nucleons inside the deuteron. Here the *isoscalar form factors* G_E^s and G_M^s are introduced,

$$G_E^s \equiv \frac{1}{2}(G_E^p + G_E^n) \quad \text{and} \quad G_M^s \equiv \frac{1}{2}(G_M^p + G_M^n) \tag{2.41}$$

and the deuteron's so-called *body form factors*, D_x, [52] which are Fourier transforms of the S and D wave function densities, e.g.

$$\begin{aligned}
D_C(Q^2) &\equiv \int_0^\infty (u^2(r) + w^2(r)) j_0(Qr) dr, \\
D_M(Q^2) &\equiv \int_0^\infty \left[(2u^2(r) - w^2(r)) j_0(Qr) + (\sqrt{2} u(r) w(r) + w^2(r)) j_2(Qr) \right] dr, \\
D_E(Q^2) &\equiv \frac{3}{2} \int_0^\infty \left[j_0(Qr) + j_2(Qr) \right] w^2(r) dr, \\
D_Q(Q^2) &\equiv \int_0^\infty w(r) \left(u(r) - \frac{w(r)}{\sqrt{8}} \right) j_2(Qr) dr,
\end{aligned} \tag{2.42}$$

and finally listing the actual deuteron's form factors in terms of these new variables, the deuteron's form factors can be written in terms of these isoscalar form factors:

$$\begin{aligned}
G_C(Q^2) &\equiv G_E^s D_C, \\
G_M(Q^2) &\equiv \frac{m_d}{2m_p} \left(G_M^s D_M + G_E^s D_E \right), \\
G_Q(Q^2) &\equiv G_E^s D_Q.
\end{aligned} \tag{2.43}$$

When plotting the resulting contributions to the world's data on $A(Q^2)$, the charge monopole dominates by more than an order of magnitude up to $Q^2 \sim 0.3$ (GeV/c)^2. Since the isoscalar electric form factor is directly proportional to the charge monopole form factor of the deuteron via equation 2.43, an analysis can be performed on the world's data on $A(Q^2)$ in order to determine G_E^n[53, 54]. Data on these is included in Section 2.4.2.

2.4. Polarized Electrodisintegration of the Deuteron

Using the same kinematic formalism set up in the previous section and delineated in Figure 2.9, we now characterize electrodisintegration of the deuteron. Before diving deeper into the theory, two specific quantities can completely characterize the final kinematics of the neutron from the electrodisintegration of the deuteron; these quantities are the earlier

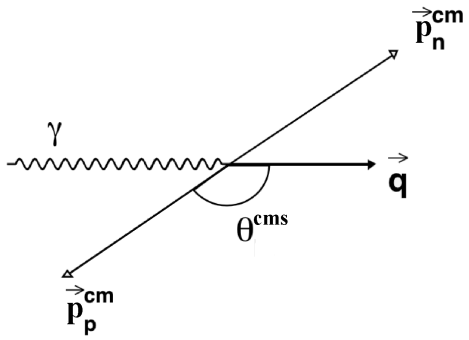

FIG. 2.10. Depiction of θ^{cms} as the angle between the outgoing momentum of the proton and the momentum transfer in the CM-frame of the deuteron.

mentioned *missing momentum* p_m, and the oft-quoted CM-frame polar angle between the momentum transfer and the outgoing momentum of the *proton*, θ^{cms}. It is essentially the angle θ_{np} from Figure 2.9 but one must be sure to remember that we must boost into the deuteron's center-of-momentum where the outgoing neutron and proton move in opposite directions. From here we can quantify perfect *quasi-elastic* scattering at $p_m = 0$ and $\theta^{cms} = 180^\circ$ (see Figure 2.10).

The differential cross-section of deuteron electrodisintegration is typically written as a linear combination of structure functions or as asymmetries weighted by the vector and tensor polarization of the target and the polarization of the electron beam, e.g.

$$\begin{aligned} \frac{d\sigma}{d\omega d\Omega_e d\Omega_{pn}^{CM}} &\equiv S(h, \tilde{P}_z, \tilde{P}_{zz}) \\ &\equiv S_0 \left[1 + \tilde{P}_z A_d^V + \tilde{P}_{zz} A_d^T + h\left(A^e + \tilde{P}_z A_{ed}^V + \tilde{P}_{zz} A_{ed}^T\right)\right] \end{aligned} \tag{2.44}$$

The electrodisintegration cross section can also be written in terms of the structure functions $f_\alpha^{(\prime)IM\pm}$ of the deuteron[10] and the virtual photon density matrices $\rho_\alpha^{(\prime)}$ where

[10]The spin of the deuteron can be taken to be quantized in the direction of the momentum transfer $\mathbf{q}$ and boosted into the CM-frame of the outgoing nucleons. Then the final dynamical structure of the deuteron can be quantified by a set of structure functions $f_\alpha^{(\prime)IM\pm}$ according to the formalism in [35]. The subscripts refer to the spin interaction between the virtual photon and the deuteron while the superscripts correspond to the bilinear hermitian forms from the reduced t-matrix which is also defined from the T-matrix between the initial deuteron state $|\lambda_d\rangle$ and the final disintegrated np-scattering state $|m_1 m_2\rangle$.

($\alpha \in L, T, LT, TT$)[11] refers to the longitudinal and transverse components of the polarization of the virtual photon and deuteron. The unpolarized cross section is thus written,

$$S_0 \equiv S(0,0,0) = c(\rho_L f_L + \rho_T f_T + \rho_{LT} f_{LT} \cos\phi_{pn} + \rho_{TT} f_{TT} \cos 2\phi_{pn}). \tag{2.45}$$

Using earlier notation described in Section 3.2.5, except expanding our generalized yields to accommodate the changing helicity of the beam, i.e. $V_+ \to V_+(+)$ for *vector-plus* polarization ($m_J = +1$) and *positive* helicity ($h = +1$). Accordingly, $V_+(-)$ will be used for vector-plus and *negative* helicity; $V_-(+)$ and $V_-(-)$ for *vector-minus* combined with positive and negative helicity states; $T_-(+)$ and $T_-(-)$ for *tensor* polarization combined with both helicity states, positive and negative, respectively. The sum of the yields from all six of these states will be denoted by $\sum_{i,h} S_i(h)$. I will also list the Asymmetries in terms of the deuteron's structure functions $f_\alpha^{(\prime)IM(\pm)}$ and the virtual photon density matrices $\rho_\alpha^{(\prime)}$. Here we must also introduce the variable $\tilde{\phi} = \phi_{np}^{cms} - \phi^*$.

$$\begin{aligned}
A_d^V &\equiv \sqrt{\frac{3}{2}} \cdot \frac{[V_+(+) + V_+(-)] - [V_-(+) + V_-(-)]}{\sum_{i,h} S_i(h)} \\
&\equiv \frac{c}{S_0} \sum_{M=0}^{1} \Big[(\rho_L f_L^{1M} + \rho_T f_T^{1M} + \rho_{LT} f_{LT}^{1M+} \cos\phi_{np}^{cms} + \rho_{TT} f_{TT}^{1M+} \cos 2\phi_{np}^{cms}) \sin M\tilde{\phi} \\
&\quad + (\rho_{LT} f_{LT}^{1M-} \sin\phi_{np}^{cms} + \rho_{TT} f_{TT}^{1M-} \sin 2\phi_{np}^{cms}) \cos M\tilde{\phi} \Big] \, d^1_{M0}(\theta^*) \qquad (2.46) \\
A_d^T &\equiv \sqrt{\frac{1}{2}} \cdot \frac{[V_+(+) + V_+(-) + V_-(+) + V_-(-)] - 2\,[T_-(+) + T_-(-)]}{\sum_{i,h} S_i(h)} \\
&\equiv \frac{c}{S_0} \sum_{M=0}^{2} \Big[(\rho_L f_L^{2M} + \rho_T f_T^{2M} + \rho_{LT} f_{LT}^{2M+} \cos\phi_{np}^{cms} + \rho_{TT} f_{TT}^{2M+} \cos 2\phi_{np}^{cms}) \cos M\tilde{\phi}
\end{aligned}$$

[11] The virtual photon density matrix is written assuming spin quantization along the axis of the momentum $\mathbf{q}$ of the virtual photon.

$$\begin{array}{lllllll}
\rho_L &=& -\beta^2 Q^2 \frac{\xi^2}{2\eta} & , & \rho_{LT} &=& -\beta^2 Q^2 \frac{\xi}{\eta} \sqrt{\frac{\xi+\eta}{8}} \\
\rho_T &=& -\frac{Q^2}{2}\left(1 + \frac{\xi}{2\eta}\right) & , & \rho_{TT} &=& Q^2 \frac{\xi^2}{4\eta} \\
\rho'_{LT} &=& -\beta Q^2 \frac{\xi}{\sqrt{8\eta}} & , & \rho'_T &=& -\frac{Q^2}{2} \sqrt{\frac{\xi+\eta}{\eta}}
\end{array}$$

where

$$\beta = \frac{|\mathbf{q}^{lab}|}{|\mathbf{q}^{breit}|} = \sqrt{1+\tau}\,, \quad \xi = \frac{Q^2}{(\mathbf{q}^{lab})^2}\,, \quad \eta = \tan^2\left(\frac{\theta_e}{2}\right)$$

$$- (\rho_{LT} f_{LT}^{2M-} \sin\phi_{np}^{cms} + \rho_{TT} f_{TT}^{2M-} \sin 2\phi_{np}^{cms}) \sin M\tilde{\phi}\Big] \, d^2_{M0}(\theta^*) \tag{2.47}$$

$$A^e \equiv \sqrt{\frac{3}{2}} \cdot \frac{[V_+(+) + V_-(+)] - [V_+(-) + V_-(-)]}{\sum_{i,h} S_i(h)}$$

$$\equiv \frac{c}{S_0} \rho'_{LT} f'_{LT} \sin\phi_{np}^{cms} \tag{2.48}$$

$$A_{ed}^V \equiv \sqrt{\frac{3}{2}} \cdot \frac{[V_+(+) + V_-(-)] - [V_+(-) + V_-(+)]}{\sum_{i,h} S_i(h)}$$

$$\equiv \frac{c}{S_0} \Big[(\rho'_T f_T^{'1M} + \rho'_{LT} f_{LT}^{'1M-} \cos\phi_{np}^{cms}) \cos M\tilde{\phi}$$

$$- \rho'_{LT} f_{LT}^{'1M+} \sin\phi_{np}^{cms} \sin M\tilde{\phi}\Big] \, d^1_{M0}(\theta^*) \tag{2.49}$$

$$A_{ed}^T \equiv \sqrt{\frac{1}{2}} \cdot \frac{[V_+(+) + V_-(+) + 2T_-(-)] - [V_+(-) + V_-(-) + 2T_-(+)]}{\sum_{i,h} S_i(h)}$$

$$\equiv \frac{c}{S_0} \Big[(\rho'_T f_T^{'2M} + \rho'_{LT} f_{LT}^{'2M-} \cos\phi_{np}^{cms}) \sin M\tilde{\phi}$$

$$+ \rho'_{LT} f_{LT}^{'2M+} \sin\phi_{np}^{cms} \cos M\tilde{\phi}\Big] \, d^2_{M0}(\theta^*) \tag{2.50}$$

$$\text{and} \quad c \equiv \frac{\alpha E'}{6\pi^2 E_0 Q^4}$$

where d^I_{M0} is defined as a rotation matrix with the elements:

$$d^1_{00} = \cos\theta^* \quad , \quad d^2_{00} = \tfrac{1}{2}(3\cos^2\theta^* - 1)$$

$$d^1_{10} = \sqrt{\tfrac{1}{2}} \sin\theta^* \quad , \quad d^2_{10} = -\sqrt{\tfrac{3}{2}} \cos\theta^* \sin\theta^*$$

$$d^2_{20} = \frac{\sqrt{6}}{4} \sin^2\theta^*$$

In the present context, the asymmetries A_{ed}^V and A_d^T show significant deviation from zero and serve the purpose of describing G_E^n and distinguishing the admixture of the D-state, respectively. A^e can be described as the parity-violating asymmetry due to flipping the helicity of the beam when analyzing ed-elastic or quasielastic breakup but is thus too small for the statistics of the present experiment. If a third particle such as a pion is produced, A^e becomes the fifth structure function and is not expected to be zero. A_{ed}^T and A_d^V are also parity-violating terms expected to be zero in one-boson exchange approximation, PWIA, and Plane Wave Born Approximation (PWBA). More realistic potentials including Meson

Exchange Currents (MEC), Isobar Configurations (IC), and Relativistic Corrections (RC) do make these asymmetries non-zero, but they are still too small to be reliably tested with the statistics of the present experiment.

The beam-vector asymmetry A_{ed}^{V} is sensitive to both the S and D states of the deuteron. Figure 2.11 shows the average projection of the neutron's spin along the axis of the deuteron's polarization vector as missing momentum goes up. The function can be written using analogous forms of the momentum density distributions from equation 2.27. When calculating the momentum density of the S and D states, we can determine the alignment of the spin of the nucleon, and thus the neutron, with the total quantized angular momentum of the deuteron. The function is written

$$P_z^n(p_m) = \frac{\rho_S(p_m) - \rho_D(p_m)}{\rho_S(p_m) + \rho_D(p_m)} \tag{2.51}$$

and is a function of the missing momentum. Again, this equation is plotted in Figure 2.11 and it can be seen that for missing momentum less than 200 MeV/c the neutron's spin is predominantly aligned with the overall angular momentum of the deuteron. For the vector-polarized deuteron in the pure S-state or D-state, the spin is in or opposite the direction of the polarization respectively, and A_{ed}^{V} is a quantity that can quantify the internal electromagnetic structure of the neutron.

2.4.1. The Neutron's Electric Form Factor From $^{2}\vec{\mathbf{H}}(\vec{\mathbf{e}},\mathbf{e'n})\mathbf{p}$. Scattering of the neutron is obviously complicated by the fact that we extract our information by dissociating it from an initial configuration within a two-nucleon system, but we can take limits to simplify the situation in order to better understand how we are extracting information about the intrinsic structure of the neutron.

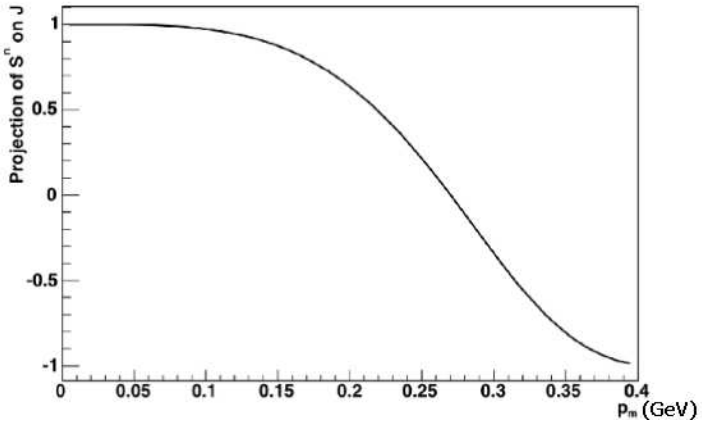

FIG. 2.11. This shows the average projection of the neutron's spin along the orientation of the deuteron's angular momentum **J** as a function of the missing momentum. At $p_m = 0$ we can see that the deuteron is entirely in the S-state while at nearly 400 MeV/c the deuteron is entirely in the D state and the two nucleons can be taken to have their spin pointing in the opposite direction of the total angular momentum of the deuteron. The vector asymmetry of the neutron is only measured as a function of $p_m < 200$ MeV/c so that the neutron's spin does not deviate to the point that we lose our sensitivity to G_E^n.

When detecting a neutron from the electrodisintegration of the deuteron, the missing momentum p_m or θ^{cms} characterizes the neutron's momentum inside the deuteron. When missing momentum goes to zero or when θ^{cms} approaches 180°, we approach the limit of quasielastic scattering and can thus interpret the virtual photon as transferring energy and momentum solely to the outgoing neutron. Further, when analyzing the trends within the asymmetry [35] $A_{ed}^V(\theta^*, \phi^*)$, it is found that at $\phi^* = 0$ and $\theta^* = \frac{\pi}{2}$ we are probing the region that is most sensitive to changes in G_E^n[12]. As a pedagogical overview, we can generally develop a double polarization measurement of the cross section in this transverse geometry. The cross-section is here composed coherently of electric and magnetic scattering

[12]For an understanding of why this is so, we can visualize the polarization of the neutron, and thus the magnetic moment, projected along the polarization of the deuteron. If there was truly no current distribution within the neutron, experiments would show that the neutron's magnetic moment is zero. Since there is an *anomalous* magnetic moment, we would expect the current to be maximized in the two-dimensional plane perpendicular to the polarization of the neutron. Further, since the neutron's magnetic moment is opposite of that of the proton, we can postulate that the charge density at short radii is most likely positive and thus at longer radii we can assume the charge density to be negative.

amplitudes which can be represented by f and g, respectively. When the helicity of the electron is flipped, g, the dipole-dipole interaction, will change sign while the coulomb interaction f will remain the same. When measuring the helicity dependent cross-section, in general is simple to define

$$\sigma_{\pm} = |f \pm g|^2 = f^2 + g^2 \pm 2\Re(f \cdot g).$$

The interference term allows the extraction of the physics of the electric scattering amplitude to first order when measuring an asymmetry, e.g.

$$A = \frac{\sigma_+ - \sigma_-}{\sigma_+ + \sigma_-} = \frac{2\Re(f \cdot g)}{f^2 + g^2}.$$

This region where we can probe the transverse geometry is called *perpendicular kinematics* for obvious reasons. When $\theta^* = 0$ or π, the configuration is typically called the region of *parallel kinematics* where the momentum transfer comes in along the direction of the polarization of the target. Also note, that the projection of the spin of the neutron onto the polarization of the deuteron can be characterized as a function of missing momentum which is directly related to the expected momentum density of the nucleon within the deuteron as determined from equation 2.27 (See Figure 2.11).

In terms of the form factors, we can rewrite the asymmetry of pure quasielastic scattering $A_{ed}^V \rightarrow A_{en}^V$,

$$A_{en}^V = hP_z \frac{a \sin\theta^* \cos\phi^* G_{En} G_{Mn} + b \cos\theta^* G_{Mn}^2}{G_{En}^2 + c G_{Mn}^2} \tag{2.52}$$

where the coefficients $a,\ b,\ c$ are determined from electron kinematics, e.g.

$$\begin{aligned} a &= -2\sqrt{\tau(1+\tau)}\tan(\theta_e/2), \\ b &= -2\tau\sqrt{1+\tau+(1+\tau)^2\tan^2(\theta_e/2)}\tan(\theta_e/2), \\ c &= \tau + 2\tau(1+\tau)\tan^2(\theta_e/2). \end{aligned}$$

where h and P_z are the respective polarizations of the electron beam and target.

Analyzing (2.52) the divisor will simplify to cG_{Mn}^2 since $G_M^n \gg G_E^n$. When probing the perpendicular kinematics region and simplifying the divisor, (2.52) will reduce to

$$A_{en}^V = \frac{a\sin\left(\frac{\pi}{2}\right)\cos(0)G_{En}G_{Mn} + b\cos\left(\frac{\pi}{2}\right)G_{Mn}^2}{cG_{Mn}^2} \tag{2.53}$$

$$\approx \frac{-2\sqrt{\tau(1+\tau)}\tan(\theta_e/2)G_{En}G_{Mn}}{\tau\left[1+2(1+\tau)\tan^2(\theta_e/2)\right]G_{Mn}^2}$$

$$\approx \frac{a}{c}\cdot\frac{G_E^n}{G_M^n} \tag{2.54}$$

This is essentially the *ideal* situation, and though these are included for pedagogical measures, they do not predict the full dynamic model. In order to accurately compare experiment to theory, the full dynamic model and the relevant structure functions $f_\alpha^{(\prime)IM\pm}$ from (2.46)-(2.50) are calculated and events are generated within the BLAST Monte Carlo (see Section 3.6) and then propagated through the BLAST acceptance. The asymmetries are extracted from the theoretical model within the Monte Carlo and compared to the experimental data. H. Arenhövel of Mainz provided the calculations for Monte Carlo generation taking into consideration those processes shown in Figure 2.12.

Included in Figures 2.13 and 2.14 is the model dependence of the vector asymmetries as calculated and generated in the Monte Carlo along with corrections corresponding to the processes shown in Figure 2.12. When starting from PWBA and adding more leading order processes to the calculation, the significance of these interactions, such as final state interactions, becomes obvious since they have a great effect on the expected asymmetries. When using the total dynamic model and swapping the model of the nucleon-nucleon potential, there is very little fluctuation in the expectation of A_{ed}^V (see Figure 2.13).

2.4.2. G_E^n data and the Friedrich and Walcher Parameterization. Until the 1990's, most of the data on G_E^n had come from unpolarized elastic e-d scattering. Galster

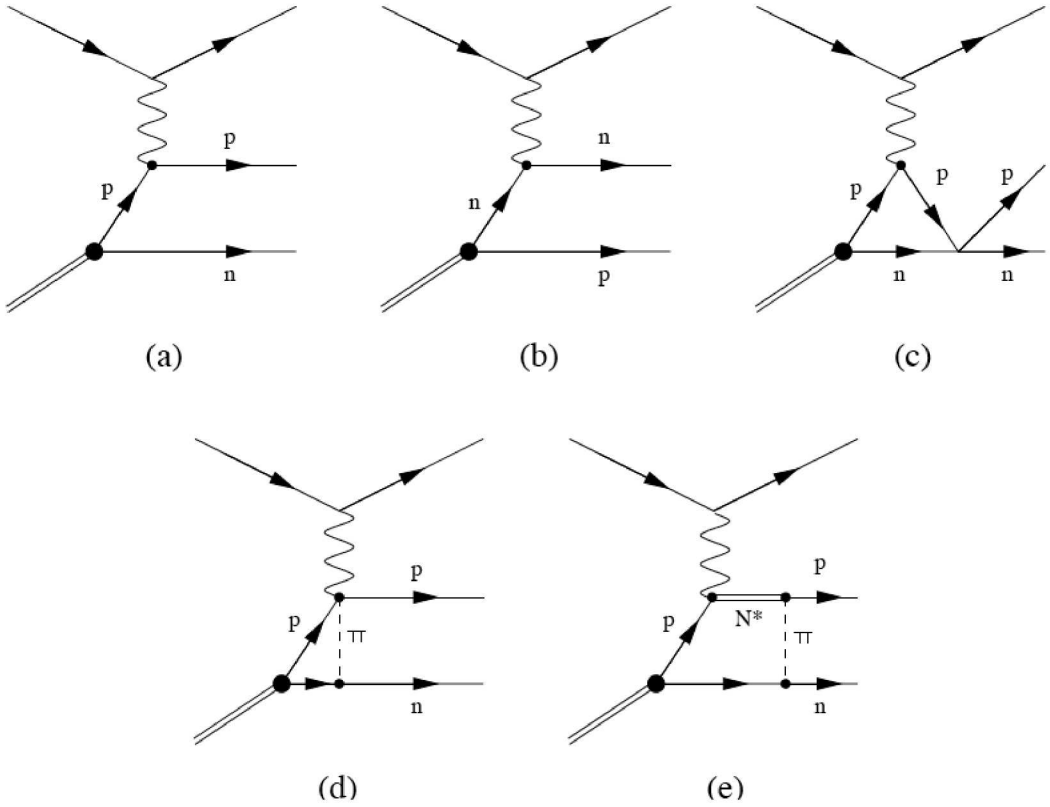

FIG. 2.12. Lowest Order Feynman Diagrams of the Monte Carlo calculations provided by H. Arenhövel of Mainz. The processes are: (a) PWIA e-p quasielastic, (b) PWIA e-n quasielastic, (c) Final State Interactions (FSI), (d) Meson Exchange Currents (MEC), and (e) Δ-Isobar Excitation Corrections (IC). The diagrams (a) and (b) approximate the Plane Wave Born Approximation when symmetrized properly to account for nucleon exchange if the detected nucleon is not that which was scattered from.

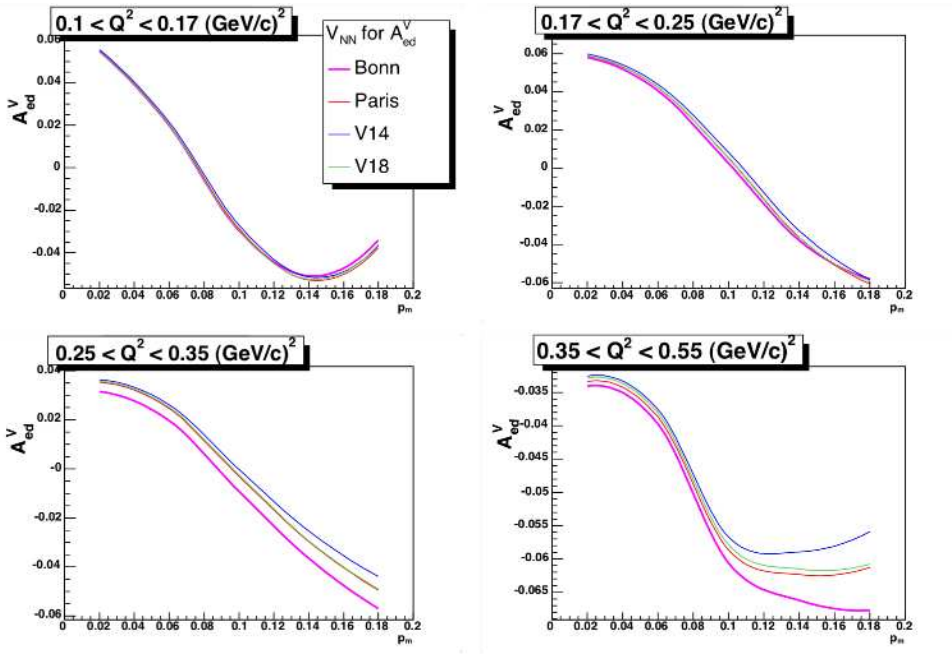

FIG. 2.13. Arenhövel's calculations of the electrodisintegration of the deuteron used in a Monte Carlo simulation to determine A_{ed}^{V}'s sensitivity to NN-Potential. This experiment uses *Bonn-Qb*.

et al. had measured G_E^n [53] and established a phenomenological fit to the data starting with the dipole fit that seemed to reproduce G_M^p, G_E^p and G_E^n. Galster's parameterization is referenced in Figure 2.15. It consisted of multiplying the dipole form by a factor that respected the condition that $G_E^n(Q^2 = 0) = 0$. It is written as:

$$G_E^n(Q^2) = \frac{a\tau}{1 + b\tau} \cdot G_D. \tag{2.55}$$

$\tau = \frac{Q^2}{4m_n^2}$ and a and b are parameters determined by the data and physical constraints. Galster's fit[13] fixed the numerator $a_G = -\mu_n$ where $\mu_n = -1.91$ is the well-known neutron's magnetic moment, and the parameter in the denominator was the global fit parameter set at $b_G = 5.6$. The Galster form is not considered to contain any essential physics other

[13]The parameterization in eq. 2.55 was used by both Galster and Platchkov and for that reason, a and b in equation 2.55 are denoted as a_G and b_G when referring to the fit used in the Galster et al. 1971 paper, and analogously as a_P and b_P when referring to the values fitted in the Platchkov et al. 1990 paper dipole fit G_D from equation 2.16.

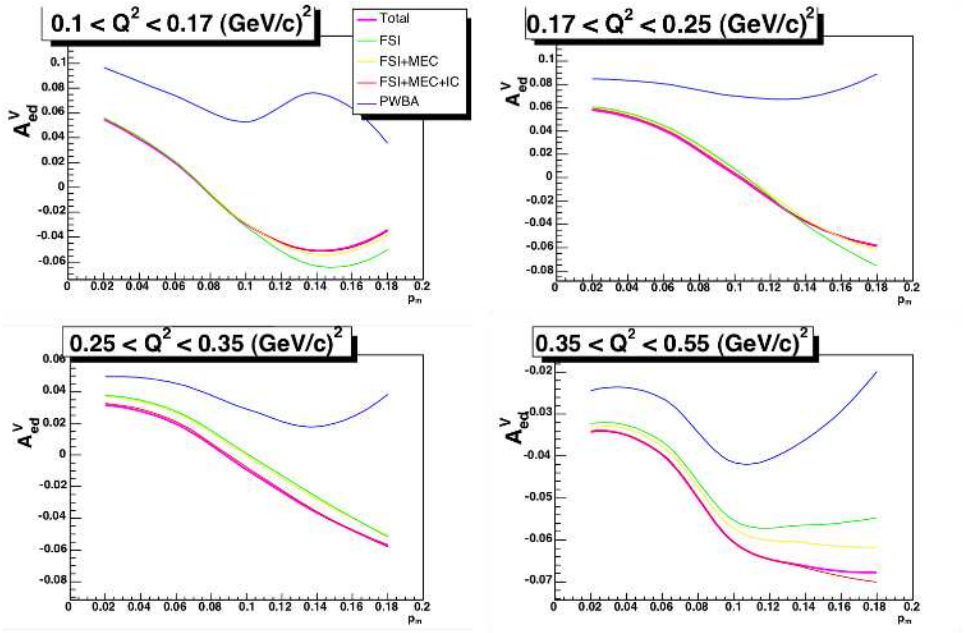

FIG. 2.14. Arenhövel's calculations of the electrodisintegration of the deuteron used in a Monte Carlo simulation to determine A_{ed}^{V}'s sensitivity to corrections to the NN interaction. PWBA is the Plane-Wave Born Approximation, FSI includes final state interactions, MEC are corrections due to meson exchange currents, and IC are Δ-isobar configurations.

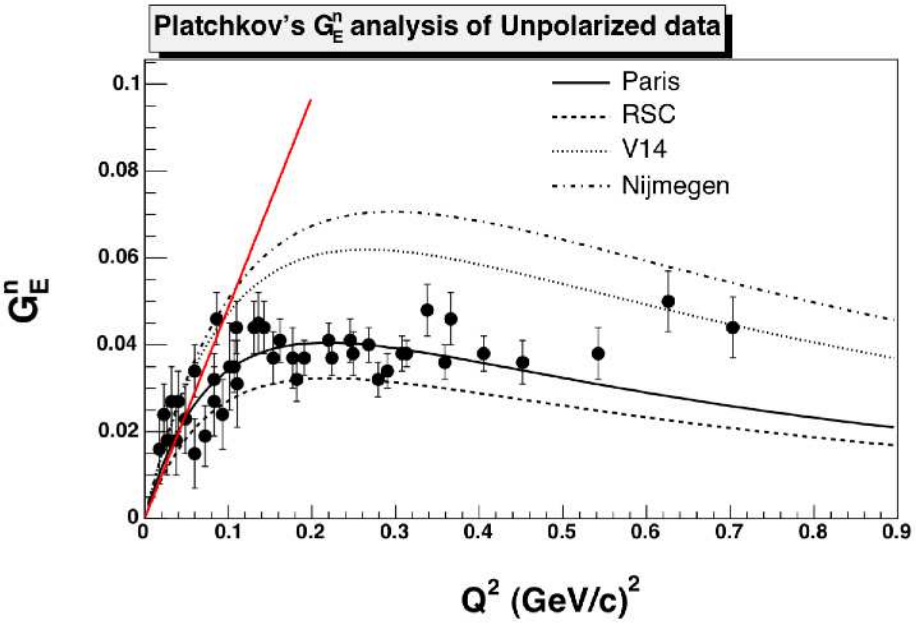

FIG. 2.15. The data in this graph is taken from Platchkov's analysis [54] of $A(Q^2)$ from unpolarized elastic scattering from the deuteron. The data here are calculated from the Paris NN-potential model. Were the data to be calculated using one of the other three NN-potentials listed in the graph, they would follow the trends delineated by the other curves. The line of constant slope shows the constraint of the neutron's charge radius at $Q^2 = 0$. This constraint is well outlined in the next section.

than the dipole factor. The data from elastic scattering on the deuteron can be seen in Figure 2.15 as analyzed in [54]. Platchkov reanalyzed a great deal of unpolarized elastic scattering data on the deuteron and using the formalism from section 2.3.1, fit the data according to several potential models. In this fit, directly analogous to the Galster form, $a_P = 0.9$ and $b_P = 3.47$ were the global fit parameters.

Using equation 2.43, Schiavilla and Sick expanded upon the treatment of elastic scattering from the deuteron by isolating the quadrupole form factor and extracting the isoscalar electric form factor [82]. The only sources of theoretical uncertainty come from the potential model and two-body currents in the form of the long-range π-exchange operator. Since π-exchange contributions dominate for the quadrupole form factor, calculations with

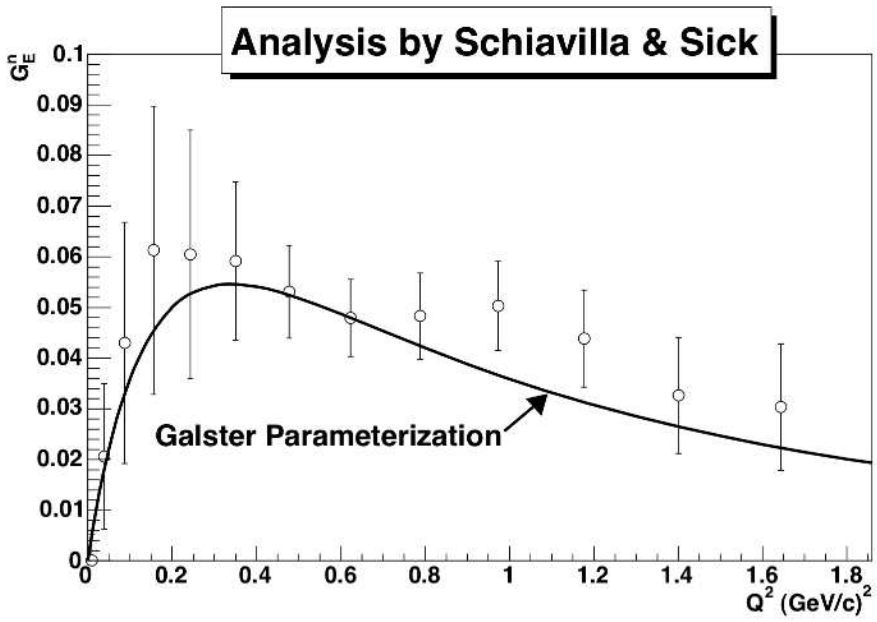

FIG. 2.16. The data from [82] on the analysis of G_E^n from the quadrupole form factor of the deuteron.

"realistic" models are shown [81] to deviate very little and thus the theoretical uncertainties involved in extracting G_E^n from $G_Q(Q^2)$ are significantly smaller than extracting G_E^n from $A(Q^2)$. Also, the meson exchange contributions are expected to be more reliable for D_Q than for D_C in equations 2.42. $G_Q(Q^2)$ is extracted from the world's data on $A(Q^2)$ and T_{20}. The results on G_E^n are shown in Figure 2.16. With the success of BLAST's measurement of T_{20} from elastic electron deuteron scattering [83], a new analysis following the process exploited by Schiavilla and Sick should soon follow.

From the early 1990's through to the present, the world has begun using polarization techniques to obtain more precise information about the nucleons and nuclear structure in general. The advantages in measuring the form factors were heavily motivated by a paper in 1981 [80]. The data that has emerged in the past 10 years has allowed a more precise determination of the structure of the nucleon. Double polarization and polarization transfer

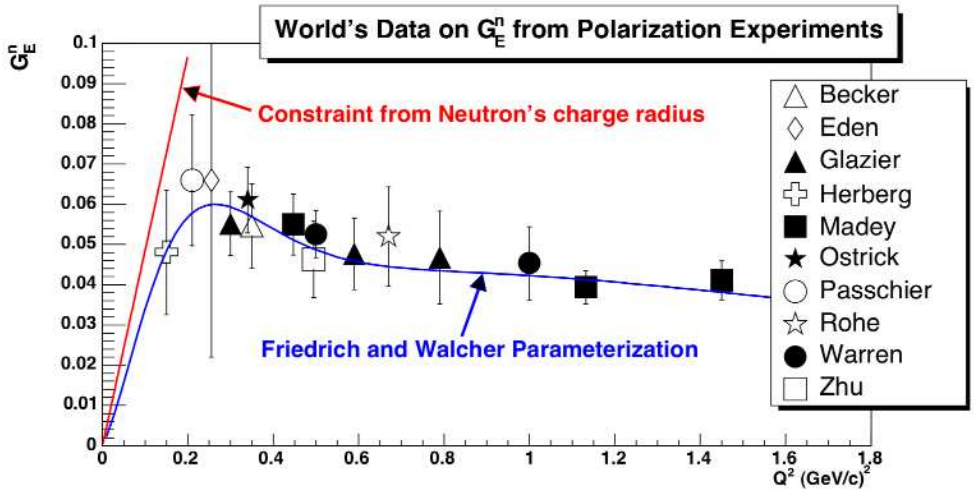

FIG. 2.17. The world's data on G_E^n from modern polarization experiments. Data included is from [84, 86, 87, 88, 89, 90, 91, 92, 93, 94].

techniques have considerably lowered the systematic uncertainties in the determination of nucleon form factors. The data in Figure 2.17 are the world's data using polarization experiments. The precision with which G_E^n is known is still the worst of the four intrinsic electromagnetic form factors of the neutron and proton, but with each advance there is a stronger constraint on parity violation and nucleon models.

In 2003, a remarkable paper [95] was published in which a phenomenological fit that starts from physical motivations of a constituent quark core surrounded by a pion cloud as is well in agreement with the best theoretical models thus introduced. The modern polarization data does not appear to conform to a smooth dipole curve as defined by the Galster parameterization nor do the low Q^2 points in Figure 2.16. The "bump," or "peak-region" as described by Friedrich and Walcher that seems to characterize the region between $0.2 < Q^2 < 0.4$ (GeV/c)^2, seems to necessitate a better picture than that of the Galster parameterization. The authors introduced a parameterization of the form

$$G_E^n(Q^2) = \frac{a_{10}}{\left(1+\frac{Q^2}{a_{11}}\right)^2} + \frac{a_{20}}{\left(1+\frac{Q^2}{a_{21}}\right)^2} + a_b Q^2 \left(e^{-\frac{1}{2}\left(\frac{Q-Q_b}{\sigma_b}\right)^2} + e^{-\frac{1}{2}\left(\frac{Q+Q_b}{\sigma_b}\right)^2} \right). \qquad (2.56)$$

The initial two terms are dipole terms that take their physical cue from the constituent quark core, while the superposition of normalized Gaussians characterizes the bump region which takes its physical cue from an assumed pion cloud. Though the neutron's electric form factor motivated the new parameterization, it seems that each of the nucleons show a bump of nearly the same width (≈ 0.2 (GeV/c)^2) at nearly the same value of momentum transfer (≈ 0.3 (GeV/c)^2, though the bump for G_E^p is much lower at about 0.07 (GeV/c)^2).

The fit must of course satisfy $G_E^n(Q^2 = 0)$=0 and is thus normalized to such a constraint. Q_b is the location of the bump and σ_b is the width. The parameters with subscripts are all fit to the data while obeying the constraint at $Q^2 = 0$. Unfortunately, as is obvious from Figure 2.17, the constraint of the neutron's charge radius does not seem to have been considered and is thus the only failure of the parameterization since the χ^2 is significantly smaller when fitting the Friedrich and Walcher parameterization rather than Galster to the data.

2.4.3. An Important Constraint on G_E^n: the Neutron's Charge Radius. The neutron's charge radius constrains the fit for G_E^n by the equation

$$< r_{ch}^2 >= -6 \left(\frac{dG_E(Q^2 = 0)}{dQ^2} \right). \tag{2.57}$$

Experiments done to determine the neutron's charge radius are well advanced and this will review the measurement as it is very important in constraining the fit to G_E^n. The formalism will primarily follow the treatment in [2].

In the collision of a neutron with an atom, a number of secondary electromagnetic interactions contribute to the process that is largely a nuclear interaction. Key corrections to the scattering lengths obtained from neutron scattering measurements include the spin-orbit (Schwinger) interaction, the Foldy interaction, a magnetic dipole interaction, electric

polarizability and the intrinsic charge radius of the neutron. These measurements provide the best data on the charge radius of the neutron. The interaction energy can be written:

$$V = V_N + V_M + V_E + V_P \tag{2.58}$$

where V_N is the contribution from the strong force, V_M is the magnetic contribution, V_E is due to the electrostatic energy of the neutron and V_P is a result of the neutron's polarizability.

The energy of the interaction can be taken directly from electrostatics, then applying a multipole expansion we show

$$\begin{aligned} V_E(\mathbf{r}) &= \int \phi(\mathbf{r}+\mathbf{r}')\rho_n(\mathbf{r}')d\mathbf{r}' \\ &= (Q_0 + \mathbf{Q_1}\cdot\nabla + \frac{1}{2}\mathbf{Q'_2} : \nabla\nabla + \ldots)\phi(\mathbf{r}) \end{aligned}$$

where Q_0 and Q_1 are the usual charge monopole and dipole terms but the quadrupole is different. Foldy showed [63, 64] that there is an important term called the *charge separation term* where r_n is the intrinsic charge radius of the neutron.

$$\begin{aligned} \mathbf{Q'_2} &= \int r'^2\rho_n(\mathbf{r}')d\mathbf{r}', \\ &= \mathbf{Q_2} + 2\varepsilon\mathbf{1}, \end{aligned}$$

and ε from the charge separation term,

$$\varepsilon = \int r'^2\rho_n(\mathbf{r}')d\mathbf{r}' \equiv \frac{1}{6}er_n^2. \tag{2.59}$$

Arguing away terms Q_l where $l \geq 2$ since the neutron is a spin-1/2 particle, V_E is then written as

$$V_E(\mathbf{r}) = (Q_0 + \mathbf{Q_1}\cdot\nabla + \varepsilon\Delta)\phi(\mathbf{r}) \tag{2.60}$$

where higher order charge separation terms are ignored. Taking the Fourier transform and deriving the scattering amplitude F_E using the Born approximation

$$F_E = -b_E e^{i\mathbf{q}\cdot\mathbf{R}},$$

where b_E is the electrostatic scattering length defined by

$$b_E = \frac{2mZe}{\hbar^2}\left[\frac{ze}{q^2} - i\frac{le}{q}\sigma\cdot\hat{\mathbf{q}} - \varepsilon\right](1 - f(\mathbf{q})) \tag{2.61}$$

$$= -b_I Z(1 - f(\mathbf{q})) \tag{2.62}$$

The coefficient and the first term of eq. 2.61 represent Rutherford scattering of a neutron with charge ze, l corresponds to the dipole term and $f(\mathbf{q})$ is the atomic form factor of the atom which comes from a Hartree Fock calculation that takes into account the screening of the nuclear charge by the surrounding electron cloud. b_I is the intrinsic neutron-electron scattering length:

$$b_I \equiv \frac{2m_n e}{\hbar^2}\varepsilon = \frac{1}{3}(m_n/m_e)\frac{r_n^2}{a_0}. \tag{2.63}$$

The *actual* neutron electron scattering length, i.e. $b_e = b_I + b_F$, measured in experiment also includes the Foldy scattering length b_F which governs several interactions, **a**) the Foldy term or the direct spin-independent interaction between the neutron magnetic dipole moment and the atomic charge density, **b**) the Schwinger term or the spin-orbit interaction between the neutron magnetic dipole moment and the atomic electric field, and **c**) the nuclear magnetic dipole interaction with the neutron's magnetic dipole.

The coherent cross section σ_c comes from the neutron's interaction with the nucleus and $\sigma_c = 4\pi b_c^2$ gives the coherent scattering length b_c. Neutron waves scattered by the nuclear interaction and the separate waves scattered by the charge density interfere coherently. From this knowledge, the neutron-electron cross section is expressed within the interference

term

$$\sigma_{ne} = -4\pi[2b_c b_e(Z - f(E))], \tag{2.64}$$

where $Z - f(E)$ is the charge density of the atom and $f(E)$ takes into account the electron cloud along with a solid angle integration over the atomic form factor $f(\mathbf{q})$. The energy dependence of σ_{ne} is summarily contained in $[Z - f(E)]$. The accurate measurements of the transmission $T(E)$ of neutrons through a sample is given by

$$T(E) = e^{-N\sigma_{tot}} \tag{2.65}$$

where $\sigma_{tot} = \sigma_{ne} + \sigma_c$. Using liquid ^{208}Pb and ^{209}Bi, the most accurate and widely accepted measurements have been done [65] and the results on the neutron's mean charge radius is

$$< r_{ch}^2 >_{exp} = -0.115 \pm 0.003 \pm 0.004 \text{fm}^2 \tag{2.66}$$

2.5. Theoretical Models of Nucleon and Deuteron Structure

The structure of the nucleons is a problem that has spawned the categorization and description of the strong force regime. The strong interaction is one of nature's fundamental forces and building upon the success of Quantum Electrodynamics (QED), Quantum Chromodynamics (QCD) is the physical theory of the strong interaction. It's special property of *asymptotic freedom* was discovered by experiment [55] and then derived as a property of non-Abelian gauge theory [56, 57, 58], explaining the interaction of quarks and gluons and the *confinement* displayed by nuclei at low energy scales.

Still today, Quantum Chromodynamics is not solvable. In the low energy, non-perturbative regime, the coupling becomes very strong and exhibits *confinement of color*. The gauge theory is a continuum and this forces the exceedingly difficult calculations to be unsolvable though it has been shown that a discrete statistical mechanical system on a

four-dimensional Euclidean Lattice may offer a possible approximation scheme [59]. The nucleons, fortunately for us and unfortunate for theory, lie in this low energy regime. Thus, calculating the large scale continuous distribution of electric and magnetic distributions determined from experiment has proven difficult and is not reliably done by any camp in the multi-nodal landscape of particle and nuclear theory save those who fit predominantly *ad hoc* phenomenological functions to the world's data. At large momentum transfer, asymptotic freedom at short distances promotes the relevance of perturbative methods; since the binding of hadrons is a long-distance effect, nonperturbative effects must also play a crucial role. The quantitative description of electromagnetic form factors requires consistency within both length scales.

Perturbative QCD (pQCD) uses the property that the interaction matrix sums over states at high momentum transfer where the partons within the hadron demonstrate small coupling. This makes pQCD a good approximation at high energies, yet typically poor at low energy where the strong coupling constant becomes large. Usually a mass scale Λ is defined and the strong coupling constant is expressed

$$\alpha_s(Q) = \frac{2\pi}{b_0 log(Q/\Lambda)}, \tag{2.67}$$

where b_0 expresses the number of quark flavors. From this approach, pQCD has allowed the most precise tests of QCD.

As far as the nucleon form factors are concerned, Brodsky and colleagues [60, 61, 62] discerned scaling laws and asymptotic behavior applicable to the nucleon form factors. The most notable result, with respect to the neutron and proton is the large Q^2 behavior of the ratio $\frac{G_M^n}{G_M^p} \rightarrow -\frac{2}{3}$, which comes remarkably close to the actual value of $\mu_n/(1+\mu_p) = -0.685$.

Lattice QCD allows non-perturbative approaches to QCD. QCD is a highly nonlinear continuum theory with analytically intractable path integrals. These can be reduced by

using a discrete set of space-time points called the *lattice*, which naturally introduces a momentum cutoff that regularizes the theory. The numerical computations associated with the non-perturbative energy scale are carried out on supercomputers since they are insoluble by means of analytic field theories. The two most active groups in predicting low energy phenomenological behavior of the nucleon are the QCDSF and LHPC collaborations.

The most recent papers [66, 67, 68, 69] are slowly approaching the actual behavior in the low momentum transfer region yet are still hindered by difficulties inherent in 3-point correlation functions, e.g. computational costs on the lattice go as m_π^{-9} and the u and d quarks are taken as larger than reality to enable inversion of the fermionic matrix, then extraction of physical quantities requires extrapolation to the physical quark masses. The state-of-the-art lattices use a grid of $32^3 \times 64$, the spacing $a \sim 1$fm or slightly less to encompass a total length of nearly 3 fm. In order to recover continuum physics, it is necessary to run computations at several values of a and then extrapolate to $a = 0$. *Quenched* calculations assume three quarks and the intermittent gauge fields, while *unquenched* lattice calculations include the u and d quark seas and are thus, much more complicated and computationally intensive. The electromagnetic form factors of nucleons predicted from lattice QCD still deviate considerably (though the isovector magnetic form factor $G_M = G_M^p - G_M^n$ is coming close to the experimental value [67]) from data and it seems that the low energy regime will remain significantly outside of measured values until a new generation of machines can handle the inherently complex numerical simulations.

Two significant models of the nucleon in recent history are the *Skyrmion*, a topological soliton model, and the *MIT Bag Model* which confines three non-interacting quarks to a spherical cavity. The Skyrmion model is considered topologically stable and is interpreted as a conservation of baryon number. The model provides interesting insight yet predicts

nucleon mass, radius, and axial coupling at approximately 30% of experimental values. The MIT bag model assumes non-interacting quarks justified by the idea of asymptotic freedom and quark confinement. There is no meson interaction and thus the MIT bag model necessitates heavy modification.

The *Chiral Bag Model* is a merging of the Skyrmion (which can be written to respect chiral symmetry [76] and is an effective pion field) and MIT bag model. The major modifications to the bag model are essentially of this nature of adding a pion field that respects chiral symmetry. A hole is removed from the middle of the Skyrmion and the bag model is thrown inside. The missing part of the baryon number density from the missing volume within the Skyrmion is entirely made up for by the quark fields inside the bag. The chiral bag models do a much better job of extracting physical properties within 5-10% of the experimental values for the mass and axial coupling constant.

A specific modification to the MIT bag model is the *Cloudy Bag Model* which inserts the missing pion field that is quantized and coupled to the quarks within the bag model. This allows relativistic quark wave functions and confinement as well as respecting the aforementioned chiral symmetry. The problem with using it to predict phenomena such as the electromagnetic form factors is that the cloudy bag model does not respect gauge invariance in all frames [70, 71], and thus may require extra terms to be added [72, 73]. Though, the model does respect gauge invariance in the Breit frame [74] and can be used within such a frame to predict form factors. Light front dynamics (Poincaré invariance) can also be used with the cloudy bag model and seems to come within 5-10% of the values for the electromagnetic form factors of the nucleon [75].

Chiral Symmetry is also a consequence of the QCD Lagrangian. Spontaneous breaking of the chiral symmetry implies pions as massless Goldstone bosons and allows formula-

tion of a perturbation theory (ChPT) at low energies. ChPT can also be used to calculate static properties [137] such as magnetic moments, radii, polarizabilities, etc. The chiral soliton model is also somewhat of a modification to the Skyrmion model and is made to introduce spontaneous symmetry breaking within the bound state of the nucleon. Similar to ChPT, this symmetry breaking necessitates the introduction of Goldstone bosons within the theory with the pion as the lightest of them. A considerable amount of work has been done on expanding this theory and form factors have been predicted generally well[77] at low Q^2.

Effective field theories such as Dispersion theory and Vector Meson Dominance are well documented and represented. Dispersion theory uses a spectral representation for the isoscalar and isovector form factors and uses existing data to parameterize the fitted dispersion relations while making strategic use of introducing residues within the complex plane in order to preserve scaling in the high energy, perturbative QCD regime. Vector Meson Dominance builds upon Dispersion theory and restricts the interaction of the virtual photon with a vector meson. Some models perform better than others in predicting the form factors of the nucleon [78, 79]. Recently the best prediction of any of the presently discussed theoretical models comes by way of Belushkin, Hammer, and Meißner [142]. They use Dispersion models that include constraints from meson-nucleon scattering data, unitarity, and perturbative QCD. The nucleon's electromagnetic form factors are well predicted within Dispersion theory compared to the rest of the theoretical formulations discussed in this section.

CHAPTER 3: **THE BLAST EXPERIMENT**

The Experimental Setup at MIT-Bates Laboratory in Middleton, MA consists of a Linearly Accelerated Electron Beam that is pumped into a high-duty factor storage ring. The Beam is Polarized and the Polarization is maintained over the course of the Storage Ring's lifetime by a set of Superconducting Siberian Snakes. The Storage Ring is approximately 190 meters long and intersects the South Experimental Hall. Within the South Hall is the Atomic Beam Source which is a Hydrogen or Deuterium Gas Internal Target. The Internal Target lies within the center of the BLAST Spectrometer. The BLAST Spectrometer consists of symmetric Drift Chambers, a symmetric array of Cerenkov Counters, a symmetric array of Time-Of-Flight Scintillators, and an asymmetric array of several Neutron Counters - weighted for higher neutron detection efficiency in the sector where we wish to measure $A_{ed}^{V}(\theta_d^* = \pi/2 + \delta, \phi_d^*)$.

My contributions to the experiment includes modeling of the magnetic field of the toroid (Section 3.3), quality control of the wire chambers (Section 3.4.1) and cerenkov detectors (Section 3.4.2), and neutron detector calibrations (Section 3.4.4).

3.1. MIT-Bates And The South Hall Ring

Figure 3.1 shows a schematic of the MIT-Bates South Hall Ring. The internal target area is indicated along with the placement of the Siberian Snakes and the Compton Polarimeter. The following Table 3.1 summarizes the key specifications of the Linear Accelerator and South Hall Ring.

Longitudinally Polarized Electrons are extracted from a Laser driven GaAs crystal and accelerated to an energy of 850 MeV in a pulsed LINAC and recirculator. The pulsed

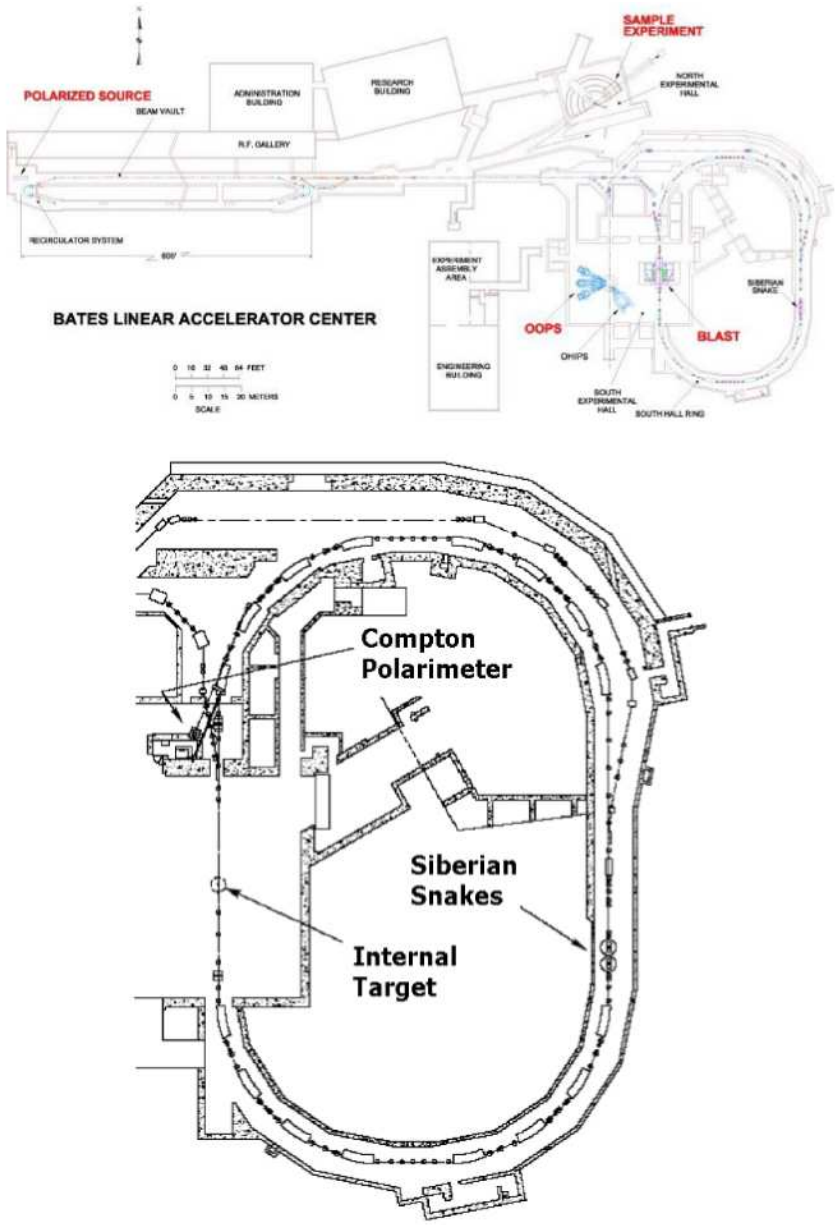

FIG. 3.1. The MIT-Bates South Hall Ring is depicted with clear delineations of the Internal Target, the Siberian Snake, and the Compton Polarimeter.

TABLE 3.1. Characteristics of the MIT-Bates Linear Accelerator and South Hall Ring.

Total Length	160 m
Number of Klystrons	12
Number of Transmitters	6
RF Pulse Length	0-25 μs
Accelerator Frequency	2.865 GHz
Recirculated Beam Energy MAX	1.06 GeV
Max Beam Duty Cycle	1%
Max Pulse Repetition Rate	1 kHz

LINAC can accelerate the beam to a maximum of 500 MeV in one cycle, then must recirculate once to accelerate the electrons to the final energy. The beam is then injected into the South Hall Ring head-to-tail and can reach currents in excess of 200 mA by stacking beam pulses of a few mA at an injection rate of about 10 Hz. The electron beam has two operational modes within the Storage Ring, the stretcher and Internal Target mode. In stretcher mode, the beam has operated above a 50-minute lifetime. In Internal Target mode the lifetimes are typically above 20 minutes.

Longitudinal Beam Polarization is maintained at the Internal Target by a Siberian Snake Spin Rotator. Strong depolarization effects due to non-linear spin resonance were observed but the vertical betatron tune was adjusted and the high polarization (70%) is maintained for the entire lifetime of the beam. A Compton Polarimeter located upstream of the Internal Target measures beam polarization continuously. An RF-driven spin flipper is located downstream of the Internal Target providing the capability for multiple reversals of the polarization in a single storage cycle. Two sets of slits position the beam to minimize beam halo and experimental background. Beam Quality information comes from four symmetrically placed phototubes Beam Quality Monitors (BQMs) located downstream of the Internal Target and from the total hit multiplicity within the Drift Chambers used for particle tracking. Strong correlations are evident between both, the signals from the BQMs

and the signal-to-noise ratio within the Drift Chambers[96]. When the BQMs are showing a small signal and the signal-to-noise ratio of the Wire Chambers is high, the lifetime of the beam also shows significant improvement.

The current in the storage ring is measured with a zero-flux DC current transformer (LDCCT). The beam charge from the ring LDCCT is converted by a voltage-to-frequency converter and is monitored and measured in the VME scalers. There are two channels. One measures all of the charge passing through the ring while the other measures the charge when the Data Acquisition system (DAQ) is alive. This latter channel is the beam-gated integrated charge used to normalize experimental yields from selective spin orientations of beam and target.

3.1.1. Siberian Snakes. The schematic in Figure 3.1 shows the MIT-Bates South Hall Ring. The location of the Internal Target is clearly marked. On the far side of the ring, also indicated in Figure 3.1, a Siberian Snake [97] has been installed. This apparatus can maintain longitudinal electron polarization at the internal target for electron energies up to 1.1 GeV [98].

Maintaining longitudinal polarization for internal target operation during beam operation is complicated by the fact that for the electron $g-2$ is non-zero. At all but 'magic' energies the spin precesses with respect to the momentum through each circulation in the SHR. A Siberian Snake was implemented to ensure purely longitudinal polarization at the location of the internal target.

The Siberian Snake was designed by the Budker Institute of Nuclear Physics. There are two superconducting solenoid magnets within. The insertion point was widened to accommodate the field of the Snake (10.5 Tm/GeV). At the point of Snake insertion the

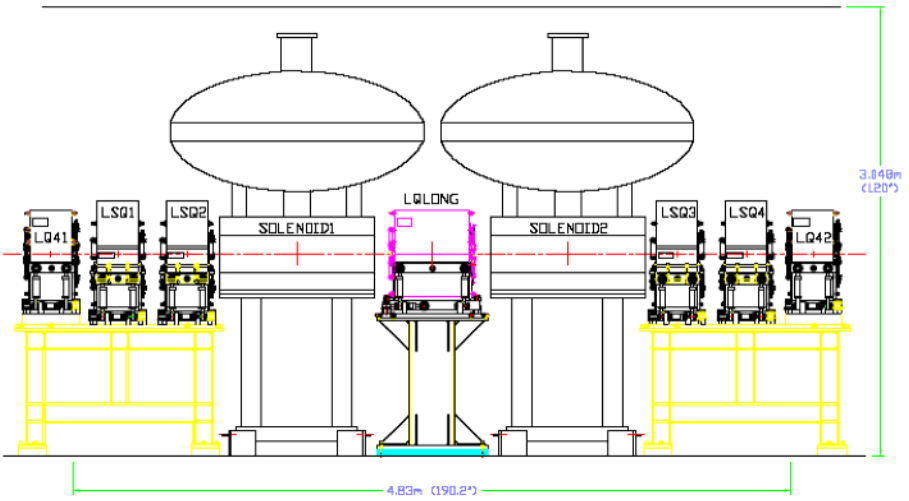

FIG. 3.2. The dimensions of the Siberian Snakes and adjacent magnets used for electron beam optics.

optics is equivalent to a space free of magnets and therefore the optical properties of the SHR are negligibly changed whether or not the Snake is powered on. The two 0.8 m superconducting solenoids maintain peak fields in excess of 7 Tesla.

The beam is injected with longitudinal polarization. The Siberian Snake within the opposing straight region precesses the spin vector by π about the momentum vector to cancel the precession in the south arc with the precession over the north arc of the SHR[99]. Any transverse polarization components resultant of traversing the southern half of the ring are rotated back into the longitudinal direction by the dipoles in the northern half of the SHR. The Siberian Snake eliminates the linear dependence of the spin tune on the beam energy.

3.1.2. Compton Polarimeter. The laser back-scattering Compton Polarimeter took its design from AmPS[100]. BLAST uses a 5-Watt Coherent Verdi laser of 532 nm light. The laser contains a lithium triborate (LBO) frequency doubling crystal. This acts as

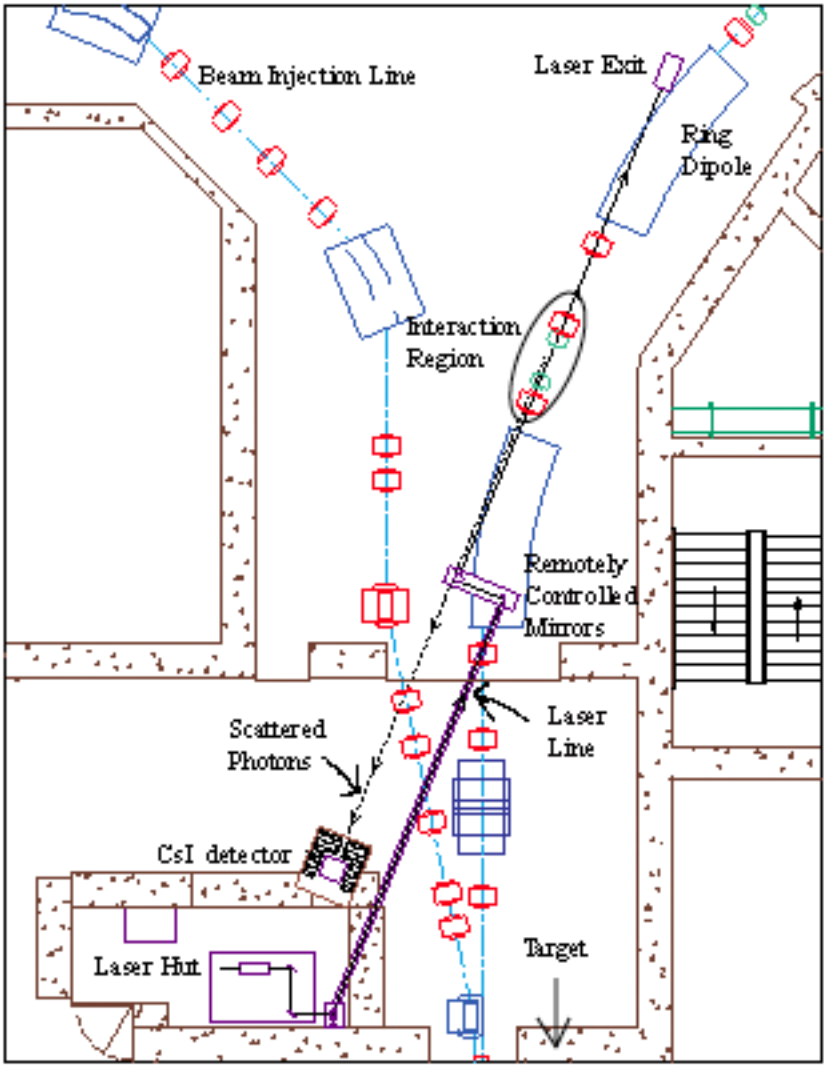

FIG. 3.3. The Compton Polarimeter is clearly outlined. The laser exits the hut, is reflected through mirrors and sent in a collinear path with an arc of the Storage Ring. Photons are backscattered to the Cesium Iodide crystal calorimeter.

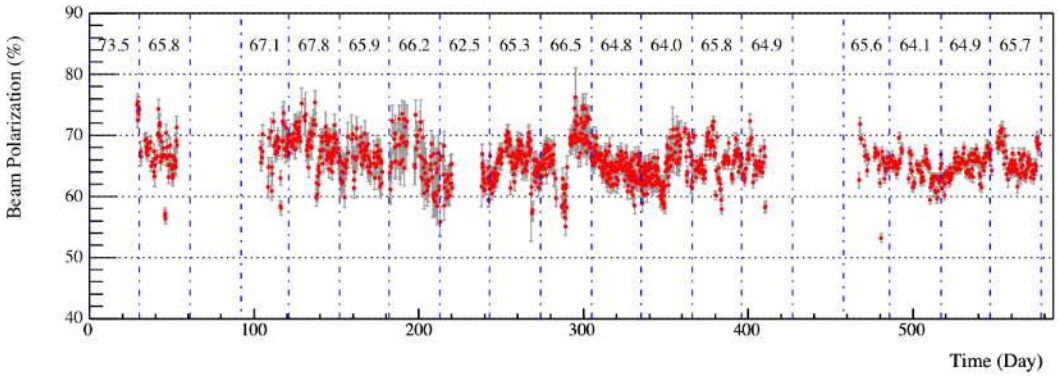

FIG. 3.4. This plot shows the daily results of the Compton Backscattering asymmetry data. The finalized average of the South Hall Ring's polarization of the electron beam is $0.6500 \pm 0.0004 \pm 0.0400$ over the course of the entire experiment analyzed as the subject of this dissertation.

a single-mode cavity and the output of the laser is extremely monochromatic. The analyzing power is about 2% at maximum.

The laser light is circularly polarized by a Helicity Pockels Cell which allows for rapid helicity reversal. The laser is constrained to interact with the beam at an angle of less than 2 mrads[101] over a straight region of about 4 m. The laser undergoes Compton scattering within the interaction region upstream of the Internal Target so to easily avoid background bremstrahlung radiation. A series of collimators, absorbers, and sweep magnet and charged particle veto counters are employed to reduce charged particle and synchrotron light backgrounds. The photon calorimeter for measurement of the backscattered photons' energy spectrum is located 10 meters from the interaction area so as to further prevent background. For the photon calorimeter, a pure CsI crystal was selected for its fast resolving time, < 100 ns, and reasonable light output.

Asymmetries are formed as a function of energy from subtracted yields of detected photons. The asymmetry is then fit with a function that represents the polarimeter's analyzing power. Plots of the Compton Polarimeter's measurements can be seen in Figure 3.4.

The average polarization over the course of the nine months of experimental running as measured by the Compton Polarimeter is $0.6500 \pm 0.0004 \pm 0.0400$. The uncertainty of this measurement is dominated by systematics, predominantly due to the meager $\sim 2\%$ analyzing power.

Tremendous difficulties came with overcoming a decrease in conductance of the ring due to the combination of the collimator and storage cell, the increase in the beam's emittance due to the ionization of the gas in the storage cell, and the indirect steering of the electron beam due to the magnetic field within the internal target region. The BLAST operations group astoundingly overcame each of these obstacles. Were the DOE to close Bates and assimilate the hardware and manpower to locations in remote regions of the country, it would be a tremendous brain drain and quite debilitating to the expertise of MIT and the Bates staff.

3.2. Polarized Hydrogen/Deuterium Gas Target

The demand for Polarized Nuclear targets is on the rise in Nuclear and Particle Physics. The advantages of such experiments are well evident when considering the measurements allowed. In general, polarized targets probe the properties of Spin dependence of the strong and weak interactions, Few-Body physics, Tests of Fundamental Symmetries, and production and analysis of polarized particle beams.

Polarized targets come in two forms, solid and gaseous. The considerations to take into account when choosing a polarized target are numerous. Solid targets are advantageous when considering target thickness, Isotopic Purity, and determination of the Polarization of the target. The cons of using a solid target include heating of the target, radiation damage to the target, and time constraints in reversing the polarization. A gaseous target has low

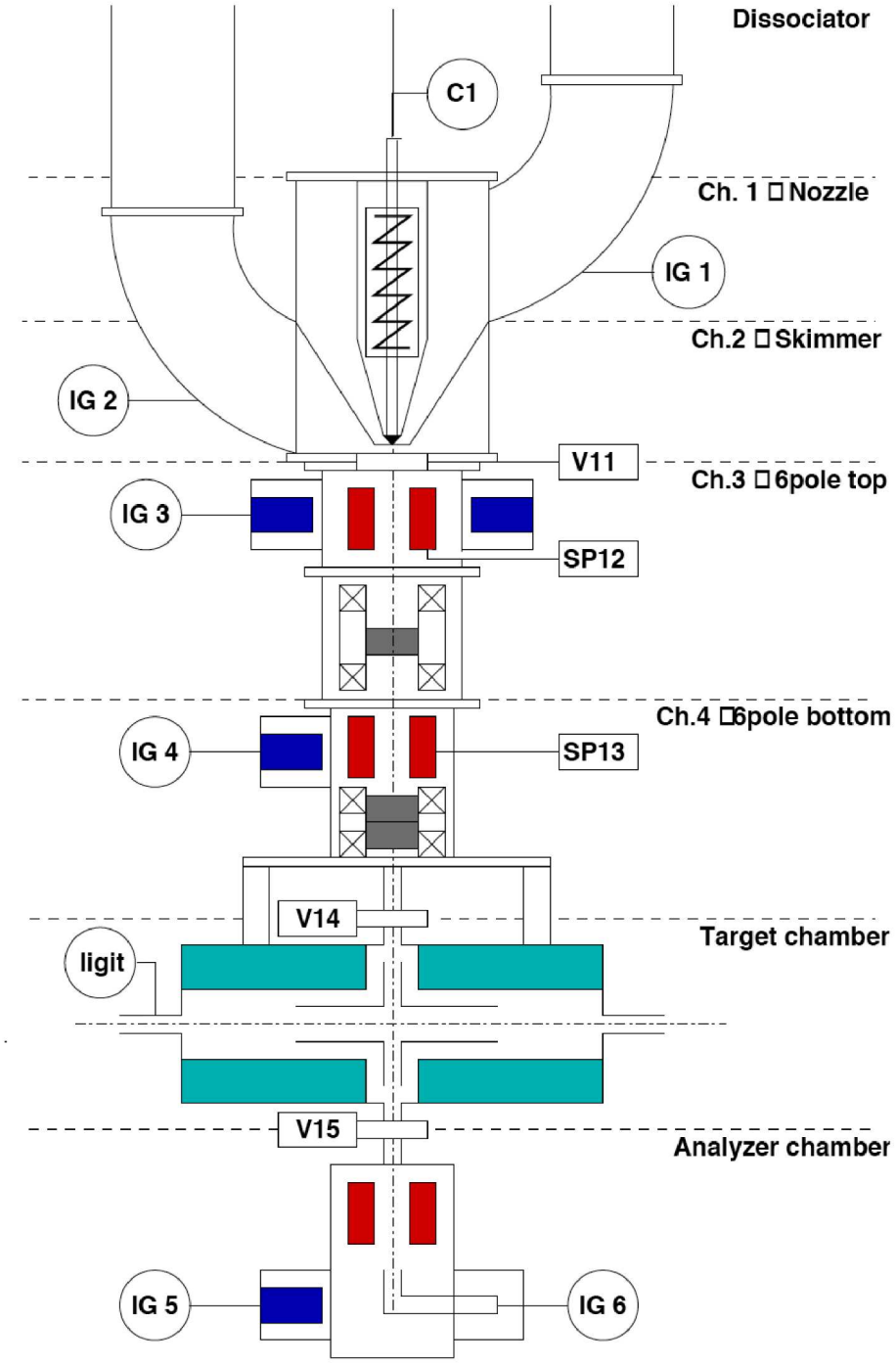

FIG. 3.5. All of the ABS is shown here. IG stands for ion gauges and V11, V14, and V15 are valves. SP's are the sextupole magnets.

thickness and high systematics in determining polarization and spin direction, but there is high isotopic purity, minimal radiation damage, and a high figure-of-merit can be achieved. When coupling the advantages of a high figure-of-merit and the minimal time required to reverse polarization, the use of a gaseous target proves highly favorable for Asymmetry measurements. Despite these cheat sheets of pros and cons, the decision to use a gaseous target was incontestable since a solid target cannot be used with a stored beam.

The BLAST internal Polarized Hydrogen and Deuterium target is a transplant from NIKHEF AmPs Ring. The Atomic Beam Source (ABS) arrived to Bates Laboratory in August, 2000. The system had to be heavily modified to be configured to work with the BLAST experiment. Specific modifications include: shrinking the system to fit between the BLAST coils, modifying the ABS to operate within a 3 kGauss magnetic field, automation of several controls and components since there would be limited access to the mechanism during operation, increased polarization of the atoms within the target to obtain a high Figure-of-Merit, and finally a new design to allow fast transition between Hydrogen and Deuterium polarized targets.

3.2.1. Dissociator. The Atomic Dissociator uses an RF field fixed at exactly 27.12 MHz to separate Hydrogen and Deuterium gaseous diatomic molecules. Gas was fed from the Polarized Gas Feed System through Mass Flow Controllers of accuracy $\sim 2-3\%$. These gases are injected into a Pyrex tube cooled by a flow of deionized water that is pumped through a concentric glass tube. Around these two tubes is a concentric RF Coil which is connected to a fixed RF generator which supplies a power of up to 500 Watts. The apparatus is surrounded by a grounded aluminum can which shields the rest of the working components from the field inside the dissociator. On the bottom of the RF coil a capacitor

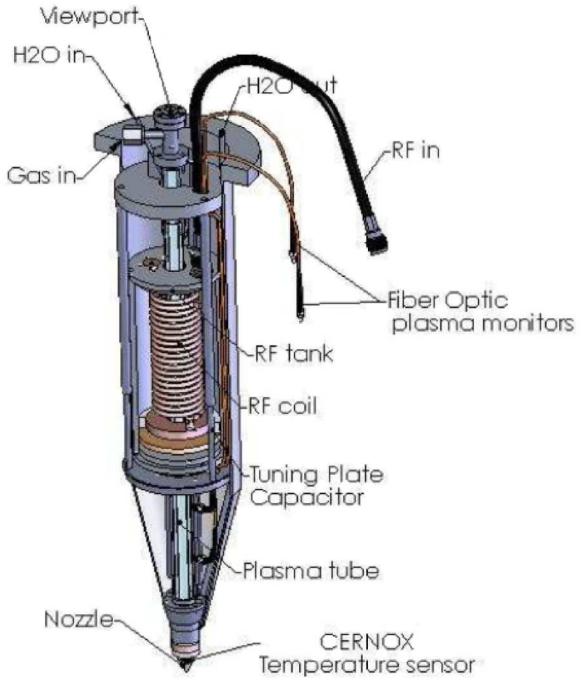

FIG. 3.6. A schematic of the Dissociator used in the Atomic Beam Source for BLAST.

is connected. The capacitor is a piece of dielectric that is placed between the bottom of the RF coil and the aluminum can. The field inside the RF coil ionizes the gas producing a plasma, free electrons are accelerated and collide with diatomic molecules in order to dissociate the gas. Essentially, the RF coil (L), the Capacitor (C), and the plasma (R) create an effective LRC circuit.

The atomic gas is ejected out of the dissociator through a system of apertures that effectively produce the Atomic Beam. They are the *nozzle-skimmer-collimator*. The system was routinely optimized in order to produce the highest flux. The temperature of the nozzle was set at 70 Kelvin in order to achieve maximum flux and lowest recombination rates. A coldhead maintains this temperature. A small amount of Oxygen is mixed into the gas. The Oxygen combines with some of the hydrogen [deuterium] atoms to form water which then freezes and coats the nozzle. This has been found to prevent further recombination of the

ejected atoms. Due to the continuous stream of freezing water, the nozzle must be allowed to warm to room temperature and then refrozen once a week. When running deuterium, a residue slowly builds and forces nozzle replacement approximately every three weeks.

Before installation, the dissociator's performance was well studied with a Quadrupole Mass Analyzer. The dissociation fraction,

$$\alpha_{H/D}^{max} = \frac{n_{H/D}^{a}}{n_{H/D}^{a} + n_{H/D}^{m}} \tag{3.1}$$

was determined to be $\sim 90\%$ for both gases with the BLAST field off, where $n_{H/D}^{a}$ and $n_{H/D}^{m}$ are the numbers of atoms and molecules, respectively.

3.2.2. Exploit of Deuterium's Hyperfine Structure. The sextupole magnet system is a sequence of three tapered sextupole magnets followed by four constant diameter sextupoles. They use the Stern-Gerlach effect and act to focus the atomic beam in selective hyperfine states. Between the sextupole groups, the ABS employs three separate RF field transitions that can be used separately or in combination in order to extract vector and tensor polarized hydrogen [deuterium]. We will focus on deuterium since that is the dataset that will be analyzed here.

Each focusing/defocusing sextupole consists of twenty-four magnets epoxied together at Bates. They were tested and carefully mapped. The atoms adiabatically align their electron spins with the radial field of the sextupoles since the magnetic moment of both hydrogen and deuterium is dominated by the electron spin. Using the ideal field components of a sextupole, it is easy to invoke the equation for the focusing/defocusing force on the atoms:

$$\mathbf{F} = \nabla(\mu \cdot \mathbf{B}) = \mu B_{sp} \nabla \left(\frac{r^2}{r_{sp}^2} \right) = 2\mu B_{sp} \left(\frac{\mathbf{r}}{r_{sp}^2} \right). \tag{3.2}$$

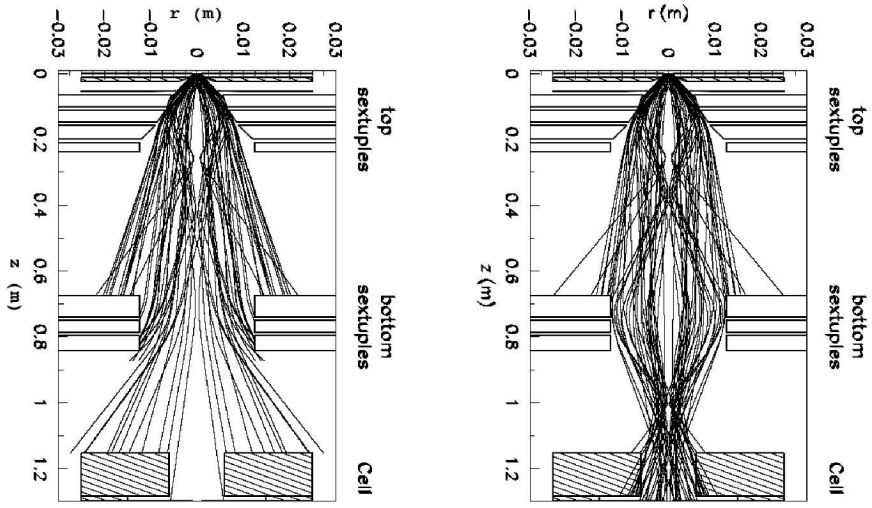

FIG. 3.7. These are RAYTRACE simulations of the injected atoms traveling through the Atomic Beam Source's sextupole fields. The atoms pumped from the dissociator enter the first group of sextupole magnets. The electron in the atoms are in the spin-up ($m_S = \frac{1}{2}$) state and thus focus. In the diagram on the left, the atoms undergo an RF transition that reorients the spin into a spin-down ($m_S = -\frac{1}{2}$) state and they defocus through the second group of sextupoles. On the right, the atoms maintain the spin-up configuration and are focused in the second sextupole group.

The variables B_{sp} and r_{sp} are the characteristic pole-tip field and radius of an ideal sextupole. The radial force guarantees the separation of electron spin-up and spin-down states. Effectively this will separate the deuterium states 1, 2, and 3 from states 4, 5, and 6 that are described below in Equation 3.4. When the ABS is immersed in the BLAST field, it was noticed that the external BLAST field was causing the atomic beam to defocus. This effect has never been observed in any other experiment involving atomic beam sources because the were all operated in the presence of weak external fields. The external field was then included in the calculations for the final intensity of the beam and verified a 50% decrease from zero external field calculations. In order to correct the situation, steel was used to shield the sextupoles from the external magnetic field induced by the Toroid.

The ABS uses RF fields to force transitions in the hyperfine states of deuterium.

The energy levels in deuterium can be split into a quadruplet and a doublet when immersed in a magnetic field. The Hamiltonian of the interaction is written as

$$H_{HF} = \frac{2}{3}h\nu_0 \mathbf{I}\cdot\mathbf{S} + \mu_B(g_I\mathbf{I} + g_S\mathbf{S})\cdot\mathbf{B}, \tag{3.3}$$

where μ_B is the Bohr magneton, ν_0 is the "characteristic" frequency of deuterium's hyperfine interaction, and $g_I = -0.00047$ and $g_S = 2.0023$ are the gyromagnetic factors for deuterium nuclei and the electron, respectively. As mentioned above, when applying a magnetic field, it is easy to see that the electron's gyromagnetic factor will dominate the interaction that couples to the static magnetic field. The sextupoles exploit the Stern-Gerlach effect for the spin of the electron in the deuterium atoms that are ejected from the ABS in order to focus or defocus selective states of the atomic beam. To proceed further and motivate the use of the RF transitions that follow the sextupole separation, the Hyperfine states from the interaction Hamiltonian in Equation 3.3 must be delineated. In the *Breit-Rabi basis*[102] the possible states of deuterium can be completely accounted for. The states are written in the form $|F, m_f; m_I, m_S\rangle$ where $\mathbf{F} = \mathbf{S} + \mathbf{I}$, and $m_{F,I,S}$ are the z-components are of the respective quantum vectors.

$$\begin{aligned}
|1\rangle &= |\tfrac{3}{2}, \tfrac{3}{2}; 1, \tfrac{1}{2}\rangle \\
|2\rangle &= \cos\theta_+|\tfrac{3}{2}, \tfrac{1}{2}; 0, \tfrac{1}{2}\rangle + \sin\theta_+|\tfrac{3}{2}, \tfrac{1}{2}; 1, -\tfrac{1}{2}\rangle \\
|3\rangle &= \sin\theta_-|\tfrac{3}{2}, -\tfrac{1}{2}; -1, \tfrac{1}{2}\rangle + \cos\theta_-|\tfrac{3}{2}, -\tfrac{1}{2}; 0, -\tfrac{1}{2}\rangle \qquad \text{where} \\
|4\rangle &= |\tfrac{3}{2}, -\tfrac{3}{2}; -1, -\tfrac{1}{2}\rangle \qquad \tan 2\theta_\pm = \tfrac{\sqrt{8}}{3B/B_0 \pm 1} \\
|5\rangle &= \cos\theta_-|\tfrac{1}{2}, -\tfrac{1}{2}; 0, -\tfrac{1}{2}\rangle - \sin\theta_-|\tfrac{1}{2}, -\tfrac{1}{2}; -1, \tfrac{1}{2}\rangle \\
|6\rangle &= \sin\theta_+|\tfrac{1}{2}, \tfrac{1}{2}; 1, -\tfrac{1}{2}\rangle - \cos\theta_+|\tfrac{1}{2}, \tfrac{1}{2}; 0, \tfrac{1}{2}\rangle
\end{aligned} \tag{3.4}$$

B_0 is the characteristic magnetic field of deuterium. Both characteristic hyperfine

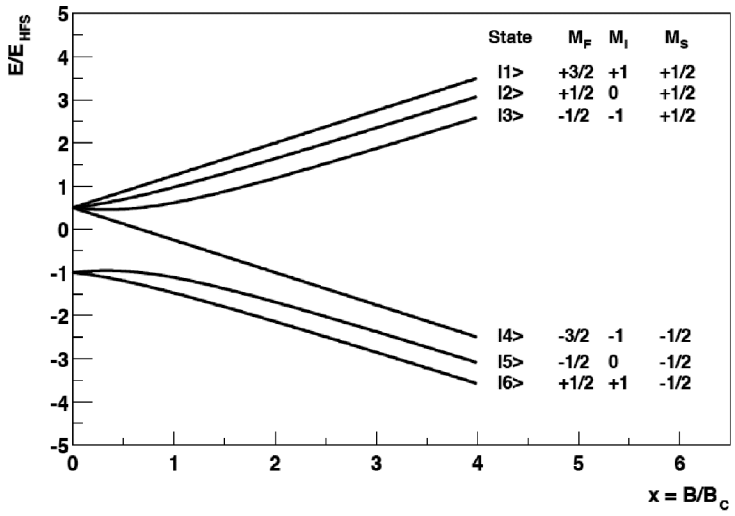

FIG. 3.8. A plot of the energy separation in the Hyperfine states of Deuterium as B/B_0 is increased. The sextupole magnet system in the Atomic Beam Source operates to focus the states $|1\rangle - |3\rangle$ and to defocus the states $|4\rangle - |6\rangle$ through the Stern-Gerlach effect.

quantities of deuterium, B_0 and ν_0, are known to great precision[103]. Respectively, their values are 117 Gauss and 0.327 GHz. The probability amplitudes determined by the mixing angle $\theta_\pm$ are solved by calculating the expectation values from the interaction Hamiltonian *Equation* 3.3 and these states are expressed in the formalism used by Stenger and Rith[104]. It can be noticed that the functional probability amplitudes depend solely on the static field. When immersed in a static field, the probability amplitudes of the spin-down populations in states $|2\rangle$ and $|3\rangle$ decrease asymptotically along with the spin-up populations in states $|5\rangle$ and $|6\rangle$. Immersed in an increasing static field B, the resultant energy levels of the respective hyperfine states in deuterium atoms can be seen to behave as in Figure 3.8.

In a static field, the hyperfine populations remain unchanged. When an external time-dependent magnetic field is applied, the hyper-fine states can follow well defined transitions. There are two possible RF transitions that can be employed. The time-dependent magnetic field B_{RF} can be oriented parallel to the static field or perpendicular. The ap-

plication of a parallel time-dependent field is known as an RF σ-transition and obeys the $\delta m_F = 0$ selection rule. It is obvious from the defined states in Equation 3.4 that the possible σ-transitions are $|3\rangle - |5\rangle$ and $|2\rangle - |6\rangle$. The application of a perpendicular time-dependent magnetic field is known as an RF π-transition and obeys the selection rule $\delta m_F = \pm 1$. The Maxwellian velocity distribution of the atoms in the beam limit the efficiency of the π-transitions since the atoms would spend a different amount of time within the static field in which the time-dependent transition would take place. Therefore, the π-transitions can only take place adiabatically [105, 106]. The adiabatic regime for π-transitions includes a gradient magnetic field B_{gr}. R.J. Philpott found an analytic solution in which only two hyperfine states exchange their population[106]. In order for the transition probability in this selective case of an adiabatic regime to be close to unity, the gradient field must obey

$$B_{gr} \ll \frac{\mu_J B_{RF}^2}{2 v_x \hbar}. \tag{3.5}$$

This is an amazing solution since it provides the potential for nearly 100% efficiency in RF π-transitions when B_{gr} and B_{RF} are properly matched.

In the ABS scheme, Mean Field Transitions (MFT) and Weak Field Transitions (WFT) are the induced π-transitions exploited between sextupole focusing and the internal target. The possible π-transitions with deuterium are

$$\begin{aligned}
|1\rangle &\Longleftrightarrow |2\rangle \quad \text{(MFT1-2, WFT1-2}^*\text{)} \\
|2\rangle &\Longleftrightarrow |3\rangle \quad \text{(MFT2-3, WFT2-3}^*\text{)} \\
|3\rangle &\Longleftrightarrow |4\rangle \quad \text{(MFT3-4, WFT3-4}^*\text{)} \\
|5\rangle &\Longleftrightarrow |6\rangle \qquad \text{(MFT5-6)}
\end{aligned} \quad .$$

The * is indicated because the WFT is operated at a low frequency where the static magnetic fields of the hyperfine transitions are not separated. They result in a cascading transition from $|1\rangle - |4\rangle$ and the transition $|2\rangle - |3\rangle$. The MFT's can be processed individually or

in succession. Using the proper combination of sextupole focusing and RF transitions the proper sequestered states of deuterium can be extracted from the atomic beam. One example of a transition sequence, the extraction of *vector plus*, is shown here:

$$\begin{pmatrix} n_1 \\ n_2 \\ n_3 \\ n_4 \\ n_5 \\ n_6 \end{pmatrix} \begin{matrix} \\ \\ \text{sextupole} \\ \longrightarrow \\ \\ \\ \end{matrix} \begin{pmatrix} n_1 \\ n_2 \\ n_3 \\ 0 \\ 0 \\ 0 \end{pmatrix} \begin{matrix} \\ \\ \text{MFT3-4} \\ \longrightarrow \\ \\ \\ \end{matrix} \begin{pmatrix} n_1 \\ n_2 \\ 0 \\ n_3 \\ 0 \\ 0 \end{pmatrix} \begin{matrix} \\ \\ \text{sextupole} \\ \longrightarrow \\ \\ \\ \end{matrix} \begin{pmatrix} n_1 \\ n_2 \\ 0 \\ 0 \\ 0 \\ 0 \end{pmatrix} \begin{matrix} \\ \\ \text{SFT2-6} \\ \longrightarrow \\ \\ \\ \end{matrix} \begin{pmatrix} n_1 \\ 0 \\ 0 \\ 0 \\ 0 \\ n_2 \end{pmatrix}$$

Remember from Equation 3.4 that states $|1\rangle$ and $|6\rangle$ in the limit of $B/B_0 \gg 0$ are indeed polarized with $m_I = +1$. These two states are then injected into the Internal Target.

3.2.3. Internal Target. The internal target scattering chamber was also included in the NIKHEF ABS package. It consists of a holding field magnet, a target cell that rests inside, a cooling system, and has thin aluminum windows. The target shares the beam vacuum and thus necessitated strong vacuum pumping in order to ensure that beam quality does not deteriorate. The aluminum internal target cell is motivated by an increase in Luminosity by orders of magnitude with respect to a target consisting of a single ballistic jet of atoms. Despite a larger probability of loss of polarization due to atomic collisions with the cell walls, atomic recombination into diatomic molecules, and higher number of interatomic spin exchange collisions, the increase of Figure of Merit (FOM) of an order of magnitude easily outweighs the slight loss of polarization. The FOM for polarization experiments is defined as:

$$FOM = Polarization^2 \times Luminosity, \tag{3.6}$$

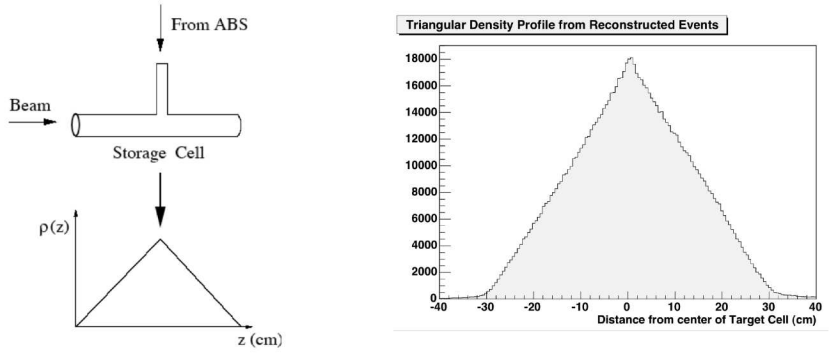

FIG. 3.9. The density profile of the target. On the right is the actual vertex traced back from the reconstructed track of charged particles through the Drift Chambers. The triangular profile is well recreated and nonexistent beyond the edges of the 60 centimeter cell.

The depolarization effects of the storage cell were never extensively studied at BLAST and thus the discussion as to contributing processes are *a posteriori* and not fully quantified.

The design of the storage cell is cylindrical. It has a diameter of 15 mm with an 11.9 mm inlet fed from the ABS. It is composed of 50 μm aluminum foil. It is kept chilled at a temperature of 90° K in order to minimize the dwell time[107] on the cell wall. There is an inlet from the ABS, a small outlet through which the atoms could be sampled by a Breit-Rabi Polarimeter and Quadrupole Mass Analyzer, and open sides for allowing the electron beam easy entrance and exit as well as through which the diffusive monatomic gas would exit the chamber. Since the ABS injection is aligned at the center and there is vacuum at the lateral ends of the target, a triangular density profile is immediately expected and can be proven by showing that density as a function of the position along the axis of the cell, $\rho(z) = \rho_0 \left(1 - \frac{|z|}{L}\right)$ is a solution of the diffusion equation written for an ideal tube along the z-direction with steady flow entering from the inlet at center where ρ_0 is the density at the center and L is the length of the cell.

As mentioned earlier, depolarization effects were studied extensively[107, 32]. The three dominant interactions potentially causing the depolarization of the target atoms are

cell wall collisions, recombination, and spin exchange collisions. Depolarization through cell wall collisions is a function of the time spent on the cell wall in which it can interact with the unpaired electrons and magnetic dipoles on the wall through spin exchange and Pauli Exclusion interactions. The probability of these interaction is characterized by its frequency of polarization relaxation which only affects the nucleus's polarization if the atom is in a weak field regime where the electron and nuclear spin are coupled $\langle \mathbf{S} \cdot \mathbf{I} \rangle$[109, 110]. The holding field of the target, when the ABS is pumping deuterium, is in the strong field regime and thus the electron spin and nuclear spin are decoupled. Recombination is characterized by the number of interatomic collisions inside the cell on the cell wall since the density is low enough inside the cell to neglect recombination in the volume of the target. The probability of recombination must thus be proportional to number of collisions with the wall as well as the amount of time spent on the wall. The number of collisions with the wall is characterized by the total Conductance C_{tot} of the cell and the average thermal velocity $\langle v \rangle = \sqrt{\frac{k_B T}{M}}$. Conductance is in units of $Pressure \times Volume$ and with the geometry of the cell, gives the overall average time that an atom spends inside the cell. The average number of wall collisions $\langle N \rangle$ during that time works out to be a simple function of geometry. The resulting dwell time $\tau_d = \frac{h}{\delta E} \exp \frac{E_a}{k_B T}$ arises from Arrhenius Law as a function of the adsorption energy E_a and δE being the energy difference of possible states at the adsorption site. In the end there are competing effects over a range of temperatures in which low temperature favors a decrease in adsorbed atoms and high temperature favors a decrease in the time an atom spends on the wall of the target cell. The optimal temperature to minimize recombination as fit with this ansatz was found to be in the range 100-120°K[111]. Finally, spin-exchange collisions were expected to be negligible in the BLAST configuration though Bulten et al. found a 10% drop in polarization at densities at $\sim 10^{12}$ atoms/cm^3[112] which is precisely

the density at the center of the target. The expected rate of spin-exchange collisions in Bulten et al. was calculated using the two formulae

$$\frac{1}{T_{dd}} = \rho_d \langle \sigma_{se} v \rangle, \text{and} \frac{d}{dt} n_i = \frac{1}{T_{dd}} \sum_{a,b} n_a n_b A^i_{a,b}(x) \tag{3.7}$$

where T_{dd} is the average time between d-d collisions, ρ_d is the density and v is the relative velocity of the deuterium atoms. $\langle \sigma_{se} \rangle$ was taken from Desaintfuscien and Audoin[113]. n_i is the fractional density of deuterium in state i and the coefficients $A^i_{a,b}$ that describe the probability for states $|a\rangle$ and $|b\rangle$ to transform into state $|i\rangle$ are taken from Stenger and Rith[104].

In order to further limit the possibility of recombination and interactions when collisions occur with the cell wall the cell was coated with *Dryfilm*. *Dryfilm* is in a class of chemical compounds known as organosilicons which are non-reactive compounds with low dielectric constants, and thus, low polarizability. These compounds are also hydrophobic. During the coating process, *Dryfilm* undergoes hydrolysis preventing the accumulation of H^2OandD^2O molecules to the surface of the target cell that are ejected by the Dissociator (See Section 3.2.1). *Dryfilm* also prevents spin exchange depolarization effects with atoms that may still adsorb to the surface of the target[108]. In order to test the *Dryfilm* coating, a water bead test was performed both before installation and after a period of running in order to determine if it was damaged. High heat, direct interaction with the electron beam, and radiation can all damage the coating on the cell. Commissioning runs showed substantial damage to the target surface from the electron beam halo. A tungsten collimator was installed upstream from the internal target and Monte Carlo simulations were run in order to determine the proper dimensions of the collimator. After testing a few designs, the final collimator design was obviously cylindrical with a large concentric tungsten ring, it included a region of constant diameter for about a centimeter followed by a sharp edge where

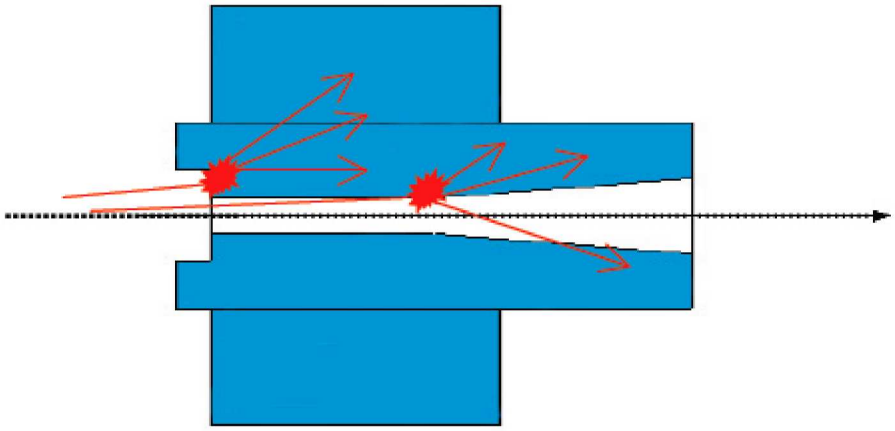

FIG. 3.10. Simple sketch of the final collimator design.

the diameter was approximately halved, then tapered out to the end of the collimator see Figure 3.10. Despite great efforts, there was still a considerable positron shower emanating from the area of the collimator, though the internal target cell was much better protected and injection and lifetime of the electron beam showed a negligible difference.

3.2.4. Target Holding Field. The last piece of the target necessitating discussion is that of the Holding Field of the Internal Target. It is comprised of longitudinal and transverse electromagnetic water cooled copper coils within the scattering chamber that houses the target cell. The longitudinal and transverse fields allow orientation in any direction within the two-dimensional plane parallel to the earth's surface, i.e. $\phi_{BLAST} = 0$. The holding field also maintains the polarization of the incoming atoms by preventing Hyperfine interactions that can occur readily when B/B_0 falls below the critical value that allows the electron and nuclear spins to recouple.

The field was measured before installation of the cell. Surveys of the field were also taken during downtime in between production runs in July, 2004 and January, 2005 and June, 2005. TOSCA simulations were also done and compared. During running, there was

also an effective measurement using electron-deuteron elastic tensor asymmetries. The essential algorithm for this real-time measurement is as follows. P_{zz} is the tensor polarization of our target. It is also the ratio of our raw asymmetries to the asymmetries expected and simulated with Monte Carlo at 100% polarization. The detector is roughly symmetric and we are measuring electron-deuteron elastic interactions where our momentum transfer is both, roughly parallel to the orientation of spin ($A^{\parallel}_{raw}$) and roughly perpendicular to the orientation of spin ($A^{\perp}_{raw}$). The Monte Carlo is simulated over a range of angles and the data is compared.

$$P^{\parallel}_{zz}(\theta_S) = \frac{A^{\parallel}_{raw}}{A^{\parallel}_{MC}}, \text{and} P^{\perp}_{zz}(\theta_S) = \frac{A^{\perp}_{raw}}{A^{\perp}_{MC}}. \tag{3.8}$$

When $P^{\parallel}_{zz}(\theta^S) = P^{\perp}_{zz}(\theta^S)$ we have our measured average spin angle. See section 4.8.1 for a more in depth demonstration of this procedure and how the systematics affect the experiment.

Despite the real-time monitoring and the surveys and TOSCA simulation, there were found to be considerable discrepancies between the spin angle measurements (see Figure 3.11). When surveying the angle with transverse and longitudinal settings at 32°, the difference between January 2005 (31.2°) and June 2005 (30.6°) surveys is found to be about 0.6°. When surveying the configuration for the orientation of the spin angle set at 47°, the survey from July 2004 depicted an average spin angle of 47.0°, 0.3° more than January 2005 and 0.8° more than the June 2005 survey. All the surveys used a 3D probe. Despite the different values, the actual shape of the surveyed maps differed by no more than 0.1°. The final spin angle profile is also shown (see Figure 3.11) and is a 9^{th} order polynomial function of the spin angle $\theta_{nominal}$ at the center of the target. The results from the analysis of ed-elastic tensor asymmetries are dependent upon which model is used but by fitting in the lowest momentum-transfer region ($\mathrm{Q}^2 < 0.18\mathrm{GeV}^2/\mathrm{c}^2$), the model dependency

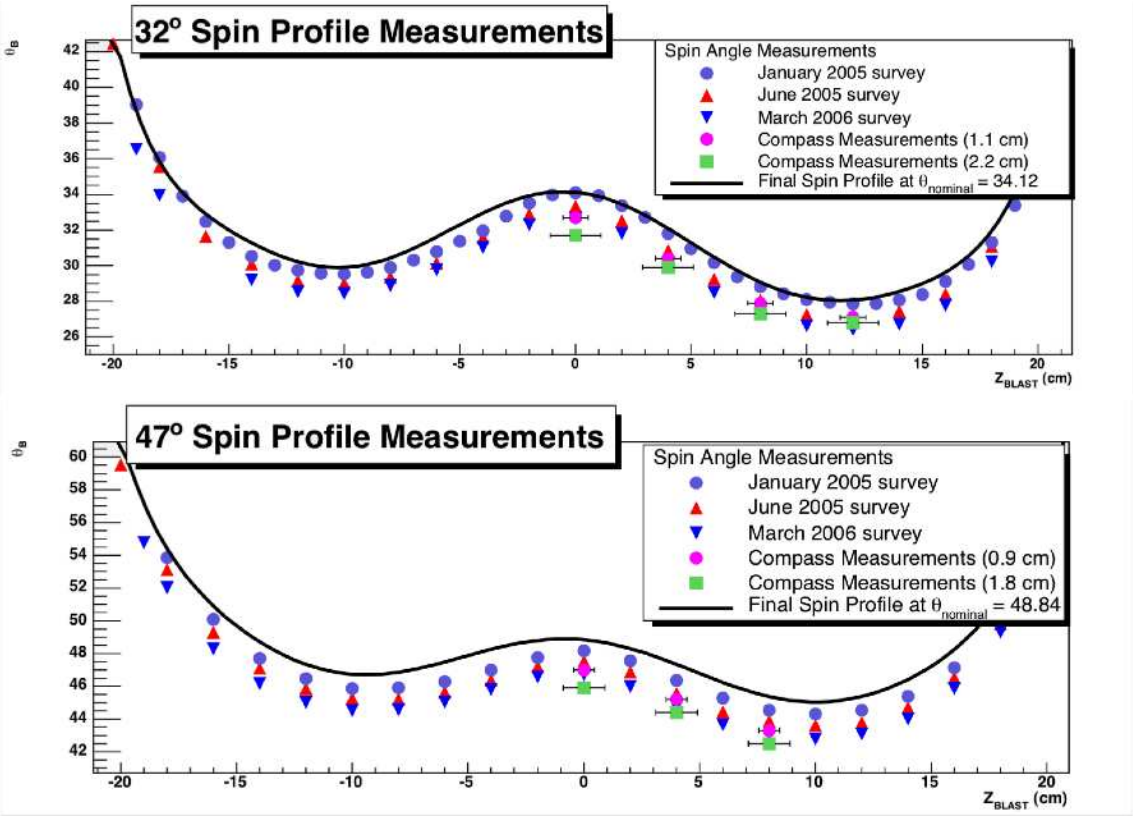

FIG. 3.11. The measurements of the two configurations of spin profiles are shown with the data from several measurements of the spin angle along the beam line's intersection with the internal target.

TABLE 3.2. Essential Spin Angle quantities.

Year	$\bar{\theta}^S$	*Longitudinal Field (G)*	*Transverse Field (G)*	$\theta^S_{nominal}$
2004	$31.3^\circ \pm 0.43^\circ$	500	250	34.12°
2005	$47.4^\circ \pm 0.45^\circ$	500	500	48.84°

is minimal. The measured values of the average spin angle turned out to be $31.3^\circ \pm 0.43^\circ$ and $47.4^\circ \pm 0.45^\circ$. Another result in the 47° configuration comes from the vector asymmetries in elastic electron proton collisions from a Hydrogen target. The result from that experiment, which is less sensitive than ed-elastic, is $47.7^\circ \pm 0.8^\circ$ which was well in agreement with the measurement from the ed-elastic tensor asymmetries.

Final conclusions as to the spin angle in the two configurations were arrived at in May, 2006. The agreement between the January 2005 survey and the ed-elastic asymmetries in the 32-degree configuration are nearly spot on. The ed-elastic was agreed to give the best value for the 47-degree configuration as well. Thus for final analysis, the final spin angle profile convoluted with the triangular density profile of the internal target gave average spin angles listed in the Table 3.2. Maintaining and configuring the polarization and direction proves to be one of the largest systematics in the calculation of the electric form factor of the neutron (see Section 4.8).

3.2.5. Polarization at BLAST. The polarization of an ensemble of particles can be defined by the respective probabilities p_i to find a nucleon in a state associated with a cross-section σ_i where, for deuterium, $\sigma_d^{total} = \sigma_{+1} + \sigma_0 + \sigma_{-1}$.

$$\begin{aligned} 1 &= p_+ + p_0 + p_- \\ P_z &= p_+ - p_- \\ P_{zz} &= p_+ + p_- - 2p_0 = 1 - 3p_0 \end{aligned} \tag{3.9}$$

The Atomic Beam Source operates in three modes of injection and the yields V_+, V_-, and T_- can be characterized by the state in which they were injected. Using these yields, the vector and tensor asymmetries, A_V and A_T, are defined, assuming equal or normalized yields, as

$$\begin{aligned} A_V &= \frac{3}{2} \cdot \frac{V_+ - V_-}{V_+ + V_- + T_-} \\ A_T &= \frac{1}{2} \cdot \frac{V_+ + V_- - 2T_-}{V_+ + V_- + T_-} \end{aligned} \tag{3.10}$$

At BLAST it has become customary define the vector polarization as $\tilde{P}_z = \sqrt{\frac{3}{2}} P_z$ and the tensor polarization as $\tilde{P}_{zz} = \sqrt{\frac{1}{2}} P_{zz}$. The reason for these definitions stems from the normalization constants from A_V and A_T as Arenhövel's formalism defines the vector and tensor asymmetries with coefficients of $\sqrt{\frac{3}{2}}$ and $\sqrt{\frac{1}{2}}$, respectively, rather than those that are customary in equation 3.10, e.g. $\frac{3}{2}$ and $\frac{1}{2}$. The three can be displayed by a simple schematic triangle showing the accessible states of the deuterium target polarization as demonstrated in Figure 3.12.

3.3. BLAST Toroid

The discrimination of momentum and charge of the particles exiting from the scattering chamber and entering the detector region is provided by the Toroidal Magnetic Field. The Toroidal field is used to prevent fringe fields from heavily affecting the Photomultiplier Tubes (PMTs) of the Scintillators and Cerenkov Counters used in the Detector Package discussed in Section 3.4. The field is strong enough to bend Mø ller scattered electrons inward to prevent their entrance into the Detector package and to strongly bend positrons outwardly enough for identification by their tight curvature.

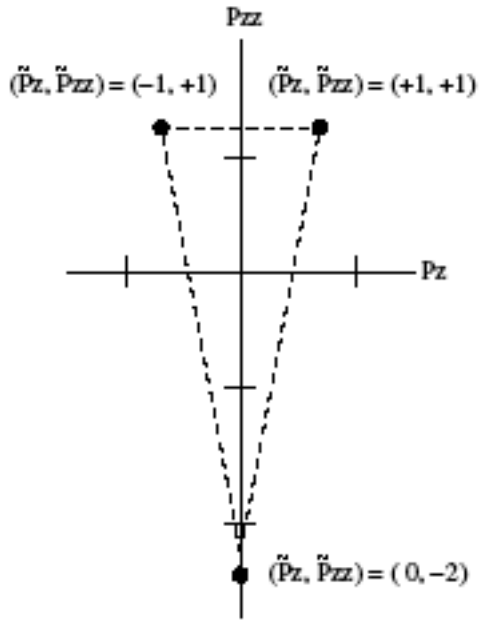

FIG. 3.12. A schematic triangle demonstrating the accessible states of the BLAST deuterium target polarization.

The BLAST Toroid consists of eight copper coils that are fixed on an aluminum subframe azimuthally symmetric to one another around the beamline. Each coil is comprised of 2 adjacent layers of 13 turns of hollow copper conductors of cross-sectional dimensions 1.5×1.5 $mathrmin^2$. The conductors are water cooled. The power to the Toroid is provided by a *BTSPS MON 1 250/7000 C5* power supply from BRUKER and is capable of providing 7000 A at 250 Volts. The operating current in the magnetic field was 6730 A. At the operating current, the maximum magnetic field (which is known to preside within the vicinity of the Drift Chambers) is approximately 0.38 T. The magnetic field of the Toroid has been extensively mapped and the magnetic field grid is used for reconstruction of the tracked particles within the BLAST Spectrometer. The ideal magnetic field was initially calculated from the geometry using a Biot-Savart algorithm and separately using a *Vector Fields* TOSCA simulation. A plot of the discrepancy between the Biot-Savart

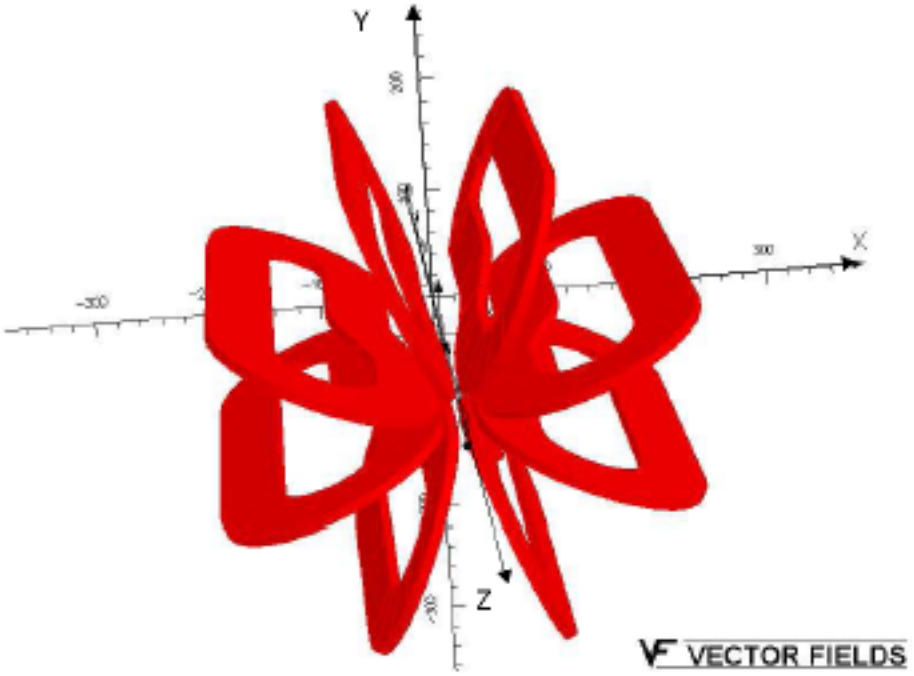

FIG. 3.13. A schematic of the BLAST Toroid and the BLAST coordinate system.

calculation and the actual measured field is shown in Figure 3.14. In Table 3.3 the early discrepancies between calculations and the measured field values at coordinates within the BLAST coordinate system[1] can be seen. The major discrepancy between measured and calculated values in the first row was concluded to be the failed inclusion of the target's holding field that would have a large effect within a region a small distance from the vertex ($\vec{r} = (0, 0, 0)$) in the center of the target. Also, the earliest Biot-Savart calculations did not account for a 7-10mm radial shift outward that occurs when powering up the Toroid. The measured field values from a final survey with both Holding Field and BLAST Toroidal Field on were used in actual reconstruction algorithms.

During commissioning, the performance of the photomultiplier tubes (PMTs) of the

[1]See Figure 3.13, $+\vec{z}$ in direction of momentum of beam, $+\vec{y}$ to ceiling, $+\vec{x}$ finishes a right-handed coordinate system, origin ($\vec{r} = (0, 0, 0)$) or 0cm in vertex distribution in Figure 3.9 is at the center of the target cell

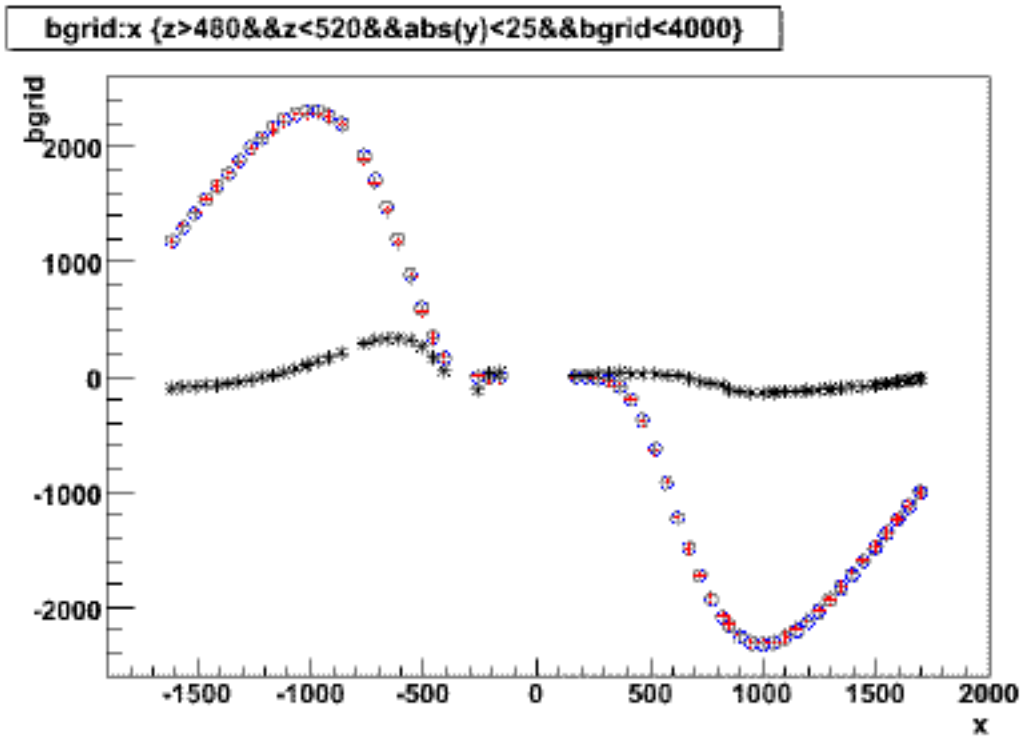

FIG. 3.14. The Biot-Savart calculations of the magnetic field along the BLAST-x axis using ideal locations of the BLAST coils is shown in this plot. The measured values without the Holding Field on are also superimposed. The discrepancy between the two values is multiplied by 10 to make the discrepancy better visible.

TABLE 3.3. At particular coordinates within the BLAST system, the magnetic field of the Toroid is measured and calculated. The columns of calculations are listed as Ideal BS, and Offset BS. Respectively these are Biot-Savart calculations at an ideal position of the coils and with the coils radially offset by 8mm. The factor of 2 discrepancy between measured and calculated field at $x = 41.5cm$ is caused by the failure to include the holding field in the Biot-Savart calculations.

Position **(cm)**			**B_y (Gauss)**		
X	Y	Z	Ideal BS	Offset BS	**Measured**
41.50	0.26	28.70	147	164	**292**
91.50	0.20	28.70	2221	2254	**2329**
141.50	0.14	28.70	1663	1657	**1672**
191.50	0.08	28.70	577	566	**548**

Cerenkov Counters (discussed later in Section 3.4.2) were being heavily affected by the presence of a longitudinal magnetic field consequential to the proximity of the BLAST coils. Due to the measurements of an ambient field of 100 Gauss in the region of the PMTs, two concentric cylinders of low-carbon steel with an air gap encasing the PMTs was implemented. A field of 10 Gauss has been shown in simulations to lower the efficiency of a single PMT to essentially zero. During operation the efficiency was still being affected by the BLAST Field even though the ambient field was shown to be a few Gauss. Another solution was implemented, a layer 0.5-inch low-carbon steel was installed in front of and behind the twelve sets of Cerenkov PMT's. Though this was successful with respect to increasing the efficiency of the Cerenkov Counters (CC), the affect on the BLAST field was unknown (though assumed to be small). Though there had been discrepancies between the calculated ep-elastic kinematics since commissioning, the possibility of the shielding affecting the grid of magnetic field values used in reconstruction needed to be quantified.

Figure 3.15 shows the simulation of an electron track within the BLAST field calculated by TOSCA and the schematic of the BLAST coils with steel shielding used for the CC. TOSCA was used to simulate the BLAST field with and without shielding and an electron with the same initial kinematics was propagated through the two calculated fields. The TOSCA simulation used a step size of 1cm for the electron kinematics. Figure 3.16 shows two plots over the total displacement from the origin (x-axis). of the BLAST coordinate system. The y-axis of the left plot is a calculation of the total magnitude of the difference of the position vectors at each step in the simulation of the two electron tracks. The y-axis of the right plot shows the magnitude of the difference in the momentum vectors at each step. Since the Drift Chambers (sometimes called Wire Chambers and will be abbreviated as WC) give the coordinates used to track particles, these deviations are only

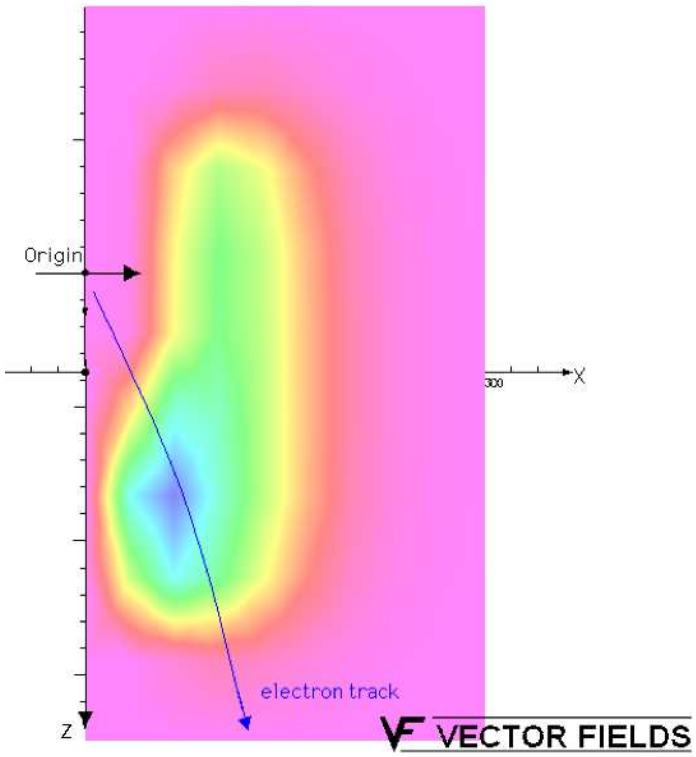

FIG. 3.15. Electron tracks were simulated with the same initial kinematics in two simulated magnetic fields, the BLAST field with and without Steel Shielding in front of the Cerenkov Photomultiplier tubes.

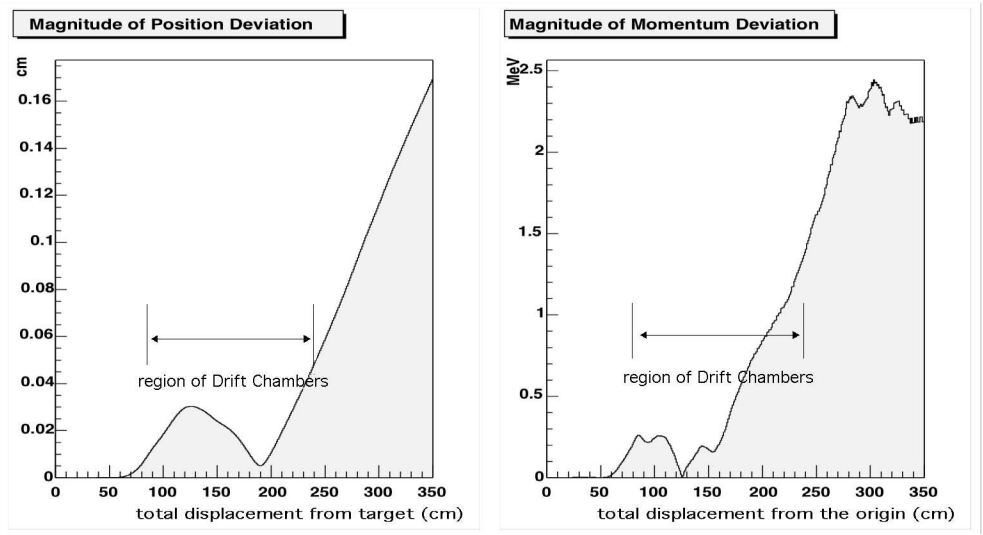

FIG. 3.16. Electron tracks were simulated with the same initial kinematics in two simulated magnetic fields, the BLAST field with and without Steel Shielding in front of the Cerenkov Photomultiplier tubes. The left plot describes the total magnitude of the deviation of the position vectors along the tracks. The right plot describes the total deviation of the momentum vectors. The drift chambers are located within the region indicated. Since the resolution of the wires within the Drift Chambers is approximately 200 microns, the deviation of position along the tracks shows to be below the resolution for the majority of the track's displacement from the origin. The linear growth of the deviation in position shows the deviation of the continued trajectory as the electrons leave the magnetic field. The actual deviation in the momentum within the region of the Drift Chambers is less than 3% of the resolution of the Drift Chambers and is thus negligible.

important with respect to the resolution of the WC. From Figure 3.16 we can see the region from where we obtain information useful for tracking the charged tracks ejected from the scattering chamber. The resolution of the wires used to track the charged particles is 200 microns and the resolution of the software's calculation of momentum from the fitted tracks is approximately 35 MeV. From both plots it is obvious that the tracks do not deviate from each other considerably. The deviation of position along the tracks is below the resolution of the sense wires for the majority of the region of the WC and then grows linearly as expected when the electrons leave the region of the field's influence and continue along their final trajectories. The magnitude of the deviation of the momentum vectors is completely negligible at a maximum of 1 MeV within the region of the WC.

When plotting the fields along lines traced from the origin to the faces of the 3 Cerenkov Counters in a single sector, we can plot the ratio between the fields simulated with and without Cerenkov PMT shielding. Figure 3.17 shows one of these ratios and the actual superimposition of the fields. Since there is no way to ensure that TOSCA creates equivalent meshes for two different physical situations, there is always a possibility of fluctuations at specific points within the finite element analysis. The plot on the right in Figure 3.17 shows these fluctuations in the region of the maximum field gradient. The essential part of this graph is the ratio of $\sim$1.0 in the region of maximum field contained within the region of the WC.

3.4. BLAST Detector

The BLAST Detector is shown in Figure 3.18. The apparatus was built on site. The ABS enters vertically from directly above the internal target and cutting through the BLAST coils. The BLAST Detector fills in the horizontal region on both sides of the beam

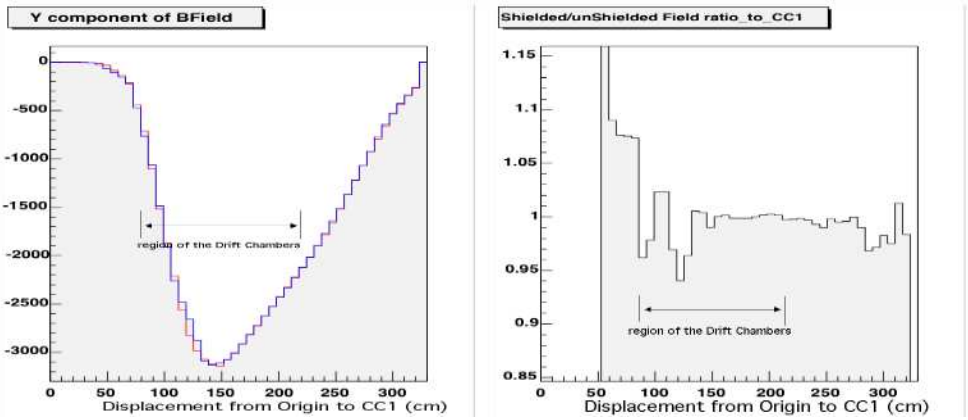

FIG. 3.17. TOSCA was used to simulate the difference in the fields with and without Shielding used for the Cerenkov Counter's PMTs. The two simulated fields are superimposed and plotted along the line from the origin to the face of the middle Cerenkov Counter (CC1) on the left. The right plot shows the ratio of the values of the field. There are fluctuations in the region of the largest field gradient which can be attributed to the difference in the automatic meshing implemented in TOSCA. The ratio of ∼1.0 in the region of maximum field contained within the region of the Drift Chambers is the important result used to imply a negligible difference in reconstruction between the two physical situations.

pipe. The Spectrometer was designed to be left-right symmetric. Left-Right azimuthal symmetry allows for coincidence measurements. The Detector is large acceptance to compensate for the low luminosity of a gaseous internal target. This also has the advantage of acceptance of out-of-plane angles.

From the view of a charged particle ejected from the scattering chamber and moving through a single sector of the Spectrometer, it would first enter the BLAST Toroidal Field allowing for charge discrimination. The coils have a pair of left-right symmetric Drift (Wire) Chambers (WC) nestled in the region of maximum field. In these WCs the particle will pass through 18 alternately crossing layers of wires slightly off vertical alignment. Upon exiting the WC, the next set of detectors is a set of 3 Cerenkov Counters (CC) used for electron-pion discrimination. Directly behind the CCs is a layer of 16 panels of scintillating material used for accurate Time-Of-Flight measurements (TOF). Behind the layer of TOFs is the

only left-right asymmetric detector array, the Neutron Counters (NC). The spin angle of the target was predicated to always point into the left sector. The right sector was overloaded with NCs to ensure smaller statistical uncertainties in the measurement of asymmetries in the perpendicular kinematics sector[2].

The BLAST Coordinate system is defined with $+z_{lab}$ as the direction of the incoming electron beam, $+y_{lab}$ points directly upward toward the ceiling and $+x_{lab}$ points into the left sector of the detector finishing a right-handed xyz coordinate system. The origin of the system is located at the center of the internal target. A spherical coordinate system can be set up in the usual way,

$$x_{lab} = r\sin\theta\cos\phi, y_{lab} = r\sin\theta\sin\phi, z_{lab} = r\cos\theta \tag{3.11}$$

3.4.1. Drift Chambers. The Drift Chambers (WC - Wire Chambers) are without a doubt, the most complicated and fragile piece of the BLAST machinery. The WCs were built on site. They are shown in Figure 3.18. A single sector contains one full set of 3 chambers. Each chamber has 2 superlayers, each consisting of 3 layers of sense wires. In total, one sector's WC package contains 18 layers of sense wires. The 6 superlayers have an increasing number of cells as you go further along r from the internal target, the sequence being 18, 19, 26, 27, 34, and finally 35 cells in the superlayer farthest from the internal target. Each cell is a box of 3 wires with the same orientation (5° from vertical), the middle wire shifted by one millimeter from a plane that can be drawn through the near and far wires. The cells of adjacent superlayers have their respective sense wires oriented at opposite stereo angles ($\pm 5°$) with respect to the vertical. The three Sense Wires of each cell are set at 3570V and are surrounded by a box of Field Wires of different voltages, creating a field

[2]explained somewhere in theory chapter, yet to be written

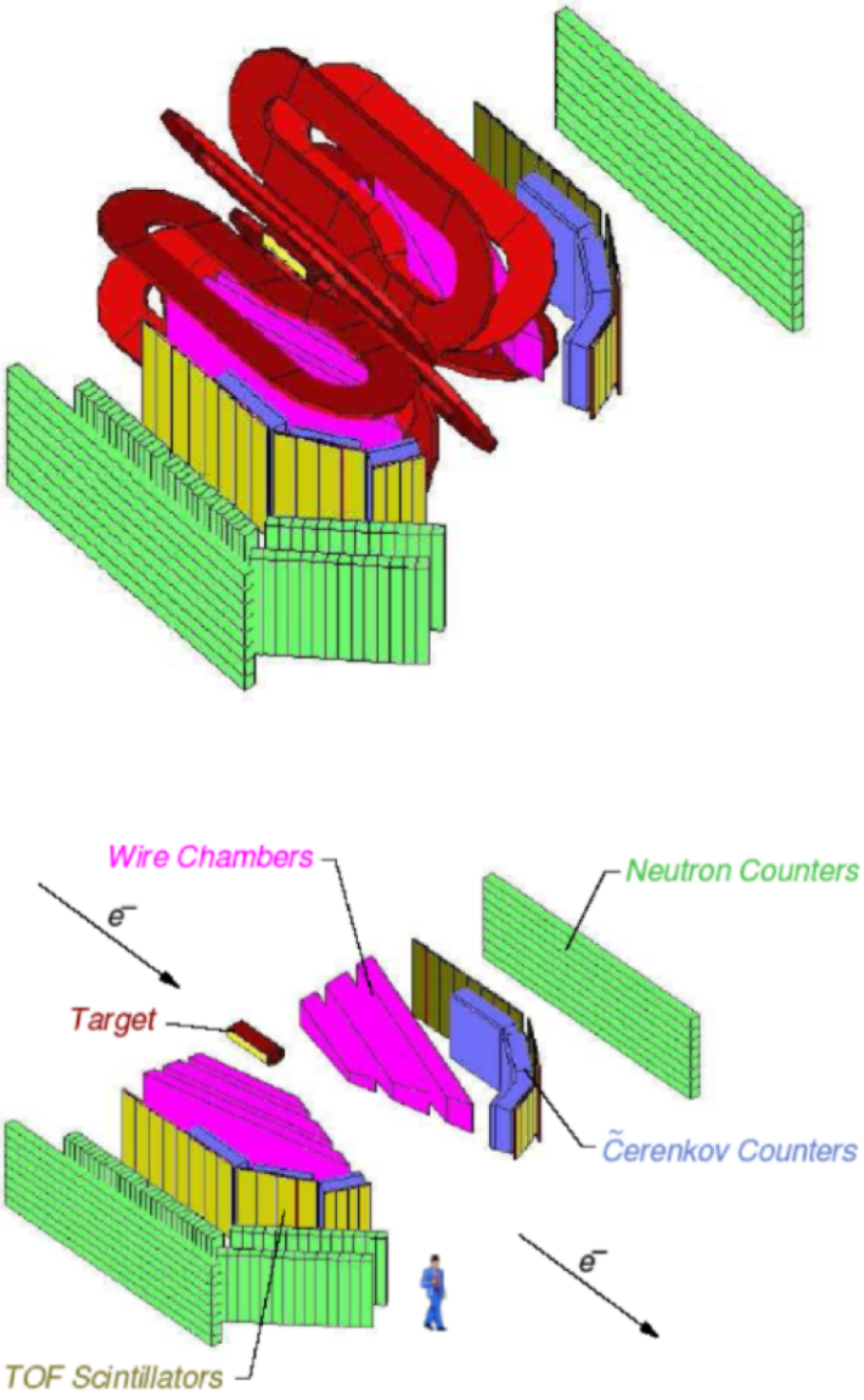

FIG. 3.18. The BLAST Detector is shown with respective subgroups clearly indicated.

gradient within each cell (see Figure 3.19). Each Sense Wire is separated from one another by a Guard Wire set at 2100 V and from the rest of the outer box of Field Wires by two Guard Wires set at 1900V.

The entire WC box is filled with a mixture of helium (82.3%) and isobutane (17.7%). Helium ionizes and isobutane quenches energetic photons resulting from high fields in the immediate vicinity of the sense wires. The Helium gas ionizes when a charged particle passes through the WC and the resulting electrons drift toward the sense wires. When the drift electrons come close enough to the sense wire, the field increases dramatically and the electrons accelerate and ionize the nearby environment providing a snowball effect that registers a hit to the sense wire (this effect can create the energetic photons earlier mentioned, these can cause secondary effects leading to noisy signals and thus the quenching gas isobutane is mixed in with the Helium). The sense wire's signal is amplified by this cascading snowball effect. Each sense wire has a diameter of approximately 10 - 30 μm. This cascade only happens in the region very close ($\sim 75\mu$m) from the wire, and thus the dependence of the time of the readout is dominated by the drift velocity of the electrons from the initial ionization.

The WCs are used to track charged particles that exit the scattering chamber. The locations of the hits within the wire chambers are used to fit a track, a line x, that corresponds to four variables where $x = f(p, \theta, \phi, z)$. p is the initial momentum, θ and ϕ are the polar and azimuthal angles in spherical coordinates (same as in Equation 3.11), and z is the point at which the track intersects the axis of the beamline which is also the z-axis in the BLAST lab coordinate system. The general algorithm for identifying the points in space which the software fits to is demonstrated in Figure 3.21. The procedure is as follows:

1. The charged particle ionizes gas and the electrons drift toward the high voltage sense

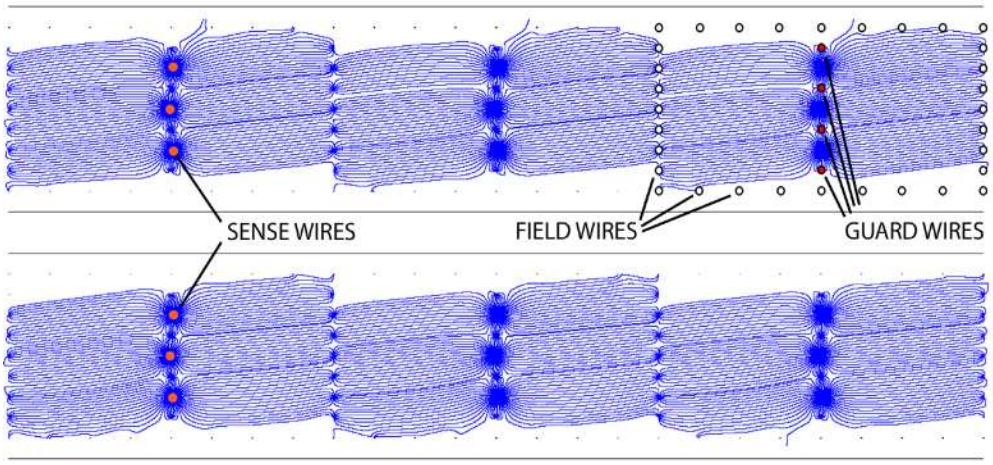

FIG. 3.19. A demonstration of simulated electron drift lines within the cells of adjacent superlayers in the Drift Chambers. There are a total of 6 cells shown, the 3 sense wires lie at the center of each cell and the guard wires completely surround each cell and divide the sense wires from one another.

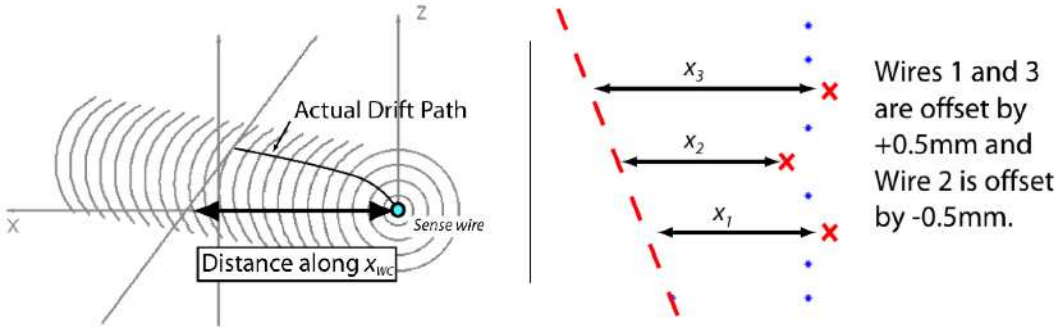

FIG. 3.20. The drift electrons time of arrival is characterized by arcs called isochrones. From GARFIELD simulations it is shown that all electrons from ionization by charged tracks will reach the sense wire no matter what point along the arc the track is tangent to. This overall distance is then converted to a horizontal distance by a simple trigonometric relation with the angle at which it crosses the axis x_{WC}. After all three sense wires have their horizontal distances from their respective wires, the combinatorics are computed and the combination that quantifies as the best fit for a line, e.g. $(x_1 - 0.5) - 2(x_2 + 0.5) + (x_3 - 0.5) \sim 0$, is determined to be the true location of the track. This combination of 3 points is called a *stub*.

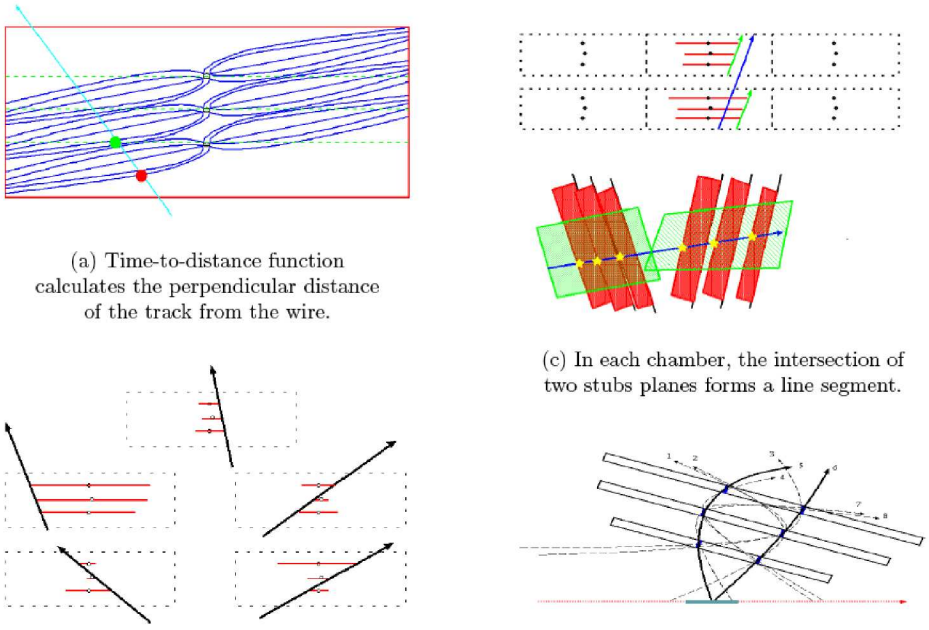

(a) Time-to-distance function calculates the perpendicular distance of the track from the wire.

(b) Stub-finder determines which side of each wire the track passed.

(c) In each chamber, the intersection of two stubs planes forms a line segment.

(d) The line segments are linked to form the most likely tracks.

FIG. 3.21. Drift Chamber hits are converted into charged particle tracks.

wires. The time for this drift is calculated by a function called the time-to-distance relation. GARFIELD, a program for gaseous detectors from CERN, simulates the drifting electrons from points of origin and a sixth order polynomial is fit to results, $t = f(x)$. The simulated paths of the drifting electrons are shown in Figure 3.19. The time it takes for the signal to drift to the sense wire is converted into a distance by taking the inverse of the 6th order polynomial. This distance is converted into a horizontal distance along x_{WC} axis, indicated in Figure 3.20.

2. When three hits are recorded in the three sense wires comprising a single cell, we are left with a combinatorics problem. The wire has no way of sensing from which side the ionization came. For each possibility, the slight shift of the middle wire allows us to quantify a particular combination of three points and its departure from a line.

This is shown in Figure 3.20. The wires are each offset by $d = 0.5$mm from the center line of the cell. The relation,

$$\chi = (x_1 \mp d) - 2(x_2 \pm d) + (x_3 \mp d) = 0 \tag{3.12}$$

would define a perfect line (the addition or subtraction of the offset is dependent on which distance is being used, see (b) of Figure 3.21). Combinations of all possible sides and distances are computed alternating the sign of the center offset where appropriate. The combination in which $\chi \sim 0$ is awarded the true location of the track and the 3 point combination is fit with a line called a *stub*.

3. Since these 3 wires run from the upper face to the lower face of the wire chambers at the same stereo angle, the stub defines a 2D plane. Adjacent superlayers have the wires of their respective cells tilted in opposite directions with respect to the vertical. When adjacent superlayers detect hits within cells and *stubs* are formed, the resultant 2D planes coinciding with the *stubs* are shown to intersect along a line in 3D space. This is illustrated in (c) of Figure 3.21. The resultant line in 3D space is called a *segment*.

4. In each sector, there are 3 groups of 2 adjacent superlayers. This allows for the formation of 3 separate *segments* in 3D space when the charged particle leaves the appropriate number of signals in the WC. These 3 *segments* are now fit to a curve. There is also the possibility that 2 charged particles peruse the chambers in a single event. In such a case, the combination of segments can also be a combinatorics problem as indicated in (d) of Figure 3.21. The fitted tracks in this step are traced back to the axis of the beamline and to the face of a TOF were one to register a hit. This final curve is the function $x = f(p, \theta, \phi, z)$ in 4D space. In this step, the

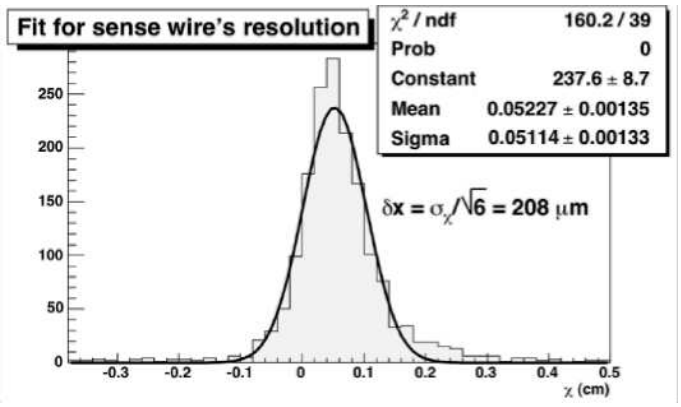

FIG. 3.22. For stubs recorded upstream of all three wires, we can plot the result of Equation 3.12 and fit for the resolution of the sense wires δx.

function is fit to the actual locations individually measured by each sense wire (18 hits in a perfect track, 3 wires per superlayer in 6 superlayers) and allocated into 3D space by the combinatorics of the previous steps. The fitting procedure uses a modified Newton-Raphson method where the 18 points are fit by altering the 4 initial parameters and walking the resultant track through the magnetic field grid taken from survey. The quality of the fit is extracted from a simple χ^2 function, $\chi^2 = \sum_{i=1}^{18} f(p,\theta,\phi,z) - x_i/\delta x$. δx is ~200 microns (see Figure 3.22) and can be shown by fitting the results of Equation 3.12 to a Gaussian for a single *stub-type*[3]. From χ it is easily shown that $\delta x = \sigma_\chi/\sqrt{6}$.

The 4 parameters p, θ, ϕ, which correspond to the initial momentum vector of the charged particle and z the point at which it exited the target have resolutions listed in

[3]The types of stubs can be classified by the side of the sense wire that the final track is determined to pass. Values s_1, s_2, s_3 are assigned to each sense wire. All 3 sense wires are assigned a value of 0 if the track passes upstream of the sense wire. Wire 1, 2, and 3 are assigned values of 1, 2, and 4 respectively if the track passes on the downstream side of the sense wire. By adding these values $stubtype = s_1 + s_2 + s_3$, it can be seen that a total value of zero puts the track on the upstream side of the wires. A value of 1 would give a track passing on the downstream side of wire 1, crossing the middle plane of the cell and passing on the upstream side of wires 2 and 3. From this system it can be shown that *stub-types* 0, 1, 3, and 7 occur the most often with negative particles, *stub-types* 4 and 6 are added to the list for positive particles, and types 2 and 5 should almost never occur, especially because type 5 is physically impossible due to the upstream shift of the middle sense wire.

TABLE 3.4. The resolutions with which the reconstruction software fits the Drift Chamber information from tracked events.

Variable	σ
p	35 MeV
θ	0.5°
ϕ	1°
z	1cm

Table 3.4 (see Section 4.8 for calculations).

Lastly, the Drift Chambers were not only useful to reconstruct the track followed by the charged particles in this experiment. The chambers provided a continuous charged particle *veto*. The Time-of-Flight Scintillator array are $> 99\%$ efficient but do not provide a continuous region of coverage. Each layer of wires within the Drift Chambers has been measured at 98% efficient in detecting ionization from passing charged particles. Using 18 layers of wires, the chance that a charged particle would *not* be detected is on the order of 0.02^{18}, which you can guess is a mighty small probability. This measurement of quasi-elastic electroscattered neutrons from a polarized deuterium target has nearly zero proton contamination due to the continuous region of the Drift Chambers. I would highly recommend the use of even a rudimentary ionization chamber for exclusive neutron detection in all future neutron experiments.

3.4.2. Cerenkov Counters. The Cerenkov Counters (CCs) provide the primary electron/pion particle identification for BLAST. Arizona State University was made responsible for the design and construction and operation of the CCs. The main design considerations are: a uniform, high ($\geq 90\%$) electron detection efficiency; the CCs should be compact and minimize energy loss, and they should operate in a region with high ($\sim$100

G) longitudinal magnetic fields. The final design of the CCs was adopted as an array of counters having silica aerogel as a radiator with indices of refraction n = 1.020 for angles forward of 40° and n = 1.030 for angles backward of 40°. Aerogel provides a very compact detector in the confined space of BLAST. This arrangement is good enough to discriminate pions up to at least 700 MeV/c. Each counter is equipped with a large single diffusion box to collect light into properly arranged photomultiplier tubes.

A complete conceptual design of a CC is shown in Figure 3.23. The front and rear covers of the boxes themselves are constructed of an extremely light-weight honeycomb material sandwiched between 1 mm thick Aluminum panels as the outer casing. The side panels were constructed of singular 8-inch aluminum plates. The interior of the boxes is covered with a diffusely reflective coating, Spectraflect designed by LabSphere, Inc. Spectraflect is tested to have 96%-98% reflectivity at 600nm wavelengths. Two identical sets of four counters were constructed, one for each sector of BLAST. Each set consists of a counter at forward angles viewed by six Photomultiplier Tubes (PMTs) and subtending 20°-35°, a counter viewed by eight PMTs and subtending 35°-50°, and two counters each viewed by 12 PMTs and subtending 50°-80°. In the final configuration, the rearmost CC was pulled from the region of the 65°-80° Time-of-Flight Scintillators and placed in front of a subset of the Back Angle Time-of-Flight Scintillators (BATS) for electron-pion discrimination at angles $\geq 95°$. All boxes cover the entire azimuthal acceptance of the respective BLAST sector and their dimensions vary slightly due to the magnetic coil shape. The dimensions of the largest boxes were 100 cm wide, 150 cm height, and 19 cm deep. Each counter is fed with a laser pulse for timing and gain monitoring.

The conceptual design of a BLAST CC is shown in Figure 3.23. The aerogel was purchased from Matsushita Electric Works Ltd. The optical quality of aerogel has signif-

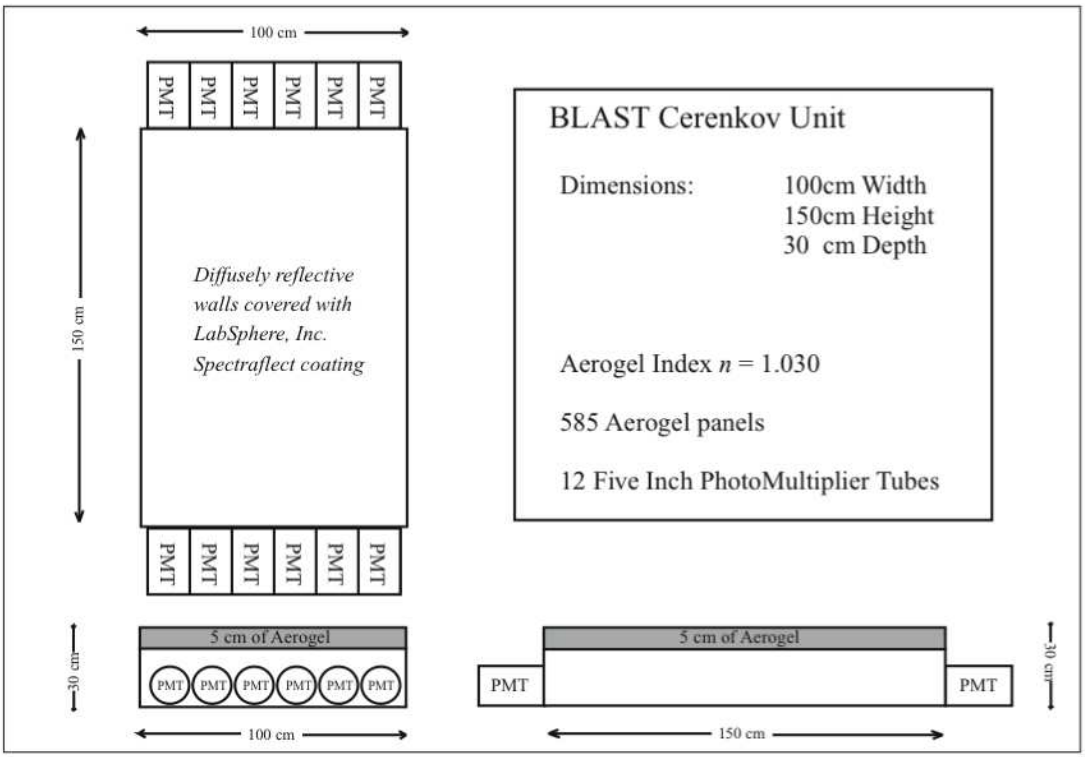

FIG. 3.23. Conceptual design specifications for a Cerenkov Counter used at BLAST.

icantly improved in recent years. The aerogel comes in tiles of approximately 11 cm by 11 cm with an average thickness of 1 cm. The tiles are extremely fragile and great care is taken to avoid chipping the edges. The largest counter boxes contain approximately 580 tiles. The tiles were mounted on top of each other and separated into rows by a stretched, thin mylar foil. Each row was also covered by a similar mylar strip to hold the aerogel in place when the counter is configured in its vertical position. To properly fit a row of aerogel it was occasionally necessary to cut the ending tiles. A common razor was sufficient for the task. The initial estimation of the thickness of aerogel necessary to extract an optimal Cerenkov light yield was gauged at 15 cm. The back-angle CCs, instead, support 5 cm of aerogel and the forward-angle CCs support 7 cm necessitated by the slightly lower index of refraction.

The PMTs used in the CCs are 5-inch diameter fast tubes (type XP4500B, Photonis). One challenge to our design is the presence of a longitudinal magnetic field within the region of our photomultiplier tubes (PMTs). As expected, preliminary measurements had resulted in a field of 100 gauss at the proposed location of the PMTs of the CCs when the BLAST Toroid was on. At 10 gauss the overall efficiency of one photomultiplier tube can be reduced to effectively zero. An initial solution was implemented to install two concentric cylinders of low-carbon steel with an air gap encasing our PMTs as shown in Figure 3.24. Modeling this new arrangement with TOSCA, the magnetic field in the region of the PMTs proved to be reduced to a few gauss. Low carbon steel was chosen as a shield because μ-metal shielding saturates at flux densities of more than a few milliteslas. The shielding needs to extend beyond the PMT window for at least one diameter. The configuration shown in Figure 3.24 was modeled using the computer code OPERA-3d and it was found that the configuration of a 10mm thick inner tube with a 75mm radius, surrounded by a 6mm thick outer tube

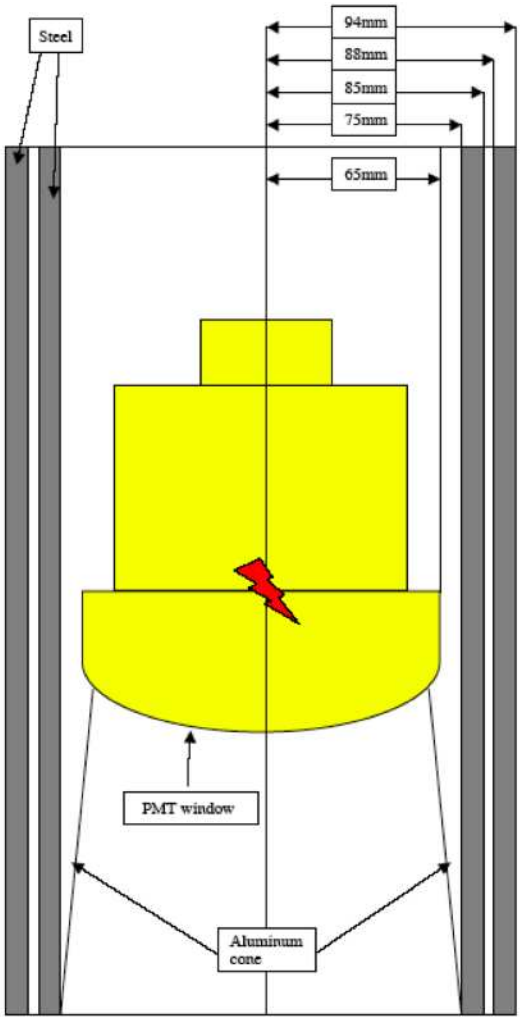

FIG. 3.24. A schematic of the concentric cylinders used for shielding the Cerenkov Counters' Photomultiplier Tubes. An aluminum cone was also added to minimize the loss of photons.

with an 88mm radius was the best configuration in order to cancel the longitudinal BLAST fields. Actual dimensions of the shielding tubes were slightly different to accommodate to commercially available tubes.

A single counter with the dimensions of the largest boxes that would be installed at BLAST was first constructed as a prototype. This unit was tested with cosmic rays and with the electron beam in conjunction with other BLAST detector elements. During the tests the prototype counter performed as expected although it was not possible to test it with the full BLAST magnetic field. The construction of the entire array proceeded with no significant changes from the prototype.

Initially the above design was modeled using the simulation technique used by Higinbotham[115]. The corresponding computer code predicts the photoelectron signal, the uniformity of the signal, the average number of PMTs which trigger per event, and the timing resolution of the detector. Again, the larger Cerenkov box was modeled as the prototype and it was found that the CC should produce an average signal of nearly 4.5 photoelectrons in the absence of an external magnetic field[115, 116].

The information from the simulation, namely the photoelectron signal and the average number of PMTs which trigger per event, were used to perform a Monte Carlo simulation of the ADC spectrum for a particular CC. A Poisson event generator[117] was used to simulate the number of photoelectrons that pass from the outer photocathode to the successive dynodes, positively charged secondary-emission electrodes. The electrons are multiplied throughout the dynode stages in a linearly focusing PMT. The Poisson distributed signal takes into account how fluctuations around the mean diminish from the first dynode to the

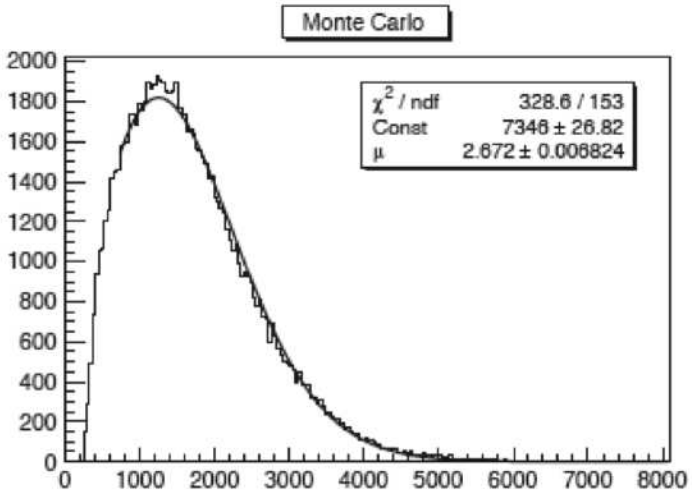

FIG. 3.25. The expected ADC signal from a Cerenkov Counter with four PMTs producing a single photoelectron. This is a Monte Carlo simulation using a Poisson generating function.

next. This can be expressed by the equation,

$$\sigma_i = \left(PE \cdot \prod_{j=1}^{m} g_j \right)^{\frac{1}{2}}, m = i - 1. \tag{3.13}$$

where σ_i is the fluctuation in the distribution of the number of electrons at the ith stage, PE is the mean of the photoelectron distribution and g_j's are the gains of the stages which precede the ith stage. The ADC spectrum for a particular CC was obtained by doing an event by event sum of the individual PMT ADCs that trigger an event. A pedestal-subtracted ADC spectrum produced by the Monte Carlo for a multiplicity of 4 is shown in Figure 3.25.

The ADC spectrum of the Monte Carlo simulated ADC is scaled to a Poisson function that gives an approximate number of photoelectrons μ[114].

$$y = (\text{Const.}) \times \frac{\mu^x \exp -\mu}{\Gamma[x+1]}, \quad \text{where} \quad \Gamma(x) = \int_0^\infty t^{x-1} \exp -t dt \tag{3.14}$$

y is the number of counts per channel, x is the ADC channel. The fit to the Monte Carlo in Figure 3.25 with a fitted value of 2.7 for μ is reasonably accurate for the input multiplicity

and allows a relative expectancy for the CCs within the BLAST detector and a variable by which we can gauge the performance of the CCs within the BLAST package.

The performance of the CCs have been obtained during the on-going measurements with the BLAST detector. By using elastic scattering from hydrogen we have determined the respective efficiencies of the CCs. The elastic events were selected based on cuts from the reconstructed kinematic variables including coplanarity and timing cuts from the Time-of-Flight scintillators (TOFs) that are nestled directly behind the CCs. There are approximately four TOFs behind each CC. The CCs are numbered 0, 1, and 2 over increasing polar angles from the target. Behind CC0 are TOFs 0, 1, 2, and 3. Behind CC1 are TOFs 4-7, and behind CC2 are TOFs 8-11. The two central TOFs that are completely shadowed by the CCs because they are centered behind the CCs are used for the efficiency measurements. The TOFs are discussed in the following Section 3.4.3.

Since commissioning, the efficiency of the detectors has been routinely monitored in order to optimize the voltages of the PMTs and to scrutinize the performance of the detectors relative to the magnetic field of the BLAST Toroid. From the measured ADC signal and the Monte Carlo simulation, a general idea of the strength of our signal was evident. While in commissioning we had noticed a strong difference between the widths of our ADC signals when running the experiment with and without the BLAST toroid operating. Despite the concentric cylinders of iron shielding around each PMT, residual fields of 3-5 Gauss were found when the entire array of CCs was operated with the full magnetic field of BLAST. This resulted in a significant loss of efficiency for most counters. Taking notice that the magnetic field had been affecting our PMT tubes and the overall efficiency of the CC signal, a layer of 0.5-inch low carbon steel was used to shield the PMTs of the CCs forward of the polar angle 40° and two layers to shield the PMTs of the CCs

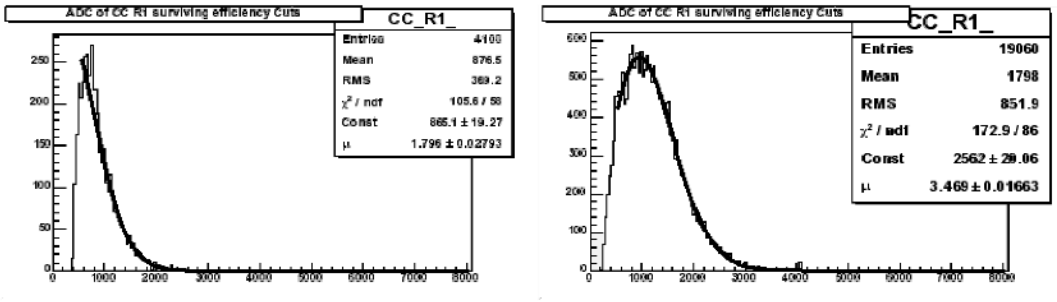

FIG. 3.26. This Cerenkov Counter's analog-to-digital (ADC) signal is plotted before and after two layers of low carbon steel magnetic shielding were attached to the front and back of the frame that held the PMTs in place. The fit is done with Equation 3.14 Counter used at BLAST. The number of photoelectrons μ can be seen to have doubled when further shielding was added.

backward of the polar angle 40°. These layers of steel shielding are *in addition to* the cylindrical containers previously mentioned and shown in Figure 3.24.

Referring to Equation 3.14, a higher photoelectron yield μ means a stronger signal, a greater width of our ADC spectrum, and a greater overall efficiency of the CC. In Figure 3.26, we have two separate plots of one CC's ADC distribution before the installation of additional shielding and after. Our current efficiencies of the respective Cerenkov detectors are listed below in Table 3.5.

We have analyzed data for three Cerenkov counters per BLAST sector. All quoted efficiencies are after all magnetic shielding had been installed. The last Cerenkov box in each sector was moved to backward angles, outside the acceptance of the drift chambers and TOFs, to allow for a measurement of backscattered electrons from elastic electron-deuteron scattering. There are four additional scintillator bars in each sector that are shadowed by those back angle CCs. Total efficiency results for the three CCs covering the scintillators within the drift chamber acceptance in both left and right sectors of BLAST are shown in Table 3.5. Edge effects are neglected by only requiring the center two scintillators shadowed

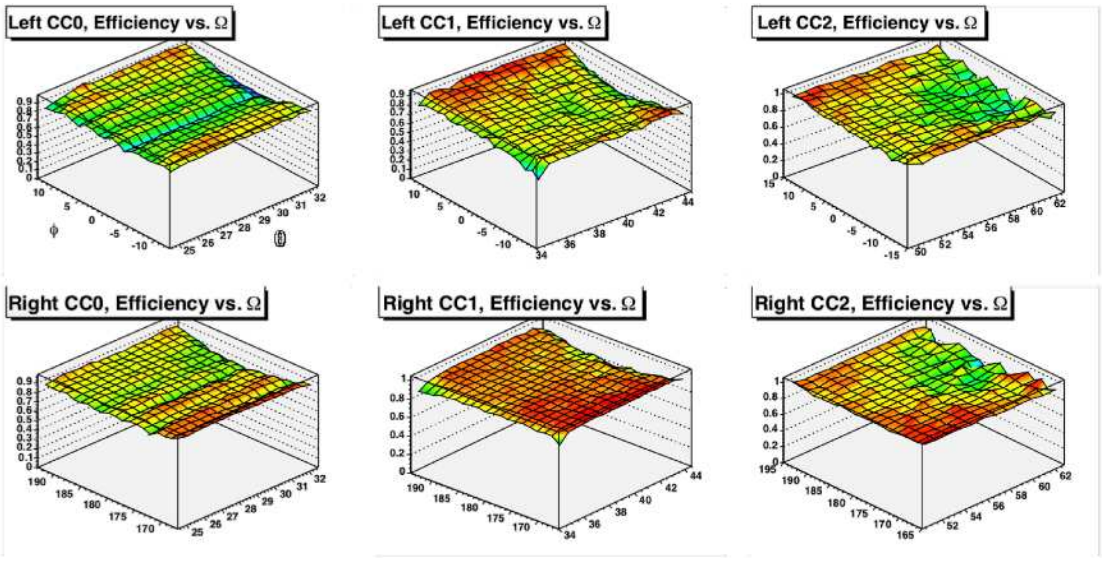

FIG. 3.27. The efficiency of each Cerenkov Counter over the BLAST Ω acceptance. The axes are (assuming right-handed with z-axis pointing vertical) x:ϕ, y:θ, and z:efficiency. No holes in efficiency of each Cerenkov Counter are present over the ∼400 bins shown in each plot.

by each CC. Since each scintillator is equipped with a PMT at each end, the efficiency has also been studied as a function of position along each scintillator as well as the polar angle along the BLAST acceptance. The respective pion/electron discrimination efficiencies over the solid angle covered by the two central scintillators shadowed by each CC are shown in Figure 3.27.

The ADC distributions of each Cerenkov counter have been fitted with the Poisson function discussed in the previous section. A typical result for one of the large Cerenkov boxes after shielding is shown on the right in Figure 3.26. The measured ADC is very similar to that of Figure 3.25 indicating a very good agreement between simulation and experimental measurement. The mean of the fitting function yields $\mu = 3.4$ detected photoelectrons per event in a Cerenkov counter which translates into a detection efficiency of 95%, well in agreement with the Monte Carlo results.

TABLE 3.5. Respective efficiencies of the 6 CCs used in production running at BLAST. 1.42 M electron-proton elastic events were used. "*" is indicated to note that the entire array of 11 Time-Of-Flight Scintillators that are mostly shadowed behind the Cerenkov Counters were used for "TOTAL" efficiencies

Left Sector CC	***Efficiency %***	***Right Sector CC***	***Efficiency %***
Forward Angle	0.886 ± 0.006	Forward Angle	0.883 ± 0.006
Middle	0.854 ± 0.009	Middle	0.944 ± 0.014
Back Angle	0.911 ± 0.024	Back Angle	0.935 ± 0.028
LEFT TOTAL*	0.878 ± 0.003	**RIGHT TOTAL***	0.894 ± 0.003

The promise of triggering on a Cerenkov signal is evident in the two plots in Figure 3.28. A colleague studying the quasi-elastic electroscattering on Deuterium has noted that cutting his data on a CC signal acts like a "magic bullet" against his background.

3.4.3. Time-Of-Flight Scintillators. The long, thin detectors in Figure 3.18 are the Time-of-Flight Scintillators (TOFs). The TOFs were constructed and tested on site by the collaborators from the University of New Hampshire. The TOFs are made from *Bicron BC-408* organic plastic scintillating material Polyvinyltoluene. This material was chosen for its fast response time ($\approx$ 0.9 ns) and long attenuation length ($\approx$ 210 cm), as plastic it is also structurally sound. Each sector contains an array of 16 TOFs. The farthest forward four bars are 119.38 cm high, 15.24 cm wide, and 2.54 cm thick. The remaining 12 bars are 180.0 cm high, 26.2 cm wide, and 2.54 cm thick. There are also four Back Angle Time-of-Flight Scintillators (BATS) just outside of the region of drift chamber coverage, 90°-120°. Each is surrounded by a 2 mm thick lead foil which attenuates X-rays from the target and prevents back-scattered radiation that could potentially misidentify electrons by firing the Cerenkov detector in front of the TOF. The foil is absent from the four most back angle TOFs to improve sensitivity to low energy elastically scattered deuterons.

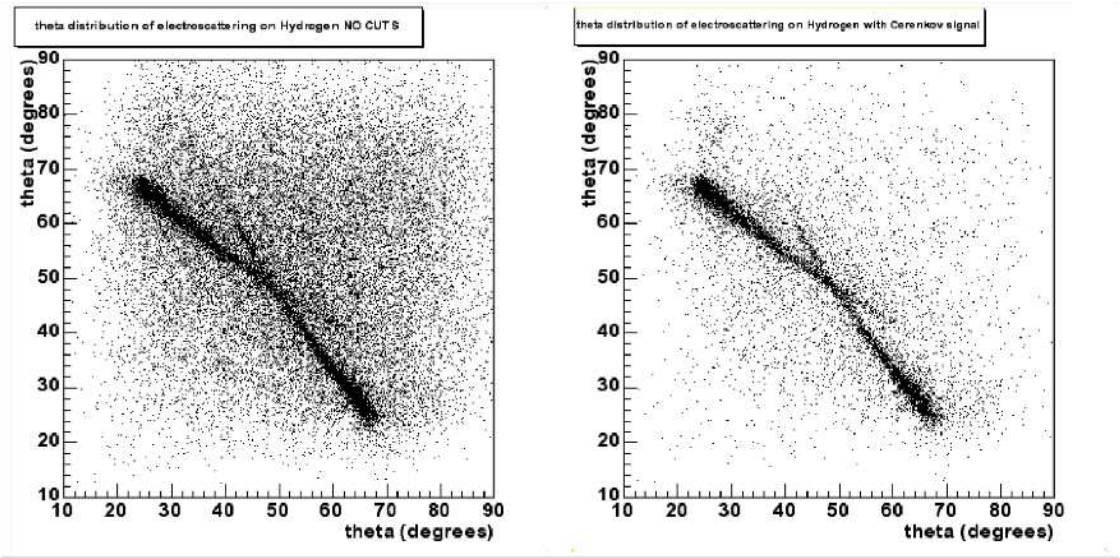

FIG. 3.28. The x and y axes are the polar angles of the outgoing particles entering the right and left sectors, respectively, of the BLAST detector. Tracking reconstructs the polar angle of particles exiting from electron scattering on a Hydrogen target. On the left, we notice the elastic scattering polar angle distribution deeply embedded in an overall background of, as yet, unidentifiable events. On the right we require that our Cerenkov counter registers a signal, i.e. we require an electron to be detected, and as a result, our noise significantly decreases such that our elastic electron-proton scattering distribution lies clearly in the foreground.

The readout for the TOFs is done at both ends of the scintillating bar. Lucite light guides couple the TOF to three inch diameter Electron Tubes photomultiplier tubes (model 99822B02) which use the Lucite guides to position the PMTs at a further distance from the BLAST field and to ensure that any nearby fringe fields are roughly perpendicular to the PMTs. The PMTs are also surrounded by a wrapping of highly permeable mu-metal magnetic shielding to further minimize effects of the BLAST field. The base electronics unit for each PMT is an Electron Tubes model Model EBA-01 which is an actively stabilized voltage divider which supplies the high-voltage for the PMT's operation and the readout for the data acquisition system (DAQ).

A single sector's PMTs' signals are fed to two LeCroy Model 3420 constant-fraction discriminators (CFD), one for the 16 PMTs along the top of the TOF array and one for the 16 PMTs along the bottom. The CFD provides timing that is independent of gain and pulse signal rise time. This standard is extremely important because the TOFs act as the trigger for the DAQ. The logic signals from each CFD are passed along a series of logic gates where top and bottom PMT signals are ANDed together. This coincidence requirement of a top AND bottom PMT of a single scintillator creates a much cleaner event stream and eliminates many counterfeit signals.

The effect of a pair of PMTs covering the ends of each individual TOF provide rough position mapping along the length of the TOF by recording the time difference, but the timing signal that is measured independent of the location along the TOF comes from a meantimer that is fed by the output of the coincidence logic. This allows for equalization of signal timing between different PMTs of a single scintillator. The meantime gives the event timing signal that is fed to the memory lookup units (MLU) and initiates the trigger for the DAQ (To be later described in Section 3.5). The resolution of the timing from the TOFs

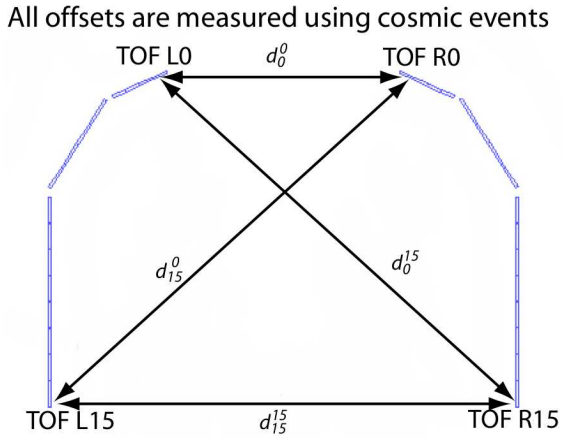

FIG. 3.29. The Calibration of the offsets of the Time-Of-Flight Scintillators can be described using a simple demonstration of four TOFs. Cosmic rays travel at roughly the speed of light. All four distances shown on this illustration $d_0^0, d_{15}^0, d_0^{15}$, and d_{15}^{15}, are known and the time it takes a particle moving at c to traverse these respective distances is easily calculated $\Delta t_j^i = c/d_j^i$. The readout of each of the 32 TOFs in the BLAST array gives a TDC signal corresponding to the time of a single event. Four TOFs will be used in this example, L0, L15, R0 and R15. Each of these has a characteristic offset that separates them from a reference time (a timed flasher signal or even the signal of a TOF can be taken as a fiducial reference). The time difference between signals when a cosmic ray passes through any of these pairs can be written: $(t_i + \text{offset}_i) - (t_j + \text{offset}_j) = c/d_j^i + (\text{offset}_i - \text{offset}_j)$. These four combinations of paddles will obviously give four equations of this form and there are exactly four unknowns corresponding to the unknown offsets. Notice that we can include the combinations of L0 and L15 and R0 and R15 which gives us two more equations with no added unknowns. For 32 TOFs the situation is over determined since, under ideal conditions, 32 TOFs have 32 unknown offsets yet can be combined to make $\frac{32(32-1)}{2} = 496$ combinations or equations.

has been determined by the method of Giles[118] to be 350 ps FWHM (BLAST design specs called for 500ps).

Although timing is the primary purpose of the TOFs, the energy deposited within a scintillator, above a certain minimum, is directly proportional to the number of photons emitted. In this sense they can separate minimum ionizing particles such as electrons from slow moving deuterons which deposit significant amounts of energy upon entering the scintillating plastic.

3.4.4. Neutron Counters. The Neutron Counters (NCs) are on the outer edges, beyond all other detectors. They are the outermost detectors from the internal target in Figure 3.18 and delineated more clearly in Figure 3.30. Asymmetrically configuring the NC array was motivated by the dependence of the asymmetries from quasi-elastic electron scattering from deuterium on the interference of the electric and magnetic form factors of the neutron (see Section 2.4.1). All the NCs on both sides are located behind the Time-Of-Flight Scintillators.

In both sectors of BLAST is a similar array of eight horizontal bars of scintillators called the OHIO Walls. The two sets of eight bars were built by Jacobo Rapaport from Ohio University. The final dimensions of these counters were fixed at 400 cm long by 22.9 cm high by 10 cm deep. The polar angle coverage of the parallel kinematics sector was set from approximately 40°-80° during the production data runs from 2004 and was shifted forward from 30°-75° during 2005 production data.

In the perpendicular kinematics sector, there are five arrays of NCs. One is the Ohio Wall mentioned and described in the previous sector. Two arrays of 14 wedge-shaped Large Angle Detection Scintillators (LADS) run vertically and are situated in between the Ohio Wall and the TOFs. These LADS form a solid wall by alternating the direction of the wedge and they are three meters in length and 20 cm thick (LADS20). Another two arrays of 14 LADS are in the more forward angle direction and are placed one in front of the other. These are wedge-shaped, 3 meters long and 15 cm thick (LADS15). Though there are small acceptance holes, approximately 30 cm of scintillating material are used throughout the perpendicular kinematics sector for neutron detection.

Since neutrons are neutral particles, there is no information that can be derived from the detection of a neutron other than the exact timing of a specific signal within

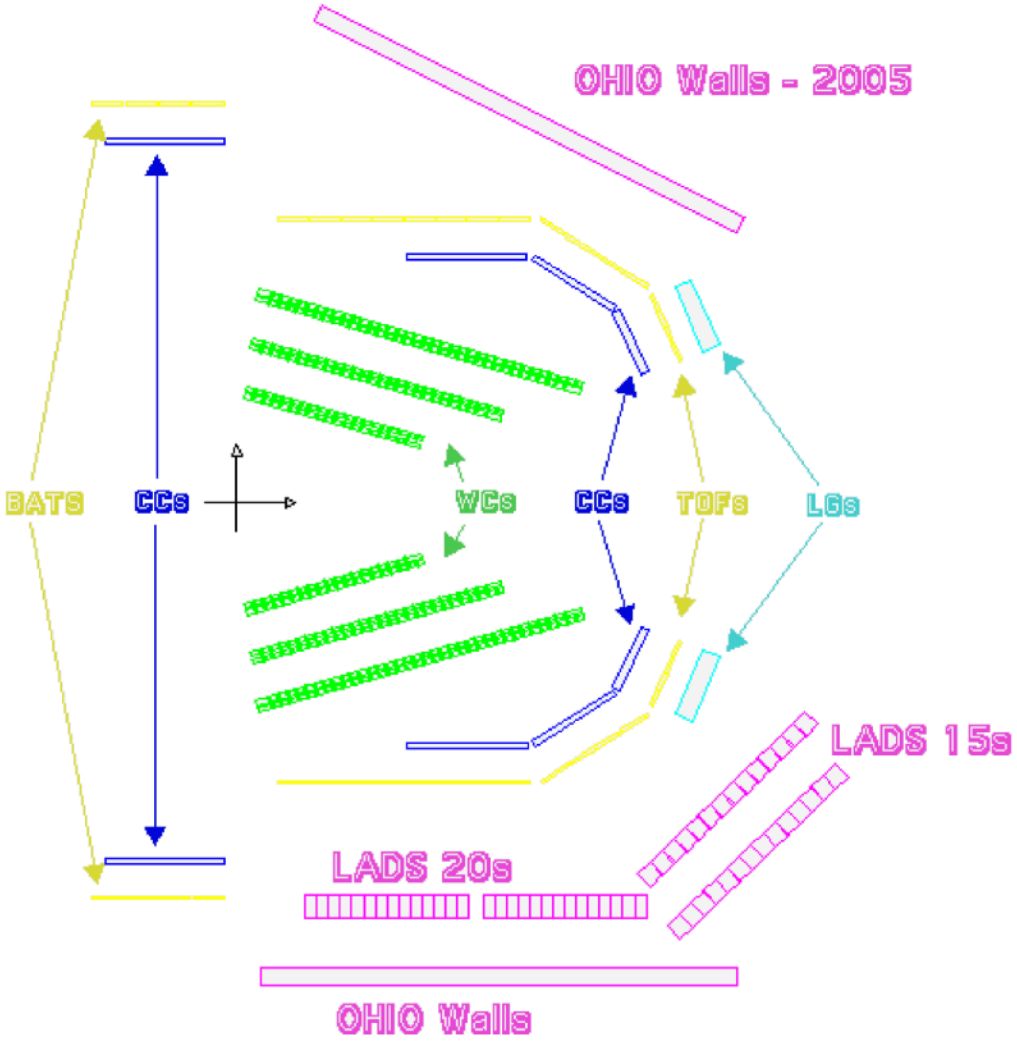

FIG. 3.30. A bird's eye view of a cross section of the detectors at the height of the target. The overloaded Neutron Detectors in the perpendicular kinematics sector are clearly visible.

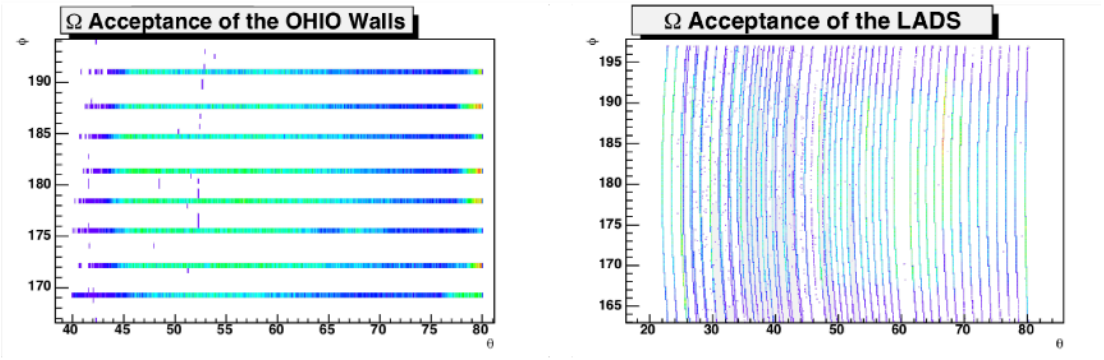

FIG. 3.31. Ω acceptance of the LADS and OHIO Wall Neutron Counters in the perpendicular kinematics sector.

one or more of the NCs. Thus, the timing of the NCs can be qualified as the only signal appropriate to the neutron's kinematics since the magnetic field does not bend a neutral particle's trajectory and the velocity can be derived directly from the Time Of Flight which is attained from the PMTs' timing. Since the Ohio Walls run horizontally, the azimuthal angle at which the neutron is detected corresponds directly to the detector that measures a signal and thus makes up a discrete system of eight phi angles corresponding to each of the eight bars in the Ohio Walls. Figure 3.31 shows the solid angle acceptance of the right sector Ohio Walls, discrete in the azimuth and continuous along the polar angle. The LADS run vertically. Since there are 28 bars directly in front of the Ohio Walls and 28 bars at forward angles, the bars must obviously correspond to 54 distinct polar angles and run a continuous acceptance along the azimuth. Figure 3.31 also shows the solid angle acceptance of the LADS.

It is very simple to characterize the main quantities necessary for the calibration of NC timing. One of these quantities is the overall mean time of particle detection as the sum of the TDCs from a single scintillator bar's respective PMTs located at opposite ends:

$$t = \frac{TDC_1 + TDC_2}{2r} \tag{3.15}$$

where r = (TDC channels)/ns conversion. The other quantity is the relative longitudinal position along a bar which is characterized by the equation:

$$x = \frac{TDC_1 - TDC_2 - \Delta}{2\eta(\frac{n}{c} + \xi)} \tag{3.16}$$

where Δ is the position offset, $n = 1.58$ is the index of refraction within the bar, $c = 30$cm/ns is the speed of light, and ξ is the rise time position dependence. These equations do not concern themselves with the offsets intrinsic to the detector's electronics and the relative performance of each PMT and electronics base. Thus, two variables need be inserted into these two equations, namely the offsets for TDC_1 and TDC_2 which will be called TDC_1^0 and TDC_2^0 and added to their respective PMT's timing signal. These non-negligible hard offsets are calculated in exactly the same way as described in Figure 3.29, using cosmic rays relative to combinations of NCs with TOFs. On top of these static offsets, a number of additional measures were employed to overcome further difficulties that became apparent through commissioning the respective detectors as well as monitoring their performance over the course of the production data.

The NCs record their timing and deposited energy measurements from leading edge discriminators (LEDs) and not constant fraction discriminators (CFDs) as is the case with the Time-Of-Flight Scintillators. CFDs are not subject to mistiming as the front edge of the PMT signal becomes weaker and rises less sharply, they are designed to produce accurate timing information from analog signals of varying heights but the same rise time. The LED is the simpler of the two types of discriminators. Given an input pulse, the LED produces an output pulse at the time when the input pulse crosses a given threshold voltage sometimes called a "pedestal". This, however, causes a problem in situations where the timing is important. If the amplitude of the incoming pulse is changed, but the rise time remains the same, a sort of "time walk" or "walk effect" occurs (Figure 3.32); an input pulse with

smaller amplitude but with the same rise time as a larger pulse will cross the threshold at a later time. Thus, the timing of the output pulse is shifted by this change in amplitude. In addition to the timing offset that arises from the *walk effect*, the overall efficiency for detecting low energy neutrons is very sensitive to the pedestals assigned to each PMT. This, in turn, creates a competing effect. We would like to minimize the *walk effect* by increasing the gain on our PMTs and requiring a higher pedestal, yet raising the pedestal will lower our neutron detection efficiency and relegate a large number of slower neutrons into the background, thus decreasing the statistics of this already statistics-dominated measurement of the neutron's form factor. We must correct for the *walk effect*.

To correct the *walk effect* and to simultaneously extract the exact pedestals of each PMT, a fit was exacted to the *mean time TDC vs. ADC* distribution of each bar of each NC array. The data for the fit was provided by using a series of flasher signals and attenuating the power over the course of the measurement. Plots of the data from one 14 bar array in the LADS is shown in Figure 3.32. The fit for the *walk effect* uses three parameters, one of which is the pedestal. The equation includes terms such as the hard offset TDC_0^i of the ith PMT (calculated using Cosmic events) and, if calibrating from actual neutron data, the actual difference in the Time Of Flight of neutrons and electrons $r(t_n - t_e)$ where $r=$ (number of TDC channels)/ns:

$$TDC^i = TDC_0^i + \frac{p_1^i}{\sqrt{ADC^i - ADC_{ped}^i - p_2^i}} + r(t_n - t_e) \tag{3.17}$$

where the data gives TDC^i and ADC^i and we fit for the pedestal ADC_{ped}^i, and the parameters that fine-tune the rise p_1^i and vertical asymptote p_2^i of the ith PMT. This fit is done for all Neutron Counter PMTs and used to accurately calculate the Time Of Flight of the neutron t_n. t_n is the Time of Flight, the time difference from Equation 3.16 (now including parameterized *walk* corrections for the respective TDCs in the equation), and the actual

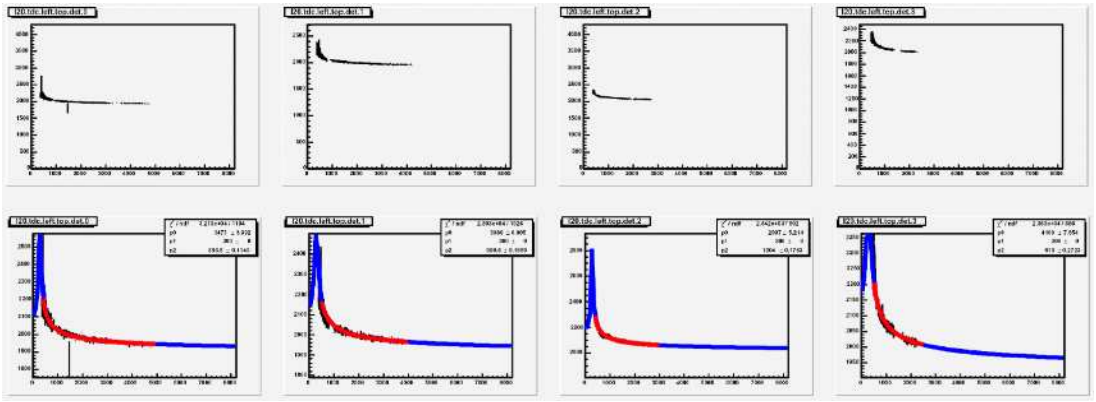

FIG. 3.32. The flasher signal is attenuated over several runs in order to demonstrate the *walk effect* within the Neutron Counters' photomultiplier tubes. The top four plots show the raw data while the bottom four plots show a fit to the same four plots but zoomed in to demonstrate the *walk effect* in greater detail. The fit utilized is demonstrated in Equation 3.17.

detector which records a hit provide all the information for the neutron's kinematics, i.e. time of flight, distance traveled, and trajectory.

Once these corrections were accounted for, production running began and flasher signals continued to monitor the TDC time offsets and the ADC pedestals. It became apparent during production running, that these hard offsets were not constant. Due to unknown effects, there have been up to 5 nanosecond jumps in the TDC offsets and jumps of more than 500 channels in the ADCs which would relegate our previous *walk effect* fits as useless (see Figure 3.33). These *jumps* were measured and tabulated run by run. The subtraction of all random walking of the timing offsets have been subtracted and implemented into the final dataset used in this analysis.

To qualify the final results of the neutron timing calibration, reconstructed kinematics from data was analyzed and used to calculate expected time of flight measurements, t_n^{calc}, and to compare them to the actual readings from neutron detectors, t_n. At this point there were still discrepancies though they were smaller than the resolution of the timing of

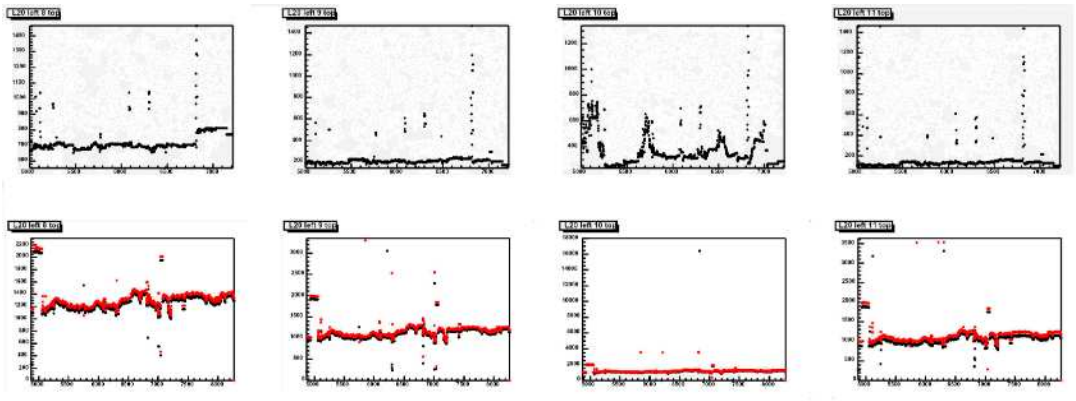

FIG. 3.33. During production running, flasher signals were used to monitor the performance of single photomultiplier tubes. The top four plots show the ADC pedestals vs. run number of the top PMTs of four adjacent pads within a LADS array of Neutron Counters. It is obvious that there are extreme jumps of up to 500 channels and some sequences of runs that seem to display complete randomness over nearly 1000 channels. The bottom four plots demonstrate the monitoring of time offsets. At 50 picoseconds/channel, a change in the timing offset of 100 channels corresponds to 5 ns. A relativistic neutron with an extra five nanoseconds of flight time over the five meters between a neutron counter and the target would give a neutron with true momentum of 400 MeV/c a final momentum of 375 MeV/c. Considering that there are variations in the offsets of almost 20 nanoseconds, failure to maintain a database of these fluctuations could take nearly 200 MeV from our fastest recoil neutrons and heavily contaminate the data.

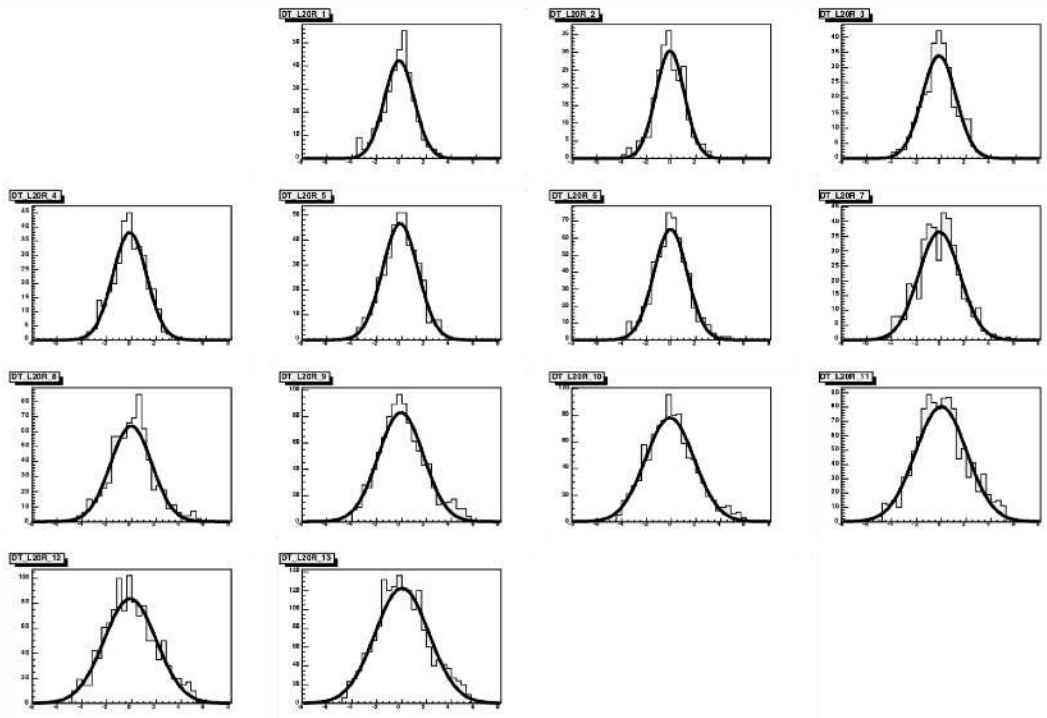

FIG. 3.34. The plots here demonstrate the difference between the calculated neutron time of flight, $t_n^{calc}(p_e, \theta_e, \phi_e, \theta_n, \phi_n, M_m = M_p)$ and the corrected time of flight, i.e. $t_n^{calc} - t_n$. All distributions shown here are for the individual bars within one of the two 20 cm LADS arrays. The mean of the Gaussian fits shown are within two tenths of a nanosecond from zero.

the Neutron Counters. The corrections were calculated as hard offsets per Neutron Bar. Two iterations of these offsets had to be calculated in order to reduce the systematic errors in the time of flight of the neutron in order to make the measured time of flight match the expected time of flight. Figure 3.34 shows the final distribution of $t_n^{calc} - t_n$ of one set of the LADS20s. Gaussians are fit to each distribution demonstrating the success of the calibration of the neutron timing.

3.5. BLAST Trigger and the Data Acquisition System

The BLAST trigger is constructed from an emitter coupled logic (ECL) discriminator and several layers of logic modules constructed by LeCroy. The modules reside in two Computer Automated Measurement And Control (CAMAC) crates, both of which are controlled by one Creative Electronic Systems (CES) CBD-8210 Versa Module Europa (VME) card. One crate is dedicated to each sector of BLAST's detector system electronics, with two-sector correlations being computed in the right sector's crate. Within each crate, the logic modules are arranged by detector type (TOF, NC, CC, WC) in groups of two to five modules.

For a simplification of the description of the trigger processing, it can be divided into three basic parts. The first part of the trigger converts the analog signals of the detectors into digital logic signals that indicate specific information about which detector fired. The second part takes these detector signals, combines them into specific arrays of detector type, and passes them to software controllable Memory Lookup Units (MLUs). The MLUs process correlations between different detector elements within their respective sectors. The third and final logic computation takes the signals from the two sector MLUs and sends gate and start signals to the digitization electronics. It also writes a trigger type tag (see Table 3.6) to each event as an indicator of the specific combination of detectors that recorded hits. This allows for much quicker processing in later analysis.

The Time-Of-Flight scintillators are used to commence the trigger signal. As obvious from Table 3.6, the TOFs are included in all trigger types including the Flasher Monitor which fires all the detectors simultaneously for offset and pedestal monitoring. Two Constant Fraction Discriminators are used for the PMTs on the top and bottom of the TOFs,

TABLE 3.6. Trigger Types and their description. TOF is a Time-Of-Flight scintillator, NC is a Neutron Counter, CC is a Cerenkov Counter, BATS is a Back Angle Time-of-flight Scintillator. See Figure 3.18 or Figure 3.30.

Trigger	*Prescale*	*Description*
1	1	TOF coincidence (Charged Coincidence - ep, e'p, e'π^+, ...)
2	1	TOF & NC coincidence (Charge-Neutral Coincidence - e'n, e'π^o, ...
3	10	At Least two TOFs in One Sector with CC
4	100	At Least two TOFs in One Sector
5	1	TOF and BATS coincidence
6	1000	Single Back Angle TOF (TOF12-15)
7	3	Single TOF with CC
8	1	Flasher Monitor

respectively. From each of these CFDs, a set of outputs goes to TDCs and scalers for visualization. Another set of outputs is sent to a logic module that ANDs together the signals from the top and bottom PMTs of a single TOF in order to eliminate any sporadic misfiring. From this coincidence logic, the output is sent for time equalization and the output of this mean time is numbered with the respective TOF that fired and sent to the Sector Logic.

An analogous process is used for the Neutron Counters except that the Neutron Counters do not have the privilege of CFDs. The NCs are also not the *initiator* of the event signal and are thus relegated to the sector logic to await the proper allocated window for a TOF signal in order to be recorded as a proper event.

The Cerenkov Counters are allocated a similar role to the NCs in respect to the fact that they do not initiate a trigger type. The only other major difference is that the signals from the six or eight PMTs that detect Cerenkov radiated photons are added since it is very possible that only a single photon enters the photocathode of a PMT.

The sector MLUs which receive the pulses from a single sector's detectors send a total of six output signals to the cross-sector MLU. This allows for 2^6 possible trigger conditions which is more than sufficient for this experiment. The cross-sector MLU also has

several test/calibration inputs which allow for calibration and testing to take place without disturbing the trigger setup for an experiment.

Lastly, a JLab trigger supervisor receives the cross-sector MLU output, prescales it[4], and outputs gates and starts to the digitization electronics. At the beam energy used in BLAST there are no hadron showers and there is a relatively low rate of physical processes. Still, high background rates in some trigger types can cause the data acquisition rate to exceed the maximum rate able to be handled by the system. This can result in significant *deadtime*. Deadtime is the period of time in which the data acquisition cannot respond to incoming events within the data stream and which are consequently lost. To limit the computer deadtime, less important triggers with high background were prescaled.

The software used for controlling the data acquisition system consists of the CEBAF Online Data Acquisition (CODA) program from JLab and a modest compilation of shell scripts used for communicating with the hardware and for visualizing the raw scalers of the detectors. CODA is used for the BLAST detector and includes a graphical user interface, Runcontrol, which allows its users not only to start and stop runs but also to set run parameters. There are three main parts which make up the Coda program: ROCs, EB and Coda itself. The Read Out Controllers (ROCs) read out the data as processed by the MLUs. The Event Builder (EB) then compiles and sorts the data fragments from the ROCs as well as EPICS and scaler data and combines the data into an event.[5] Event Transport

[4]The respective prescales are listed by trigger type in Table 3.6. The utility of the prescale is to limit the time spent recording data from physics signals that are of low priority or of overwhelming statistics that saturate the data stream. Taking notice of the prescale of 1000 for the trigger type 6, a positron shower has been shown to be coming from the region of the collimator since the beginning of this experiment. The magnetic field of the Toroid is set to bend positive particles outward. The positrons are low momentum, are not in coincidence with any specific particle and produce no prioritized physics results. The prescale of 1000 allows only 1 in 1000 signals that correspond to this trigger logic to be recorded in the data stream.

[5]The ROCs produce about 500 physics events per second. The EPICS (Experimental Physics and Industrial Control System) are slow controls used to control target gas flow, wire chamber gas, the ABS, and the high voltage system for the detectors. EPICS events are recorded once per second. Scaler events are also recorded once per second and are raw rates used to visualize the ongoing performance of the detectors. The physics events from the ROCs are sent to ET in blocks along with scalers and EPICS which are not neces-

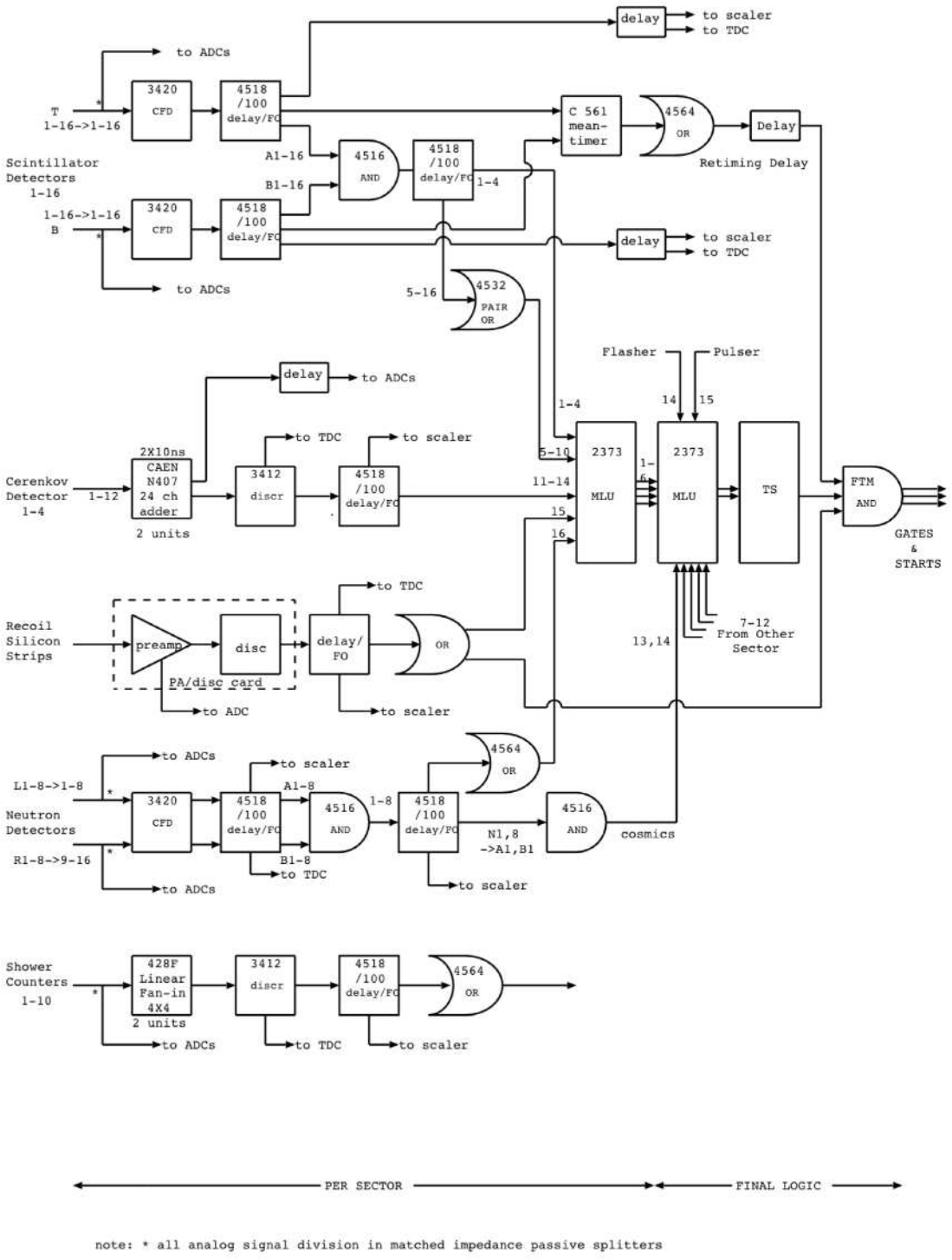

FIG. 3.35. A schematic of the BLAST Trigger electronics. Most of the four digit number correspond to LeCroy Model numbers of the individual units employed.

(ET) then takes these compiled events from EB, and *caServer* sends them to the Event Recorder (ER). *visual_scal* is a shell script for scalers visualization and is run to monitor the performance of all individual PMTs and sense wires of the detector.

3.6. BLAST Monte Carlo

GEANT-based Monte Carlo simulations were used to model the performance of the detector as well as the physical processes being measured at BLAST. The geometry of the detector was explicitly coded and input to GEANT to model the acceptance of the detector. GEANT propagates the particles through the magnetic field, simulates detector performance, and simulates important physical properties such as multiple scattering, continuous energy loss and an array of other less important physical processes that were not necessary in the BLAST configuration. A C++ event generator library, DGen, was specially written for the BLAST Monte Carlo to be input into the GEANT simulation. Cross sections and spin dependent observables are computed within DGen including ${}^2\vec{H}(\vec{e}, ed)$, ${}^2\vec{H}(\vec{e}, e'p)n$, ${}^2\vec{H}(\vec{e}, e'n)p$, $\vec{H}(\vec{e}, ep)$ and pion production from the nucleons. Radiative Corrections are carried out by an implementation of a translated version of MASCARAD[119].

Events can be generated in two ways, distributed according to a cross section, or according to a white generator with a uniform distribution across the phase space, tagging the cross section as a weight to each event. The generator's deuteron calculations are based on structure function calculations by H. Arenhövel[120] for various channels (elastic, electrodisintegration, inclusive etc). In the case of electrodisintegration the structure functions were computed on a 5-dimensional grid (θ_e, ϕ_e, θ_{cms}, ϕ_{cms}, ω)[6]. In the case of the inclusive

sarily time-interleaved. Event times are written to all three types of event trees to prevent misinterpretation of the recorded data.

[6]According to Arenhövel's convention

channel a 3-dimensional grid (θ_e, ϕ_e, ω) was used. The vertex position for the event must be included as another variable but uses a simple triangular distribution, associated with the density profile of the internal target, and this can be integrated out before calculating the other probability distributions associated with the actual physics of the reaction. The calculations used a cubic spline and other interpolations in order to obtain the relevant cross section at each kinematic point. DGen was initially designed to work with the deuterium channels but was later modified to incorporate Hydrogen channels and MAID's calculation of pion-production from nucleons.

CHAPTER 4: **DATA ANALYSIS**

4.1. Overview of the BLAST Experiment

The BLAST experiment was compiled over approximately 9 months and consisted of two independent datasets. The conditions of the experiments are summarized within Table 4.1. Approximately 450 kC of integrated charge were accumulated with the deuterium target from August 2004 until November 2004. In this dataset, the deuterium target was polarized at a polar angle of 32 degrees into the left sector. Two target cells were used (switched after the first 40 kC), both were kept at ∼90° K and the first cell provided an average vector polarization of 68% and the second cell maintained a vector polarization of 80% over the majority of this time period. The accuracy of these numbers is about half a percent and are further discussed in Section 4.8. The electron beam's injected current over the 2004 deuterium run increased from ∼100 mA to a maximum current of ∼140 mA and showed ∼65% longitudinal polarization in the electron beam. During the second production run, ∼490 kC of charge were accumulated with a deuterium target from March 2005 until May 2005. During this second production run, the polarization of the deuterium target was directed at a polar angle of 47° into the left sector. There were also two target cells used over the course of this production running period, each showing ∼68% vector polarization. The cells were meant to be kept at a temperature of 90° K though the higher injected current pushed temperatures upwards of 120° K over the run period. The electron beam

TABLE 4.1. Characteristics of the two independent deuterium datasets included in this work.

Year	θ^{pol}	$\int i \cdot dt$	$< i >$	i_{max}	$< h >$	$< P_z >$	<cell T>
2004	32°	451 kC	100 mA	140 mA	65%	80%	90 K
2005	47°	492 kC	180 mA	200 mA	65%	68%	120 K

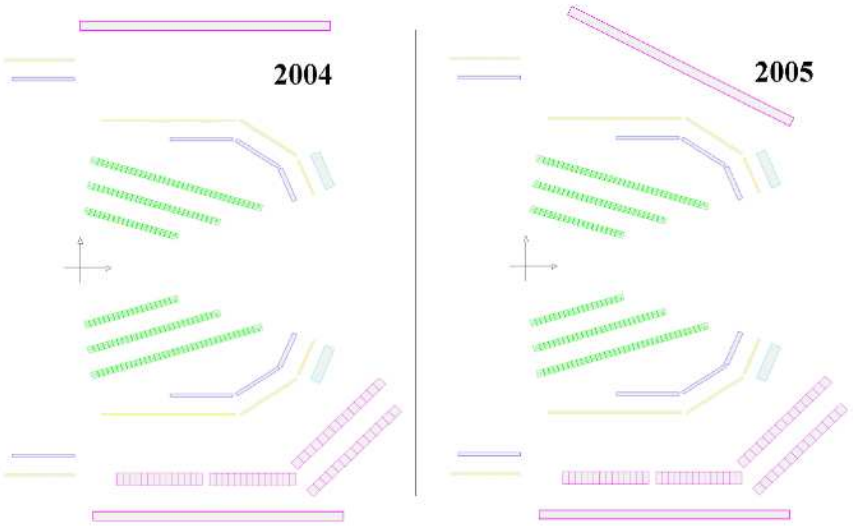

FIG. 4.1. The left sector OHIO neutron counters are shifted from the 2004 configuration for the 2005 run period.

for the 2005 dataset operated on an average injection of > 200 mA. This second running period also showed $\sim$65% longitudinal polarization in the electron beam.

Further differences accompany these datasets in the geometry of the neutron detectors. In the 2005 dataset, the OHIO Walls in the left/parallel sector (described in Section 3.4.4) were shifted forward and rotated slightly clockwise so that the downstream edge of the detector array was brought medial to the beamline. Figure 4.1 shows this displacement.

4.2. Reconstructed Kinematic Variables and Corrections Applied

It was noticed that the internal geometry of the wire chambers used in the BLAST experiment showed deviations from the pre-installed survey. Three superlayers of criss-crossed wires are used for locating the path of charged particles in 3D space. If the middle layer was displaced by exactly one millimeter from its assumed location, it was calculated that it would create a false measure of the curvature of the fit to a particle's trajectory

resulting in an offset of > 35 MeV in the reconstruction of the momentum of an electron or proton.

Monte Carlo simulations were used to test this estimation (see Figure 4.2). A shift was created in the geometry file used to feed GEANT the positions of the superlayers of the drift chambers. Elastic collisions of electrons and protons from the target hydrogen were generated with the proper *unshifted* geometry, then reconstructed and analyzed with the *shifted* geometry. When calculating the electron beam energy (850 MeV) from the reconstructed outgoing momentum and angle of the electron or the proton, deviations from the known results were similar to the suspect experimental results.

The internal geometry of the wire chambers was found to be correct in the initial survey but had been incorrectly implemented. There were still discrepancies (see Figure 4.3) between the measured angles and momenta of scattered electrons and recoil protons from the well known benchmark in elastic kinematics. The first order contributions within the scope of the kinematic constraints are the elastically scattered particles' momenta (after accounting for proton's energy loss) and polar angles as defined within the BLAST frame. The azimuth shows a systematic deviation of < 0.3 degrees from the constraint of coplanarity and can thus be neglected since this deviation is less than the resolution in ϕ_{lab} and is only a second order contribution to the elastic constraints on Q^2. A χ^2 minimization over Q^2 was attempted over all four first order variables, p_e, p_p, θ_e, and θ_p[1]. The resolution of the wire chambers proves much better in θ, e.g. $\theta_e - \theta_e(\theta_p)$ gives a σ of $< 0.5^\circ$(though it centered itself at about 0.3°), whereas $p_e - p_e(p_p)$ gives a σ of roughly 15% of the value of p_e and a systematic deviation from zero that was $> 15\%$ of p_e. Thus the χ^2 minimization effectively

[1]In this example of elastic *ep*-scattering, a relativistic particle striking a particle at rest follows from relativistic kinematics. The resulting outgoing particles are expected to be coplanar and all four first order variables describing the scattered electron and proton, p_e, p_p, θ_e, and θ_p are linearly independent. Each of these four variables are easily derived from any one of their three partners and thus Q^2 can be calculated using any of these four variables. See Appendix B.

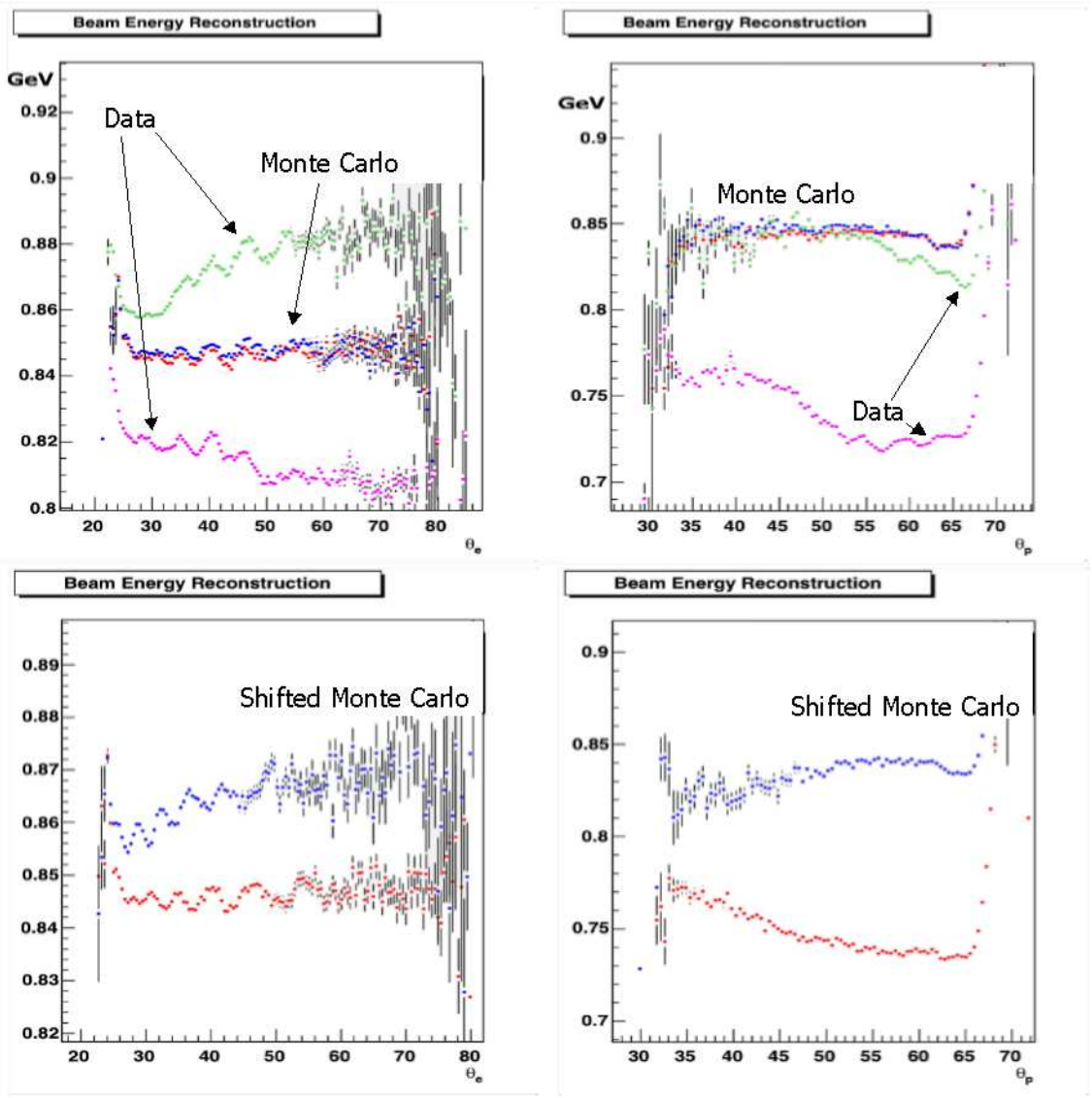

FIG. 4.2. The upper two plots show Monte Carlo simulations showing reconstructed momenta and polar angles of outgoing electrons and protons resulting from elastic collisions under ideal experimental conditions. The reconstructed variables are used to calculate the incoming electron beam energy and are quite consistent with the actual beam energy. Superimposed on the top two plots with lighter points is a profile of the same calculations from experimental elastic *ep* collisions. The miscalibrated internal geometry was suspected. The lower two plots show Monte Carlo reconstructed with a rough 1 mm shift of the middle superlayer in one sector's drift chambers. Some features of the data are clearly recreated.

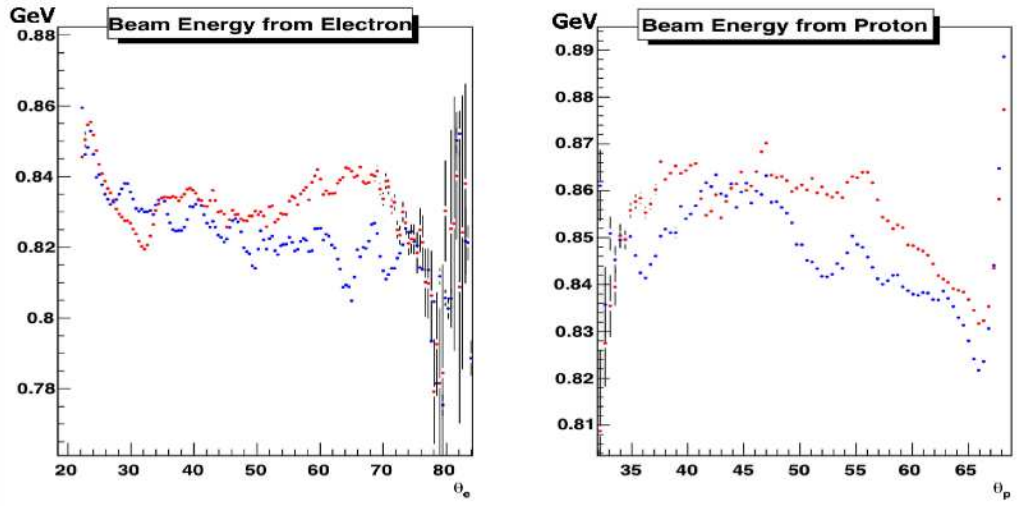

FIG. 4.3. After the internal geometry of the wire chambers was corrected, substantial deviations were still evident when the reconstructed variables were used to calculate the well-known 850 MeV beam energy. The separate sets of points are demonstrative of the necessity for sector dependent corrections.

determines the systematic deviations in θ_e and θ_p with very little influence from the values of p_e and p_p. Thus, the first step was to use the measured values of θ_e and θ_p event by event, along with the well known beam energy, and determine the first multiplicative corrections to p_e and p_p via the relations $C_e^p = p_e(\theta_e)/p_e$, and $C_p^p = p_p(\theta_p)/p_p$.

These corrections were input and then the χ^2 minimization in Q^2 was taken over the new values of $p'_e = p_e * C_e^p$, $p'_p = p_p * C_p^p$, and the old values of θ_e and θ_p in order to determine the best values of θ_e and θ_p from the best value of Q^2 as determined from the measured values of θ_e and θ_p and the corrected values of p'_e and p'_p.

$$\begin{aligned} \chi^2(p'_e, p'_p, \theta_e, \theta_p) \quad = \quad & (Q^2 - Q^2(p'_e))^2/dp_e^2 + \\ & (Q^2 - Q^2(p'_p))^2/dp_p^2 + \\ & (Q^2 - Q^2(\theta_e))^2/d\theta_e^2 + \\ & (Q^2 - Q^2(\theta_p))^2/d\theta_p^2, \end{aligned} \tag{4.1}$$

The values p_e and p_p were corrected to prevent the large systematic discrepancies from influencing the χ^2 minimization. After the best Q^2 was found per event, we can now use this *best* value, Q'^2, and derive the best values for θ_e and θ_p. Additive corrections are then found for θ_e and θ_p, i.e. $\Delta\theta_e = \theta_e(Q'^2) - \theta_e$, etc.

These corrections were found to be less than 0.3° nearly everywhere in the BLAST acceptance and when plotting the corrected distribution of $\theta'_e - \theta_e(\theta_p)$ and $\theta'_p - \theta_p(\theta_e)$, the mean was found to be centered on zero where it was originally off by ~ 0.3 degrees (see Figure 4.4).

Since the checks on the constraints from elastic kinematics using corrected values of θ_e and θ_p were found to be well within the resolution, the final multiplicative corrections to the momentum were determined by using the functional dependence of $p_e(\theta'_e)$ and $p_p(\theta'_p)$. A check on the utility of these corrections that is employed is a calculation of the incoming electron beam energy using a single particle's p and θ from one sector, i.e. $E(p_i^J, \theta_i^J)$ (where $i = e, p$ and $J = L, R$) should amount to ~ 850 MeV. When convoluting these first order contributions by reconstructing the beam energy from final corrected values, we show a correlation with the expected beam energy and deviations that are at least a factor of 2 less than the resolution of the momentum of both the proton and electron (see Figure 4.5).

Corrections for the polar angle and momentum have been applied and proven useful in deuterium channels. There is a question of the applicability of these corrections for a different target since the corrections are defined with the well-defined phase space of the *ep*-elastic. When shifting to quasielastic kinematics, it can be argued that the outgoing particles from the reaction may traverse different regions within the Drift Chambers that give different systematic offsets in the measured momenta. For the proton, this point has much more force. Since $^2\vec{H}(\vec{e}, e'n)p$ uses only the corrections to the electron, and the

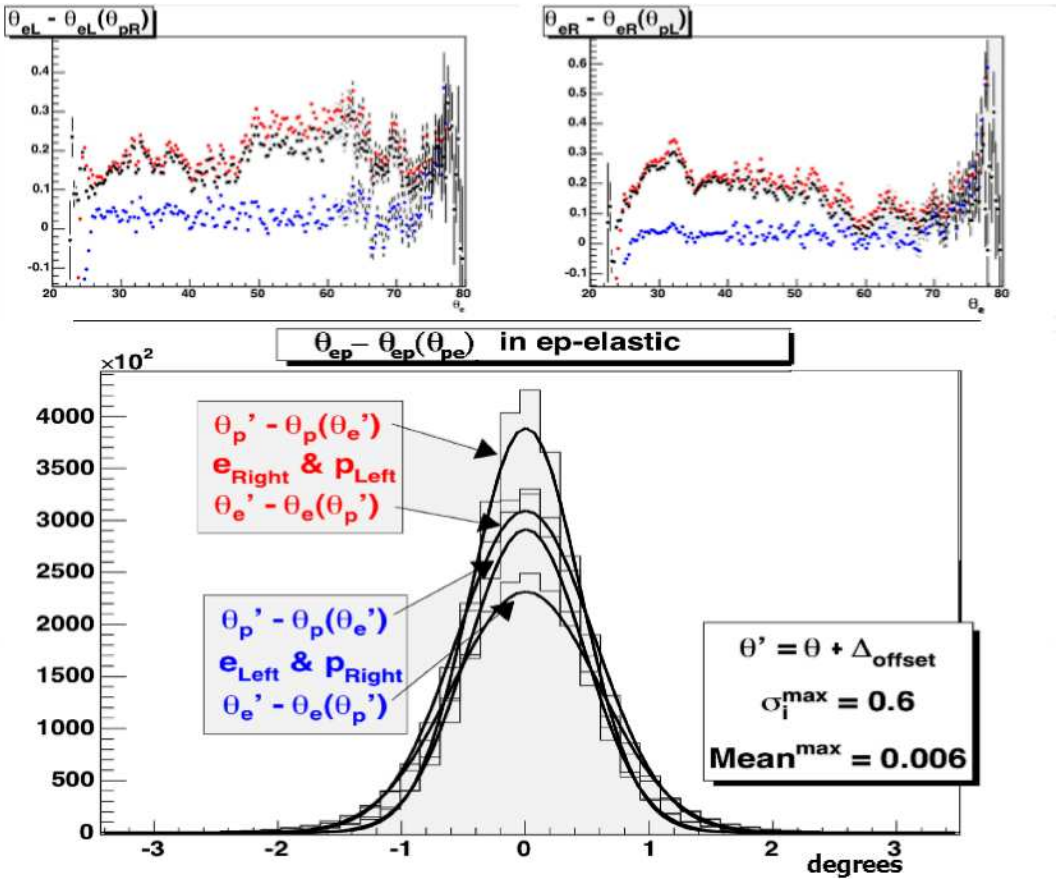

FIG. 4.4. The top two plots show the distributions resulting from the relation $\theta_e - \theta_e(\theta_p)$. These are calculated per coincident event tracked by the wire chambers. There are three sets of data plotted, two software versions of reconstruction that show clear deviations from 0° and a final recrunched dataset using corrected polar angles of the outgoing particles. The two profiles show that both sectors have been independently corrected. The 1D distributions with fitted Gaussians on bottom are the results of the sector dependent corrections to θ_e and θ_p event by event. The maximum deviation from a mean of zero is shown at 6 thousandths of a degree while the maximum convolution of the resolutions is 0.6° which gives an experimental $\sigma_\theta = 0.43^\circ$.

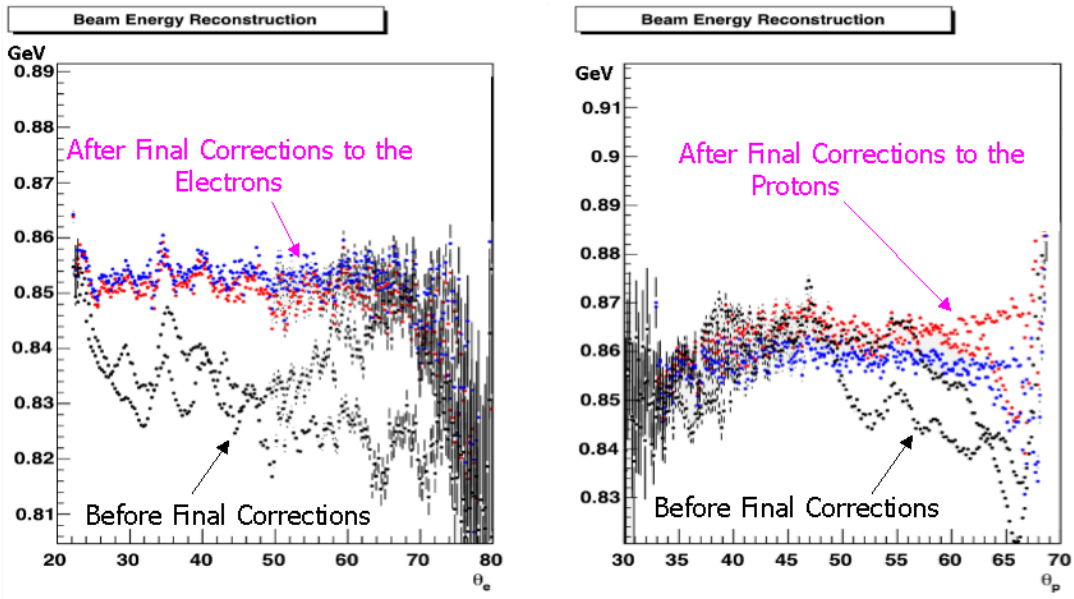

FIG. 4.5. The plot on the left features electrons while protons are on the right. The corrected data from both sectors is lumped together along with the raw data analyzed after the correction to the internal geometry of the drift chambers. Corrections using the χ^2 minimization and elastic kinematics were done in two steps and the final corrections resulted in a distribution centering itself on 850 MeV for the electrons and approximately 860 MeV for the protons. It is not clear why the reconstructed energy of the beam is overestimated from the proton kinematics but the resolution of the momentum as reconstructed in BLAST is $\sigma_p = 35$ MeV and this result is within the propagated error expected in such a calculation.

quasielastically scattered electron's outgoing momentum covers a very similar phase space to the outgoing electrons from ep-elastic, these systematic corrections to the electron's momentum were used in the final analysis of G_E^n. In other channels, such as quasielastic proton scattering and inelastic channels, other methods of momentum corrections were pursued and applied. Quasielastic proton scattering has been corrected using comparisons to Monte Carlo[122] and also using the constraints of quasielastic kinematics by enforcing the missing mass of the neutron[123]. The inelastic channels are beyond the scope of this work.

4.3. Identification of $^2\vec{H}(\vec{e}, e'n)p$ Events

The trigger logic of $^2\vec{H}(\vec{e}, e'n)p$ events are set to sequester coincident hits from the drift chambers and a scintillator of one sector with an opposite sector neutron detector (see #2 from Table 3.6). On top of the trigger logic is a redundant inclusion of realistic readings within the actual detectors that initiated the trigger logic, i.e. positive timing values along with deposited energies corresponding to realistic values from the photomultiplier tubes of the associated detectors. In the BLAST software, there was also an inclusion of a requirement of tracked particles to be of momentum greater than 150 MeV in order to exclude positrons emitted from the collimator and target holding cell which reduced a great deal of irrelevant events from the sample passing the trigger logic.

There is a possibility that events categorized within the trigger logic such as coincident opposite sector scintillators could also contribute to the $^2\vec{H}(\vec{e}, e'n)p$ yield, but there is only be a few hundred neutrons to gain while there would be considerable difficulty involved in the extraction and thus we have limited the event sample to those events that fire a neutron detector. It has been postulated that one could extract another 40% of the present

sample [138] by selecting the inclusive channel with the opposite sector charge veto, though the difficulties in extracting a clean sample along with the loss of the kinematic information of the neutron amounts to a substantial increase in the systematic uncertainties of that anecdotal data sample. It is not included here.

The following is a quick list of the cuts that are described in the succeeding paragraphs. They are easy to reference by their itemization and are as follows:

(**A**) Trigger Logic;

(**B**) Charge Veto;

(**C**) Vertex = Origin ± 20 cm;

(**D**) Polar angle neutron cut: $33^\circ < \theta_n < 76^\circ$;

(**E**) Azimuthal angle neutron cut: $\phi_n^{\perp} = 180^\circ \pm 13^\circ$, $\phi_n^{\parallel} = 0^\circ \pm 13^\circ$ (see Figure 4.7);

(**F**) Specific multiplicities of impossible detector combinations;[2]

(**G**) Kinematics: $0.02 < \beta_n < 1.0$;

(**H**) Kinematics: $|M_m - M_p| < 0.1\frac{GeV}{c^2}$;

(**I**) Kinematics: $|W - M_d| < 0.1\frac{GeV}{c^2}$;

(**J**) Kinematics: $|Q.E.| < 0.1\frac{GeV}{c^2}$.[3]

Medium energy electron scattering experiments that employ neutron detection are typically hindered by low statistics, relatively high systematic errors, and proton contamination. In the quasielastic neutron channel, a total of +500k neutrons were accumulated. The systematics are greatly reduced in the BLAST experiment since the data from ${}^2\vec{H}(\vec{e}, e'n)p$,

[2]This cut refers to multiplicities of potential neutron hits that are unrealistic. When taking notice of the neutron detector geometry in the overloaded perpendicular kinematics sector, the L20's shadow the Ohio Walls and the front wall of the L15's shadow the back wall. Combinations of hits between these sets of detectors are allowed while combinations of L20's and L15's are indicative of noise or false events and are thus rejected from the data sample.

[3]This cut is a cut around the *quasielastic ridge*, *Q.E.*, which is derived from the invariant mass formula where one would input the mass of the neutron as the mass of the target. It is redundant with respect to (**I**).

$^2\vec{H}(\vec{e}, ed)$, and $^2\vec{H}(\vec{e}, e'p)n$ were all run simultaneously and thus, under equivalent conditions. The measurement of asymmetries in double-polarized exclusive scattering most significantly reduce the systematic errors of the experiment. Furthermore, the BLAST experiment was blessed with a continuous charged particle detector which acted as an effective proton veto. The wire chambers cover nearly the entire neutron acceptance[4]. Each layer of wires is 98% efficient for detecting charged particles traversing the chambers and thus gives negligible chance for any charged particle to escape 18 layers of wires undetected. Allowing up to twelve wires to detect voltage fluctuations due to noise still gives a probability $< 0.00001\%$. Given this "charge veto," (**B**), we escape the problem of proton contamination. Also, the minimized material between the target and the veto detector (the wire chambers) minimize the number of protons from $^2\vec{H}(\vec{e}, e'p)n$ converting into neutrons in those materials before entering the veto chamber, e.g. the target wall, thin wire chamber entrance, and the small air volume due to the proximity of the wire chambers to the target cell.

A few initial cuts were needed due to limitations of the experiment. The holding field and polarization of the nuclei in the region of the internal gas target were found to be unreliable at distances greater than 20 cm from the origin in the BLAST coordinate system (see Figure 3.11). This initial cut, (**C**), restricts the vertex distribution of the scattered particles to the origin ± 20 cm.

Another cut on the acceptance was taken into account when plotting the effects of the charge veto on particular detectors, specifically the OHIO and L20 neutron detectors. The yield over the polar angle acceptance spiked in these neutron detectors at an angle

[4]In the 2004 configuration of the OHIO Walls, both sectors extend approximately four degrees further than the coverage of the wire chambers and thus requires a fiducial cut (**D**) restricting the scattered neutron's polar angle below 76°. The 2005 configuration of the left sector OHIO Walls is completely covered by the wire chamber acceptance.

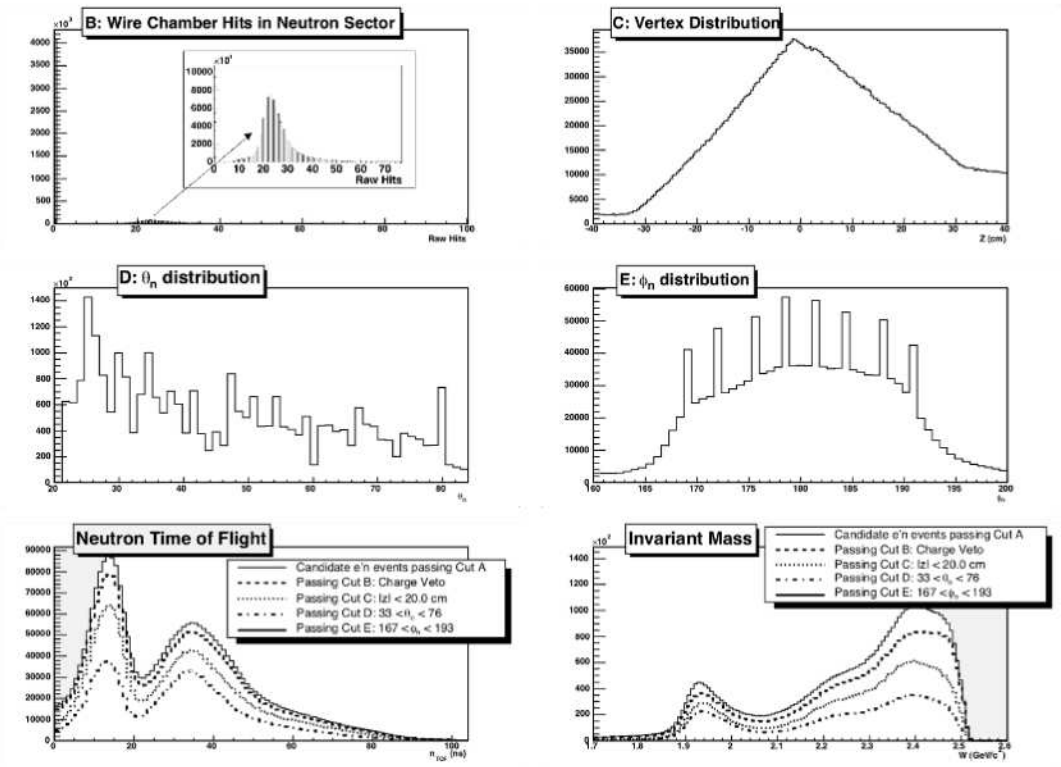

FIG. 4.6. These plots show successive distributions and cuts corresponding to those cuts listed as **A-E** as delineated in this section.

greater than 76° as plotted along with a visualization of the applied cut in Figure 4.6. Further cuts on the neutron acceptance are motivated by a comparison with edge effects from the simulated Monte Carlo events of the ${}^2\vec{H}(\vec{e}, e'n)p$ channel. A comparison is made between the solid angle acceptance of the neutron detectors from the data sample and Monte Carlo in order to identify any "edge effects". The yields are plotted over the solid angle neutron acceptance and the yields per bin are normalized to the total integral of the respective plots of data and Monte Carlo. These plots are then divided and any "edge effects" become obvious in the final plot of this quotient. This final fiducial trimming of the data is described thoroughly in Figure 4.7.

The BLAST software library enables reconstruction of the events in our sample and supplies such useful information as the momenta, time of flight, and outgoing angles of the scattered particles, e.g. p_e, θ_e, ϕ_e, p_n, θ_n, ϕ_n, and the aforementioned vertex z whose cut about the origin has already been motivated. These parameters allow us to reconstruct the kinematics of each event and plot meaningful information relevant to the measurement, e.g. $\vec{q}$, Q^2, ω, W, M_m (missing mass), p_m (missing momentum), etc. The binding energy of the deuteron is extremely small in comparison to the beam energy and kinematic resolution of the BLAST experiment. It can be neglected when considering the resulting kinematics that define a quasielastic electron-neutron scattering event.

Despite our ability to reliably make cuts on hardware and the vertex origination, we need the kinematics to further constrain our data sample by using the aforementioned quantities. For the special case of 850 MeV electrons colliding with static deuterons of energy $\frac{3}{2}kT$, which is again negligible, the undetected particle of an ${}^2\vec{H}(\vec{e}, e'n)X$ event is obviously dominated by events with $X = p$. The time of flight of the detected neutron of a quasi-elastic event is measured and should correspond to a value of at least the expected

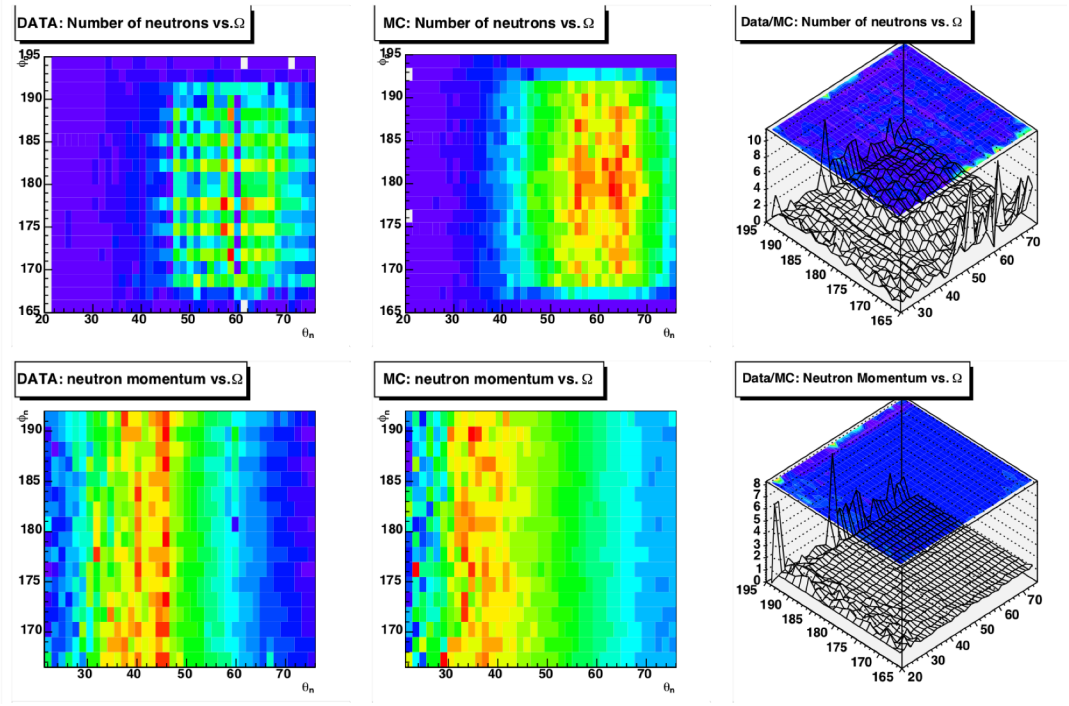

FIG. 4.7. These six plots are two dimensional histograms characterizing the BLAST acceptance, Ω_n. On the top row, in the leftmost plot, the yield is plotted over the solid angle acceptance and normalized to the total number of neutrons detected. The plot to the right is the normalized yield plotted from the BLAST Monte Carlo simulations. The rightmost plot is the quotient of the two previous plots; it should and does hover at about unity since our Monte Carlo is sufficiently descriptive of our experiment. The three plots on bottom are analogous to the top three except each bin is also convoluted with the average momentum measured as a function of solid angle. Again, the rightmost plot, the quotient of the previous plots, should and does hover at about unity showing that Monte Carlo and data are in good agreement. The acceptance cuts (**D** and **E**) introduced at this stage of analysis are used to decimate the "edge effects" that can be seen in the two rightmost plots. At low polar angle ($\theta_n < 30°$) and at excessive off-axis azimuthal angles ($|\phi_n - 180| < 13°$) the quotient describing the quality of the data deviates considerably from unity.

time of flight for a photon since the only potential neutral particles that can contaminate the neutron sample are photons from ancillary scattering processes or the decay of a π^0 from the decay of a Δ-excitation where $X = p\pi^0 \rightarrow p\gamma\gamma$. To prevent any reactions in which X involves an outgoing photon and misfires our neutron detectors, we include cut **G**. Using the time of flight of the neutron, our resulting *quasielastic* events can be defined using our kinematic quantities. To reiterate previously defined values such as the Lorentz-invariant Q^2, the missing mass M_m, the invariant mass W, and other important quantities such as missing energy and missing momentum, E_m and p_m:

$$\begin{aligned} Q^2 &= \mathbf{q}^2 - \omega^2, \\ E_m &= m_d + \omega - E_n, \\ \vec{p_m} &= \vec{q} - \vec{p_n}, \\ M_m &= \sqrt{E_m^2 - p_m^2}, \\ W &= \sqrt{m_d^2 + 2m_d\omega - Q^2}. \end{aligned} \tag{4.2}$$

These quantities give further insight into the process we observe. Knowing that we are investigating the ${}^2\vec{H}(\vec{e}, e'n)p$ channel, M_m, E_m, and p_m should reduce to the mass (Cut **H**), energy, and momentum of the proton, respectively, while W reduces to the mass of the deuteron (Cut **I**). Some of this information along with respective cuts can be seen in Figure 4.8. The invariant mass peak at m_d derives its width from the Fermi momentum of the deuteron's constituents. Any further smearing of W, along with the other important quantities here, occurs due to the resolution of the detector in determining the angle and momenta of the outgoing particles. Cuts are made on the missing mass and invariant mass to ensure that the mentioned quantities do not venture into values corresponding to inelastic processes such as Δ production where other reactions that may accompany a

detected neutron are $X = p\pi^0$ or $X = n\pi^+$. The latter are often rejected but still the high momentum π^+ mesons are emitted into a 4π solid angle and can pass outside the acceptance of the veto detector, forcing us again to require kinematic cuts.

In the plane wave impulse approximation we can use the invariant mass equation, set the mass of the target equal to the mass of the neutron and solve to find the relation $Q^2 = 2m_n\omega$. This defines the process where the virtual photon exchange occurs between the electron and a singly struck neutron, i.e. quasielastic scattering off the neutron. This provides another cut (**J**) that can be applied in order to further isolate events that occur on this *quasielastic ridge*. The Fermi motion within the deuteron along with any final state interactions or radiative effects will cause deviations from the elastic kinematic assumptions that define quasielastic scattering.

Figure 4.8 shows the diminishing features of the photon peak in the neutron time of flight and the decaying inelastic contamination in the invariant mass as we employ kinematic cuts such as **G-J**. We make sure the velocity of the accepted neutrons are not the speed of light, which practically kills the photon peak. Then we constrain the missing mass and then, somewhat redundantly, include a cut on the condition of quasielastic scattering and further, redundantly constrain the invariant mass peak.

4.4. Q^2 Bin Selection

Now that I have shown the reduction of our dataset to a clean sample, we can demonstrate the separation and organization of the data. The Lorentz-invariant Q^2 allows us to bin the data such that we are probing regions deeper within the neutron as we progress along into higher momentum transfers. In order to satisfy the most general solution of the QFT vertex where the electron interacts with the neutron via a virtual photon, it

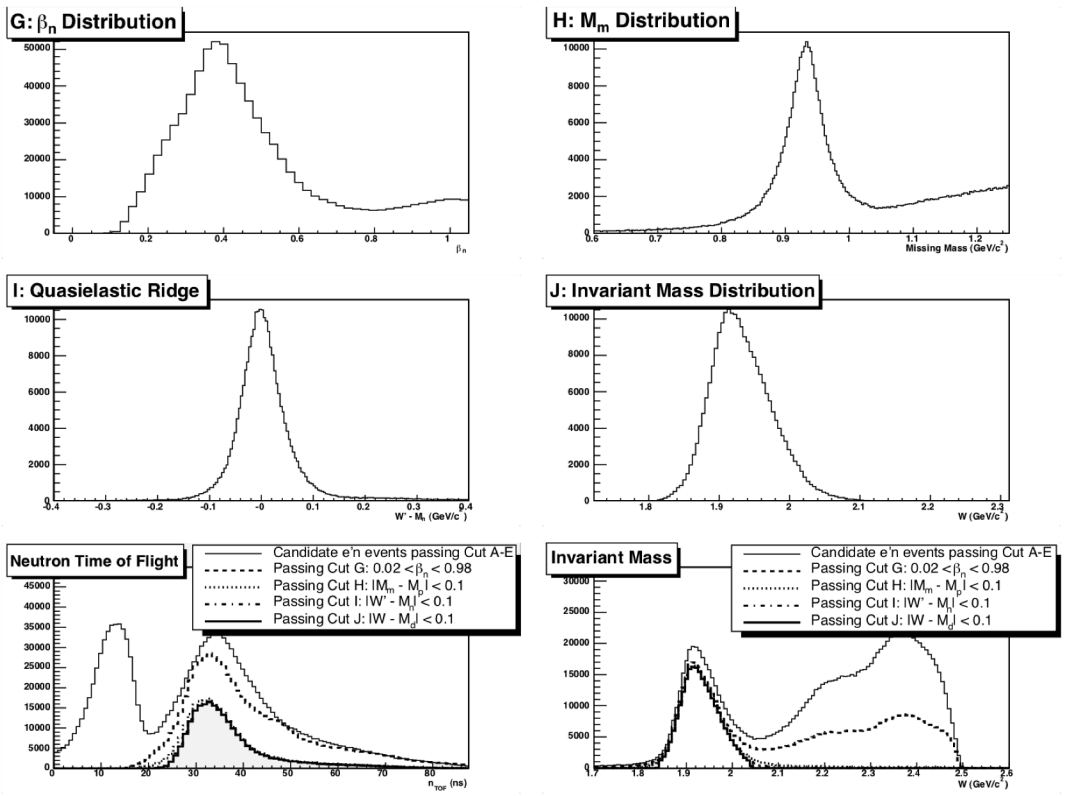

FIG. 4.8. The plots above demonstrate the distributions and cuts delineated in this section as **G-J**. The bottom two plots show the measured time of Flight of the neutron and the invariant mass as measured from the surviving events' electron kinematics.

TABLE 4.2. The resulting number of neutrons of both datasets within the selected Q^2 bins tallied after each cut is applied. The cuts are labeled as listed in the previous section. The bins are defined as $0.1 \leq Q^2 < 0.17$, $0.17 \leq Q^2 < 0.25$, $0.25 \leq Q^2 < 0.35$, and $0.35 \leq Q^2 \leq 0.55$.

Cuts	$\langle Q^2 \rangle = 0.14 \left(\frac{GeV}{c}\right)^2$	$\langle Q^2 \rangle = 0.20 \left(\frac{GeV}{c}\right)^2$	$\langle Q^2 \rangle = 0.29 \left(\frac{GeV}{c}\right)^2$	$\langle Q^2 \rangle = 0.42 \left(\frac{GeV}{c}\right)^2$
2004				
A, B, and C	979814	218263	232121	398806
D, E, and F	398165	87581	93206	160948
G and H	110794	78209	35858	23740
I and J	101759	71948	31881	18463
2005				
A, B, and C	684445	149936	155021	240479
D, E, and F	288587	62570	64305	101401
G and H	107328	73758	24856	17123
I and J	97366	67166	21166	12724

must satisfy Lorentz invariance, gauge invariance and the incoming and outgoing particles must satisfy the free particle Dirac equation[121]. Therefore, the form factors, to lowest order, must be functions of Q^2. The experiment was designed to probe the region that has historically shown to give the maximum value of G_E^n. The Q^2 binning chosen is defined in Table 4.2. The table also includes the yield in each bin after specific combinations of cuts are applied. The BLAST experiment uses six combinations of target and beam polarization states yet only four contribute to the beam-vector asymmetry. Therefore, only about two-thirds of the final yield in this table contribute to the statistical errors of our measurement.

The sophistication of the reaction requires comparison with the BLAST Monte Carlo and must also correspond to the kinematics inherent in the Monte Carlo event set. Within the four Q^2 bins, the relevant distributions characteristic of ${}^2\vec{H}(\vec{e}, e'n)p$ events and quantities descriptive of the phase space being probed can be plotted along with the distributions of the Monte Carlo simulations used to analyze the data. This data is shown in Figures 4.9-4.12. The asymmetries show the highest sensitivity to G_E^n when measured as a function of

p_m, θ^{np}_{cms}, and θ^* and these three distributions are shown with the missing mass M_m, the energy transfer ω, and the coplanarity $\phi_n - \phi_e$.

4.5. Raw Experimental Asymmetries

The BLAST experiment used six combinations of polarization states of the beam and target. The beam helicity was flipped at each fill of the Storage Ring. The target polarization was randomly flipped between the polarized vector-plus, vector-minus, and tensor-minus polarized states. Over the course of the experiment, it cannot be guaranteed that an equal amount of time was spent in each configuration, or that an equal amount of charge passed through the target in each combination of states. Therefore, the yield of each state is normalized by the respective accumulated charge in each state and will be referred to as the column vector, $n(h, P_z, Pzz)$. The associated components are,

$$n(h, P_z, Pzz) = \begin{pmatrix} n(1,1,1) \\ n(-1,1,1) \\ n(1,-1,1) \\ n(-1,-1,1) \\ n(1,0,-2) \\ n(-1,0,-2) \end{pmatrix}. \tag{4.3}$$

As stated in Chapter 2, h, P_z, and P_{zz} are the beam's longitudinal polarization, the target's vector polarization and tensor polarization, respectively. The five asymmetries that are characteristic of deuteron electrodisintegration are A_e, A^V_d, A^V_{ed}, A^T_d, and A^T_{ed} are defined in eqns. 2.46-2.50. They can be rewritten as linearly independent combinations of six normalized yields constituting the six components of our column vector. We can represent this in matrix form,

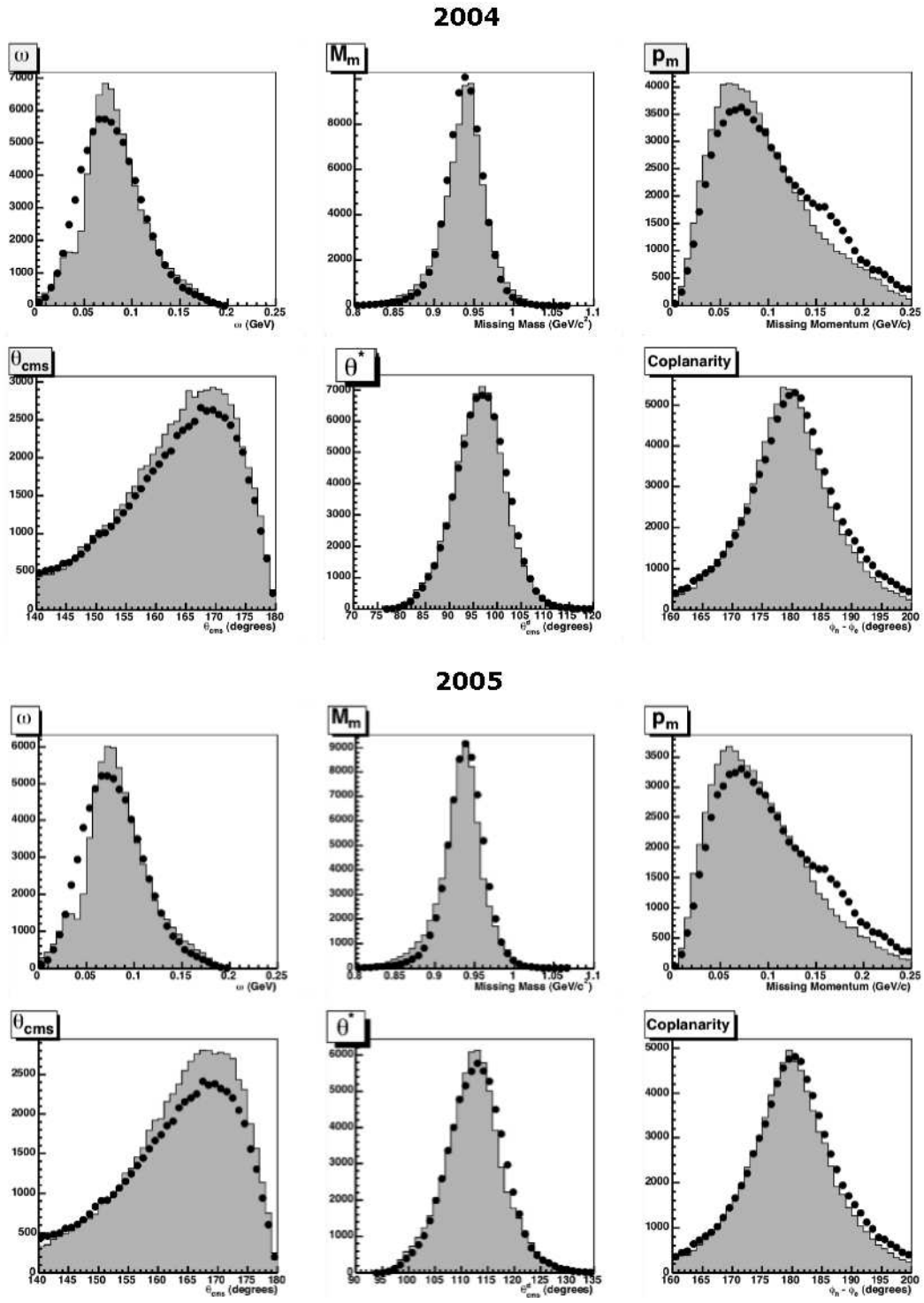

FIG. 4.9. A comparison of key Monte Carlo and Data Distributions pertinent to accurately measuring G_E^n. This is the first Q^2 bin and the Monte Carlo is represented by the dark points.

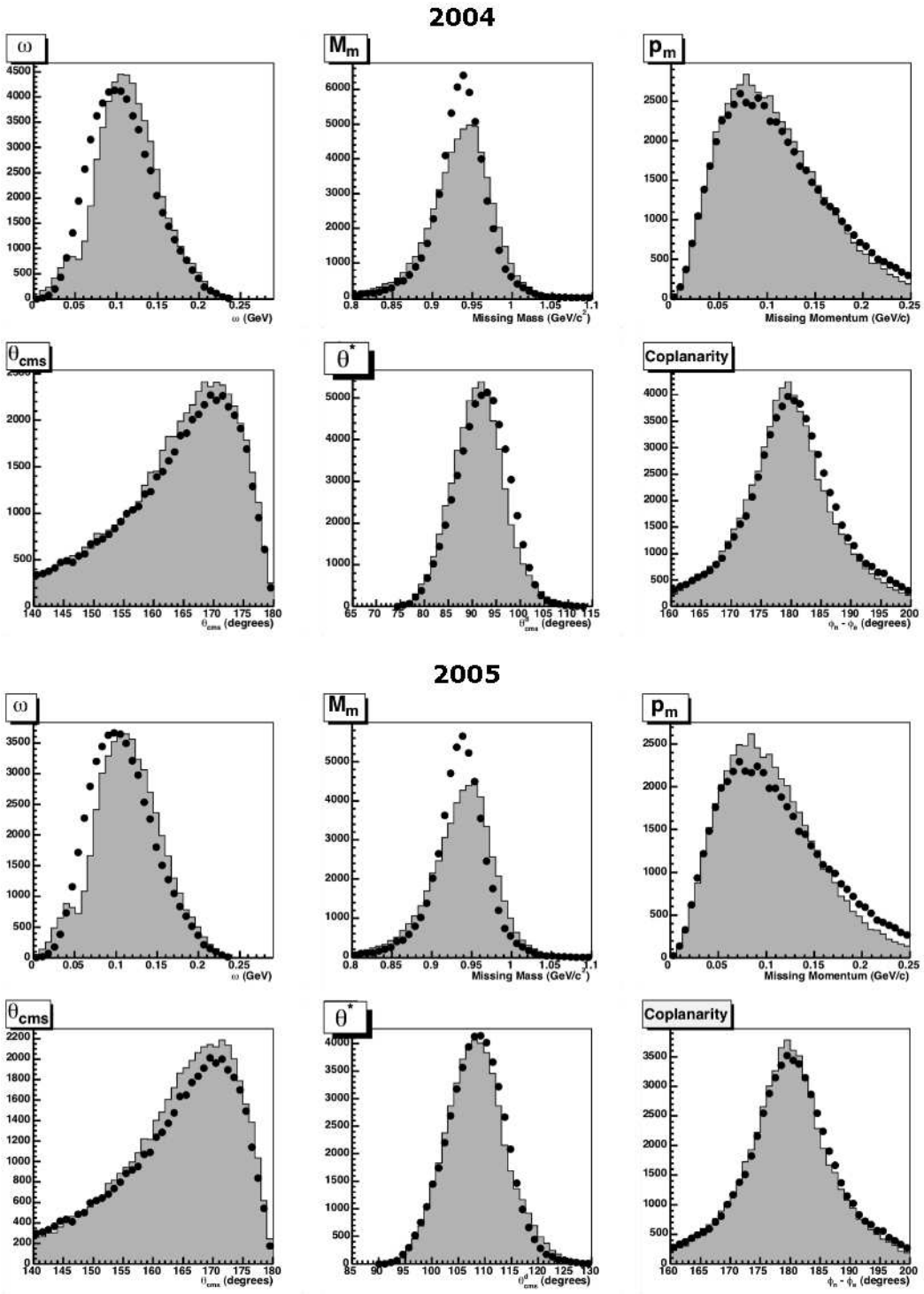

FIG. 4.10. A comparison of key Monte Carlo and Data Distributions pertinent to accurately measuring G_E^n. This is the second Q^2 bin and the Monte Carlo is represented by the dark points.

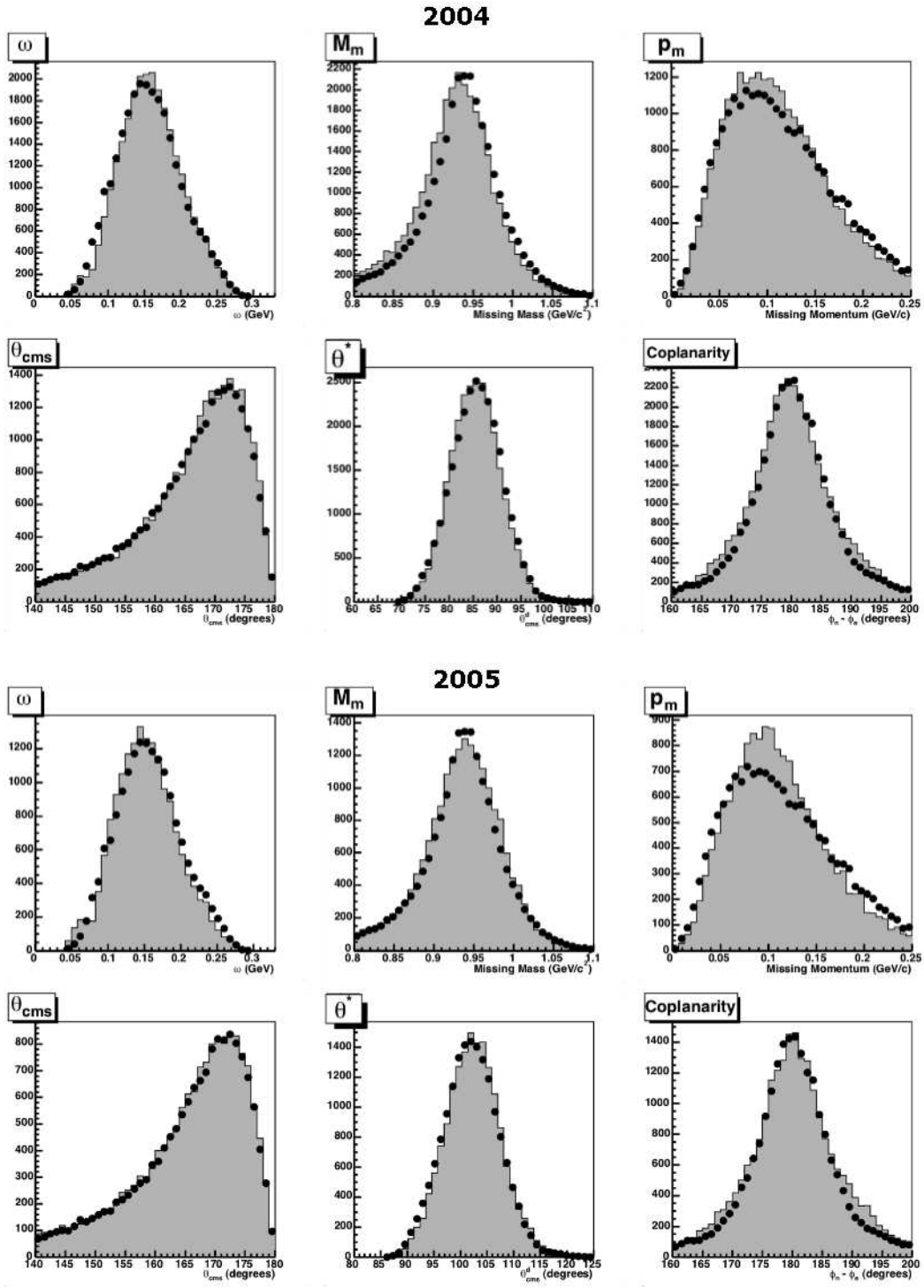

FIG. 4.11. A comparison of key Monte Carlo and Data Distributions pertinent to accurately measuring G_E^n. This is the third Q^2 bin and the Monte Carlo is represented by the dark points.

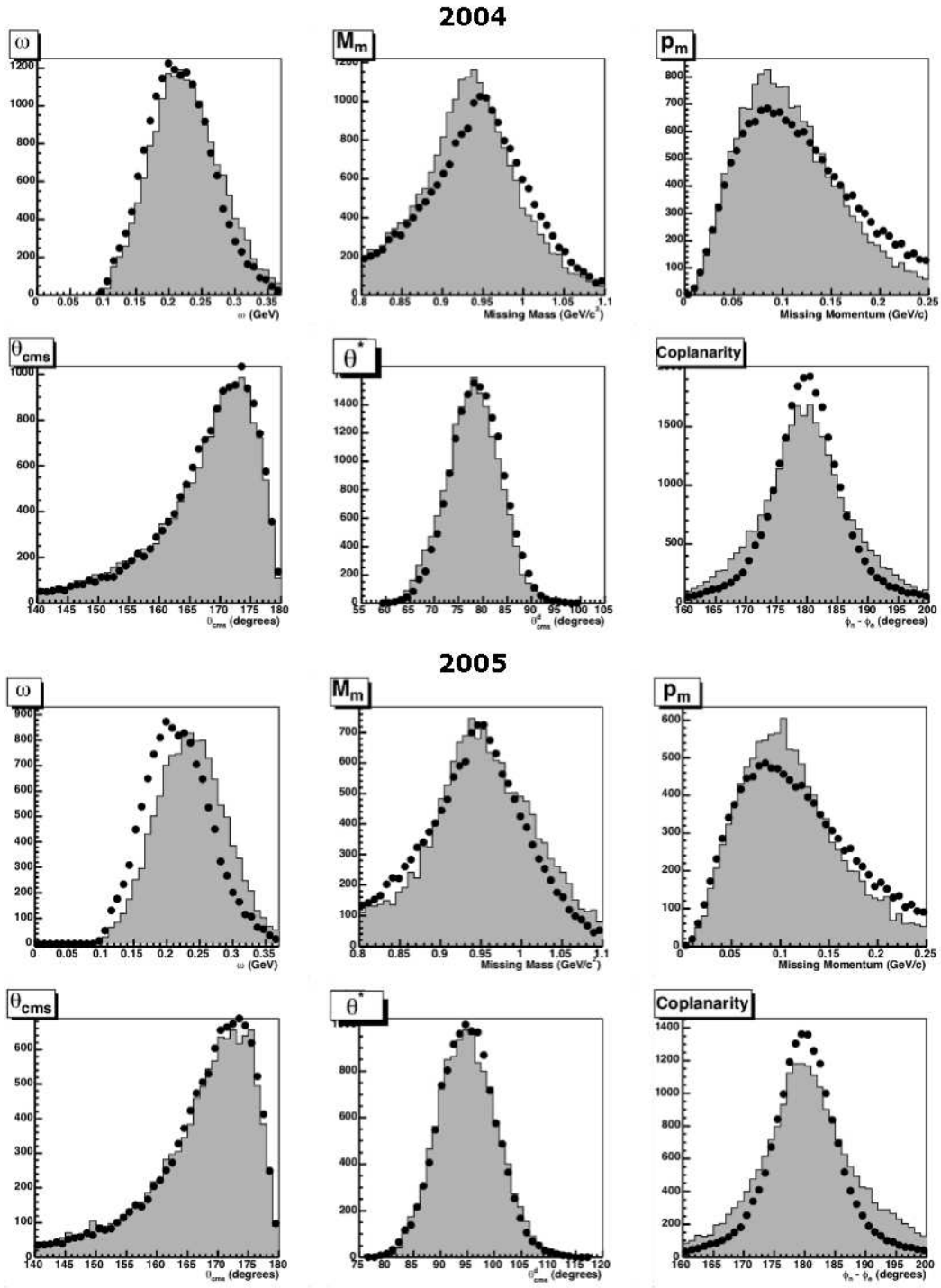

FIG. 4.12. A comparison of key Monte Carlo and Data Distributions pertinent to accurately measuring G_E^n. This is the fourth Q^2 bin and the Monte Carlo is represented by the dark points.

$$\begin{pmatrix} 6h\bar{r}A_e \\ \frac{2}{3}\sqrt{\frac{3}{2}}P_z\bar{n}A_d^V \\ \frac{2}{3}\sqrt{\frac{3}{2}}hP_z\bar{n}A_{ed}^V \\ 2\sqrt{\frac{1}{2}}\sqrt{2}P_{zz}\bar{n}A_d^T \\ 2\sqrt{\frac{1}{2}}hP_{zz}\bar{n}A_{ed}^T \end{pmatrix} = \begin{pmatrix} 1 & -1 & 1 & -1 & 1 & -1 \\ 1 & 1 & -1 & -1 & 0 & 0 \\ 1 & -1 & -1 & 1 & 0 & 0 \\ 1 & 1 & 1 & 1 & -2 & -2 \\ 1 & -1 & 1 & -1 & -2 & -2 \end{pmatrix} \begin{pmatrix} n(1,1,1) \\ n(-1,1,1) \\ n(1,-1,1) \\ n(-1,-1,1) \\ n(1,0,-2) \\ n(-1,0,-2) \end{pmatrix} \tag{4.4}$$

where $\bar{n}$ is the average of the rates of the six polarization states. The coefficients are indicative of the tallied yields in the numerator with respect to the total yield in the denominator and H. Arenhövel's definition of the asymmetries. When expressing experimental results in terms of the asymmetries, the luminosity and the detection efficiency are explicitly cancelled in this formulation. Figures 4.13 and 4.14 show the raw asymmetries as a function of p_m and θ_{np}^{cms} from the 2004 and 2005 configurations, respectively. Arenhövel [35] and Donnelly and Raskin [33, 34] show, using the coordinate system and variables defined in Section 2.3, that the electric form factor G_E^n is most sensitive to the vector asymmetry A_{ed}^V as a function of one of three variables, p_m, θ_{np}^{cms}, or θ^*. Each of these measurements are statistical convolutions of each other and can only be used to verify one another in final calculations of G_E^n.

4.6. Background Corrected Asymmetries

4.6.1. Unpolarized Background Correction. The BLAST data, even after cuts, is still subject to corrections due to background. During production running, data had been collected with an empty target cell for exactly this purpose. It is known that the

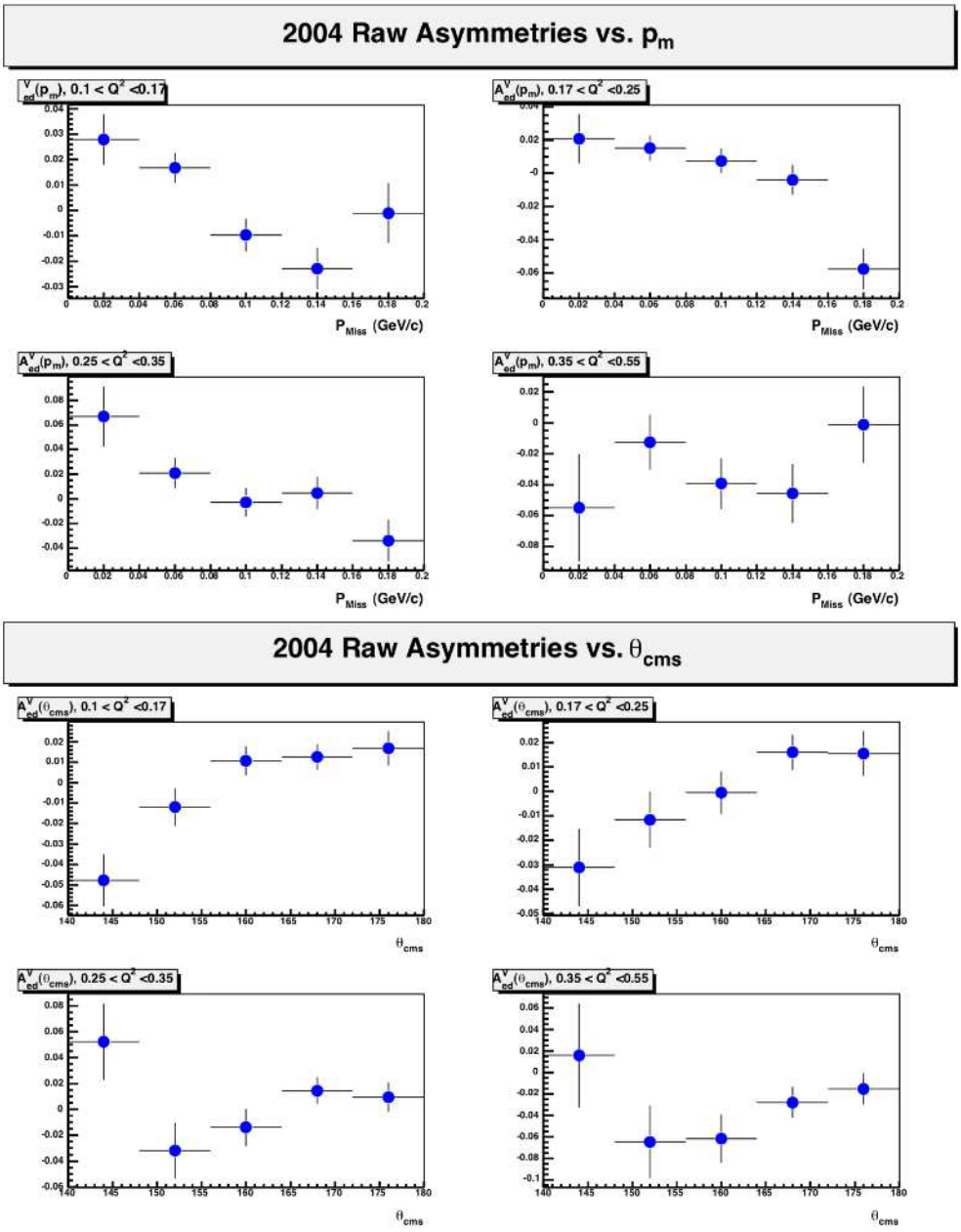

FIG. 4.13. These plots comprise the raw asymmetries, $A^V_{ed}(p_m)$ and $A^V_{ed}(\theta^{np}_{cms})$ from the data taken during the 2004 Configuration.

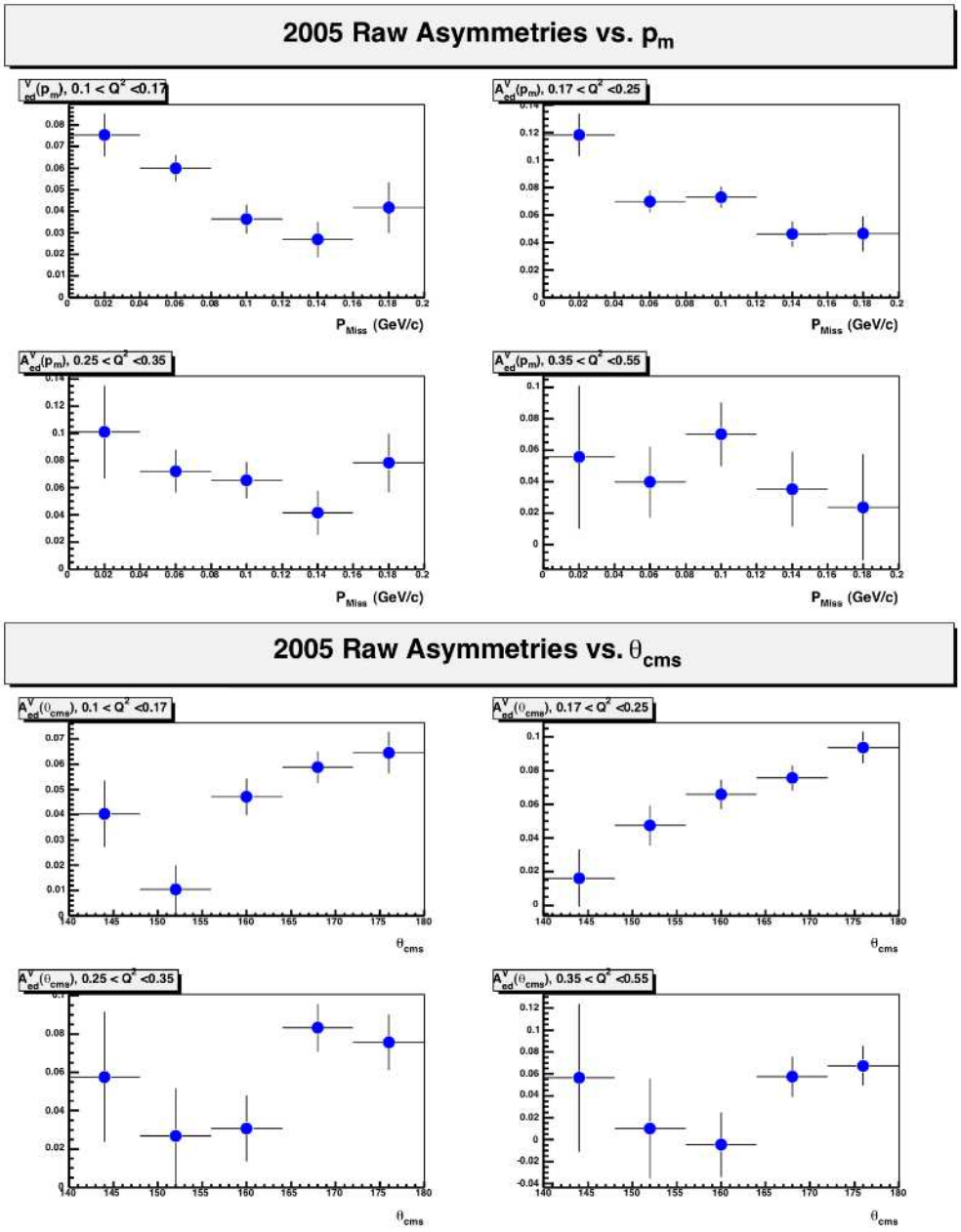

FIG. 4.14. These plots comprise the raw asymmetries, $A_{ed}^{V}(p_m)$ and $A_{ed}^{V}(\theta_{cms}^{np})$ from the data taken during the 2005 Configuration.

Aluminum cell can contribute electroscattered neutrons to the BLAST quasielastic electroscattered neutron sample. The background reaction, $Al(e,e'n)X$, would arise from the same region as the real data sample and can pass all cuts applied to the ${}^2\vec{H}(\vec{e},e'n)p$ reaction. The math used to correct the data is fairly simple. If we consider that we want the *real* asymmetry,

$$A^{Real} = \frac{\sum_i g_i n_i^{Real}}{\sum_i n^{Real}}, \tag{4.5}$$

where g_i corresponds to the six scalar coefficients specific to the asymmetry A_{ed}^V and n_i^{Real} refers to the column vector in eq. 4.3, then we must account for the fact that we are not measuring a pure sample but rather one contaminated with background events such as unpolarized quasielastic *e-n* events arising from electron scattering off of the cell wall. This means that we are not actually measuring A^{Real} but rather A^{Total} which is not made of a linear combination of n_i^{Real} but rather with $\sum_i(n_i^{Real} + n_B)$ where n_B is the background rate of $Al(e,e'n)X$ which is tallied with the *real* rate. The necessary correction is then

$$A^{Real} = A^{Total} \times (1 - f_{cell}), \tag{4.6}$$

where $f_{cell} = \frac{6n_B}{\sum_i(n_i^{Real}+n_B)}$. The actual measurement of f_{cell} can be seen in Figure 4.15 and has a maximum value of about 3.8% in the region of interest specific to this measurement of G_E^n. This number comes from the background rate *with* Hydrogen gas in the target since such a situation is obviously more related to the conditions of the experiment since we have a Deuterium gas target.[5] When factoring in the background correction, the exact correction is parameterized as a function of missing momentum since the background correction increases monotonically in missing momentum. The same parameterization is also done over θ_{cms} which is the other variable with which we will confirm the value of G_E^n.

[5]The yields from hydrogen were treated as suspect neutrons and beam-vector asymmetries were formed producing results that were consistent with zero. This also reaffirms there is negligible proton contamination.

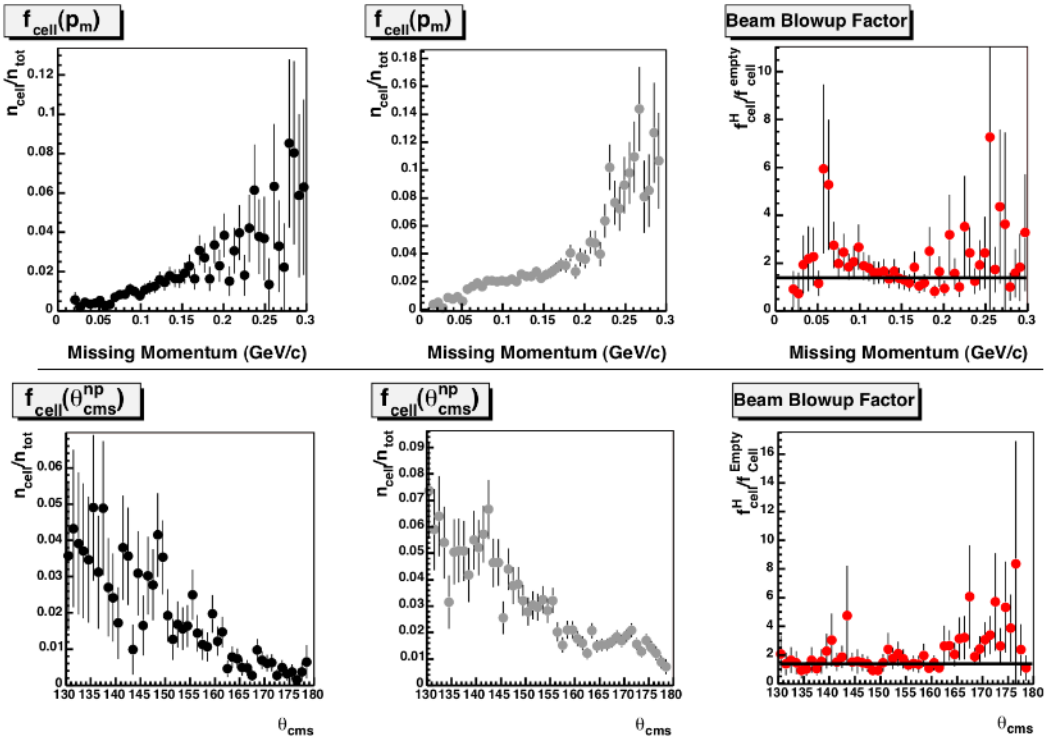

FIG. 4.15. The fraction of events arising from neutrons scattered from the cell wall are here depicted. Events were extracted from empty target runs and polarized hydrogen target runs where investigations are processed in order to determine the potential of contaminating $Al(e,e'n)X$ events in the data sample. $A_{ed}^{V}(p_m)$ is measured over a range, $0.0 < p_m \leq 0.2\frac{GeV}{c}$ and the maximum value of f_{cell} (which is normalized to the integrated charge, i.e. events/Coulomb) in the region of interest has a maximum of $\sim$3% for empty target runs, and a maximum of $\sim$4% for hydrogen runs. This is an example of how the gas inside the target affects the optical characteristics of the cell. The beam *blows up* slightly and more cell wall scattering is expected. The beam blowup factor comes from a fit on $f_{cell}^{H}/f_{cell}^{Empty}$ across the region from $0 < p_m < 0.3$ and gives a value of 1.38 ± 0.08. The exact same process is done for the background over θ_{cms}. The beam blowup is also fitted and confirms the fit from p_m at a ratio of 1.38 ± 0.09.

Since ideal quasielastic scattering occurs at $\theta_{cms} = 180°$, the background rate is decreasing from the region of $130 < \theta_{cms} < 180$. A fit was also done to determine the increase in the background rate with Hydrogen in the target and was found to agree with the fit from missing momentum, i.e. $f_{cell}^{H}/f_{cell}^{Empty} = 1.38 \pm 0.09$.

4.6.2. Polarized Background Correction. There is question of potential polarized background that needs to be verified. In order to carefully quantify the potential contamination of polarized electroscattered protons, we can analyze the Hydrogen data taken at BLAST as if it were our neutron data sample. Any contribution from this dataset would substantiate another correction to the measured asymmetry. Proton contamination constitutes a serious problem for the fact that the electron-proton coincidence rate is an order of magnitude larger than the electron-neutron rate, and further, the asymmetry specific to the polarized electron-proton coincidence events is more than three times as large and with an opposite sign.

The contribution from protons is assumed to be negligible since we have a continuous charge veto consisting of 18 layers of wires determined to have 98% efficiency per layer in detecting relativistic charged particles. This efficiency suggests that 6 layers of wires failing to detect a passing proton has a probability of less than a ten-thousandth of a percent. This makes our proton contamination negligible.

The actual background coming from polarized hydrogen runs is still from the cell wall, only there are slightly more scattered neutrons. The target's optical properties change when a gas is injected. The beam is expected to refract and blow up slightly, creating the possibility for more wall collisions. This is shown in Figure 4.15 along with the empty cell background. The value f_{cell} from the hydrogen target averages 1.38 times the value of the

empty target background rate. This is the *beam blowup factor* and is more valid for the raw asymmetry correction. The appropriate correction that will be used in eq. 4.6 is the value of f_{cell} from the hydrogen target.

4.7. Extraction of G_E^n from Corrected Asymmetries

The perpendicular asymmetry A_{ed}^V, in PWIA, is proportional to the ratio of the neutron's electric and magnetic form factors as shown in eqn. 2.52. The accepted realistic model of the deuteron is not as simple as PWIA and must account for the dynamic properties associated with final state interactions, meson exchange currents, and Δ-isobar excitation corrections as described in section 2.4.1. The validity of these modifications to the nuclear models of the deuteron are still controversial in some circles and some may propose that such changes must also be proven valid in order for results predicated on such modified models to be equally tenable. Such topics are beyond the scope of this paper but can be tersely addressed by noting the expectations of specific models and whether other measurements extracted from this experiment can verify the utility of the modifications to the model of the deuteron.

One measurement that lends credence to the Final State Interactions model, is the measurement of the tensor asymmetry from quasielastically scattered neutrons. In PWIA and PWBA pictures, the tensor asymmetry at conditions of perfect quasielastic scattering ($p_m = 0$ and $\theta_{cms}^{np} = 180$) are expected to be zero. This can be visualized as if we are striking a quasi-free neutron in a very loosely bound state with a proton. The final state interactions are calculated to be very small if the proton were struck and the tensor asymmetry goes to zero for ideal quasielastic protons[122], but the neutron has a finite asymmetry in the FSI model. In Figure 4.16 the data clearly shows consistency with the FSI models. The lowest

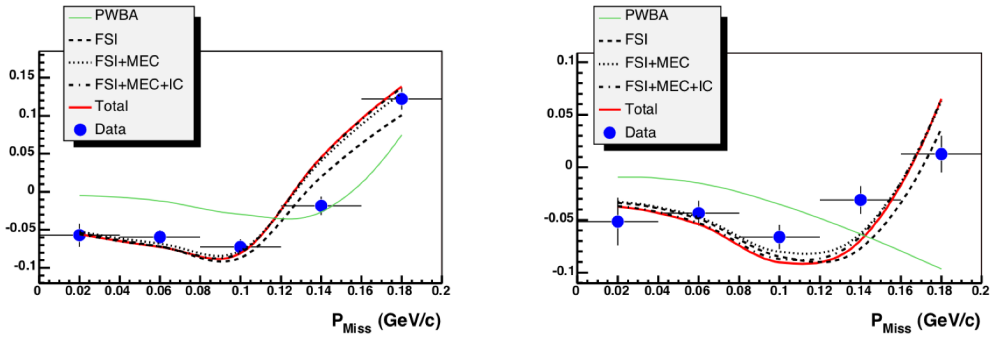

FIG. 4.16. This figure demonstrates the predictions of the simplistic Plane Wave Born Approximation as compared with modifications to the deuteron model, specifically Final State Interactions (FSI). In PWIA and PWBA, the asymmetry is expected to fall to zero at perfect quasielastic scattering, i.e. a missing momentum of zero. As soon as we inject the predictions of FSI into the model, the asymmetry becomes negative and reflects the actual data. These two plots show $A_d^T(p_m)$ as measured over a range, $0.0 < p_m \leq 0.2\frac{GeV}{c}$ within the the two lowest Q^2 bins chosen for the analysis of G_E^n. It is obvious from these plots that the FSI modification to the deuteron's model is a necessity in understanding the double polarized scattering cross-section as measured and analyzed from the data at BLAST.

two Q^2 bins are shown. As the momentum transfer increases, the difference between the PWBA and FSI models decreases and the statistics of the measurement also decrease. The points shown are obviously enough to demonstrate the value of the Final State Interactions when included into the nuclear model of the deuteron.

The vector asymmetries are measured over the kinematic variables missing momentum, p_m, and the opening angle between the proton and the momentum transfer in the center of momentum frame, θ_{cms}^{np}. Simulations within the Monte Carlo demonstrate that A_{ed}^V measured as a function of these variables gives the best sensitivity to the measurement of G_E^n. The final asymmetries, corrected for background and divided by the measured values for the product of the target and beam polarization (see Section 4.8.2), are displayed in Figures 4.17 and 4.18 along with the expected curves from Monte Carlo simulations for values of G_E^n that are parameterized as ratios of the well-known Galster parameterization [53] with $a = -\mu_n$ and $b = 5.6$. H. Arenhövel provided the deuteron model that was used

for the simulations (see Section 3.6).

Using the corrected values and the expectations of the vector asymmetries respective of the value of G_E^n used in the simulations of the BLAST experiment, a χ^2 minimization scheme is used to extract the value of G_E^n/G_M^n.

The Monte Carlo simulations provide five sets of expected results, each associated with a scale factor, a_k on the Galster Parameterization for G_E^n (see eq. 2.55). From each set, k, we can calculate a $\chi_j^2(a_k)$ for each Q^2 bin (indexed as j) where

$$\chi_j^2(a_k) = \sum_i \frac{(A_{exp}^i - A_{theory}^i)^2}{(\sigma_{exp}^i)^2}. \tag{4.7}$$

Again, j is the Q^2 bin, k is the index of the scale factor for the referenced Monte Carlo simulation, and now i corresponds to the five bins within the domain of A_{exp} whether we are plotting A_{exp} as a function of p_m or θ_{cms}^{np}. A_{theory}^i is the expected asymmetry from Monte Carlo and σ_{exp}^i is the associated experimental uncertainty of each bin.

The function $\chi_j^2(a_k)$ is expected to be parabolic about the minimum[125] and is parameterized over the five points for each Q^2 bin assuming a_k to be continuous, i.e.

$$\chi_j^2(a_k) = \tau_{min} + \frac{(a_k - \tau_1)^2}{(\tau_2 + a_k\tau_3)^2}. \tag{4.8}$$

There are four parameters to this fit represented by $\tau_{min,1,2,3}$. At the minimum, a_k^{min}, of the parameterized fit to the five values of $\chi_j^2(a_k)$ we can conclude that the value a_k^{min} best describes the actual value of G_E^n in reference to the model used in the BLAST Monte Carlo. The fit also delineates the statistical uncertainty in G_E^n as described by the relation

$$\chi_j^2(a_k^{min} + \delta a_k^{min}) = \chi_j^2(a_k^{min}) + 1. \tag{4.9}$$

where δa_k^{min} is the associated uncertainty in a_k^{min}. The fit to the five points in each Q^2 bin of the 2004 and 2005 data on A_{exp} as a function of both p_m and θ_{cms}^{np} are shown in Figures 4.19

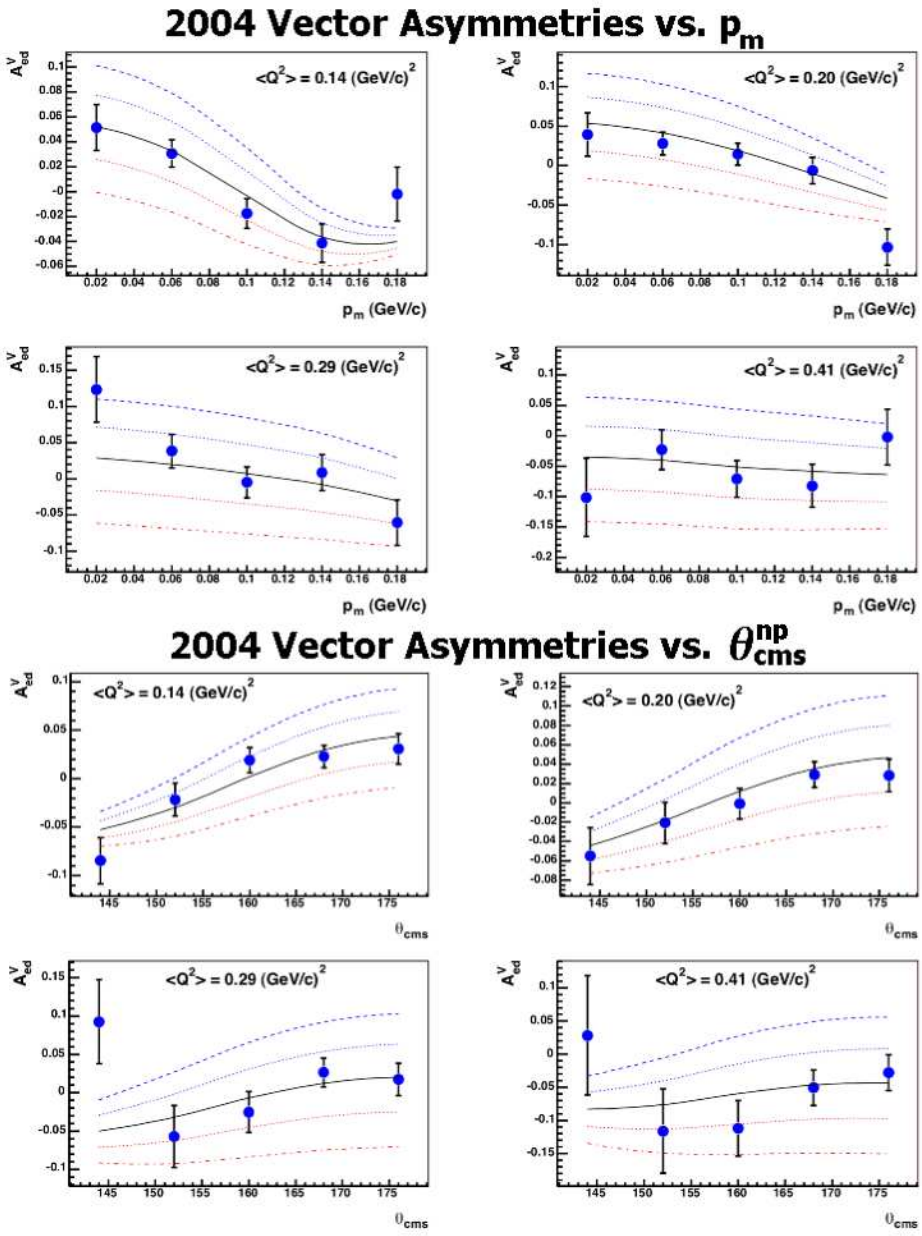

FIG. 4.17. These eight plots show A_{ed}^V, both as a function of missing momentum, p_m, and the center of momentum opening angle between the proton and the momentum transfer, θ_{cms}^{np}, within the four Q^2 bins chosen for the analysis of G_E^n. The product of the beam and target polarization has been divided out and all background corrections are included. The predictions from Monte Carlo using incremented ratios of the Galster parameterization for the value of G_E^n are also shown from 0%-200% with the highest expected value for G_E^n demonstrating the most positive asymmetry. Error bars in the plots are statistical only.

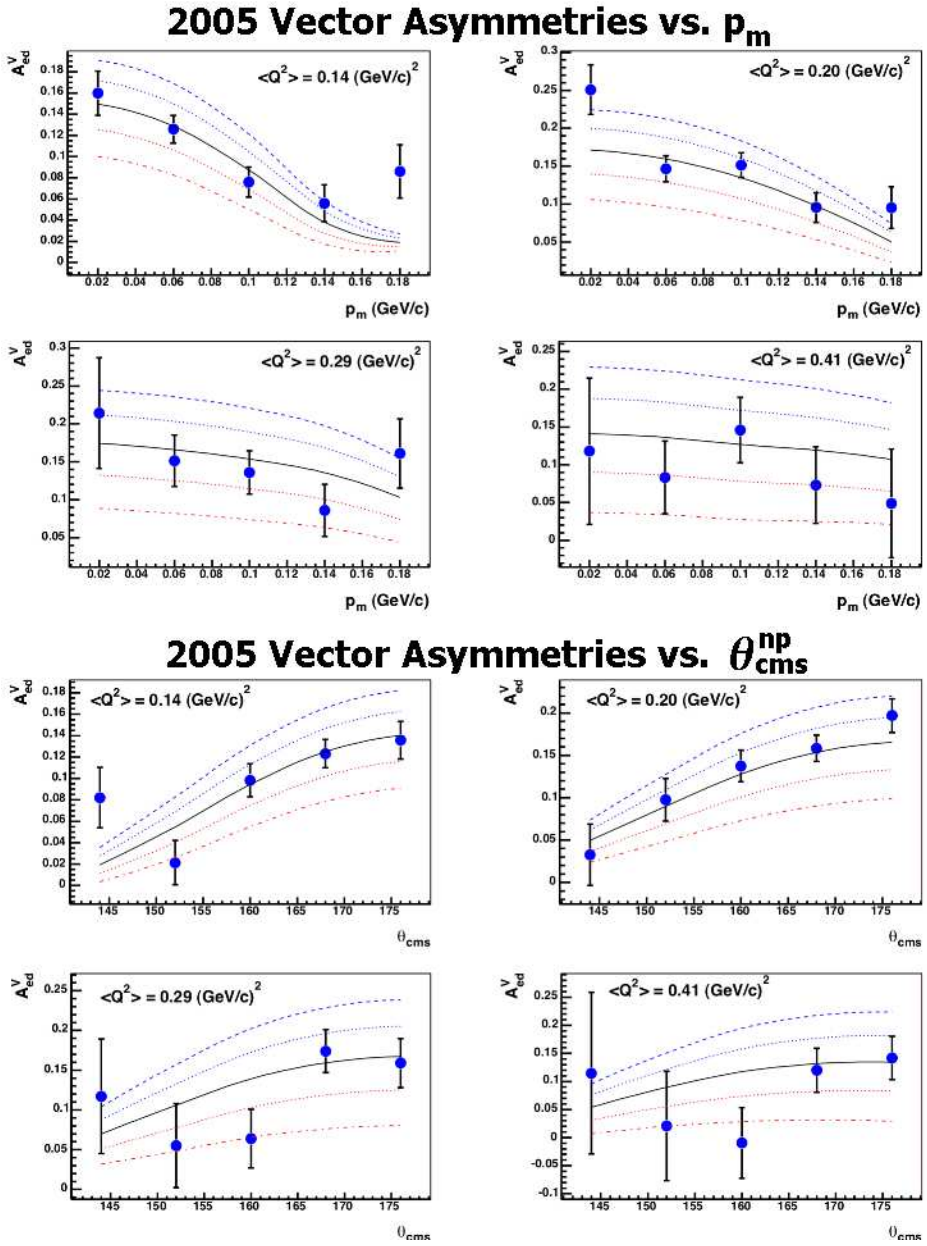

FIG. 4.18. These eight plots show A_{ed}^V, both as a function of missing momentum, p_m, and the center of momentum opening angle between the proton and the momentum transfer, θ_{cms}^{np}, within the four Q^2 bins chosen for the analysis of G_E^n. The product of the beam and target polarization has been divided out and all background corrections are included. The predictions from Monte Carlo using incremented ratios of the Galster parameterization for the value of G_E^n are also shown from 0%-200% with the highest expected value for G_E^n demonstrating the most positive asymmetry. Error bars in the plots are statistical only.

TABLE 4.3. The measured values of A_{ed}^V as a function of missing momentum and θ_{cms}^{np}. The systematic error is approximately 3% and is a convolution of the uncertainty of hP_z and the binning as defined by Q^2, p_m, and θ_{cms}^{np} (see Section 4.8).

2004								
$\langle Q^2 \rangle$ $(GeV/c)^2$	$\langle p_m \rangle$ (GeV/c)	A_{ed}^V Corrected	δA_{ed}^V Statistical	ΔA_{ed}^V Systematic	$\langle \theta_{cms}^{np} \rangle$ $(degrees)$	A_{ed}^V Corrected	δA_{ed}^V Statistical	ΔA_{ed}^V Systematic
	0.029	0.0515	0.0184	0.0019	144	-0.0846	0.0238	0.0031
	0.061	0.0306	0.0110	0.0011	152	-0.0214	0.0171	0.0007
0.141	0.099	-0.0176	0.0119	0.0007	160	0.0194	0.0130	0.0007
	0.138	-0.0413	0.0153	0.0015	168	0.0230	0.0115	0.0009
	0.177	-0.0020	0.0218	0.0001	174	0.0308	0.0156	0.0011
	0.029	0.0384	0.0274	0.0014	144	-0.0551	0.0295	0.0020
	0.062	0.0279	0.0143	0.0010	152	-0.0207	0.0215	0.0008
0.203	0.099	0.0136	0.0139	0.0005	160	-0.0009	0.0159	0.00003
	0.138	-0.0071	0.0166	0.0003	168	0.0292	0.0132	0.0011
	0.178	-0.1034	0.0228	0.0038	174	0.0284	0.0168	0.0011
	0.029	0.1236	0.0452	0.0046	144	0.0926	0.0548	0.0034
	0.062	0.0382	0.0230	0.0014	152	-0.0570	0.0401	0.0021
0.293	0.100	-0.0050	0.0215	0.0002	160	-0.0252	0.0268	0.0009
	0.139	0.0084	0.0249	0.0003	168	0.0264	0.0190	0.0010
	0.178	-0.0606	0.0317	0.0022	174	0.0173	0.0212	0.0006
	0.029	-0.1015	0.0643	0.0038	144	0.0283	0.0899	0.0010
	0.062	-0.0229	0.0329	0.0008	152	-0.1160	0.0633	0.0043
0.410	0.099	-0.0711	0.0303	0.0026	160	-0.1119	0.0419	0.0041
	0.138	-0.0824	0.0352	0.0030	168	-0.0508	0.0267	0.0019
	0.177	-0.0020	0.0458	0.0001	175	-0.0281	0.0272	0.0010

TABLE 4.4. The measured values of A_{ed}^{V} as a function of missing momentum and θ_{cms}^{np}. The systematic error is approximately 3% and is a convolution of the uncertainty of hP_z and the binning as defined by Q^2, p_m, and θ_{cms}^{np} (see Section 4.8).

2005								
$\langle Q^2 \rangle$ $(GeV/c)^2$	$\langle p_m \rangle$ (GeV/c)	A_{ed}^{V} Corrected	δA_{ed}^{V} Statistical	ΔA_{ed}^{V} Systematic	$\langle \theta_{cms}^{np} \rangle$ $(degrees)$	A_{ed}^{V} Corrected	δA_{ed}^{V} Statistical	ΔA_{ed}^{V} Systematic
	0.029	0.1598	0.0210	0.0068	144	0.0821	0.0282	0.0035
	0.060	0.1258	0.0130	0.0054	152	0.0214	0.0206	0.0009
0.141	0.099	0.0758	0.0142	0.0032	160	0.0983	0.0153	0.0042
	0.138	0.0558	0.0175	0.0024	168	0.1232	0.0132	0.0052
	0.177	0.0859	0.0251	0.0037	174	0.1358	0.0176	0.0057
	0.029	0.2509	0.0328	0.0011	144	0.0327	0.0363	0.0014
	0.062	0.1466	0.0172	0.0062	152	0.0976	0.0254	0.0042
0.203	0.099	0.1516	0.0162	0.0065	160	0.1374	0.0186	0.0058
	0.138	0.0956	0.0195	0.0041	168	0.1583	0.0156	0.0067
	0.178	0.0955	0.0275	0.0041	174	0.1970	0.0199	0.0084
	0.030	0.2141	0.0730	0.0091	144	0.1171	0.0722	0.0050
	0.062	0.1514	0.0339	0.0064	152	0.0551	0.0529	0.0023
0.286	0.100	0.1361	0.0286	0.0058	160	0.0640	0.0369	0.0027
	0.138	0.0860	0.0343	0.0037	168	0.1740	0.0269	0.0074
	0.178	0.1610	0.0455	0.0069	174	0.1589	0.0309	0.0068
	0.030	0.1180	0.0969	0.0050	144	0.1147	0.1440	0.0049
	0.062	0.0833	0.0480	0.0035	152	0.0209	0.0973	0.0009
0.410	0.100	0.1460	0.0432	0.0062	160	-0.0095	0.0627	0.0004
	0.138	0.0732	0.0508	0.0031	168	0.1201	0.0393	0.0051
	0.178	0.0488	0.0718	0.0021	175	0.1417	0.0385	0.0060

and 4.20. The results of the data are listed in the table 4.5. The final column within the table comes from the minimum of the parabolic fit and has a value that demonstrates the ability of the data to fit the model from which we generate the Monte Carlo that forms a basis for our extraction of the neutron's electric form factor. This is divided by the *number of degrees of freedom*, *ndf*, and shows that there is not a demonstrably significant deviation from the theoretical model. The points that stray from the model and significantly skew the values of χ^2/ndf have the lowest statistical weight within each Q^2 bin and lie the furthest from ideal quasielastic neutrons. They are not excluded in order to preserve consistency and scientific integrity. The G_E^n points are plotted in figure 4.21.

4.8. Systematic Uncertainties

The beauty of the BLAST experiment is the simultaneous measurement and analysis of several reaction channels that, together, minimize the systematic uncertainties of each other. Of the two largest systematic uncertainties (hP_z, θ^*), the coefficient of the multiple of beam and target polarization, hP_z, is best identified using the quasielastic ${}^2\vec{H}(\vec{e}, e'p)n$ channel. The target polarization angle, θ^*, is best derived from the elastic ${}^2\vec{H}(\vec{e}, ed)$ channel. All other systematics are intrinsic to the detectors, statistics, and internal processes such as radiative corrections that cannot be eschewed from the data. For clarity, statistical errors or intrinsic resolutions will be prefixed by δ, whereas *systematic* errors will be referred to with a Δ prefix, e.g. δp_e would refer to the resolution of the reconstructed momentum of the electron, while $\Delta\phi_e$ would refer to a systematic shift in the measurement of the reconstruction of the electron's azimuthal angle.

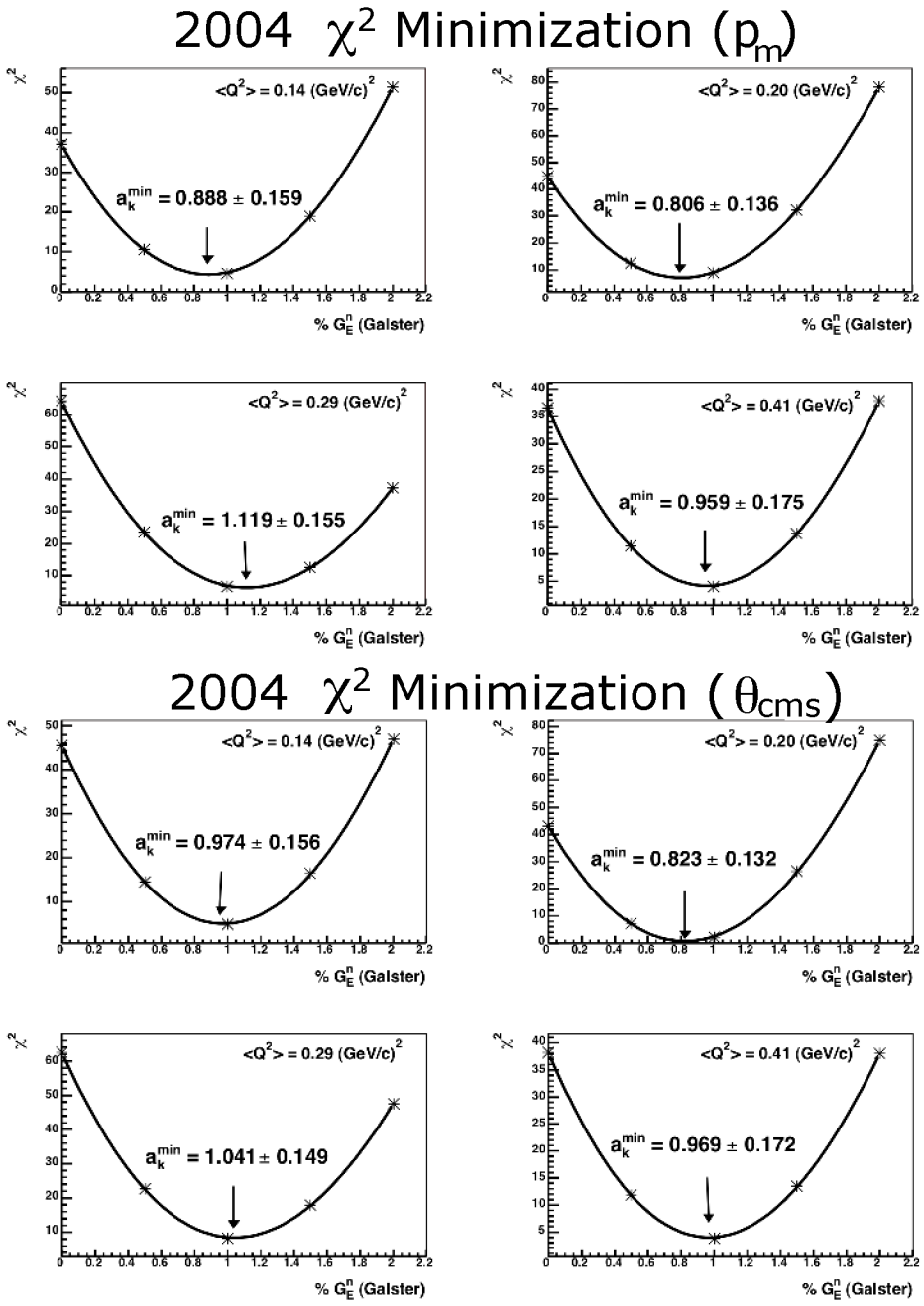

FIG. 4.19. These eight plots show the χ^2 Minimization for the asymmetries measured, both as a function of missing momentum, p_m, and the center of momentum opening angle between the proton and the momentum transfer, θ^{np}_{cms}, within the four Q^2 bins chosen for the analysis of G^n_E. The predictions from Monte Carlo using incremented ratios of the Galster parameterization for the value of G^n_E are used to determine the χ^2 at the five scaled points in G^n_E. These are then fit to the parameterization in eq. 4.8 to determine the best fit for the value of G^n_E.

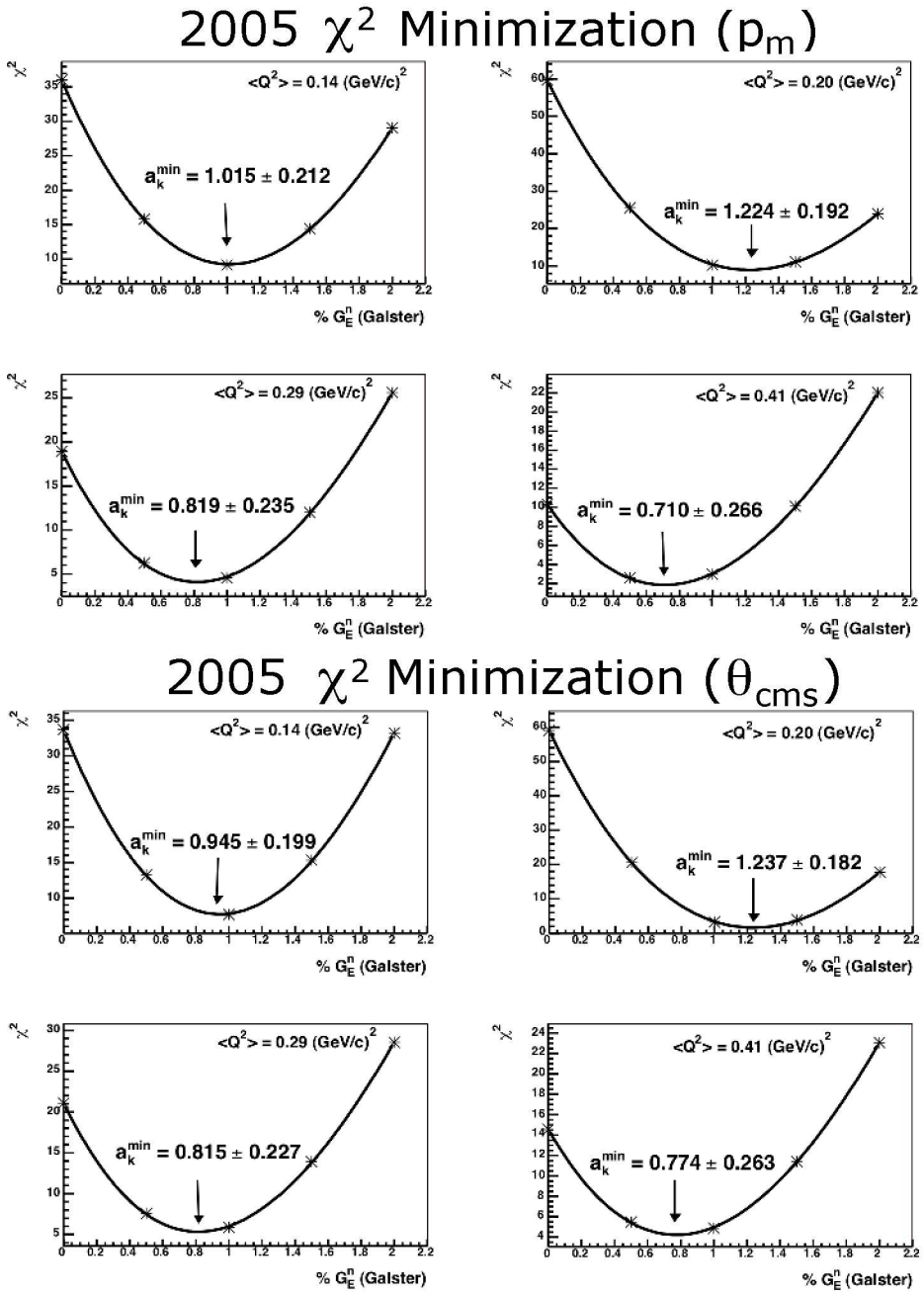

FIG. 4.20. These eight plots show the χ^2 Minimization for the asymmetries measured, both as a function of missing momentum, p_m, and the center of momentum opening angle between the proton and the momentum transfer, θ^{np}_{cms}, within the four Q^2 bins chosen for the analysis of G^n_E. The predictions from Monte Carlo using incremented ratios of the Galster parameterization for the value of G^n_E are used to determine the χ^2 at the five scaled points in G^n_E. These are then fit to the parameterization in eq. 4.8 to determine the best fit for the value of G^n_E.

TABLE 4.5. Results of the BLAST experiment. G_E^n is listed as measured from asymmetries as a function of p_m and θ_{cms}^{np} from 2004 and 2005 data as well as the combined data from both years.

$\langle Q^2 \rangle \left(\frac{GeV}{c}\right)^2$	G_E^n	δG_E^n (stat)	ΔG_E^n (sys)	$\chi^2/(ndf = 4)$
2004 p_m				
0.14	0.0387	0.0069	0.0022	1.09
0.20	0.0406	0.0068	0.0024	1.73
0.29	0.0608	0.0084	0.0035	1.58
0.41	0.0518	0.0095	0.0030	1.05
2004 θ_{cms}^{np}				
0.14	0.0424	0.0068	0.0025	1.25
0.20	0.0415	0.0066	0.0024	0.17
0.29	0.0565	0.0081	0.0033	2.12
0.41	0.0524	0.0093	0.0030	1.00
2005 p_m				
0.14	0.0441	0.0092	0.0026	2.30
0.20	0.0616	0.0097	0.0036	2.24
0.29	0.0443	0.0127	0.0026	1.02
0.41	0.0382	0.0143	0.0022	0.46
2005 θ_{cms}^{np}				
0.14	0.0411	0.0086	0.0024	1.92
0.20	0.0622	0.0092	0.0036	0.40
0.29	0.0441	0.0123	0.0026	1.33
0.41	0.0416	0.0141	0.0024	1.05
2004 & 2005 Combined, p_m				
0.14	0.0406	0.0055	0.0024	na
0.20	0.0476	0.0056	0.0028	na
0.29	0.0558	0.0070	0.0032	na
0.41	0.0477	0.0079	0.0028	na
2004 & 2005 Combined, θ_{cms}^{np}				
0.14	0.0419	0.0053	0.0024	na
0.20	0.0486	0.0054	0.0028	na
0.29	0.0528	0.0068	0.0031	na
0.41	0.0492	0.0078	0.0029	na

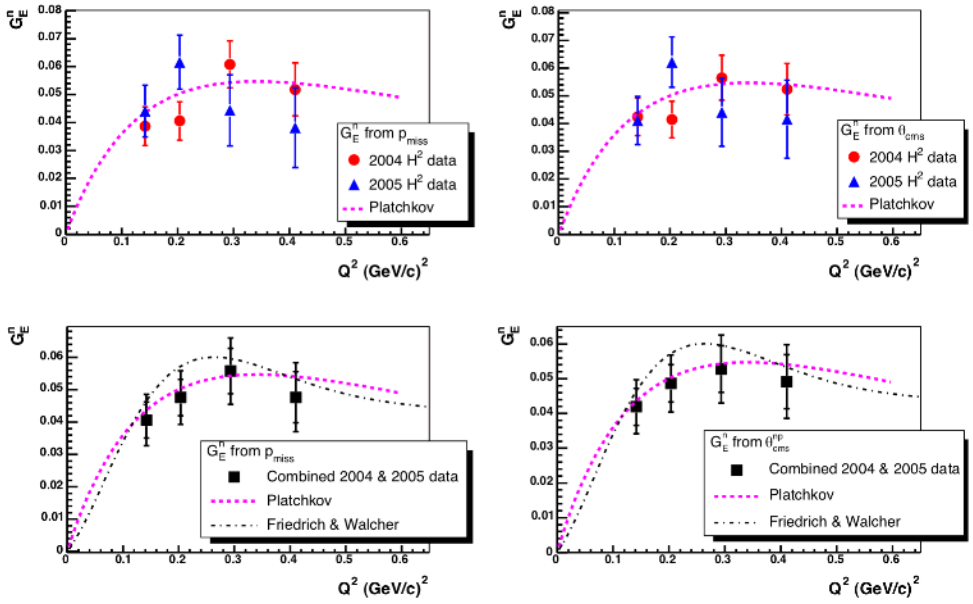

FIG. 4.21. The points listed in Table 4.5 are plotted here. The statistical errors are shown in the plots showing 2004 and 2005 data superimposed. The statistical and systematic errors are displayed in the combined plots. Systematic errors are described fully in the following section 4.8. Results from the analysis in missing momentum and the opening angle in the center of momentum frame between the proton and momentum transfer are shown.

TABLE 4.6. A tabulation of the systematic errors in the BLAST Experiment and the resultant measurement of G_E^n.

Source of Systematic Error	Contribution
Target Polarization Angle, θ^S	5%
Product of Beam and Target Polarization, hP_z	1.2%
Reconstruction, $(Q^2, p_m, \theta_{cms}^{np})$	1%
Cut Dependence, $\lvert M_m - M_p \rvert \leq n\sigma$	1.5%
Uncertainty of G_M^n	1.5%
Radiative Corrections	0.7%
False Asymmetries	1%
Total	5.8%

4.8.1. Target Polarization Angle. As mentioned earlier, the precise analysis that gives us a best fit for the polarization angle of the target comes from the elastic $^2\vec{H}(\vec{e}, ed)$ channel. The two lowest Q^2 points in the asymmetries A_d^T as measured simultaneously in both, the parallel and perpendicular kinematics sector, were used to simultaneously fit for the tensor polarization P_{zz} and for the spin angle θ^S. This determination of θ^S may be the most important determination as the sensitivity of G_E^n is estimated at 12%/degree.

Two asymmetries, $A_{raw}^{\parallel}$ and $A_{raw}^{\perp}$ were measured and compared with Monte Carlo to determine the tensor polarization P_{zz} coefficient. Mathematically,

$$P_{zz}^{\parallel}(\theta^S) = \frac{A_{raw}^{\parallel}}{A_{MC}^{\parallel}} \qquad \text{and} \qquad P_{zz}^{\perp}(\theta^S) = \frac{A_{raw}^{\perp}}{A_{MC}^{\perp}}, \tag{4.10}$$

and finding the average value $\bar{\theta}^S$ where $P_{zz}^{\parallel}(\bar{\theta}^S) = P_{zz}^{\perp}(\bar{\theta}^S)$ would give us the spin angle of the deuterium target. The error in the determination is estimated by the confidence interval where the end points are,

$$\chi = \frac{P_{zz}^{\parallel}(\theta^S) - P_{zz}^{\perp}(\theta^S)}{\sqrt{[\delta P_{zz}^{\parallel}(\theta^S)]^2 + [\delta P_{zz}^{\perp}(\theta^S)]^2}} = \pm 1. \tag{4.11}$$

The procedure is noted in Figure 4.22. The values determined from the fit are $P_{zz} = 0.683 \pm 0.015 \pm 0.02$, $\bar{\theta}^S = 31.72 \pm 0.35 \pm 0.2$ in 2004 and $P_{zz} = 0.563 \pm 0.013 \pm 0.02$, $\bar{\theta}^S = 47.74 \pm 0.42 \pm 0.2$ in 2005 [83]. The errors here are statistical and systematic, respectively. Systematic errors in the determination of P_{zz} and θ^S follow from the resolution in reconstruction that went into the calculation of Q^2 since the asymmetries used were measured as a function of Q^2. The sensitivity of G_E^n to the polarization angle describes the largest contribution to the systematic error and is estimated at 5%.

4.8.2. Product of Beam and Target Polarization. The cross-section and the respective normalized yields that contribute to the measurement of the asymmetries in

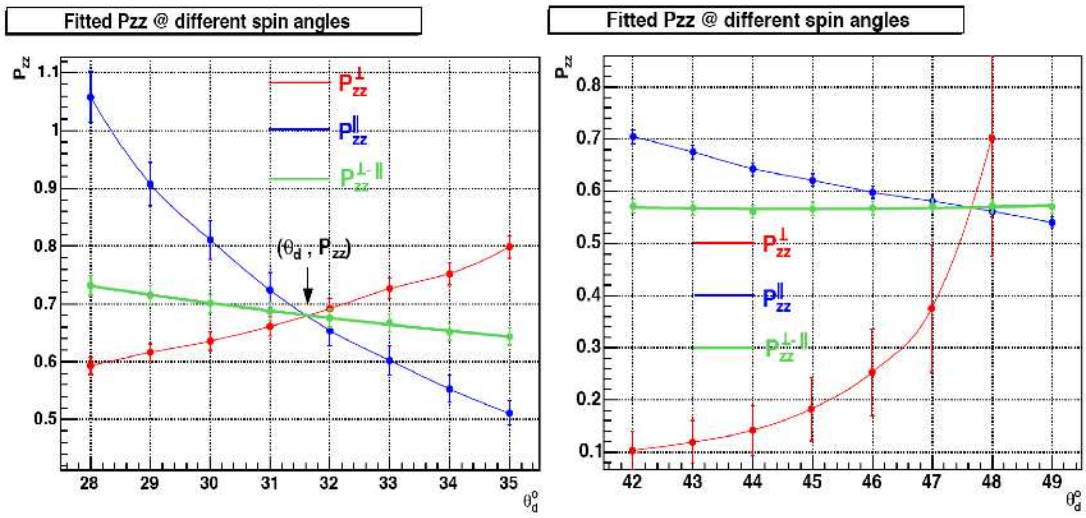

FIG. 4.22. The Monte Carlo was generated at spin angles of 1° increments in order to find the Asymmetry used to calculate the tensor polarization P_{zz} as a function of the spin angle for both datasets, 2004 (left) and 2005 (right). Where both, the parallel and perpendicular kinematics sectors cross is the best fit for the spin angle θ^S.

this experiment are directly proportional to the product of the beam polarization and the vector polarization of the target. Again, the simultaneity of the use of the double-polarized cross section of quasielastic protons and elastically scattered deuterons provides us with a unique ability to better measure values that exclusive detection of the neutron channel could severely limit our ability to estimate.

The estimate of this product, hP_z as referenced in eq. 2.52 (equations 2.46-2.50 are also each proportional to hP_z), is extracted from the well-known asymmetry of the quasielastically scattered protons. The procedure is quite simple. Monte Carlo is generated and expected asymmetries for the BLAST acceptance are calculated as a function of missing momentum. A^V_{ed} is then measured. Since the calculation and measurement are expected to be directly proportional to one another, the two highest statistics points lowest in missing momentum and the least affected by modifications to the deuteron model are scaled to match the Monte Carlo to the data. This exact ratio is our value of hP_z within the accuracy of

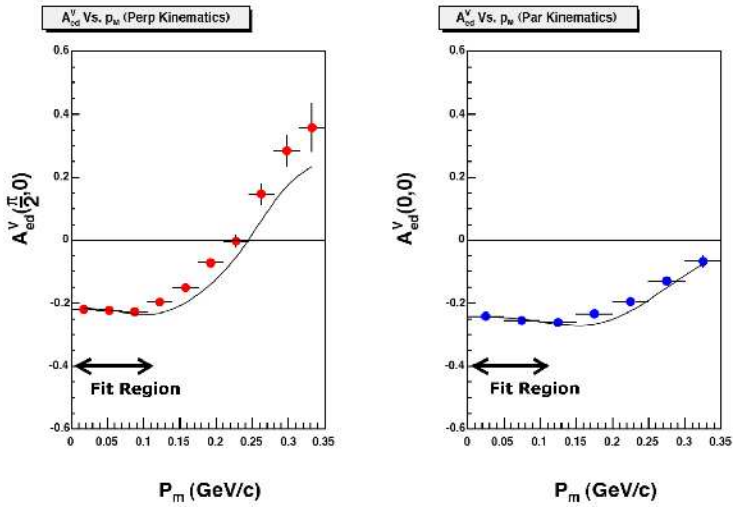

FIG. 4.23. A highly accurate fit is obtained from the vector asymmetry where the well-known form factors are used to calculate the cross-section for electroscattered quasielastic protons. In order to restrict the contributions from lesser known inelastic modifications to the proton's scattering matrix, the fit is restricted to the points below 0.15 GeV/c. The results for the 2004, 32 degree vector polarized target configuration gives a value, $hP_z = 0.541 \pm 0.0035(stat.) \pm 0.02(sys.)$. The results for the fits to 2005, 47 degree configuration gives a value of $hP_z = 0.468 \pm 0.0046(stat.) \pm 0.02(sys.)$.

the fit. The fit is performed over the first few points in missing momentum ($< 0.15 GeV/c$) in order to minimize the contributions from inelastic effects. The values for the 2004 and 2005 configurations are done separately and give values:

$$hP_z^{2004} = 0.541 \pm 0.0035(stat.) \pm 0.02(sys.),$$

$$hP_z^{2005} = 0.468 \pm 0.0046(stat.) \pm 0.02(sys.).$$

The demonstration of this measurement and fit are shown in Figure 4.23. A similar fit can also be performed as a function of the parallel kinematics asymmetries in the $^2\vec{H}(\vec{e}, e'n)p$ channel. The systematic error is a result of the use of the measured spin angle and the resolution of the reconstructed variables.

The vector asymmetry of the $^2\vec{H}(\vec{e}, e'n)p$ channel, A^V_{ed}, is completely dominated by the magnetic form factor of the neutron in the parallel kinematics sector where the

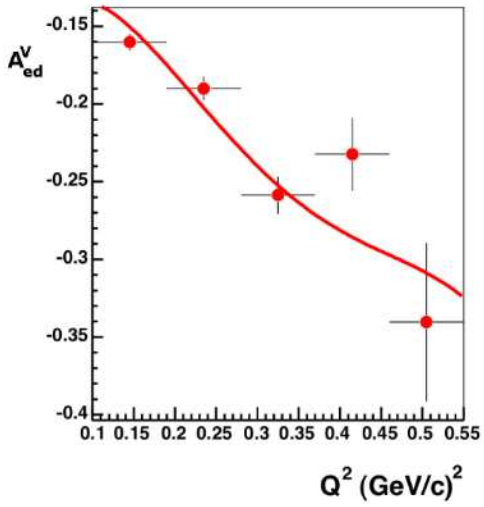

FIG. 4.24. An analogous but less accurate fit is obtained from the asymmetries in the parallel kinematics sector where the contribution from the neutron's magnetic form factor dominates. The fit gives a value, $hP_z = 0.547 \pm 0.012$, confirming the fit from quasielastic proton asymmetries.

momentum-transfer is nearly parallel with the angle of polarization. This quantity G_M^n is very well-known compared to G_E^n. An analogous procedure is followed where Monte Carlo simulations are used to calculate the asymmetry and then scaled to match the measurement in the data sample (see Figure 4.24. The fit from quasielastic neutrons in the parallel sector are consistent with the fit from quasielastic protons (see Figure 4.23). The systematic error associated with hP_z, before rounding is slightly less than 4% and translates linearly into the systematic error of the measured asymmetries. This value is revisited at the end of the following section in order to be more complete in the estimation of the systematic error of the vector asymmetry, ΔA_{ed}^V.

4.8.3. Reconstruction. The errors in p_e and θ_e are best estimated using the outgoing particles from the $H(e, ep)$ reaction channel. Using coplanar coincident electrons and protons, energy and momentum constraints allow for Gaussian fits of the distributions of $\theta_e(\theta_p^{exp}) - \theta_e^{exp}$ and $p_e(p_p^{exp}) - p_e^{exp}$. The relationship can also be done in reverse, i.e. finding

the distributions for the proton kinematics that are reconstructed. The resultant resolutions give $\delta\theta_e = 0.43^\circ$ and $\delta p_e = 0.037 GeV/c$.

Estimating the systematic errors ($\Delta\theta_e$ and Δp_e), we must assume that the proton channel is perfect and then estimate the error in the electron's kinematics. For $\Delta\theta_e$, the quantity we use is the difference of $Q^2(\theta_e)$ and $Q^2(\theta_p)$ which, again, are calculable from the outgoing polar angle. For the BLAST ep-elastic data $|Q^2(\theta_e) - Q^2(\theta_p)| = 0.0015$, which gives an underlying systematic error of $\Delta\theta_e \approx 0.1^\circ$. Since θ_p and θ_e are the most well determined variables in the BLAST experiment, it only makes sense to use them for determination of the systematic error in p_e as well, using the same difference in Q^2. $|Q^2(p_e) - Q^2(\theta_p)| = 0.0028$. This difference corresponds to an estimated systematic error $\Delta p_e \approx 0.004$ GeV/c.

The azimuthal errors can be found using very similar means, and $\delta\phi_e \approx 0.3^\circ$ comes from a Gaussian fit to the coplanarity, i.e. the $|\phi_e - \phi_p|$ distribution. The difference of the mean from 180° allows description of the systematic error, $\Delta\phi_e \approx 0.2^\circ$.

To characterize the uncertainty in the neutron's kinematics, namely the momentum, the timing resolution, δt_n, of the neutron detectors is the descriptive quantity. It has been measured at $\sim$4 nanoseconds. The kinematics of a quasielastic collision are used along with energy and momentum constraints to calculate the time of flight of the neutron, t_n^{calc} and compare it to the measured time of flight, t_n. The beam energy and acceptance at BLAST provides the capability of detecting neutrons up to a momentum of 900 MeV/c. The resolution of the neutron timing, $\delta t_n = 4$ ns, corresponds to almost 23% of a neutron's momentum at 750 MeV/c and only 8% at a momentum of 300 MeV/c. Since the measured momentum of the neutron is actually a calculation derived from the measured time of flight, the equation governing the uncertainty arises from the uncertainty in t_n, the neutron's time

of flight,

$$\frac{\delta p_n}{p_n} = \left(1 + \beta^2\gamma^2\right)\frac{\delta t_n}{t_n}. \tag{4.12}$$

This uncertainty is by far the largest loss of resolution in the reconstruction of the kinematics of the neutron channel when at high momentum. The relatively high uncertainty in the time of flight also receives a contribution from the thickness of the neutron detectors. There is no method by which we can determine where, along 20 cm thickness of scintillating material, the nuclear reaction that renders the neutron detectable is actually observed. This discrete space (the scintillating bar) also creates the lack of resolution, relative to the electron, in the polar and azimuthal angles. At low momentum, the uncertainty of the neutron's momentum more than doubles the resolution of the electron's momentum ($\delta p_e \approx 3\%$). The systematic error involved with the neutron's momentum is a convolution of the systematic error of the remaining five kinematic variables used to determine the systematic corrections to the neutron's time of flight as described in section 3.4.4 since systematic deviations from expected results were corrected through a detailed process. The timing of the neutron detectors were calibrated using the exact same process utilizing cosmic rays as is described in Figure 3.29. From these timing offsets, the calculated time of flight, t_n^{calc}, derived from the kinematics of quasielastic scattering was compared to the actual measured time of flight, t_n, and any remaining deviations were removed. The corrections to t_n were determined from the expected momentum of the neutron calculated from all other kinematic variables along with constraint of the missing mass being the mass of the proton, i.e. $t_n = f(p_e, \theta_e, \phi_e, \theta_n, \phi_n, M_m = M_p)$. The systematic error is obviously a convolution of all of these individual errors, e.g.

$$\Delta t_n = \frac{\delta f}{\delta p_e}\Delta p_e + \frac{\delta f}{\delta \theta_e}\Delta\theta_e + \ldots \tag{4.13}$$

The convolution of all systematic errors, $\Delta t_n(\Delta p_e, \Delta\theta_e, \Delta\phi_e, \Delta\theta_n, \Delta\phi_n)/t_n \approx$ 2-5%. This percentage is actually maximized at low momentum and contributes to a systematic error of $\Delta p_n \approx 0.030$ GeV/c in our first Q^2 bin, but drops to $\Delta p_n \approx 0.014$ GeV/c at the highest values of Q^2 allowable within the BLAST acceptance. As ω, β_n, and γ_n increase, the effective contribution of the electron's systematic errors decreases.

The neutron's uncertainty in the polar angle comes directly from the discrete assignment of polar angle as a function of the bar that detected the neutron and the origin along the target where the trace of the path of the neutron's flight begins. The only potential systematic in the neutron's polar angle is the trigonometric convolution of any systematic error in the reconstruction of the electron's vertex or origin along the target's axis, Δz_e. Using the *ep*-elastic dataset again, we notice that the mean of the distribution, $z_e - z_p$ is approximately 0.5 cm. Being conservative and attributing this entirely to the electron, the systematic error $\Delta\theta_n(\Delta z_e) \approx 0.1^\circ$.

The neutron's systematic error in ϕ_n can also be analyzed in reference to the electron's known deviations. Though we are analyzing *quasielastic* events, the coplanarity or difference of the azimuthal angles of the coincident electrons and neutrons should still center itself on 180°. Plotting $|\phi_e - \phi_n|$, our mean is centered at 180.3°. This gives an estimate of $\Delta\phi_n(\Delta\phi_e) \approx 0.2^\circ$.

Table 4.7 gives the uncertainties of the reconstructed variables used in the analysis of ${}^2\vec{H}(\vec{e}, e'n)p$ in the BLAST experiment. The asymmetries are sequestered into four bins in Q^2 where the convoluted uncertainty is $\delta Q^2/Q^2 \approx 1\%$. These vector asymmetries are then plotted over five bins in missing momentum and the center of momentum opening

[6]Percentage comes from $\delta p_n/p_n$, and the resolution of the decreases as the momentum of the neutron increases. The resolution of the time of flight of the neutron does not change yet its contribution to the uncertainty of the momentum of the neutron increases as β_n increases.

[7]Percentage comes from $\Delta p_n/p_n$, but the systematic error decreases monotonically as the momentum of the scattered neutron increases.

TABLE 4.7. The resolution of the reconstructed kinematics are listed here. The inability to track and measure the precise time and space of the neutron's reaction with the scintillating material creates a relatively large uncertainty in the neutron's kinematics when compared to the electron.

Electron			*Neutron*		
quantity	δ	Δ	variable	δ	Δ
p_e	0.037 GeV/c	0.004 GeV/c	p_n	8-25%[6]	2-10%[7]
θ_e	0.4°	0.1°	$\delta\theta_n$	1.5°	0.1°
ϕ_e	0.3°	0.2°	$\delta\phi_n$	1.5°	0.2°

angle between the outgoing proton and the momentum transfer, of which the convoluted respective uncertainties are $\delta p_m/p_m \approx 2\%$ and $\delta\theta^{np}_{cms} \approx 0.2^\circ$. The asymmetries carry a systematic error based on the uncertainties, $\delta Q^2, \delta p_m$, and $\delta\theta^{np}_{cms}$, and it can be denoted by $\Delta A_{exp}(\delta Q^2, \delta p_m)$ or $\Delta A_{exp}(\delta Q^2, \delta\theta^{np}_{cms})$. The systematic errors from the lowest to the highest bins of Q^2 as well as the bins of the domain of the asymmetries will be correlated. The quantification of errors for the asymmetries as a function of p_m and θ^{np}_{cms} are written as ΔA^{pm}_{exp} and ΔA^{θ}_{exp}, respectively and follow as such,

$$\begin{aligned}
\Delta A^{pm}_{exp} &= \frac{\Delta hP_z}{hP_z} A^{pm}_{exp} + \frac{\partial A^{pm}_{exp}}{\partial p_m}\Delta^* p_m + \frac{\partial A^{pm}_{exp}}{\partial Q^2}\Delta^* Q^2, \\
\Delta A^{\theta}_{exp} &= \frac{\Delta hP_z}{hP_z} A^{\theta}_{exp} + \frac{\partial A^{\theta}_{exp}}{\partial \theta^{np}_{cms}}\Delta^* \theta^{np}_{cms} + \frac{\partial A^{\theta}_{exp}}{\partial Q^2}\Delta^* Q^2,
\end{aligned} \tag{4.14}$$

where Δ^* denotes the differential rather than a systematic error. The calculated values for the derivative of the asymmetry with respect to the domain on which it is plotted is a maximum within the first Q^2 bin, while the change in the asymmetry as a function of Q^2 is quite small in the lowest bin and much larger in the highest bin where the effects of the neutron's magnetic dipole moment begin overwhelming the sensitivity to the charge distribution. The relative balance between the terms serves to prevent any excessive change in the calculated systematic uncertainty over the probed phase space of the experiment. The uncertainty of the experimental asymmetry is dominated by the uncertainty in hP_z which is slightly less than 4% and contributes directly to the total systematic error in A_{exp}

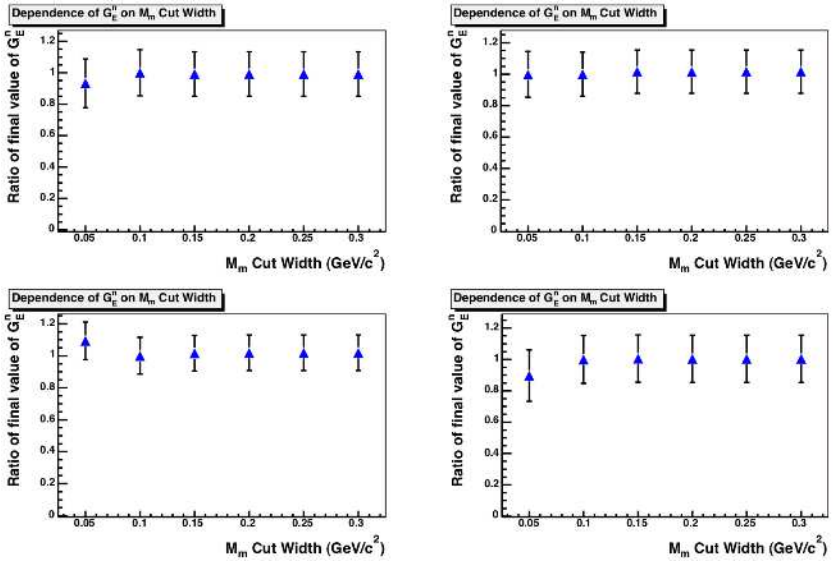

FIG. 4.25. Missing Mass cuts are varied in each of the four Q^2 Bins from 50 to 300 MeV/c^2 to determine the variation in the measurement of G_E^n in each bin. The final values plotted are ratios of the resulting measurement with respect to the final values listed in the Combined rows of Table 4.5.

which is about 5%. This error, ΔA_{ed}^V, translates as a contribution to the systematic error of the extracted value of G_E^n: $\Delta G_E^n(\Delta A_{ed}^V) \approx 1.5\%$ as calculated from the Monte Carlo.

4.8.4. Cut Dependence. The cut dependence is assumed to be small. To elicit a quantified demonstration of the effect cuts create on G_E^n, the width of the missing mass will be narrowed and then dilated three times the actual width of the cut placed on the missing mass. The difference in the measured value will serve well enough to quantify the effect of the cuts on the actual value of G_E^n resulting from the analysis. The mean of the six points in the four plots in figure 4.25. There is minimal variation after the first point corresponding to the thinnest window of events allowed into the calculation. The contribution to the systematic uncertainty is 1.5% corresponding to a fit for the mean of the six points in all four bins from which the mean with the largest deviation from 1.0 was 0.986.

4.8.5. Value of G_M^n. The kinematics of the experiment are restricted to the Q^2 region from 0.1-0.6 $(\mathrm{GeV/c})^2$. Within this region, the dipole parameterization of the form factor G_M^n has been shown to deviate from measured values by up to 5%. A better parameterization is needed to extract the value of G_E^n from the measured form factor ratio described in section 4.7.

Modern data on G_M^n([19]-[32]) are well described by a recent paper by Friedrich and Walcher[95]. In their paper, they are the first to parameterize the noticeable dip in the world's data of G_M^n (see Figure 2.3) in the Q^2 region from 0.1-0.3 $(\mathrm{GeV/C})^2$. They describe their motivation as follows:

> "...we show that, at the percentage level, the peculiar structure observed in G_E^n, namely a kind of bump around Q^2 0.2-0.3 $(\mathrm{GeV/c})^2$, is also present in the other form factors G_E^p, G_M^p, and G_M^n. ... in terms of a purely phenomenological ansatz for the form factors, we show how this can be viewed in the light of the decomposition of the nucleon states into a constituent quark core and a polarization term reflecting the contribution of the pion cloud."

The parameterization describes a Gaussian dip along with a dipole form used to describe the "inner" and "outer" charge distributions of the neutron. The mathematical form is

$$G_M^n = \frac{a_0^{out}}{(1+Q^2/a_1^{out})^2} + \frac{a_0^{in}}{(1+Q^2/a_1^{in})^2} + a_0^{\pi}\left(1 - \frac{Q^2}{6a_1^{\pi}}\right)e^{-\frac{Q^2}{4a_1^{\pi}}} \tag{4.15}$$

The contribution to the systematic error in the determination of G_E^n is the uncertainty of this fit to the world's data. The error has been determined at about 1.5% and fluctuates less than a tenth of a percent over the range of this experiment.

4.8.6. Radiative Corrections. The radiative effects on the cross section, though considerable, are not spin-dependent and therefore, would not contribute significantly to the

asymmetry A_{ed}^V. Code developed by Afanasiev et al.[124] was used to analyze the dependence of the vector polarized observable in perpendicular kinematics with the simulations corrected and uncorrected for radiative effects with a maximum of 0.7% over the region of momentum transfer within BLAST. Since the effect of the radiative corrections are shown to be small, the corrections were not implemented into the analysis of the data.

4.8.7. False Asymmetries. Along with the asymmetries A_{ed}^V and A_d^T that are expected to be significant and descriptive of spin-dependent components of the cross section, other linear combinations of the spin-dependent yields such as A_e, A_d^V, and A_{ed}^T are expected to be consistent with zero. Any significant deviations from zero would be demonstrative of systematic errors in charge counting or averaging over the out of plane acceptance of the detector. The uncertainties of these false asymmetries directly contribute to the systematic error of the experiment.

Figure 4.26 shows the false asymmetries plotted as a function of the missing momentum, one of the sensitive variables used in the G_E^n analysis from the ${}^2\vec{H}(\vec{e}, e'n)p$ BLAST data. The averaged values of the asymmetries here are as follows:

$$\begin{aligned} A_e &= 2.899 \times 10^{-3} \pm 2.412 \times 10^{-3} \\ A_d^V &= -5.158 \times 10^{-3} \pm 2.388 \times 10^{-3} \\ A_{ed}^T &= -1.926 \times 10^{-3} \pm 2.434 \times 10^{-3} \end{aligned}$$

These false asymmetries are determined over the sum of the entire Q^2 region in question. Their contribution to the systematic error is on the order of $\sim 1\%$.

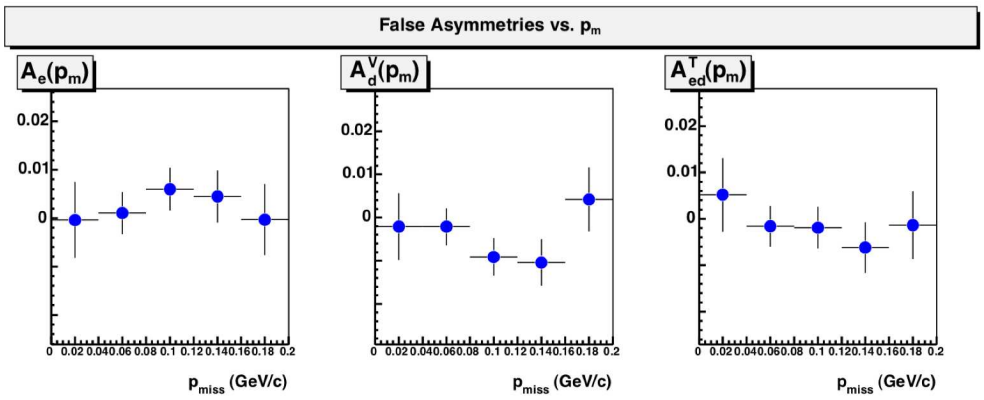

FIG. 4.26. The False Asymmetries as measured from the data used for the analysis of G_E^n.

CHAPTER 5: **CONCLUSION**

As experiments have become more sophisticated, the accuracy of the measurements have significantly improved. The neutron is not the simplest elementary particle to detect in the lab. Within this experiment, the number of protons detected through a very similar analysis overshadows the overall neutron yield by more than an order of magnitude. This difficulty in detecting neutrons is the reason that the currently measured values of G_M^n and G_E^n are much less accurate than those of the proton.

The approximation of the proton being dominantly described by the s-state wave functions of the two *up* and the one *down* quark, is different than that of the neutron in which these contributions cancel at first order, i.e. the electric form factor of the neutron is zero in this approximation. The gluons and sea quarks that are included in the constituent quark picture are a new feature relative to the hypothesized pion cloud that was expected to account for the Yukawa interaction between nucleons. The pion cloud is still realized to be an essential feature in order to preserve chiral symmetry at low momentum transfers. Through the development of nucleon models and hadronic interaction theories that evolved out of Quantum Chromodynamics such as the *MIT cloudy bag*, *chiral dynamics*, *chiral perturbation theory* as well as the effective theories spawned by Weinberg's early efforts[128, 129, 130], each has been forced to conform to the experimental tests that confirm that the pion is as decisive a component of the nucleon as the constituent quarks and gluons.

Knowledge of the neutron's *electric form factor* G_E^n is essential for the understanding of the structure of the nucleon. It is also a key ingredient in the analysis of processes involving electromagnetic interactions with complex nuclei as well as electroweak processes involving interactions between leptons and hadrons and the developing field of neutrino scattering. Unpolarized electron scattering on deuterium had been the experimental con-

figuration until Hartmuth Arenhövel cleverly demonstrated the unique opportunity to use a polarized electron beam along with detection of the outgoing neutron's polarization in 1987[126]. Polarizing a nuclear target also gives the ability to measure the same observable as Arenhövel demonstrated, namely P_x, which appeared to be directly proportional to G_E^n and proved to be independent of the choice of the deuteron wavefunction, a problem that still contorts the interpretation of unpolarized scattering from small nuclei. These experiments have now been carried out several times and the results are shown in Figure 5.1. The unpolarized data has been left out to ensure consistency in the comparison of the results of this work.

5.1. Determination of the Final Points

Table 4.5 shows the results of the analysis at BLAST. Since the analysis was performed by calculating asymmetries over two correlated but separate domains, the final G_E^n points that are quoted are set to be consistent with the values quoted by the rest of the scientific community. The calculations over the domain of missing momentum are thus shown. The four final points along with the current world data from double-polarization experiments can be seen in Figure 5.1.

5.1.1. Final Results and Phenomenological Fits. In the early 1970's, Galster et al. introduced the first phenomenological parameterization of G_E^n[53] (see eq. 2.55). The neutron's magnetic moment was fixed as the constant in the numerator, i.e. $a_G = -\mu_n$, and the free parameter in the denominator was found to best fit the 1973 unpolarized *ed*-elastic data with a value $b_G = 5.6$. In the Platchkov parameterization[54] the parameters $a_P = 0.9$ and $b_P = 3.47$. Both of these parameterizations were fitted to unpolarized data that used

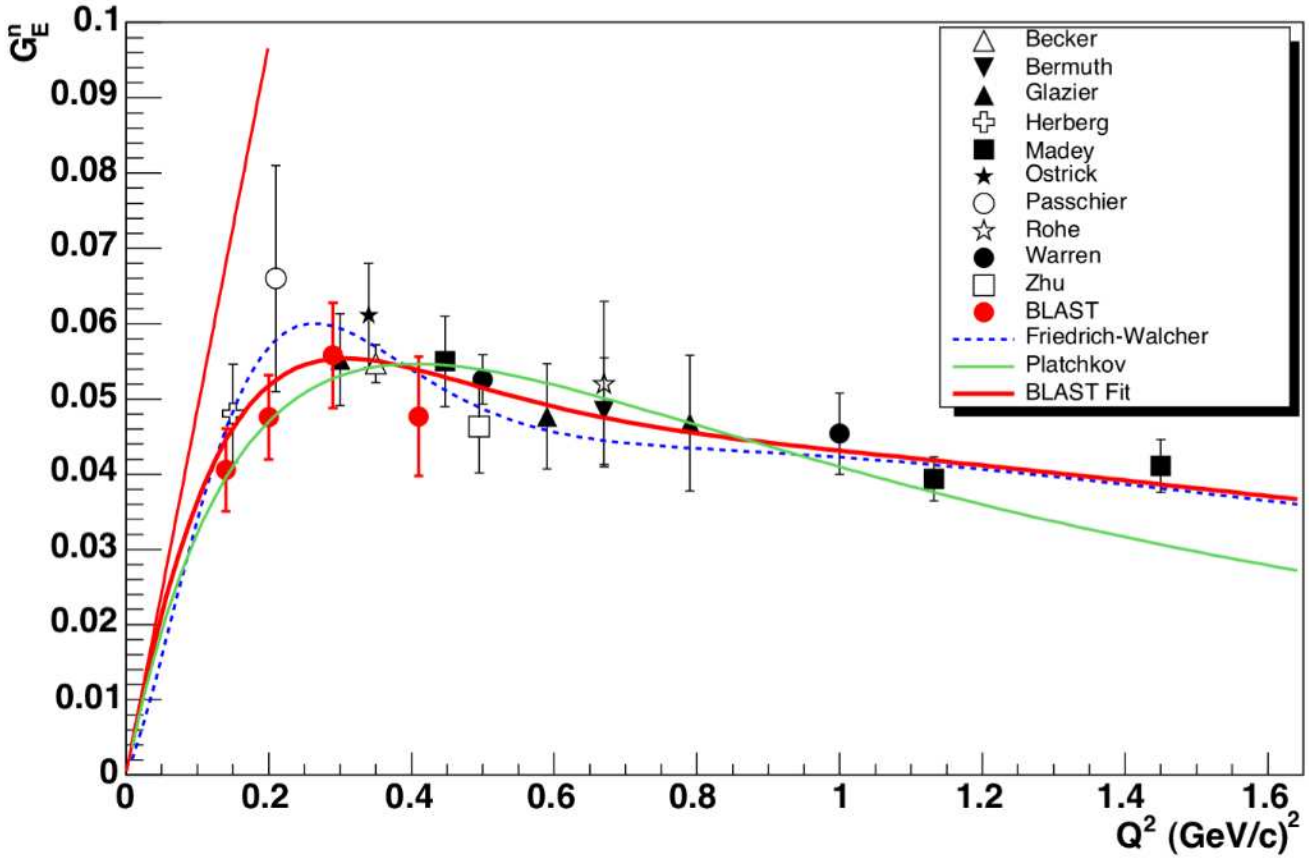

FIG. 5.1. The World's double-polarized data on G_E^n is included with the results from this experiment. Statistical errors are displayed. Bermuth [85], Zhu [94], and Rohe [92] are data taken with a ^{3}He target while all other points applied the use of deuterium. A fit of the data to the Platchkov parameterization is plotted and shows relative consistency at low Q^2 while poorly accommodating the behavior of the data at highest Q^2 point. The original parameterization presented by Friedrich and Walcher in 2003 [95] has been plotted. This fit satisfies the behavior of the world's data well but fails to fit the constraint of the slope at $Q^2 = 0$. The BLAST parameterization is shown and is constrained to fit the slope constraint. It displays the behavior of G_E^n just as well as the new Friedrich and Walcher fit discussed in this section.

the unpolarized electron-deuteron scattering cross section as noted in eq. 2.31. A fit to the new polarized data using the Galster form from eq. 2.55 is shown. It is plotted with the World's data in Figure 5.1 and is quite consistent with the data up to the highest Q^2 point measured which is underestimated by this rigid parameterization by almost 2σ.

In 2003, Friedrich and Walcher published a paper on phenomenological fits to the electromagnetic form factors of the proton and neutron[95]. The appearance of a bump in all four electric and magnetic form factors of the proton and neutron in the same Q^2 region prompted them to parameterize the anomaly and postulate the measurements as indicative of a pion cloud. When subtracting the smooth ansatz fits from the data along with their data driven parameterization including this *bump* contribution, it was noticed that the four form factors demonstrated a bump structure that is strikingly similar in width and magnitude in all four form factors G_E^p, G_M^p/μ_p, G_E^n, and G_M^n/μ_n. G_E^n happened to be the impetus under which their phenomenological ansatz was motivated since the bump contribution is the greatest in the neutron. Their parameterization of G_E^n is described in section 2.4.2. The Mainz A1 collaboration[87] used this parameterization to better fit the low and high Q^2 of the world's data. Though the fit does remarkably well, it is demonstrated that this parameterization also falls short of physical constraints, i.e. $\frac{dG_E^n}{dQ^2}|_{Q^2=0} \neq -\frac{1}{6}\langle r_n^2 \rangle$, where $\langle r_n^2 \rangle$ is the neutron's charge radius. For this reason, the BLAST parameterization was introduced[107] and is reasserted here.

The neutron's charge radius has been measured very accurately[65] and must be used to constrain the fit to the world's data. The BLAST parameterization is written exactly the same as the Friedrich and Walcher parameterization is written in equation 2.56. To

reiterate, the equation is written here:

$$G_E^n(Q^2) = \frac{a_{10}}{\left(1+\frac{Q^2}{a_{11}}\right)^2} + \frac{a_{20}}{\left(1+\frac{Q^2}{a_{21}}\right)^2} + a_b Q^2 \left(e^{-\frac{1}{2}\left(\frac{Q-Q_b}{\sigma_b}\right)^2} + e^{-\frac{1}{2}\left(\frac{Q+Q_b}{\sigma_b}\right)^2} \right). \qquad (5.1)$$

As with the Friedrich and Walcher fit, the parameterization consists of two dipole terms normalized to ensure that $G_E^n \to 0$ as $Q^2 \to 0$. The *bump* contribution is characterized by the addition of two Gaussians. This is necessary to symmetrize the first order Q terms in the exponent. The term Q_b within the exponents determine the position of the bump and is, like Q, positive definite. Friedrich and Walcher postulate that the bump term, characterized by the Gaussians, is the contribution of the pion cloud while the smooth dipole terms are indicative of the constituent quark core. The original fit by the A1 collaboration is included in Figure 5.1. A newer fit includes the data in this work and has the fitted parameters shown in Table 5.1. It has not been shown in the figure since its position is so near to the BLAST parameterization that it is left out for clarity. Both A1 fits match the world's data considerably better than the Galster and Platchkov parameterizations and demonstrate significantly better χ^2 (see Table 5.1).

The Friedrich and Walcher parameterization is highly successful in predicting the low Q^2 behavior and the high Q^2 data recently measured at Jefferson Lab Hall C[89]. Yet, as alluded to earlier, it is unphysical in that it fails to reproduce the correct slope as $Q^2 \to 0$. In order to restrict the parameterization to match the charge radius measured by Kopecki et al.[65], the following equation must be used to force the parameterization to satisfy the physical constraint,

$$-\frac{1}{6}\langle r_n^2 \rangle = \left.\frac{dG_E^n}{dQ^2}\right|_{Q^2=0} = -2\left(\frac{a_{10}}{a_{11}} + \frac{a_{20}}{a_{21}}\right) + 2a_b e^{-\frac{Q_b^2}{2\sigma_b^2}}. \qquad (5.2)$$

According to this formula, the bump term dominates the contribution to the charge radius. Separate curves are drawn in Figure 5.1 to denote the separate contributions of the bump

TABLE 5.1. Comparison between fits to the World's data on G_E^n are shown here. The errors of the last significant digits are quoted in the parentheses. Calculated χ^2 includes all points in Figure 5.1.

Fit	a_{10}	a_{11} $(\mathrm{GeV/c})^2$	a_{20}	a_{21} $(\mathrm{GeV/c})^2$	a_b $(\mathrm{GeV/c})^{-2}$	Q_b (GeV/c)	σ_b (GeV/c)	$\langle r_n^2 \rangle$ fm^2	χ^2_{total}
A1[95]	1.2974	1.73(fixed)	-1.2974(fixed)	1.5479	0.19426	0.3421	0.16758	-0.052	8.43
new A1	1.289(1.1)	1.73(fixed)	-1.289(fixed)	1.544(8.1)	0.18(2.2)	0.29(2.0)	0.21(1.2)	-0.073	5.91
BLAST	2.03(3.4)	1.73(fixed)	-2.03(fixed)	1.6114(2.8)	0.220(fixed)	0.19(1.4)	0.246(4.9)	-0.115	6.06

and dipole terms in this parameterization. Table 5.1 gives the values of the parameters of the best fit to the World's data. The Friedrich and Walcher fit is shown as given by the A1 collaboration in 2003 and a newer fit that includes the data from this thesis. The newer fit shows the best χ^2 but, again, is unphysical. It is only marginally better than the BLAST fit while the BLAST fit models the physical constraints correctly. The old A1 fit has a nearly identical dipole contribution to the newer fit and the BLAST fit but the bump contribution is substantially different between all three fits. The width of the bump is much larger in the two new fits, largest in the BLAST fit, and the location of the bump is much lower in Q^2 in the BLAST fit than the new A1 fit. The BLAST parameterization also displays the largest amplitude of the bump contribution as demonstrated by a_b. Considering that the dipole contribution at $Q^2 = 0$ is only about 30%, this translates to the charge radius being predominantly determined by the pion cloud. As predicted by pQCD calculations, the constituent quark core is expected to dominate in the high Q^2 region and this is also demonstrated by exponential decay of the bump contribution beyond $Q^2 \sim 0.8(GeV/c)^2$. Figure 5.1 shows the separate contributions of the bump and dipole terms to the BLAST parameterization.

The data from this particular experiment demonstrate remarkable consistency with the fits. The first two points lie less than half of one standard deviation from the fits, while the third point seems to balance on the exact placement of the maximum of the fits as if

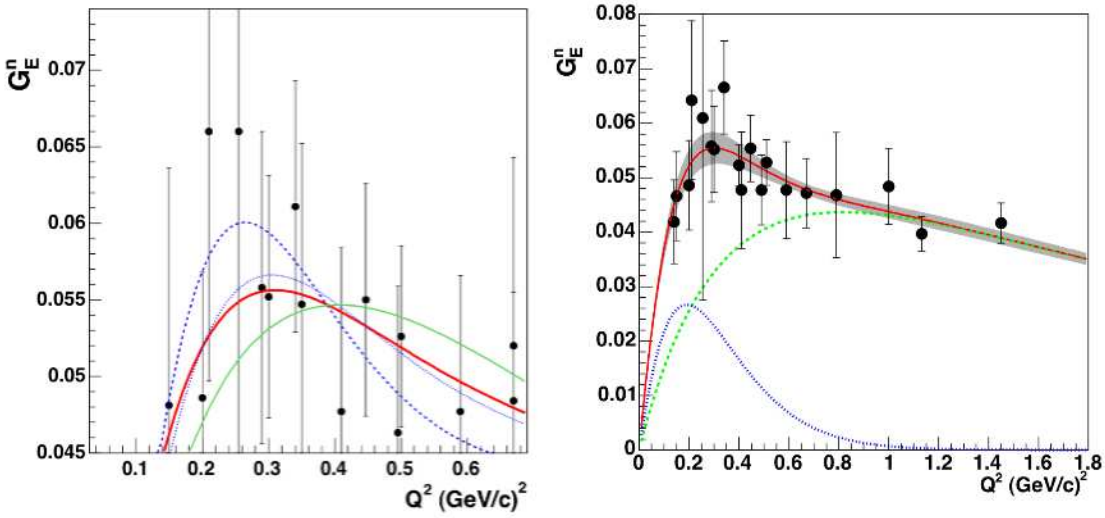

FIG. 5.2. The region of the bump from Figure 5.1 is zoomed on the top left showing the substantial differences between the best fit parameterizations of G_E^n and the uncertainty of the data points that make up this interesting region. The thinnest line is the new A1 fit whose parameters are listed in Table 5.1. It was not shown in previous figures due to its proximity to the BLAST fit. On the right is the BLAST parameterization along with its respective error band. The uncertainty is about 6% in the region of the parameterized bump and surfs slightly above 3% in the high Q^2 region. Note that in this work, the world's data and the respective statistical errors are fitted.

Sisyphus had placed it there. The fourth point drops substantially, hinting at the necessity of a parameterized "bump" while still showing that it, too, lies less than one standard deviation from the fits to the World's data. Despite the fact that the first point in this analysis is the world's lowest Q^2 point in the measurement of G_E^n, it is obvious that more low Q^2 data is needed to better isolate the behavior and the expected contribution of the pion cloud. Figure 5.2(left) gives a close-up view of the deviations between the presented fits and parameterizations along with the significant uncertainty within the data that still plays a heavy role in the uncertainty of the behavior of G_E^n. On the right side of Figure 5.2 is a plot of the BLAST parameterization, the respective contributions of the dipole and bump terms, and an error band demonstrating the region of the bump in G_E^n to carry the

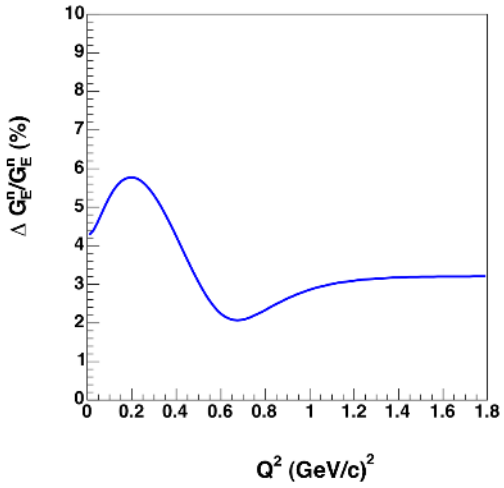

FIG. 5.3. The precision of the BLAST fit, $\Delta G_E^n/G_E^n$.

highest respective uncertainty. With the data from this work, the best fit allows us to determine G_E^n with an uncertainty of 5.8% at the highest point in the fit where the dipole and bump contributions cross. This demonstrates a need for more data in this region near $Q^2 \approx 0.3(GeV/c)^2$. In the high Q^2 region, the accuracy of the dipole contribution results in approximately a 3% uncertainty (see Figure 5.3). Though there is still much progress to be made, the present picture of the neutron's electric form factor is considerably clearer.

5.1.2. Charge Density of the Neutron. The interpretation of G_E^n requires a relativistic transformation and is not as simple as a charge distribution with the neutron at rest. The motivation behind the Rosenbluth separation was to present a "non-relativistic" model in which the Fourier transform of the electromagnetic form factors could be quantitatively depicted as a charge distribution within the Breit frame. More complex relationships have been discussed within a relativistic framework and corrections such as these require model assumptions[127] but these are not considered here. Also ignored is the controversy over this simplistic interpretation which is discussed thoroughly in [131]. The Fourier trans-

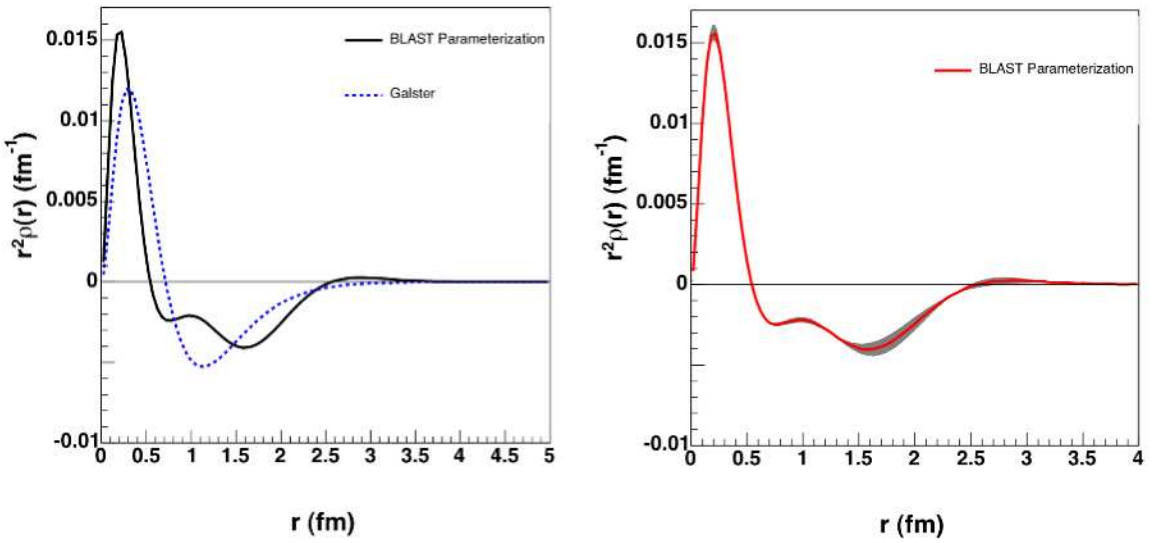

FIG. 5.4. The Fourier transform of the BLAST parameterization along with the respective charge distribution as it would be described by the Galster parameterization. There is a significant change between the models as can be noticed by the difference in the density of the positive core and with the broadness of the negative cloud in the outer region of the neutron. The error band has also been carried through the Fourier transform and can be seen in the right figure.

form of the BLAST parameterization presented here has been depicted in Figure 5.4 along with the Fourier transform of the Galster parameterization. It is generally assumed that the *up* and *down* quarks within the constituent quark picture are not evenly dispersed, but rather the *up* quark with its charge of $+\frac{2}{3}$ tends to situate itself closer to the center of the neutron while the *down* quarks are pushed further out resulting in the more negative outer region of the neutron and the resultant negative charge radius.

The Fourier transform of the Galster parameterization shows the general characteristics that one might expect from this simple constituent quark interpretation, yet its inability to reproduce the behavior of the world's data forces a new interpretation. The Fourier transform of the A1 fit and the BLAST fit sheds an interesting light on the neutron in the sense that it increases the density of the positive core of the neutron and broadens

the negative region in the outer region of the neutron. There is a slightly positive region extending beyond the negative cloud and this is indicative of the nearly complete cancellation of the positive core and the diffuse negative pion cloud. The Q-space bump structure contributes a change in the r-space charge density, $\Delta\rho_b$, which must sum to zero by its construction and thus must contribute to an oscillatory behavior in the charge density as can be seen in Figure 5.4. The wavelength of this oscillation λ_ρ is determined by the position of the bump in Q-space while the dampening of the oscillation is determined by the width of the bump. The width of the bump results in a wavelength $\lambda_{rho} = 2\pi\hbar/Q_b \approx 2.4$fm, and such an oscillation, in accordance with the results from Friedrich and Walcher, results as a common feature of all four form factors.

5.1.3. Model-Independent Sum of Gaussians Parameterization. One more fit has been included to elucidate the world's current data on G_E^n. A model-independent fit has been included using the Sum of Gaussians (SOG) method used by Sick in 1974 [139]. The methodology is to add a series of gaussians to approximate a fit to the world's data.

The electric and magnetic form factors and the charge and magnetization densities of the neutron can be related by a Fourier transform. The charge density must be normalized to

$$\int_0^\infty drr^2\rho_{ch}(r) = Z \tag{5.3}$$

while the magnetization density is normalized as

$$\int_0^\infty drr^2\rho_m(r) = 1. \tag{5.4}$$

The electric form factor as we have written it can also be generally parameterized by a series of gaussians

$$G_E^n(Q^2) = \sum_n^N a_n e^{\frac{(q-Q_n)^2}{\gamma^2}} \tag{5.5}$$

where a_n is the coefficient of the nth Gaussian, Q_n is the radius of the nth gaussian term and γ is representative of the width. The $FWHM$ is commonly quoted as the definition of the smallest structure within the form factor's distribution and is mathematically defined in terms of the width of the gaussian as

$$\Gamma = 2\gamma\sqrt{\ln 2} = FWHM. \tag{5.6}$$

The parameterization is also *model-independent* since the only parameter that is input is the width of the gaussians. The width used in the parameterization here comes from the 2004 Friedrich and Walcher (A1) fit since it was fit to actual data and yields the thinnest width to a structure that Friedrich and Walcher define as the *bump* contribution. The widths of the corresponding gaussians in q and r-space are related and can be defined as the relationship between the rms radius R_G of the r-space gaussian and the $FWHM$ of the q-space gaussian,

$$R_G = \Gamma\left(\frac{3\ln 2}{8}\right)^{\frac{1}{2}} \tag{5.7}$$

The number of terms N from equation 5.5 is unimportant. The important strategy is to fit a small number of gaussians from the outer limits of the region in question and to increase the number of gaussians until the fit is good and stable using a minimum χ^2. Restrictions can obviously be made on the height of each gaussian which should be limited by the maximum q-space density. The width need be restricted as well since instability quickly arises once widths smaller than the smallest noticeable structure are included. This width remains a constant feature of each gaussian within the parameterization to limit the number of free parameters.

A fit using the SOG method is shown in Figure 5.5. Three gaussians were all that was needed to describe the data. The error band is much more realistic than the previous

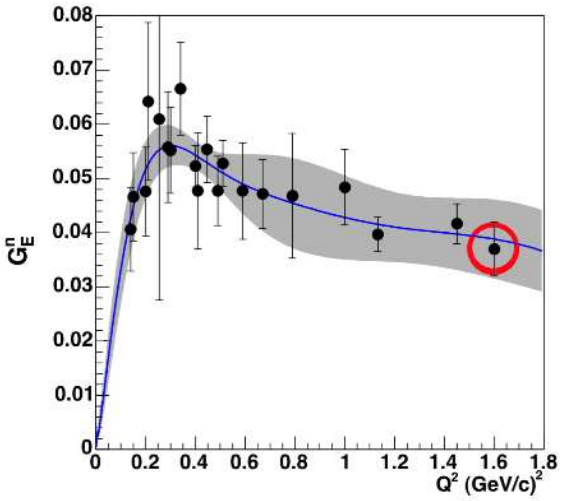

FIG. 5.5. A Sum of Gaussians parameterization is fit to the World's data on G_E^n. The final point circled is a fiducial point added to stabilize the fit of the third gaussian which would asymptotically deviate from the behavior of the other form factors due to the slight increase of G_E^n over the highest two points in Q^2.

parameterizations since they are constrained by the form of the equations used in the fits. The resultant χ^2 of the fit is 5.45. It makes little sense to plot any higher in Q^2 than what is shown here since there is no data published in a higher range. The analyzed data from Jefferson Lab's E02-013 experiment is highly anticipated.

5.1.4. Theoretical Revisit. The subject of theoretical models is difficult to analyze in concise terms. The development of QCD has been worked on extensively and the number and applicability of models are as diverse as the philosophical interpretations of Quantum Mechanics. The types of models applicable to the study of the electromagnetic form factors of the proton and neutron are described in section 2.5. Available model predictions are plotted alongside the world's data in Figure 5.7.

The purpose of this work is present a new measurement and the behavior with respect to theory will be terse and qualitative. Not one of the theoretical models is capable of

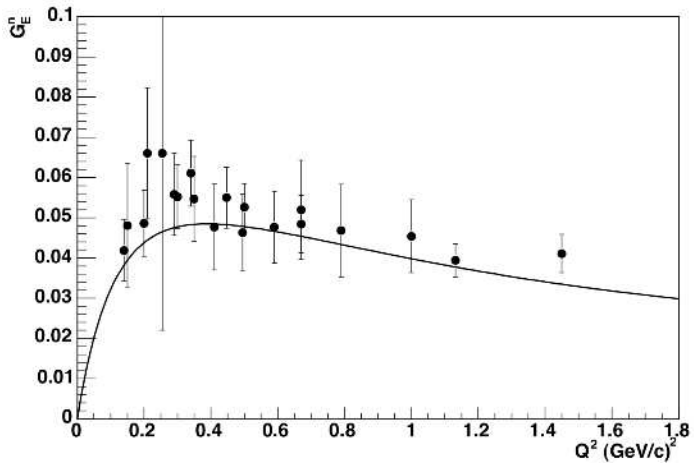

FIG. 5.6. The world's double-polarized scattering data on G_E^n and the prediction from Dispersion Theory as taken from [142]. The theory shows the best description of the world's G_E^n data.

describing the low *and* high Q^2 behavior of the form factor ratio. The Light Front calculations by Miller[75] and those by Cardarelli and Simula[135] are very successful in predicting the behavior of the dipole contribution at high Q^2 and even resemble a smooth dipole parameterization. Since it resembles a dipole term, it is far too rigid to accommodate the distinguishable bump contribution at low Q^2. In opposition, the Kaskulav calculation[134], the Diquark model[132], and the chiral soliton calculation[77] all reproduce the amplitude and general behavior below $Q^2 = 0.3(GeV/c)^2$ but deviate significantly from the high Q^2 behavior. The best fit to the behavior of the data comes from [142]. It builds upon Dispersion theory and the constraints of Chiral Perturbation Theory to sufficiently model the assertion of the pion cloud about the nucleon. It is plotted separately from the other theories since it demonstrates a superior ability to exhibit the behavior of the world's G_E^n data (see Figure 5.6) at both low and high Q^2.

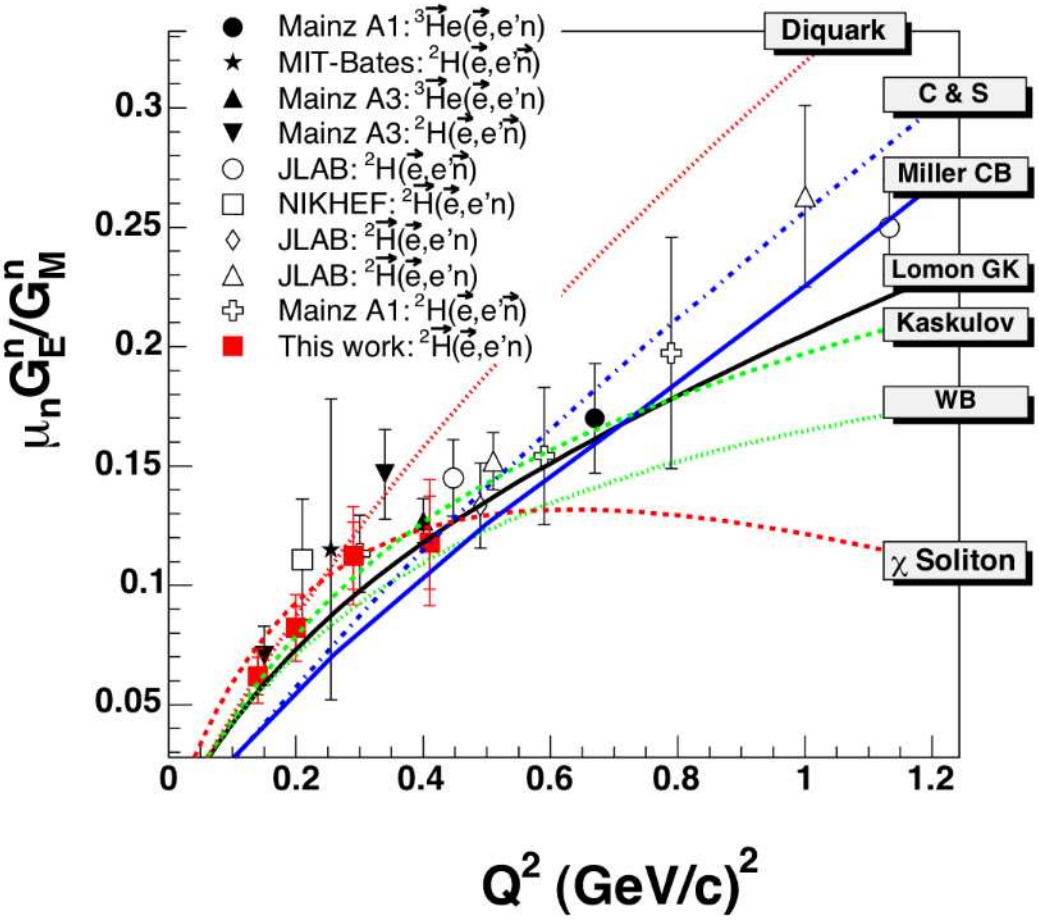

FIG. 5.7. Comparison of the data on $\mu_n G_E^n/G_M^n$ in reference to theoretical calculations. The "Diquark" model comes from Ma *et al.*[132], "Miller CB" is a Cloudy Bag model from G. Miller[75] using a One-Gluon-Exchange potential in a core nucleon, "Lomon GK" is an extended Gari-Krümpelmann calculation by E. Lomon[133], the "χ Soliton" calculation comes from Holzwarth[77], "Kaskulov" is a relativistic constituent quark One-Gluon-Exchange model with a pion cloud[134], "C & S" is a Light-Front description with One-Gluon-Exchange calculated by Cardarelli and Simula[135], "WB" is a point-form spectator approximation based on Goldstone-Boson-Exchange by Wagenbrunn *et al.*[136]. The data are from [85, 86, 84, 87, 88, 89, 90, 91, 92, 93, 94].

5.2. Summary

This work presents the measurement of G_E^n at four-momentum transfers of 0.14, 0.20, 0.29, and 0.41 $(\mathrm{GeV/c})^2$. The calculated values of G_E^n at the respective values of four-momentum transfer are $0.0406 \pm 0.0055 \pm 0.0024, 0.0476 \pm 0.0056 \pm 0.0028, 0.0558 \pm 0.0070 \pm 0.0032$, and $0.0477 \pm 0.0079 \pm 0.0028$. The first point is lowest four-momentum transfer at which the value of G_E^n has been analyzed.

The production runs took place at MIT-Bates Linear Accelerator Center in Middleton, MA from the summer of 2004 until late Spring of 2005. The measurement employed the use of a linearly accelerated polarized electron beam at an energy of 850 MeV. This beam was incident upon a monatomic deuterium target that was cycled through states of vector-plus, vector-minus, and tensor polarization oriented at angles of approximately 32° and 47° into the left sector of a symmetrical large acceptance spectrometer. This target is a modified Atomic Beam Source transported to Bates from NIKHEF. The spectrometer was placed into a toroidal field allowing for charge discrimination and kinematic reconstruction of the scattered particles exiting the target cell. Scintillating detectors were used to trigger the detection of electrons while lead glass detectors were used for the detection of coincident neutrons.

The data has shown to be consistent with the World's data on the electric form factor of the neutron. The Friedrich and Walcher (A1) parameterization was modified to constrain the slope at zero momentum transfer to be consistent with the world's best measurement of the charge radius of the neutron. The uncertainty of the fit of this parameterization shows a maximum uncertainty of 5.8% within the highest region of G_E^n and an uncertainty of only 3% in the higher region of momentum transfer. The data disagrees with the theoretical models

presently available. The low momentum transfer points are expected to significantly enhance the current precision of the strange form factor, and the precision of the phenomenological fit is expected to greatly enhance the precision of parity violation experiments which directly contribute to the neutral weak form factors.

APPENDIX A

KINEMATIC CALCULATIONS

Two Lorentz frames are relevant to the BLAST calculations for the reaction of $e + d \rightarrow e + p + n$: 1. the lab frame in which we do the experiment (this includes a simple rotation into the momentum transfer frame), and 2. the center-of-momentum frame (which is sometimes referred to as the center of mass frame). The reactions at BLAST can be quantified within these coordinate systems with relative ease.

A.1. BLAST Lab Frame Coordinate System

These variables are defined in the BLAST coordinate system in the Lab frame unless otherwise noted by a superscript suggesting a rotation or a boost. This BLAST coordinate system in the lab frame is defined as the frame in which the deuteron has zero momentum and the electron's momentum is 850 MeV and in the direction of the electron beam flow, $+z^B$. These cartesian axes are given a B superscript to denote that they define the BLAST coordinate system in the lab frame. The masses of the particles intrinsic to the experiment are defined as m_e, m_d, m_n, and m_p, corresponding to the electron, deuteron, neutron, and proton respectively. The binding energy is far below the resolution of the experiment and will be included as E_b for pedagogy.

$+\hat{z}^B$	$\equiv$	Points in the direction of electron beam's momentum in the BLAST Coordinate System
$+\hat{y}^B$	$\equiv$	Points directly upward towards the ceiling of the South Hall in the BLAST Coordinate System

$+\hat{x}^B$ $\equiv$ Points in the remaining direction so to create a right-handed coordinate system as defined by: $\hat{x}^L \equiv \hat{y}^L \times \hat{z}^L$, in the BLAST Coordinate System

θ_e $\equiv$ The polar angle of the outgoing electron in the BLAST Coordinate System

ϕ_e $\equiv$ The azimuthal angle of the outgoing electron in the BLAST Coordinate System

Ω_e $\equiv$ The solid angle of the outgoing electron in the BLAST Coordinate System

E_0 $\equiv$ The energy of the incoming electron beam

E_e $\equiv$ The energy of the outgoing scattered electron

$\vec{k_e}$ $\equiv$ The momentum of the incoming scattered electron in the BLAST Coordinate System

$\vec{k'}_e$ $\equiv$ The momentum of the outgoing scattered electron in the BLAST Coordinate System

θ_n $\equiv$ The polar angle of the outgoing scattered neutron in the BLAST Coordinate System

ϕ_n $\equiv$ The azimuthal angle of the outgoing scattered neutron in the BLAST Coordinate System

Ω_n $\equiv$ The solid angle of the outgoing scattered neutron in the BLAST Coordinate System

E_n $\equiv$ The energy of the outgoing scattered neutron

$\vec{p}_n$ $\equiv$ The momentum of the outgoing scattered proton in the BLAST Coordinate System

θ_p	$\equiv$	The polar angle of the outgoing scattered proton in the BLAST Coordinate System
ϕ_p	$\equiv$	The azimuthal angle of the outgoing scattered proton in the BLAST Coordinate System
Ω_p	$\equiv$	The solid angle of the outgoing scattered proton in the BLAST Coordinate System
E_p	$\equiv$	The energy of the outgoing scattered proton
$\vec{p}_p$	$\equiv$	The momentum of the outgoing scattered proton in the BLAST Coordinate System
$\vec{q}$	$\equiv$	The momentum of the virtual photon or momentum transfer in the BLAST Coordinate System
θ_q	$\equiv$	The polar angle of the virtual photon or momentum transfer in the BLAST Coordinate System
ϕ_q	$\equiv$	The azimuthal angle of the virtual photon or momentum transfer in the BLAST Coordinate System
Q	$\equiv$	The four-momentum of the virtual photon

From these variables we construct the necessary relations that define our reaction. The relations that do not require a rotation or a boost are few and defined here.

The energy transfer $\omega = E_0 - E_e$ and the four-momentum transfer which is a Lorentz invariant:

$$Q^2 = 4E_0E' \sin^2\left(\frac{\theta_e}{2}\right) = \vec{q}^2 - \omega^2, \tag{A.1}$$

allows us to calculate the magnitude of the three momentum transfer as can be seen the second part of this equation. Then to calculate polar and azimuthal angles of the virtual

photon in the BLAST Coordinate system,

$$\cos\theta_q = \frac{E_0 - E_e\cos\theta_e}{q}, \tag{A.2}$$

$$\phi_q = \phi_e + \pi. \tag{A.3}$$

The complete four-momentum transfer is now known and a rotation into the direction of the momentum transfer along with a boost to the center of momentum is possible. First, there are a few useful relations that help to identify the characteristics of the reaction.

The invariant mass W is useful in kinematic cuts. It can be considered the total system energy that the electron scatters from divided by c^2. It is defined as such,

$$W = \sqrt{m_d^2 + 2m_d\omega - Q^2}. \tag{A.4}$$

Continuing with useful relations for the identification of the deuteron electrodisintegration reaction, we can calculate the missing energy E_m, the missing momentum p_m, and the missing mass M_m,

$$\begin{aligned} E_m &= m_d + \omega - E_n - E_b, \\ \vec{p}_m &= \vec{q} - \vec{p_n}, \\ M_m &= \sqrt{E_m^2 - p_m^2}. \end{aligned} \tag{A.5}$$

A.2. Rotations within Lab Frame

The two rotations that need to be considered are the rotation from the BLAST Coordinate system, **B**, into the Coordinate system in which the z-axis is pointed along the direction of the momentum transfer **Q**, i.e. $+\hat{z}^L \rightarrow +\hat{z}^Q$.

The mathematical definition of a rotation is defined by a rotation matrix $\mathcal{R}$ which takes one three-dimensional vector in the **B**-system to one in the **Q**-system. It can be

written as such,

$$\begin{pmatrix} p_x^Q \\ p_y^Q \\ p_z^Q \end{pmatrix} = \mathcal{R} \begin{pmatrix} p_x^B \\ p_y^B \\ p_z^B \end{pmatrix}. \tag{A.6}$$

The general equation for a momentum vector in the **B**-system with energy E^B is written here in cartesian and spherical coordinates,

$$\begin{aligned} \vec{p}^B &= p_x^B \hat{x}^B + p_y^B \hat{y}^B + p_z^B \hat{z}^B \\ &= p^B(\sin\theta_p^B \cos\phi_p^B \hat{x}^B + \sin\theta_p^B \sin\phi_p^B \hat{y}^B + \cos\theta_p^B \hat{z}^B). \end{aligned} \tag{A.7}$$

Analogously, we can write the vector in the **Q**-system,

$$\begin{aligned} \vec{p}^Q &= p_x^Q \hat{x}^Q + p_y^Q \hat{y}^Q + p_z^Q \hat{z}^Q \\ &= p^Q(\sin\theta_p^Q \cos\phi_p^Q \hat{x}^Q + \sin\theta_p^Q \sin\phi_p^Q \hat{y}^Q + \cos\theta_p^Q \hat{z}^Q). \end{aligned} \tag{A.8}$$

The vector which defines our rotation is the momentum transfer $\vec{q}^B$ which is given the B superscript to denote that we calculate it within the BLAST coordinate system. It is written in an identical form to $\vec{p}^B$,

$$\begin{aligned} \vec{q}^B &= q_x^B \hat{x}^B + q_y^B \hat{y}^B + q_z^B \hat{z}^B \\ &= q^B(\sin\theta_q^B \cos\phi_q^B \hat{x}^B + \sin\theta_q^B \sin\phi_q^B \hat{y}^B + \cos\theta_q^B \hat{z}^B). \end{aligned} \tag{A.9}$$

By definition, $\hat{z}^Q \equiv \vec{q}^B/|q^B|$, and thus the definition of $\hat{z}^Q$ is inside the parentheses of eq. A.9. The definition of a three-dimensional rotation allows us to demonstrate that $\hat{y}^Q = \hat{k}_e^B \times \hat{k'}_e^B = \hat{z}^Q \times \hat{z}^B$, and so we can then show:

$$\hat{y}^Q = \sin\phi_q^B \hat{x}^B - \cos\phi_q^B \hat{y}^B. \tag{A.10}$$

The final axis is simply the cross product, $\hat{x}^Q = \hat{y}^Q \times \hat{z}^Q$. In matrix form we can rewrite $\mathcal{R}$

from eq. A.6,

$$\mathcal{R} = \begin{pmatrix} -\cos\theta_q^B \cos\phi_q^B & -\cos\theta_q^B \sin\phi_q^B & \sin\theta_q^B \\ \sin\phi_q^B & -\cos\phi_q^B & 0 \\ \sin\theta_q^B \cos\phi_q^B & \sin\theta_q^B \sin\phi_q^B & \cos\theta_q^B \end{pmatrix} \tag{A.11}$$

In order to boost in the center-of-momentum frame with less ambiguity, the transformations of the polar and azimuthal angles in spherical coordinates is much more useful. Using the results of our rotation on the vector $\vec{p}$,

$$\begin{aligned} \cos\theta_p^Q &= \frac{\vec{p}^Q \cdot \hat{z}^Q}{|\vec{p}^Q|} \\ &= \cos\theta_p^B \cos\theta_q^B + \sin\theta_p^B \sin\theta_q^B \cos(\phi_q^B - \phi_p^B) \end{aligned} \tag{A.12}$$

$$\begin{aligned} \tan\phi_p^Q &= \frac{p_y^Q}{p_x^Q} \\ &= \frac{sin\theta_p^B \sin(\phi_q^B - \phi_p^B)}{\cos\theta_p^B \sin\theta_q^B - \sin\theta_p^B \cos\theta_q^B \cos(\phi_q^B - \phi_p^B)} \end{aligned}$$

Since the transformation has not left the rest frame, we know that the energy and the magnitude of the three momentum in the **Q**-system is equal to that of the **B**-system, i.e. $E^Q = E^B$ and $|\vec{p}^Q = p^Q = p^B = \vec{p}^B$. To go backwards from $\vec{p}^Q \rightarrow \vec{p}^B$, one need only use the inverse of the $\mathcal{R}$ matrix, or even simpler, to use the property of orthogonal matrices which states that the transpose is the inverse and carry out the same general rotation.

We are now ready to boost into the center-of-momentum frame.

A.3. Boosts to CM-Frame

The boost that will be carried out is along the direction of the momentum transfer. Since the deuteron was at rest and then experienced a momentum transfer along the $\hat{z}^Q$ direction equal to q, we must boost the system into that frame. Using a Lorentz boost, our final frame will consist of the neutron and proton moving away from each other at an angle

of exactly 180° with equal momentum. We will be boosting from the lab coordinate system defined as the **Q**-system in the previous section into the center-of-momentum system, the **C**-system which will be denoted by the superscript C. The Lorentz boost is defined as,

$$\begin{pmatrix} E^C \\ p_x^C \\ p_y^C \\ p_z^C \end{pmatrix} = \begin{pmatrix} \gamma & 0 & 0 & -\gamma\beta \\ 0 & 1 & 0 & 0 \\ 0 & 0 & 1 & 0 \\ -\gamma\beta & 0 & 0 & \gamma \end{pmatrix} \begin{pmatrix} E^Q \\ p_x^Q \\ p_y^Q \\ p_z^Q \end{pmatrix}. \tag{A.13}$$

The definitions for γ and β are as follows and can be determined solely from variables that come from the lab system and do not require any such transformations,

$$\beta = \frac{|\vec{q}^B|}{\omega + m_d} \tag{A.14}$$

$$\gamma = \frac{\omega + m_d}{\sqrt{(\omega + m_d)^2 - (\vec{q}^B)^2}} \tag{A.15}$$

These equations define the Lorentz boost and allow us to transform our coordinate system into the center of momentum system! To go backwards, one need only take the inverse of the matrix defining the Lorentz transform which simple changes the signs of the non-zero off-diagonal elements. A quicker method by which to decipher the polar and azimuthal angles of the spherical coordinate system in the boosted **C**-system, is to adapt eq. A.12 for this transformation by substituting it into the bottom row of eq. A.13, i.e.

$$\cos\theta_p^C = \frac{\gamma}{p^C}(p^B \cos\theta_p^Q - \beta E^B) \tag{A.16}$$

where:

$$(p^C)^2 = (p^B \sin\theta_p^Q)^2 + \gamma^2(p_B \cos\theta_p^Q - \beta E^B). \tag{A.17}$$

Since the azimuthal angle is perpendicular to the direction of the boost, $\phi_p^C = \phi_p^Q$. It is in this frame that the other important kinematic variable θ_{cms}^{np} is defined. It is the angle

between the outgoing proton and the momentum transfer, i.e.

$$\cos\theta^{np}_{cms} = \pi - \frac{\bar{p}^C \cdot \hat{z}^C}{p^C}. \tag{A.18}$$

APPENDIX B

EQUATIONS FOR KINEMATIC CORRECTIONS

B.1. *ep*-Elastic Kinematics

The corrections for the reconstructed momentum and polar angles of the electron come from the physics of relativistic elastic collisions. The calculations shown here are specific to the BLAST lab frame and the convenient convention $\hbar = c = 1$. Ideal kinematics constrains the reaction to be coplanar and the resultant equations are solely functions of the incident beam energy (E_0), the outgoing electron momentum (p_e[1]) and its polar angle (θ_e), the mass of the proton (m_p) and the outgoing momentum and polar angle of the proton (p_p and θ_p). The results allow us to calculate the outgoing momentum or polar angle as a function of the initial energy of the system and any other ougoing polar angle or momentum, e.g. $\theta_p = f(E_0, m_p, \theta_e)$ or $p_e = f(E_0, m_p, \theta_p)$.

A simple result to obtain $p_e(p_p)$ and its inverse comes directly from energy conservation, i.e.

$$E_0 + m_p = p_e + \sqrt{p_p^2 + m_p^2} \tag{B.1}$$

$$\rightarrow p_e = \sqrt{p_p^2 + m_p^2} - (E_0 + m_p) \tag{B.2}$$

$$\rightarrow p_p = \sqrt{(E_0 + m_p - p_e)^2 - m_p^2} \tag{B.3}$$

These two equations can now serve as substitutions in later results.

The simplest way to begin the more complex derivations of these first-order relationships is to use the four-momenta P_e, P_e', P_p, and P_p' which are four-momenta of the incoming

[1]The momentum of the outgoing electron can be considered to be equal to the final energy of the electron since it is ultra-relativistic.

and outgoing electron and the incoming and outgoing proton, respectively. To enumerate,

$$\begin{aligned} P_e &= (E_0, E_0\hat{z}) \\ P'_e &= (E_e = p_e, \vec{p}_e) \\ P_p &= (m_p, 0) \\ P'_p &= (E_p = \sqrt{p_p^2 + m_p^2}, \vec{p}_p) \end{aligned} \tag{B.4}$$

Energy and momentum conservation give,

$$P_e + P_p = P'_e + P'_p \tag{B.5}$$

These can be rearranged to make a set of two equations:

$$P_e + P_p - P'_e = P'_p \tag{B.6}$$

$$P_e + P_p - P'_p = P'_e \tag{B.7}$$

We square these and use the Minkowski inner product to obtain, respectively,

$$m_e^2 + P_e P^p - P_e P'^e - P'_e P^p = 0 \tag{B.8}$$

$$m_p^2 + P_e P^p - P_e P'^p - P_p P'^p = 0 \tag{B.9}$$

where the masses on both sides of the equation have cancelled and a factor of 2 has been divided out. The mass of the electron is more than 3 orders of magnitude smaller than the energies we are calculating and can be neglected. The terms will now be calculated individually,

$$P_e P'^e = E_0 p_e - E_0 p_e \cos\theta_e \tag{B.10}$$

$$P_p P'^p = m_p E_p = m_p \sqrt{p_p^2 + m_p^2} \tag{B.11}$$

$$P_e P^p = E_0 m_p \tag{B.12}$$

$$P'_p P^e = E_0 m_p - E_0 p_p \cos\theta_p. \tag{B.13}$$

$$P_e P'^p = E_0 * \sqrt{p_p^2 + m_p^2} - E_0 p_p \cos\theta_p \tag{B.14}$$

From eq. B.8, the terms allow us to calculate the momentum of the electron as a function of its outgoing angle, i.e.

$$p_e = \frac{E_0 m_p}{m_p + E_0(1 - \cos\theta_e)} \tag{B.15}$$

This equation can be easily inverted to give $\theta_e(p_e)$. From this equation and eq. B.2 and B.3, we can easily derive $\theta_e(p_p)$ and $p_p(\theta_e)$. Lastly, the second equation, B.9 is rewritten as,

$$0 = m_p^2 + E_0 m_p + E_0 p_p \cos\theta_p - (E_0 + m_p)\sqrt{p_p^2 + m_p^2} \tag{B.16}$$

$$\rightarrow p_p = \frac{2m_p(E_0 + m_p)}{E_0 \cos\theta_p \left[\left(\frac{E_0 + m_p}{E_0 \cos\theta_p}\right)^2 - 1\right]}, \tag{B.17}$$

$$\rightarrow \cos\theta_p = \frac{(E_0 + m_p)(sqrt(p_p^2 + m_p^2) - m_p)}{E_0 p_p} \tag{B.18}$$

These equations obviously give us the last remaining piece of the puzzle. Since we have $p_p(\theta_p), p_e(\theta_e), p_e(p_p)$ and their inverses, it is mere substitution and some hefty algebra to pull out the last relations between θ_e and θ_p. As a token of love, one of the relations has been included here:

$$\cos\theta_p = \frac{(E_0 + m_p) * \left(\sqrt{\left(m_p + E_0 - \frac{E_0 m_p}{m_p + E_0 - E_0 * \cos\theta_e}\right)^2} - m_p\right)}{E_0 \sqrt{\left(m_p + E_0 - \frac{E_0 m_p}{m_p + E_0 - E_0 * \cos\theta_e}\right)^2 - m_p^2}} \tag{B.19}$$

REFERENCES

[1] I. Esterman and O. Stern, The Physical Review **45**, 761 (1934)

[2] V.F. Sears, Physics Reports **141**, 281 (1986)

[3] J.J. Thomson, On the Charge of Electricity carried by the Ions produced in Röntger Rays, Philosophical Magazine (1898)

[4] H. Goldstein, C. Poole, J. Safko, Classical Mechanics (2nd ed.), New York, Addison-Wesley, 105-119 (2002)

[5] J. D. Jackson, Classical Electrodynamics (3rd Ed.), New York, John Wiley & Sons, 456 (1998)

[6] E. Rutherford, The Scattering of α and β Particles by Matter and the Structure of the Atom, Philosophical Magazine, Series 6, vol. 21 (1911)

[7] R. Hofstadter et al., The Physical Review **92**, 978 (1953)

[8] M.N. Rosenbluth, The Physical Review **79**, 615 (1950)

[9] F.J. Ernst, R.G. Sachs, and K.C. Wali, The Physical Review, **119**, 1105 (1960)

[10] T. Janssens et al., The Physical Review **114**, 922 (1966)

[11] L. E. Price et al., Backward-angle electron-proton elastic scattering and proton electromagnetic form-factors, The Physical Review D **4**, 45 (1971)

[12] C. Berger, V. Burkert, G. Knop, B. Langenbeck, and K. Rith, Electromagnetic form-factors of the proton at squared four momentum transfers between 10 fm^2 and 50 fm^2. Physical Letters B **35**, 87 (1971)

[13] K.M. Hanson et al., The Physical Review D **8**, 753 (1973)

[14] G. Höhler, Nuclear Physics B **114**, 505 (1976)

[15] G. G. Simon, C. Schmitt, F. Borkowski, and V. H. Walther, Absolute electron proton cross-sections at low momentum transfer measured with a high pressure gas target system., Nuclear Physics A **333**, 381 (1980)

[16] A. F. Sill et al., Measurements of elastic electron-proton scattering at large momentum transfer. The Physical Review D **48**, 29 (1993)

[17] L. Andivahis et al., Measurements of the electric and magnetic form-factors of the proton from $Q^2 = 1.75$ (GeV/c)^2 to 8.83 (GeV/c)^2. The Physical Review D **50**, 5491 (1994)

[18] R. C. Walker et al., Measurements of the proton elastic form-factors for 1 (GeV/c)$^2 \leq Q^2 \leq 3$ (GeV/c)^2 at SLAC. Physical Review D **49**, 5671 (1994)

[19] W. Bartel et al., Phyics Letters **39B**, 407 (1972)

[20] S.Rock et al., Physical Review Letters **49**, 1139 (1982)

[21] R.G.Arnold et al., Physical Review Letters **61**, 806 (1988)

[22] A.Lung et al., Physical Review Letters **70**, 718 (1993)

[23] P.Markowitz et al., Physical Review C **48**, R5 (1993)

[24] H.Anklin et al., Physics Letters B **336**, 313 (1994)

[25] H.Gao et al., Physical Review C **50**, R546 (1994)

[26] E.E.W.Bruins et al., Physical Review Letters **75**, 21 (1995)

[27] G.Kubon et al., Physics Letters B **524**, 26 (2002)

[28] J.Jourdan et al., Physical Review Letters **79**, 5186 (1997)

[29] H.Anklin et al., Physics Letters B **428**, 248 (1998)

[30] W.Xu et al., Physical Review Letters **85**, 2900 (2000)

[31] W.Xu et al., Physical Review C **67**, R012201 (2003)

[32] N. Meitanis, A Measurement of the Neutron Magnetic Form Factor G_M^n from Quasi-elastic $^2\vec{H}(\vec{e}, e')$ at low Q^2, Ph.D. thesis, MIT (2006)

[33] T.W. Donnelly and A.S. Raskin, Annals of Physics **169**, 247 (1986)

[34] A.S. Raskin and T.W. Donnelly, Annals of Physics **91**, 78 (1989)

[35] H. Arenhövel, W. Leidemann, E.L. Tomusiak, General Survey of Polarization Observables in Deuteron Electrodisintegration, European Physical Journal A **23**, 147 (2005)

[36] J. Carlson and R. Schiavilla, Reviews of Modern Physics **70**, 743 (1998)

[37] J.L. Friar, Physical Review C **20**, 325 (1979)

[38] M. Garcon and J.W. Van Orden, The Deuteron: Structure and Form Factors, Advances in Nuclear Physics **26**, 293 (2001)

[39] P.U. Sauer and H. Henning, Few-Body Systems, Suppl. **7**, 92 (1994)

[40] J. Martorell, D.W.L. Sprung and D.C. Zheng, Physical Review C **51**, 1127 (1995)

[41] J. Arrington and I. Sick, Coulomb distortion in high-Q^2 elastic e-p scattering, Physical Review C **70**, 028203 (2004)

[42] R.B. Wiringa, V.G.J. Stoks, and R. Schiavilla, An accurate nucleon-nucleon potential with charge independence breaking, Physical Review C **51**, 38 (1995)

[43] J.L. Friar and G.L. Payne, Physical Review A **56**, 5173 (1997)

[44] R. Machleidt. The high precision, charge-dependent Bonn nucleon-nucleon potential (CD-Bonn), Physical Review C **63**, 024001 (2001)

[45] A.J. Buchmann, H. Henning, and P.U. Sauer, Meson and Quark Degrees of Freedom and the Radius of the Deuteron, Few Body Systems **21**, 149 (1996)

[46] M. Bernheim et al., Momentum Distribution of Nucleons in the Deuteron from the $^2H(e,e'p)n$ Reaction, Nuclear Physics A **365**, 349 (1981)

[47] S. Turck-Chieze et al., Physics Letters B **142**, 145 (1984)

[48] H. Breuker et al., Nuclear Physics A **455**, 641 (1986)

[49] K.I. Blomqvist et al., Physics Letters B **424**, 33 (1998)

[50] J.E. Ducret et al., Physical Review C **49**, 1783 (1994)

[51] D. Jordan et al., Physical Review Letters **74**, 4775 (1996)

[52] R. Gilman and F. Gross, Electromagnetic Structure of the Deuteron, Journal of Physics G **28**, R37 (2001)

[53] S. Galster et al., Nuclear Physics B **32**, 221 (1971)

[54] S. Platchkov, Nuclear Physics A **510**, 740 (1990)

[55] J.S. Poucher et al., Physical Review Letters **32**, 118 (1974)

[56] unpublished (1973)

[57] H.D. Politzer, Physical Review Letters **30**, 1346 (1973)

[58] D.J. Gross and F. Wilczek, Physical Review Letters **30**, 1343 (1973)

[59] K. Wilson, Quarks and Strings on a Lattice, Erice Lecture Notes, published 1975)

[60] S.J. Brodsky and G.R. Farrar, Scaling laws for large-momentum-transfer processes, Physical Review D **11**, 1309 (1975)

[61] S.J. Brodsky and B.T. Chertok, Asymptotic form factors of hadrons and nuclei and the continuity of particle and nuclear dynamics, Physical Review D **14**, 3003 (1976)

[62] G.P. Lepage and S.J. Brodsky, Exclusive processes in perturbative quantum chromodynamics, Physical Review D **22**, 2157 (1980)

[63] L.L. Foldy, Physical Review **87**, 692 (1952)

[64] L.L. Foldy, Review of Modern Physics **30**, 471 (1958)

[65] S. Kopecky et al., Neutron charge radius determined from the energy dependence of the neutron transmission of liquid ^{208}Pb and ^{209}Bi, Physical Review C **56**, 2229 (1997)

[66] C. Alexandrou, Hadron Deformation and Form Factors from Lattice QCD, from Workshop "The Shape of Hadrons", Greece, April 2006.

[67] C. Alexandrou et al., Nucleon electromagnetic form factors from lattice QCD, Physical Review D **74**, 34508 (2006)

[68] J.D. Ashley et al., Nucleon electromagnetic form factors from lattice QCD, European Physical Journal A, S **19**, 9 (2004)

[69] Göckeler et al., Nucleon electromagnetic form factors on the lattice and in chiral effective field theory, Physical Review D **71**, 34508 (2005)

[70] M.J. Musolf and M. Burkhardt, Stranger Still Kaon Loops and the Strange-Quark Content of the Nucleon, Zeitschrift für Physik C **61**, 433 (1994)

[71] W. Koepf and E.M. Henley, Physical Review C **49**, 2219 (1994)

[72] F. Gross and O. Riska, Physical Review C **36**, 1928 (1987)

[73] K. Ohta, Physical Review C **40**, 1335 (1989)

[74] G.A. Miller and A.W. Thomas, Electromagnetic gauge invariance of the cloudy bag model, Physical Review C **56**, 2329 (1997)

[75] G.A. Miller, Light front cloudy bag model: Nucleon electromagnetic form factors, Physical Review C **66**, 32201 (2002)

[76] T.H.R. Skyrme, Nuclear Physics **31**, 556 (1962)

[77] G. Holzwarth, Electromagnetic Form Factors of the Nucleon in Chiral Soliton Models, Nucleon05 workshop, Frascati, Oct. 12 2005.

[78] W.H. Hammer and Ulf-G. Meißner, Updated dispersion-theoretical analysis of the nucleon electromagnetic form factors, European Physical Journal A **20**, 469 (2004)

[79] M.F. Gari and W. Kruempelmann, Semiphenomenological synthesis of meson and quark dynamics and the electromagnetic structure of the nucleon, Zeitschrift für Physik A **322**, 689 (1985)

[80] R.G. Arnold, C.E. Carlson, and F. Gross, Polarization transfer in elastic electron scattering from nucleons and deuterons, Physical Review C **23**, 363 (1981)

[81] R. Schiavilla, Nuclear Physics A **689**, 84c (2001)

[82] R. Schiavilla and I. Sick, Neutron charge form factor at large q^2, Physical Review C **64**, 41002 (2001)

[83] C. Zhang, Measurement of Tensor Analyzing Powers in Elastic Electron Deuteron Scattering with BLAST, Ph.D. Thesis, MIT (2006)

[84] J. Becker et al., Determination of the neutron electric form factor from the reaction ^{3}He(e,e'n) at medium momentum transfer, European Physical Journal, A **6**, 329 (1999. Reanalyzed by J. Golak et al., Extraction of electromagnetic neutron form factors through inclusive and exclusive polarized electron scattering on a polarized ^{3}He target, Physical Review C **63**, 34006 (2001)

[85] J. Bermuth et al., Physics Letters B **564**, 199 (2003)

[86] T. Eden et al., Physical Review C **50**, R1749 (1994)

[87] D.I. Glazier et al., Measurement of the Electric Form Factor of the Neutron at $Q^2 =$ 0.3-0.8 (GeV/c)^2, European Physical Journal A **24**, 101 (2005)

[88] C. Herberg et al., European Physical Journal A **5**, 131 (1999)

[89] R. Madey et al., Physical Review Letters **91**, 122002 (2003)

[90] M. Ostrick et al., Physical Review Letters **83**, 276 (1999)

[91] I. Passchier et al., Physical Review Letters **82**, 4988 (1999)

[92] D. Rohe et al., Physical Review Letters **83**, 4257 (1999)

[93] G. Warren et al., Measurement of the Electric Form Factor of the Neutron at $Q^2 = 0.5$ and 1.0 (GeV/c)^2, Physical Review Letters **92**, 42301 (2004)

[94] Zhu et al., Physical Review Letters **87**, 81801 (2001)

[95] J. Friedrich and T. Walker, A Coherent Interpretation of the Form Factors of the Nucleon in terms of a Pion Cloud and Constituent Quarks, European Physical Journal A **17**, 607 (2003)

[96] J. van der Laan et al., Bates South Hall Ring Commission For Internal Target Experiments, IEEE Proc. PAC2003, 2324 (2003)

[97] P. Ivanov, Y.M. Shatunov, T. Zwart, A Universal Superconducting Spin Rotator for the MIT-Bates South Hall Ring, Bates Doc. B/SHR 93-10 (1993)

[98] T. Zwart et al., Polarized Electrons in the MIT-Bates South Hall Ring, IEEE Proc. PAC2001, 3597 (2001)

[99] T. Zwart et al., A Spin Control System For The South Hall Ring At The Bates Linear Accelerator Center, UNKNOWN Conference Proceedings (1989)

[100] I. Passchier et al., Nuclear Instruments and Methods A **414**, 446 (1998)

[101] B. Franklin, The MIT-Bates Compton Polarimeter, Presentation from Workshop on EIC Polarimetry, Brookhaven National Laboratory (2002)

[102] I. Rabi, S. Millman, P. Kusch, and J. Zacharias, Physical Review **55**, 526 (1939)

[103] D.J. Larson, P.A. Valberg, N.F. Ramsey, Physical Review Letters **23**, 1369 (1969)

[104] J. Stenger, K. Rith, Nuclear Instruments and Methods A **361**, 60 (1995)

[105] A. Abragam and J.M. Winter, Physical Review Letters **1**, 374 (1958)

[106] R.J. Philpott, Nuclear Instruments and Methods A **259**, 317 (1987)

[107] V. Ziskin, A Measurement of the Electric Form Factor of the Neutron at Low Momentum Transfers Using a Vector Polarized Gas Deuterium Target at BLAST, Ph.D. thesis, MIT (2005)

[108] J.A. Fedchak et al. Nuclear Instruments and Methods S **391**, 405 (1997)

[109] L.W. Anderson and D.R. Swenson, Nuclear Instruments and Methods B **12**, 157 (1985)

[110] M.A. Bouchiat and J. Brossel, Physical Review **147**, 41 (1966)

[111] C. Baumgarten, Studies of Spin relaxation and Recombination at the HERMES Hydrogen/Deuterium gas target, Ph.D. thesis, University of Munich (2000)

[112] Bulten et al., Physical Review A **58(2)**, 1146 (1998)

[113] M. Desaintfuscien and C. Audoin, Physical Review A **13(6)**, 2070 (1976)

[114] L.C. Alexa et al., Nuclear Instruments and Methods A **365**, 299 (1995)

[115] D.W. Higinbotham, Nuclear Instruments and Methods A **414**, 332 (1998)

[116] BLAST Technical Design Report, Bates Linear Accelerator Center (1997)

[117] W.H. Press et al., Numerical Recipes in Fortran 77, Second Edition, Cambridge University Press, Cambridge (1992)

[118] R.T. Giles, Nuclear Instruments and Methods in Physics Research A, 252 (1986)

[119] A. Afanasiev, I. Akushevich, and N. Merenkov. arXiv:hep-ph/0102086 (2005)

[120] H. Arenhövel, W. Leidemann, and E. Tomusiak, Physical Review C **46**, 455-470 (1992)

[121] S.D. Drell and F. Zachariasen, Electromagnetic Structure of Nucleons, Oxford University Press, London (1961)

[122] A. Maschinot, Analysis of Scattered Protons in Deuteron Electrodisintegration with a Polarized Electron Beam and an Internal Polarized Target, PhD Thesis, MIT (2005)

[123] A. Degrush, Personal Correspondence.

[124] A. Afanasiev, I. Akushevich, and N. Merenkov, Physical Review D **64**, 113009 (2001)

[125] P.R. Bevington and D.K. Robinson, Data Reduction and Error Analysis for the Physical Sciences, McGraw-Hill, New York City (2003)

[126] H. Arenhövel, Physical Letters B **26**, 13 (1987)

[127] J. Kelly, Physical Review C, **66**, 065203 (2002)

[128] S. Weinberg, Physics Letters B **251**, 288 (1990)

[129] S. Weinberg, Nuclear Physics B **363**, 3 (1991)

[130] S. Weinberg, Physics Letters B **295**, 114 (1992)

[131] N. Isgur. Physical Review Letters, **83**, 272 (1999)

[132] B. Ma, D. Qing, and I. Schmidt, Physical Review C **65**, 035205 (2002)

[133] E. Lomon, Physical Review C **64**, 035204 (2001)

[134] M. Kaskulov and P. Grabmayr, arXiv:nucl-th/0308015 (2003)

[135] F. Cardarelli and S. Simula, arXiv:nucl-th/9909025 (1999)

[136] R. Wagenbrunn et al., arXiv:hep-ph/0212190 (2002)

[137] J. Gasser and H. Leutwyler, Annals Phys. **158**, 142 (1984)

[138] Michael Kohl, private communication.

[139] I. Sick, Nuclear Physics A **218**, 509 (1974)

[140] Ulf-G. Meißner, arXiv:nucl-th/0701094 (2007)

[141] H. W. Hammer, Eur. Phys. J. **A 28**, 49 (2006)

[142] M. A. Belushkin, H. W. Hammer, and Ulf-G. Meißner, arXiv:hep-ph/0608337 (2006)